Ion Implantation into Boron Suboxide: Formation of Boron-Rich Structures and Related Phenomena

Ronald Machaka

School of Chemical and Metallurgical Engineering
University of the Witwatersrand, Johannesburg

A thesis submitted to the Faculty of Engineering and Built Environment, University of the Witwatersrand, Johannesburg, in fulfillment of the requirements for the degree of Doctor of Philosophy.

May 2012

Ion Implantation into Boron Suboxide: Formation of Boron-Rich Structures and Related Phenomena

Ronald Machaka

May 14, 2012

AUTHOR'S DECLARATION FOR ELECTRONIC SUBMISSION OF A THESIS

I declare that this thesis is my own unaided work. It is being submitted for the degree of Doctor of Philosophy to the University of the Witwatersrand, Johannesburg. It has not been submitted before for any degree or examination to any other university.

I understand that my thesis may be made electronically available to the public.

Ronald Machaka
May 14, 2012

Abstract

This thesis focuses on the boron suboxide B_6O, a boron-rich super-hard ceramic material. With hardness values previously reported between 24 GPa and 45 GPa, B_6O is one of the hardest known materials. Although first reports on boron suboxides date back as far as 1909 (Weintraub E., *Transactions of the American Electrochemical Society*, **16** (1909) 165), it is the B_6O-based composites that have attracted considerable interest in recent years due to their enormous technological potential, especially as an alternative to polycrystalline diamond and polycrystalline cubic boron nitride for wear and abrasive applications. Investigations into the properties of B_6O itself appear to have been neglected in favour of the improvement of densification and fracture toughness of the composites.

The B_6O samples used for the work reported in this work was hot-pressed was prepared under an argon environment at 1800 °C and 50 MPa for 20 minutes followed metallographical preparation. The density of the hot-pressed compacts measured 2.44 g/cm^3. The starting B_6O powder material was supplied from the Fraunhofer Institute for Ceramic Technologies and Systems, Dresden.

This thesis primarily seeks to generate and report as much practical data for polycrystalline B_6O materials prepared by uniaxial hot-pressing as possible from a variety of characterization techniques. Firstly, the Raman spectra of hot-pressed B_6O, which was until now poorly understood, was investigated using using a 514.5 nm green Ar^+ laser excitation source. Secondly, the fundamental nature of some mechanical properties of hot-pressed B_6O were investigated by means of Vickers and Berkovich indentation techniques. New approaches for data analysis, especially the investigations of the nanomechanical properties of hot-pressed B_6O by Berkovich nanoindentation, were also suggested. Thirdly, the intrinsic hardness of hot-pressed B_6O was investigated by means of a comprehensive inter-model comparison study. Fourthly, a combined experimental and simulation approach for determining mechanical properties of hot-pressed B_6O by nanoindentation was also carried out, based on the outcomes of the study, the deformation response of the material under dynamic indentation was investigated at different stages using a custom developed

finite element model. Finally, based on the preliminary *ab initio* density functional calculations of the structural properties of B_6O conducted by Lowther showing that the presence of a high electronegativity interstitial in the B_6O structure could enhance the strength of the bonding in B_6O, fluorine ion implantation into B_6O were conducted. The effects to the structural and the nanomechanical properties of radiation damage induced by ion implantation was investigated. The possible formation of novel nanostructures in the ion-irradiated B_6O matrix near-surface was also investigated.

Results obtained from this study provides a vast amount of practical data for hot-pressed B_6O materials as well as a number of novel analysis approaches for the extraction useful properties from the measured raw data. Firstly, using an automated background subtraction method, observable first- and second-order Raman spectra of B_6O were obtained. A comparative analysis with previously reported spectra of other α-rhombohedral boron-rich ceramic materials demonstrate a good agreement. Results also confirm the existence of highly resolved Raman modes measured at ambient conditions using a green Ar^+ excitation source which is contrary to the conventional understanding. Secondly, results from the micro-indentation investigations indicate the measured microhardness exhibits indentation load dependence. A model inter-comparison study of indentation size effects in the microhardness measurements of hot-pressed B_6O is comprehensively discussed. Thirdly, the intrinsic hardness value of 30 GPa was deduced. Fourthly, a quantitative analysis approach was developed to simulate multi-cycling loading load-displacement curves from a single measured load-displacement nanoindentation curve. Based on the results, the nature of the indentation size effect in the nanoindentation hardness as well as the intrinsic nanomechanical properties of hot-pressed B_6O were established. Fifthly, a combined experimental and finite element method simulation approach for determining mechanical properties of hot-pressed B_6O by nanoindentation was developed. Based on the outcomes of the combined experimental and simulation studies, the deformation response of the material under dynamic indentation was also investigated at different stages using a custom developed finite element model. Finally, results from the structural characterization of the ion implanted B_6O material demonstrates the formation of novel nanostructures by means of the ion bombardment of B_6O. In addition, the study presented here also seeks to investigate the effects of the fluorine ion implantation on the near-surface nanomechanical properties of hot-pressed B_6O.

The principal conclusions that the study provide are both comprehensive practical data for B_6O materials prepared by uniaxial hot-pressing. A number of properties, including the Raman spectra, the intrinsic hardness, and the radiation resistance and the effects of radiation damage are reported in the thesis.

Acknowledgements

The work reported in this thesis was generously funded through the DST/NRF Centre of Excellence in Strong Materials and a University of the Witwatersrand Mellon Postgraduate Award. I gratefully acknowledge their support.

Thanks to my supervisors T.E. Derry and I. Sigalas for their dynamic and sustained support over the past years. I wish to thank M. Herrmann, B.W. Mwakikunga, and E. Manikandan for the valuable discussions and diligently reviewing numerous manuscripts.

I would like to express my appreciation to O.T. Johnson, W. Matizamhuka, T. Mawela, S. Srivastava, R.M. Erasmus, D. Billing, M. Fernandes, N. Coville, M. Mamo, S. Masete, and R. Cruise for their valuable time and lending hands to my research. Thanks to J. Dean and T. Clyne (both from University of Cambridge), A.K. Arora (IGCAR, Kalpakkam, India) and H. Werheit (University Duisburg-Essen, Duisburg) for sharing references and interesting discussions on specific aspects of my project despite not knowing me at all!

I also wish to acknowledge the invaluable technical support from the following institutions: Fraunhofer Institute for Ceramic Technologies and Systems, Dresden, Wits Schools of Chemical and Metallurgical Engineering, Physics, and Chemistry, NMMU Department of Physics, CSIR National Centre for Nano-Structured Materials, Diamond Research Laboratory at Element Six, and the iThemba LABS (Gauteng).

I am greatly indebted to the social support I got from my siblings, the M5 pandits, and especially my ambitious parents. The mere thought of extending my deepest appreciation to my bundles of joy - Nono and Sibu, simply tickles me...

My sincere apologies to those whose contributions I have omitted by mistake or by resolve.

Ndopfirira nekupupurira simba nengoni dzaJehovha.

List of Publications and Awards

A. Awards

1. 2011 *Advanced Materials Letters Scientist* Award (Nominated)
2. Mellon Postgraduate Mentoring Scheme Award (January 2011 – December 2011)
3. Best oral PhD student presentation – 2010 *55th Annual South African Institute of Physics, CSIR ICC, Pretoria*

B. Peer review journals

1. R. Machaka, R.M. Erasmus, & T.E. Derry, 'Formation of cBN nanocrystals by He^+ implantation into hBN', *Diamond & Related Materials* 2010, **19** pp 1131-1134
2. R. Machaka, B.W. Mwakikunga, E. Manikandan, T.E. Derry, & I. Sigalas, 'Raman spectrum of hot-pressed boron suboxide', *Advanced Materials Letters*, 2011 **2**(1) pp 56-64
3. R. Machaka, T.E. Derry, I. Sigalas & M. Herrmann, 'Analysis of the indentation size effect in the microhardness measurements in B_6O', *Advances in Materials Science and Engineering*, (2011), Volume 2011, Article ID 539252, doi:10.1155/2011/539252
4. R. Machaka, T.E. Derry & I. Sigalas, 'Nanoindentation hardness of hot-pressed boron suboxide', *Materials Science and Engineering A*, 2011 **528** 5778
5. R. Machaka, B.W. Mwakikunga, E. Manikandan, T.E. Derry, I. Sigalas & M. Herrmann, 'Structural and mechanical properties modifications of hot-pressed boron suboxide by fluorine ion implantation', *Advances in Materials Science and Engineering* Special Issue on the *Modification, Synthesis, and Analysis of Advanced Materials Using Ion Beam Techniques*, (2012) Volume 2012, Article ID 792973, doi:10.1155/2012/792973 (Invited paper)

6. R. Machaka, B.W. Mwakikunga, E. Manikandan, T.E. Derry & I. Sigalas, 'Structural transformation in ultrahard B_6O induced by F-ion implantation studied by micro-Raman spectroscopy', *Submitted*, 2012

C. Conference publications

1. R. Machaka, T.E. Derry, & I. Sigalas, 'Some nanomechanical properties of hot-pressed boron suboxide', *6^{th} International Conference of the Africa Materials Research Society, 11 – 16^{th} December 2011, Elephant Hills Resort Victoria Falls, Zimbabwe*
2. R. Machaka, T.E. Derry, I. Sigalas &, M. Herrmann, 'Measurement and modelling of the nanoindentation response of hot-pressed boron suboxide', *The 9^{th} International Meeting of Pacific Rim Ceramic Societies, 10 – 14^{th} July 2011, Cairns Convention Centre, Cairns, Australia*
3. R. Machaka, T. E. Derry, I. Sigalas &, M. Herrmann, 'Analysis of the nanoindentation load-depth curves measured on fluorine ion implanted B_6O ceramics', *2010 Powder Metallurgy Association (South Africa) Annual Conference, 27^{th} October 2010, Debtech Auditorium Crown Mines, Johannesburg*
4. R. Machaka, B. W. Mwakikunga, E. Manikandan, T. E. Derry & I. Sigalas, 'Raman spectrum of hot-pressed boron suboxide: Some new results', *55^{th} Annual South African Institute of Physics, 27^{th} September – 1^{st} October 2010, CSIR ICC, Pretoria*
5. R. Machaka, B. W. Mwakikunga, E. Manikandan, T. E. Derry & I. Sigalas, 'Nanoindentation characterization of hot-pressed B_6O', *55^{th} Annual South African Institute of Physics, 27^{th} September – 1^{st} October 2010, CSIR ICC, Pretoria*

Ah Love! could thou and I with fate conspire
To grasp this sorry Scheme of Things entire,
Would not we shutter it to bits – and then,
Re-mould it nearer to the heart's desire!

Omar Khayyam (1048 – 1131)

Contents

List of Figures

List of Tables

Part I

General Presentation

Chapter 1

Introduction

1.1 Introduction and motivation

Boron is an element of fascinating chemical complexity. It has the second most complicated structural chemistry among all elements at ambient conditions only after carbon. Thus boron in it's molecular, ionic, and solid state environments can form a wide range of structural variations of boron modifications and boron-rich compounds characterized by B_{12} icosahedra as their essential common structure elements extends from α-rhombohedral boron with 12 B atoms to YB_{66} and its homologous compounds with 1632 B atoms per unit cell [1, 18]. Oganov [29] states that "Boron is an element of fascinating chemical complexity ... Boron's complexities arise from frustration: situated between metals and insulators in the Periodic Table, boron has only three valence electrons, which would favour metallicity, but they are sufficiently localized that insulating states emerge".

Boron-based structures form an important class of materials with scientific, industrial, and commercial importance as a direct result of their unique and superior physicochemical properties and possible applications [1, 14, 41]. Such properties include strong and short covalent bonded structures, low density values, high hardness, high melting point, high mechanical strength, inferior in abrasive wear resistance, high thermal conductivity, neutron scattering cross-section, and high chemical inertness. Some of the application fields include synthesis of chemically inert and refractory borides, abrasives, dopants to heat-resistant alloys, components of multi-purposes ceramic materials, nuclear energy (boron), elements of cutting tools, composites, abrasives (boron carbides), high-temperature ware, semiconducting devices, chemical engineering (nitrides, phosphides, and arsenides),

important precursors for the preparation of other numerous boron compounds (oxides) [1, 14]. Of relevance to this work is hexaboron suboxide B_6O, is considered one of the hardest materials after diamond, cubic boron nitride *c*BN and the boron carbonitride BC_2N [11, 41]. The work presented in this thesis is focussed on B_6O prepared by uniaxial hot-pressing.

1.1.1 Boron suboxide

Boron suboxides belongs to the important group of non-metallic hard ceramic materials, which includes boron carbide, silicon carbide, cubic boron nitride and diamond [1, 24]. Although no commercial applications are available yet, boron suboxides, especially B_6O appears to be a suitable candidate for cutting tool (for both ferrous and non-ferrous materials) and other applications where abrasive wear resistance is important (see Figure 1.1 and Table 1.1) [9, 19, 35]. The material might be suitable for applications in nuclear power engineering and chemical industries, in thermoelectric energy converters and composites due to their attractive combination of properties.

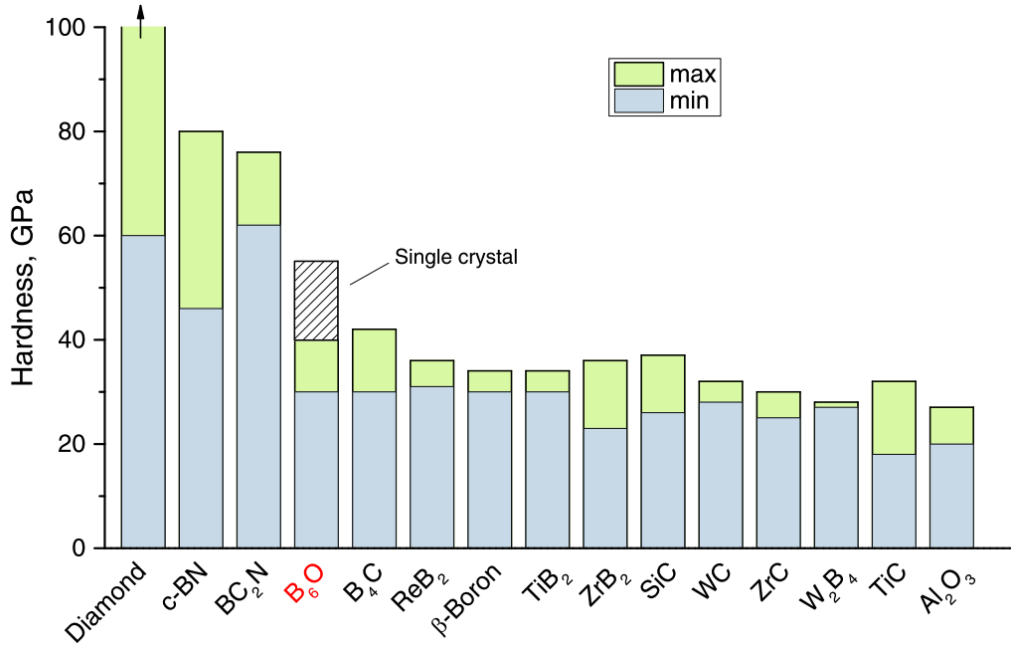

Figure 1.1: *A comparison of the microhardness of B_6O and other hard materials, Hermann et al. [11].*

Boron suboxides are perhaps the earliest boron-rich compounds studied by chemists. Although the suboxide B_7O was first thought to exist by Weintraub in 1909 [42] and only later proven [13, 31], other suboxides $B_{12}O_2$ (or B_6O) [6, 7, 33], and $B_{13}O_2$ [17] were reportedly synthesized by chemists with firmly established formulae four decades later

with lacking structural information. Since Badzian in [4] and others [2, 8, 35] have pointed out that B_6O is a superhard material with a hardness rivalling that of *c*BN since B_6O bulk powders may be produced without the need for high pressures [35], scientists began to pay more attention to these borides. Today, the synthesis and consolidation of powders of boron suboxides have been extensively reported in literature [1, 15, 23], various methods are well established [2] and the structure of B_6O is now well established [1, 2], see also next section. Although B_6O can be synthesized at or near ambient pressure conditions, unlike diamond and *c*BN, there are serious challenges to be addressed before the material and its synthesis mechanisms are adopted by the industry. For example, B_6O composites formed at or near ambient pressure are generally non-stoichiometric and oxygen deficient with reported compositions ranging from $B_6O_{0.72}$ to $B_6O_{0.96}$ [1, 19, 26]. The densification of B_6O powders is generally between 97% and 80%, and most of all, some properties of the hot-pressed material are not well understood [5, 16, 19].

1.1.2 Properties of boron suboxide

First and foremost, B_6O bulk powders may be produced without the need for high pressures [35], in addition to that its considered the third hardest material after diamond and *c*BN [41]. The material has high hardness with low density, high mechanical strength, high melting point, and is chemically inert [16, 19]. Table 1.1 lists some of the properties of the material.

1.1.3 Crystal structure

B_6O is characterised by an α-rhombohedral boron-type structure ($R\bar{3}m$ space group) [24, 41, 43]. A structure similar to other super-hard boron-rich materials, namely boron carbide (B_4C) [39] aluminium magnesium boride ($AlMgB_4$) [34], and the newly synthesized boron subnitride ($B_{13}N_2$) [21, 38].

The α-rhombohedral boron-type structure is based on slightly distorted 12-atom B_{12} icosahedra located at the corners of the unit cell [43, 44]. Two oxygen atoms sit on the spatial diagonal of the rhombohedral unit cell, each connecting three B_{12} icosahedral units. This leads to the composition $B_{12}O_2$ (or B_6O, as will be used throughout this text). Figure 1.2 depicts the widely accepted B_6O crystal structure. The O−O distance was determined as 306 – 308 pm, and the shortest distance between an O atom and the icosahedra is 143 pm. Olofsson and Lundstrom report an underoccupancy of the 6*c* site, and measured an O−O distance of 300.4 pm and short O−B distances of 147.6 pm [30]. The O−O bond is practically not practicable.

Property	Boron suboxide, B_6O	Refs.
Bulk density (g/cm^3)	2.51	[3]
Crystal structure	Rhombohedral	[24, 30]
Space group	R$\bar{3}$m	[1, 11, 24]
Unit cell dimensions		[24, 28]
a (Å)	5.3974	
c (Å)	12.3173	
V (Å^3)	314.5	
Vickers hardness (GPa)	28 – 45	[11, 15]
Fracture toughness (MPa· m$^{1/2}$)	2.1	[26, 40]
Young's modulus (GPa)	280 – 480	[27, 35]
Bulk modulus (GPa)	230	[22, 35]
Shear modulus (GPa)	206	[22, 35]
Strength (MPa)	280	[10]
Poisson ratio	0.18	[22]
Thermal decomposition (°C)	1200	[20]
Melting point (°C)	2366.85 – 2640 at 4.3 GPa	[22, 37]
Thermal conductivity (W/mK)	18.1	[40]
Thermal diffusivity (mm^2/s)	9.1	[40]
Coefficient of thermal expansion (K$^-$)	5.65 $\times 10^{-6}$	[12, 40]
Standard enthalpy of formation (kJ/mol)	527	[25]

Table 1.1: *Some properties of hot-pressed B_6O.*

The role of oxygen in the structure B_6O crystal structure has been reported upon [22, 28], the structure of the material is now well studied with various reports confirming expectations that three-dimensional short covalent bonding in B_6O favours superhardness [1, 45]. It is widely accepted that the hardness of B_6O materials relate to the electronic charge densities associated with the boron icosahedra [22]. The B_{12} icosahedron is generally electron deficient. The introduction of highly electronegative oxygen reportedly helps to reduce the electron deficiency of the β-rhombohedral structure [36], leads to stronger B_{12} intra-cluster bonds in B_6O [28], and improves the overall rigidity of the structure through cross-linking B_{12} icosahedra and filling voids [36]. This explains why B_6O is a superhard material [28, 36, 45].

1.2 Research objectives

Despite being an object of intense interest in recent years, some properties of the hot-pressed ceramic material remain unreported and poorly understood. For example, a

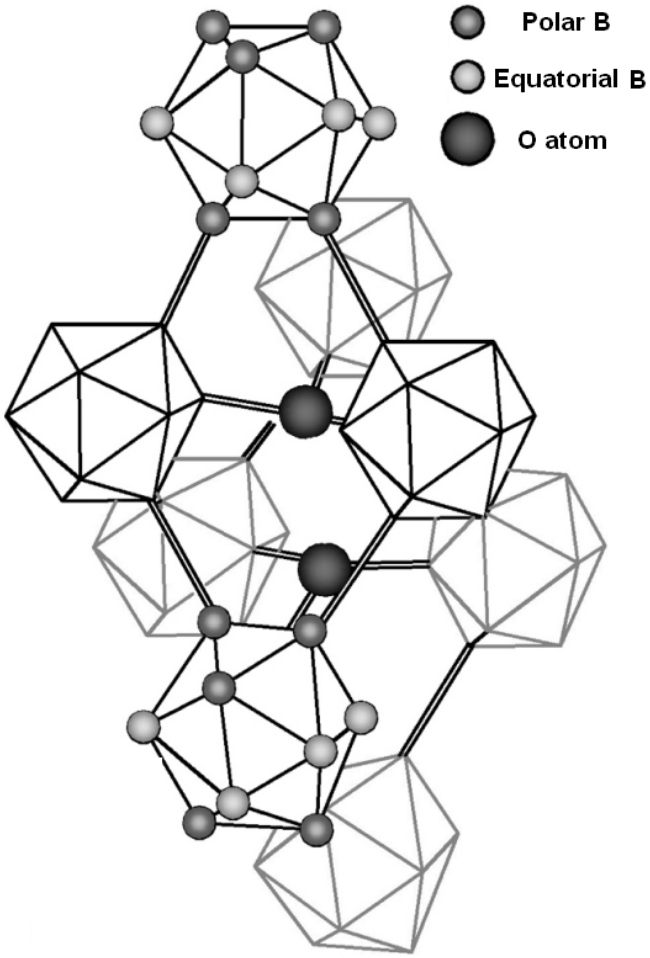

Figure 1.2: *The phenomenological model of chemical bonding in B_6O McMillan et al. [26].*

comprehensive literature survey conducted at the beginning of the study shows that the Raman spectra of the hot-pressed material, the nanomechanical properties (hardness, elastic modulus, and plastic deformation) investigated by microindentation and nanoindentation techniques, the indentation load-size dependence, as well as the effects of radiation damage (introduced by ion implantation) on the integrity of the material's superior properties all appear to have been neglected in favour of the improvement of densification and fracture toughness of the B_6O-based composites and are therefore still poorly understood.

The thesis seeks to generate and report practical data for B_6O materials prepared by uniaxial hot-pressing using a variety of characterization techniques. The objectives of this thesis are fourfold: Firstly, to contribute towards a better understanding of the Raman spectra of hot-pressed B_6O measured using a 514.5 nm green Ar^+ laser excitation source. Secondly, to provide fundamental understanding into the nature and the origins of (micro- and nano-) hardness load-dependence phenomenon of the ceramic material by means of

a comprehensive inter-model comparison study using the classical Meyer's law, propositional resistance models, and the multi-fractal scaling law. The intrinsic hardness of the material can be deduced. Thirdly, to present a combined experimental and finite element method simulation approach for determining mechanical properties of hot-pressed B_6O by nanoindentation. Based on the outcomes of the combined experimental and simulation studies, the deformation response of the material under dynamic indentation was also investigated at different stages using a custom developed finite element model. And finally, the thesis also seeks report on the of ion beam-synthesized nanostructures possibly formed by means of the ion bombardment of B_6O. In addition, the study presented here also seeks to investigate the effects of the fluorine ion implantation on the near-surface nanomechanical properties of hot-pressed B_6O.

1.3 Thesis organization

The thesis is based and organized by publications. Some of the material in this thesis has been presented previously in the publications listed in the List of Publications (see Section on page v).

The thesis is structured as follows. Chapter 2 provides a very brief overview of the the material preparation methods, and relevant techniques used. In Chapter 3, the existence of observable first- and second-order Raman spectra of hot-pressed B_6O measured using the Ar^+ laser excitation source is discussed. In Chapter 4, the indentation load-size dependence phenomenon in the measured microhardness of hot-pressed B_6O is investigated. The nature and the origins of indentation size effect (ISE) are also discussed. Chapter 5 describes a combined experimental and finite element method simulation approach for determining nano-mechanical properties of hot-pressed B_6O by nanoindentation is presented. Chapter 6 presents the applications of SEM and EDX, AFM, and Raman spectroscopic in the characterization of ion-implanted B_6O.The formation of ion beam induced formation of a nanostructured phase embedded in the B_6O matrix is also discussed. Based on a Richter-Wang-Ley phonon confinement interpretation [32], the average crystallite size of the nanoparticles is numerically determined. In Chapter 7 an investigation of the modifications of the mechanical properties of B_6O specimen implanted with 150 keV ions to fluences of up to 5.0×10^{16} fluorine ions/cm^2 is reported. The closing chapter, Chapter 8, contains a summary of the study and suggestions for future work, while Appendices A and B contain the supplementary literature on Raman spectroscopy and ion implantation, respectively. In Appendix C the articles published from this work are attached.

All relevant literature is discussed in context.

Bibliography

[1] B. Albert and H. Hillebrecht. Boron: Elementary challenge for experimenters and theoreticians. *Angewandte Chemie International Edition*, 48:8640 – 8668, 2009.

[2] A. Andrews. *Development of boron suboxide composites with improved toughness*. PhD Thesis, School of Chemical and Metallurgical Engineering, University of the Witwatersrand, September 2009.

[3] A. Andrews, M. Herrmann, T.C. Shabalala, and I. Sigalas. Liquid phase assisted hot pressing of boron suboxide-materials. *Journal of the European Ceramic Society*, 28:1613 – 1621, 2008.

[4] Andrzej Badzian. Superhard material comparable in hardness to diamond. *Applied Physics Letters*, 53:2495, December 1988.

[5] P.M. Bills and D. Lewis. Non-stoichiometry of boron suboxide (B_6O). *Journal of the Less Common Metals*, 45:343 – 345, March 1976.

[6] C. Brodhag and F. Thévenot. Hot pressing of boron suboxide $B_{12}O_2$. *Journal of the Less Common Metals*, 117:1 – 6, March 1986.

[7] C. Brodhag and F. Thévenot. Hot pressing of various boron phases. *Journal of the Less Common Metals*, 117:175 – 180, March 1986.

[8] C. Chen, D. He, Z. Kou, F. Peng, L. Yao, R. Yu, and Y. Bi. B_6O-based composite to rival polycrystalline cubic boron nitride. *Advanced Materials*, 19:4288 – 4291, 2007.

[9] G.J. Davies, I. Sigalas, M. Herrmann, and T.C. Shabalala. Boron suboxide composite material. US Patent No. 20080317654, December 2007.

[10] M. Herrmann, H.J. Kleebe, J. Raethel, K. Sempf, S. Lauterbach, M.M. Muller, and I. Sigalas. Field-assisted densification of superhard B_6O materials with Y_2O_3/Al_2O_3 addition. *Journal of the American Ceramic Society*, 92:2368 – 2372, 2009.

[11] M. Herrmann, I. Sigalas, M. Thiele, H.J. Kleebe, A. Michaelis, and M.M. Muller. Liquid phase assisted densification of superhard B_6O materials. *Journal of the European Ceramic Society*, 29:2611 – 2617, 2009.

[12] M. Herrmann, A. K. Swarnakar, M. Thiele, O. Van der Biest, and I. Sigalas. 2011.

[13] C.E. Holoeombe Jr. and O.J. Home Jr. Preparation of boron suboxide, B_6O. *Journal of the American Ceramic Society*, 55:106, 1972.

[14] A.L. Ivanovskii. Boron and its compounds with nonmetals: chemical bonding and the electronic properties. *Russian Chemical Reviews*, 66:459 – 482, 1997.

[15] X. Jiao, H. Jin, F. Liu, Z. Ding, B. Yang, F. Lu, X. Zhao, and X. Liu. Synthesis of boron suboxide (B_6O) with ball milled boron oxide (B_2O_3) under lower pressure and temperature. *Journal of Solid State Chemistry*, 183:1697 – 1703, 2010.

[16] O.T. Johnson, I. Sigalas, E.N. Ogunmuyiwa, H.J. Kleebe, M.M. Muller, and M. Herrmann. Boron suboxide materials with Co sintering additives. *Ceramics International*, 36:1767 – 1771, 2010.

[17] A.I. Kharlamov and N.V. Kirillova. Properties of boron suboxide $B_{13}O_2$. *Powder Metallurgy and Metal Ceramics*, 41:97 – 106, January 2002.

[18] R. Bruce King. Boron chemistry at the millennium. *Journal of Organometallic Chemistry*, 581:ix, 1999.

[19] H.-J. Kleebe, S. Lauterbach, T.C. Shabalala, M. Herrmann, and I. Sigalas. B_6O: A correlation between mechanical properties and microstructure evolution upon Al_2O_3 addition during hot pressing. *Journal of the American Ceramic Society*, 91:569 – 575, 2008.

[20] O. Kurakevych and V. Solozhenko. Experimental study and critical review of structural, thermodynamic and mechanical properties of superhard refractory boron suboxide B_6O. *Journal of Superhard Materials*, 33:421–428, 2011.

[21] O.O. Kurakevych and V.L. Solozhenko. 300-K equation of state of rhombohedral boron subnitride. *Solid State Communications*, 149:2169 – 2171, December 2009.

[22] T. Letsoalo and J.E. Lowther. Computational investigation of elastic properties of bulk and defective ultrahard B_6O. *Journal of Superhard Materials*, 33(1):19 – 28, 2011.

[23] Xiaoyang Liu, Xudong Zhao, Weimin Hou, and Wenhui Su. A new route for the synthesis of boron suboxide B_7O. *Journal of Alloys and Compounds*, 223(1):L7 – L9, May 1995.

[24] J.E. Lowther. Possible ultra-hard materials based upon boron icosahedra. *Physica B: Condensed Matter*, 322(1 – 2):173 – 178, 2002.

[25] V.S. Makarov and Y.A. Ugai. Thermochemical study of boron suboxide B_6O. *Journal of the Less Common Metals*, 117:277 – 281, March 1986.

[26] P.F. McMillan, H. Hubert, A. Chizmeshya, W.T. Petuskey, L.A.J. Garvie, and B. Devouard. Nucleation and growth of icosahedral boron suboxide clusters at high pressure. *Journal of Solid State Chemistry*, 147:281 – 290, October 1999.

[27] D. Music and J. M Schneider. Elastic properties of amorphous boron suboxide based solids studied using *ab initio* molecular dynamics. *Journal of Physics: Condensed Matter*, 20:195203, 2008.

[28] D. Nieto-Sanz, P. Loubbeyre, W. Crichton, and M. Mezouar. X-ray study of the synthesis of boron oxides at high pressure: phase diagram amd equation of state. *Physical Review B*, 70:214108, 2004.

[29] Artem R. Oganov, Jiuhua Chen, Carlo Gatti, Yanzhang Ma, Yanming Ma, Colin W. Glass, Zhenxian Liu, Tony Yu, Oleksandr O. Kurakevych, and Vladimir L. Solozhenko. Ionic high-pressure form of elemental boron. *Nature*, 457:863 – 867, February 2009.

[30] M. Olofsson and T. Lundstrom. Synthesis and structure of non-stoichiometric B_6O. *Journal of Alloys and Compounds*, 257:91 – 95, July 1997.

[31] R.A. Pasternak. Crystallographic evidence for the existence of B_7O. *Acta Crystallographica*, 12:612 – 613, 1959.

[32] H. Richter, Z.P. Wang, and L. Ley. The one phonon Raman spectrum in microcrystalline silicon. *Solid State Communications*, 39:625 – 629, 1981.

[33] H.F. Rizzo, W.C. Simmons, and H.O Bieistein. The existence and formation of the solid B_6O. *Journal of the Electrochemical Society*, 109:1079, 1962.

[34] D.J. Roberts, J. Zhao, and Z.A. Munir. Mechanism of reactive sintering of $MgAlB_{14}$ by pulse electric current. *International Journal of Refractory Metals & Hard Materials*, 27:556 – 563, 2009.

[35] T.C. Shabalala, D.S. McLachlan, I. Sigalas, and M. Herrmann. Hard and tough boron suboxide based composites. *Ceramics International*, 34:1713 – 1717, 2008.

[36] I. Sigalas. *Chapter 1.4: New Ultrahard Materials*, volume 2, pages 521 – 527. Wiley-VCH Verlag GmbH, 2000.

[37] V. Solozhenko and C. Lathe. On the melting temperature of B_6O. *Journal of Superhard Materials*, 29:259 – 260, 2007.

[38] V.L. Solozhenko and O.O. Kurakevych. New boron subnitride $B_{13}N_2$: HPHT synthesis, structure and equation of state. *Journal of Physics: Conference Series*, 121:062001, 2008.

[39] A.K. Suri, C. Subramanian, J.K. Sonber, and T.S.R.Ch. Murthy. Synthesis and consolidation of boron carbide: a review. *International Materials Reviews*, 55:4 – 40, 2010.

[40] M. Thiele, M. Herrmann, J. Rathel, H.J. Kleebe, M. M. Mueller, T. Gestrich, and A. Michaelis. Preparation and properties of B_6O/TiB_2-composites. *Journal of the European Ceramic Society*, 32(8):1821 – 1835, 2012.

[41] Z. Wang, Y. Zhao, P. Lazor, H. Annersten, and S.K. Saxena. In situ pressure Raman spectroscopy and mechanical stability of superhard boron suboxide. *Applied Physics Letters*, 86:041911, January 2005.

[42] E. Weintraub. Preparation and properties of pure boron. *Transactions of the American Electrochemical Society*, 16:165 – 184, 1909.

[43] H. Werheit. Chapter 23: Boron and boron-rich compounds. In Y. Kumashiro, editor, *Electric Refractory Materials*, pages 589 – 654. CRC Press, 2000.

[44] H. Werheit and V. Filipov. Raman effect in boron and boron-rich compounds. NATO ARW, Boron-Rich Solids, Orlando, Florida, USA, 2009. Dec. 14 – 18.

[45] R.F. Zhang, Z.J. Lin, Y.S. Zhao, and S. Veprek. Superhard materials with low elastic moduli: Three-dimensional covalent bonding as the origin of superhardness in B_6O. *Physical Review B*, 83:092101, March 2011.

Chapter 2

Experimental Details

2.1 Introduction

This chapter provides details of the relevant experimental techniques and methods utilized to produce the material and specimens used for this research.

2.2 Specimen preparation methodology

2.2.1 Synthesis of B_6O powder

The B_6O powder used in this work was produced at Fraunhofer Institute for Ceramic Technologies and Systems (IKTS), Dresden, Germany by reacting boric acid and amorphous boron powder as shown in the chemical Equation (2.2.1). Details of the precise synthesis method have been presented elsewhere in detail by Andrews [1], Johnson [5], and Freemantle [4]. In summary, starting amorphous boron powder of about 0.8 μm average particle size was admixed with H_3BO_3 in a WAB T2C turbular mixer for 3 hours using molar ratio B:H_3BO_3 = 8:1.03, according to Andrews [1], the molar ratio includes a 3% excess of H_3BO_3 in comparison to the stoichiometric Equation (2.2.1) which accounts for the evaporation of B_2O_3 that occur during synthesis:

$$16\,B + 2\,H_3BO_3 \longrightarrow 3\,B_6O + 3\,H_2O \tag{2.2.1}$$

As-synthesized B_6O powder with an average agglomerate particle size of 100 μm was supplied supplied by IKTS for the purposes of this study. In order to prepare B_6O sintered compacts with improved mechanical properties such as the hardness and strength a smaller average particle size of the B_6O powder grains, preferably in the submicron size range, is prerequisite [1]. In addition, such particle sizes are apparently too large for the successful sintering of fully dense compacts [4]. Details of the further processing to reduce residual contaminant and the milling to drive down the particle size done at the University of the Witwatersrand are provided in the following sections.

Firstly, the as-received B_6O powder was washed in warm ethanol to reduce the amount of B_2O_3 and residual amorphous boron present on the surfaces of B_6O particles after synthesis. The washed powder was baked under flowing argon to rid of excess moisture at 150 °C. The dried powder was crushed by hand and sieved. The average particle size of the as-synthesized B_6O powder was approximately 4 μm, as determined using the Hydro2000MU Malvern Mastersizer particle size analyzer. As such, further reduction of the average particle size of this starting powder is achieved by ball milling.

2.2.2 Milling

The purpose for milling as-synthesized B_6O powder is to produce particles of submicron size range. The strength of polycrystalline ceramic materials depends on grain size and other parameters such as porosity and surface finish [1, 6]. There exist an inverse relationship between the average grain size and material strength dictated by the Hall-Petch relation [3, 6, 7]. The relation is traditionally presented in the form: $\sigma_Y = \sigma_0 + k \cdot d^{0.5}$ [2, 6, 7], where σ_Y is the yield stress, σ_0 the Peierl stress, k the Hall-Petch constant, and d the average grain size. The relation can also be presented in the form: $H = H_0 + k \cdot d^{0.5}$ [7], where H is the material hardness and H_0 a materials constant. According to the relation, the smaller the material grain size, the smaller the repulsion stress felt by a grain boundary dislocation and the higher the applied stress needed to propagate dislocations through the material. This implies that the grain boundary acts as pinning points impeding further dislocation propagation – grain-boundary strengthening [2, 6, 7]. Therefore in order to achieve fully-dense B_6O compacts with improved hardness and strength properties at ambient conditions submicron-grained B_6O powder through grain-boundary strengthening [1].

The B_6O powder were charged into a Szegvari Attritor System stainless steel attrition mill. The milling was carried out in two stages; 2.5 mm and 1 mm diameter stainless steel balls were used in each respective stage. Each time a ratio by weight of charge to steel balls was

kept at approximately 1:10. The milling speed was kept constant at 200 rpm [1] at room temperature, except when 1 mm diameter steel balls were used; in that case a mill speed of 300 rpm was used. Weight of the balls was measured before and after milling to determine weight loss during milling. The attrition mill was stopped at selected milling times of 5, 20, 30, and 50 hours to investigate the variations of the particle size distributions with time.

Propan-1-ol was used as the milling media in order to assist the mixing of the powder during milling and to aid lubrication, to preventing excessive wear and friction between the steel stirrer and the balls and to prevent reactions with air. In addition to 30-hour 2.5 mm ball milling, the powder was milled for 5 hours using 1 mm diameter steel balls at 300 rpm to further reduce the particle size. After every requisite time interval, powders were withdrawn for washing and particle sizing. This was carried out in order to understand the milling kinetics, the results are not relevant to this work and are therefore not reported here, see reference [4].

2.2.3 Washing

A substantial amount of iron and chrome contaminants is known to exist inevitably in the milled B_6O powder [1, 4, 5]. The origins of the contaminants can easily be traced to erosive action of the balls on the mill container as well as the balls on each other, and powder on the balls, given that B_6O is a superhard material.Washing to minimize the amount of the contaminants is therefore mandatory.

Washing with dilute hydrochloric acid solution has been observed to minimize the amounts of contaminants which can then be decanted off of the washed medium and the washing procedure is repeated until the acid solution is clear [4]. Each time, 50 ml of 90% HCl was added to 450 ml of distilled water into a 1 litre glass beaker. The acid solution was used to wash the powder and allowed it to settle, followed by decanting and repeated as many times as necessary. Typically, the iron contaminants can be seen to visibly bubble and react when the acid is introduced as well as changing the liquid colour to a semi-transparent dirty yellow. Once the washing has been repeated multiple times (ten times in this case), this becomes clearer and clearer in appearance. Once the solution is clear enough, it is washed firstly with distilled water and subsequently decanted to reduce HCl concentration, followed by washing with ethanol. After completing this stage, the powder was dried in a rotary evaporator, crushed as finely as possible and removed for chemical analysis. See also reference [4] for further details.

[1] The milling speed was set at 200 rpm as opposed to 400 rpm, because lowering the mill speed is known to reduce the abrasive wearing of the stainless steel balls and ultimately lower the ion contamination of the milled B_6O powder.

Particle size analysis

The primary goal of the milling process is to produce homogeneously grained structure in the powders whilst washing necessitates to minimize the amount of the (milling) contaminants and retain the purity of the raw materials to be used for the manufacture of the B_6O samples.

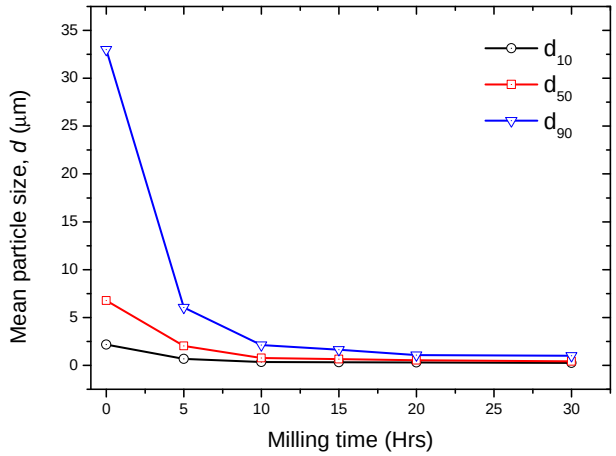

Figure 2.1: *Effect of milling time on particle size distribution.*

Milling time (Hours)	d_{10} μm	d_{50} μm	d_{90} μm
0	2.171	6.773	32.990
5	0.666	2.021	6.055
10	0.338	0.777	2.127
15	0.318	0.652	1.637
20	0.291	0.538	1.065
30	0.253	0.429	1.014

Table 2.1: *Effect of milling time on particle size distribution.*

In order to ensure that the required sub-micron particle size was obtained, powder particle size analysis was performed on batches of milled powder using the Hydro2000MU Malvern Mastersizer particle size analyzer instrument. A small amount of powder was suspended in distilled water were analyzed. Small amounts of sodium hexametaphosphate in distilled water was used as a dispersive medium. The dynamics of the (mean) particle size distribution with milling time is summarized in Figure 2.1 and Table 2.1.

Chemical analysis

After washing, a sample of the powder was analyzed for elementary chemical composition in order to determine the amount iron and chromium contaminants and the purity of the powder. Inductively coupled plasma (ICP) spectroscopic analysis was used. The analysis was performed using a Spectrociros CCD IPCP analyser at the School of Chemistry, University of Witwatersrand, Johannesburg.

0.1 g of sample was digested in a 55% HNO_3 and a 40% HF containing solution by microwave digestion in a Multiwave 3000 SOLV sample preparatory microwave. The digestion process was allowed to proceed for 65 minutes after which the scan was performed. Results of the chemical analysis performed are tabulated in Table 2.2.

Table 2.2: *Iron and chromium weight percentages in the B_6O powder batches after washing as determined by ICP analysis.*

	Composition (wt. %)	
Powder sample	iron	chromium
No. I	0.052	0.054
No. II	0.057	0.039
No. III	0.058	0.024
Average	0.056	0.039

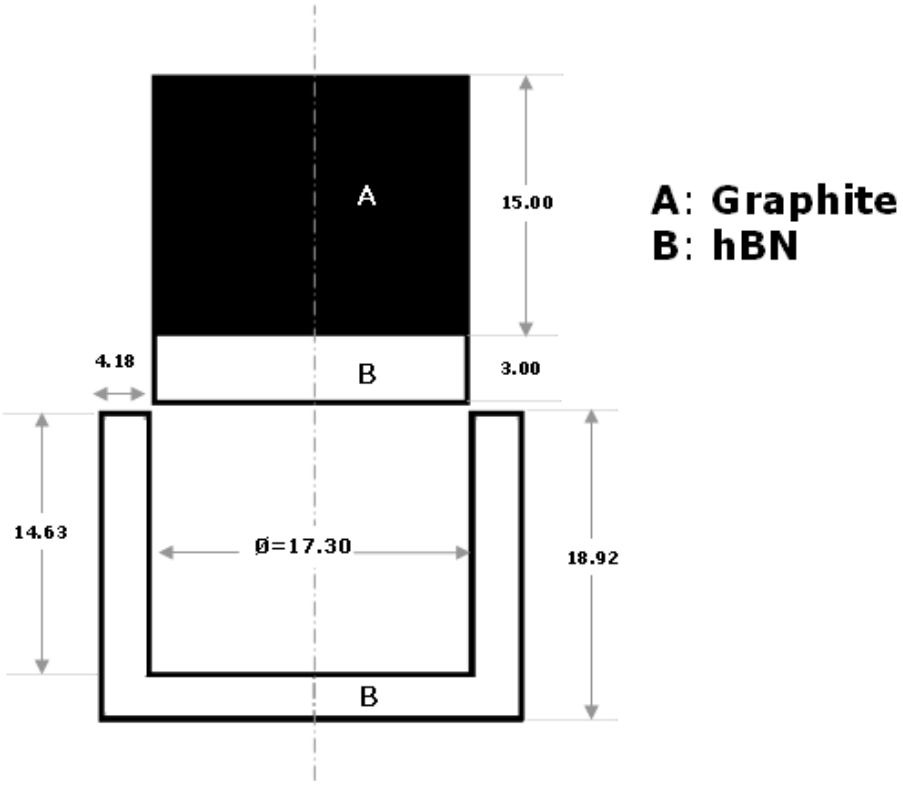

Figure 2.2: *Drawing of capsule assembly used in the production of the B_6O compacts used for this research.*

2.2.4 Hot-pressing of B_6O compacts

Unlike both diamond and *c*BN, bulk B_6O powders may be consolidated without the need for high pressures. Figure 2.2 shows a drawing of capsule assembly used in the production of the B_6O compacts used for this research. A cylindrical hBN cup of outside diameter 21.40 mm and inner diameter of 17.30 mm was used to contain B_6O powder for densification. A graphite piston was used to transmit the applied force from the punch directly onto the powder. An hBN disc was placed on top of the B_6O powder to prevent

contamination of the sample from the graphite piston. hBN disc was preferred due to its pressure transmission properties, high chemical inertness, and thermal stability.

The B_6O specimen used in this work were consolidated by hot pressing at temperatures of up to 1900 °C and at 50 MPa of pressure in an inert argon atmosphere. A HP20-2560-FP20 Thermal Technology uniaxial hot press was used for all the hot pressing experiments. The press load was applied uniaxially as illustrated in the sintering profile shown in Figure 2.3.

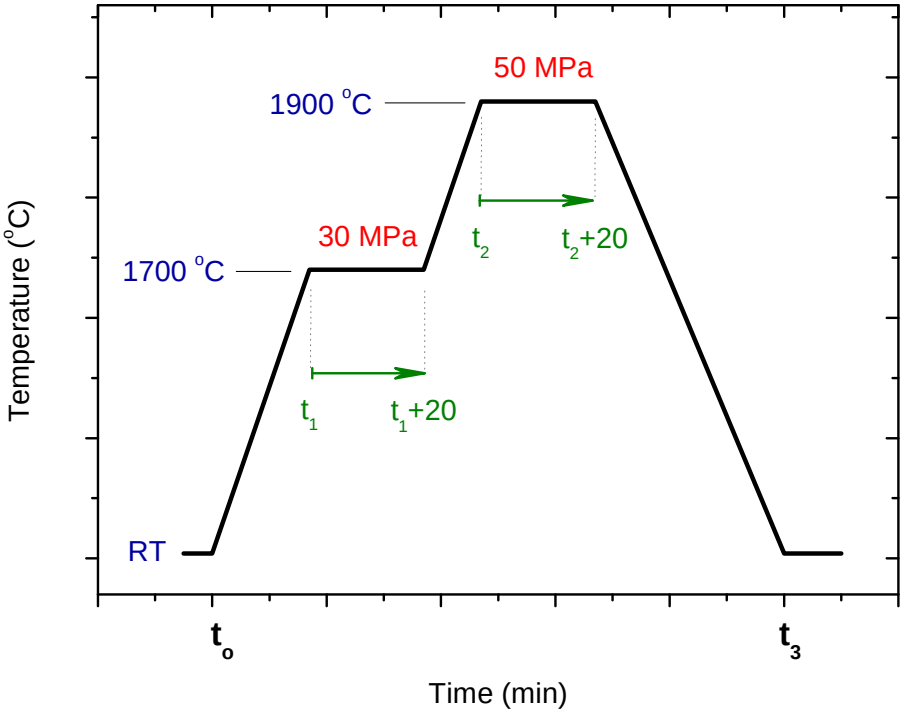

Figure 2.3: *The sintering profile for hot pressing B_6O compacts used in this research.*

The hot pressing procedure of B_6O powder material is as follows [5]: the hot press was evacuated to pressures less than 200 mtorr and then back-filled with argon gas. Argon gas was allowed to flow through the furnace during the entire furnacing cycle. The furnace was heated to from room temperature to 1700 °C at 15 °C/min. The temperature was held at 1700 °C for 20 minutes whilst applying a 30 MPa load. The furnace heating was resumed and increased to 1900 °C at 10 °C/min. The temperature was held at 1700 °C while raising the applied load to 50 MPa load. After 20 minutes, the furnace was then cooled to room temperature at 20 °C/min. Once the temperatures were lower than 500 °C the load was completely removed from the sample.

At room temperature the sample cell was recovered from the capsule assembly. The hot-pressing process produces a solid dense B_6O compacts[2] from a volume of starting powder, well below the melting point of the B_6O material.

[2]The solid dense B_6O compacts is refereed to as hot-pressed B_6O throughout the text.

2.2.5 Metallographical preparation procedure

The polishing procedure involved the use of progressive grinding pads from 80 to 120, 240, 600 and 1200 grit followed by fine grinding with 9 μm diamond paste followed by 6, 3 and finally 1 μm paste. Mechanical grinding/polishing time was approximately doubled from each subsequent step, for example, 30 seconds on an 80 grit pad to 60 seconds on the 120 grit pad and so on. Optical microscopy was used to ensure that the introduced scratches at each stage were uniformly directional and of the same size, after which the next step of grinding commenced. Similar methods were used in the final polishing steps, although time spent on each pad varied according to the requirements of the sample. Some samples can be more difficult to polish effectively and may require more time for fine grinding and polishing than others. For this reason, microscopy was used to monitor the quality of each stage in the process.

2.2.6 Characterization of hot-pressed B_6O powder

Microstructural characterization

Since the powder impurity composition and particle size distribution alone are insufficient to guarantee the quality of the powders, morphological and further chemical analysis were conducted to fully characterize the powders. SEM with an attached EDX spectrometer and AFM imaging were used for the morphological and compositional characterization whilst XRD was used for the study of the crystal structure of the samples. These results are discussed in context in Chapter 3.

Density measurements

The density and porosity of the B_6O samples after hot press compaction was measured using the Archimedes method: the following steps were executed:

1. The hot pressed samples were first solvent cleaned and dried in air.
2. The dry weight of the sample M_d was determined using a balance.
3. The hot pressed samples were then boiled in distilled water for three hours in order to get rid of air bubbles trapped in the pores of the specimen.
4. The sample was allowed to cool down.
5. The suspended weight of the specimen M_s was determined.

6. The wet weight M_w of the specimen was determined after lightly dabbing the sample with paper towel in order to remove excess surface water.

The entire procedure was repeated at least three times to verify measurement reproducibility. The mean values were used to calculate the samples' bulk density ρ_s.

Equation (2.2.3) was used to determine samples' bulk density

$$\rho_s = \frac{M_d \cdot \rho_w}{M_s - M_w} \tag{2.2.2}$$

where ρ_w is the density of water (= 1000 g/cm^3), and M_d, M_s, and M_w are average values.

The bulk density of the samples was determine to be 2.44 g/cm^3. The theoretical density of B_6O is 2.55 g/cm^3 [5].

The porosity or open porosity P_o of the hot pressed samples was determined to be 3.5 % using the following equation:

$$P_o = \frac{M_w - M_d}{M_w - M_s} * 100\% \tag{2.2.3}$$

.

Bibliography

[1] A. Andrews. *Development of boron suboxide composites with improved toughness*. PhD Thesis, School of Chemical and Metallurgical Engineering, University of the Witwatersrand, September 2009.

[2] V. Bata and E.V. Pereloma. An alternative physical explanation of the Hall-Petch relation. *Acta Materialia*, 52(3):657 – 665, 2004.

[3] A. Cottrell. *An introduction to metallurgy*. Edward Arnold, London, 1967.

[4] C.S. Freemantle. The wear studies of boron suboxide based cutting tool materials in machining applications. MSc Dissertation, School of Chemical and Metallurgical Engineering, University of the Witwatersrand, September 2010.

[5] O.T. Johnson. Improvement on the mechanical properties of boron suboxide (B_6O) based composites using other compounds as second phase. MSc Dissertation, School

of Chemical and Metallurgical Engineering, University of the Witwatersrand, July 2009.

[6] J. P. Singh, Anil V. Virkar, D. K. Shetty, and R. S. Gordow. Strength-grain size relations in polycrystalline ceramics. *Journal of the American Ceramic Society*, 62(3 – 4):179 – 183, 1979.

[7] A. S. Taha and F. H. Hammad. Application of the hall-petch relation to microhardness measurements on Al, Cu, Al−MD 105, and Al-Cu alloys. *Physica Status Solidi (A)*, 119:455–462, 1990.

Part II

Characterization of Bulk B_6O

Chapter 3

Raman Spectra of Hot-Pressed B_6O

In this chapter, results of the characterization of hot-pressed B_6O starting material are presented and discussed. The chapter is based on a paper published in the *Advanced Material Letters* journal under the title *Raman spectra of hot-pressed boron suboxide* [21]. Contrary to prior knowledge, the existence of observable first- and second-order Raman spectra of hot-pressed B_6O measured using the Ar^+ laser excitation source is reported.

3.1 Introduction

A literature survey of the vibrational investigation of polycrystalline B_6O prepared by hot-pressing shows that very little has previously been reported on the characterization to understand the Raman spectrum B_6O prepared by of uniaxial hot-pressing; partly because the material has complex structure and the material is characterized by a relatively weak Raman signal and a strong inherent fluorescence background [24]. In fact, some of the previously reported spectra are far from observable [26, 28, 30] as illustrated in Figures 3.1(a.) and 3.1(b.), for example. As a result, despite having possessing wealth of fascinating physico-chemical and mechanical properties, being considered the third hardest material only after diamond and cubic boron nitride, and being an object of intense interest in recent years, the Raman scattering response of hot-pressed B_6O material is still poorly understood [24, 26], especially when a green Ar^+ laser excitation source is used.

The Raman spectrum of boron suboxide is rather complicated [15]. Recent reports show that the first- and second-order Raman spectra of B_6O powders *becomes* observable when conventional green or red excitation laser wavelengths are used [16, 24].

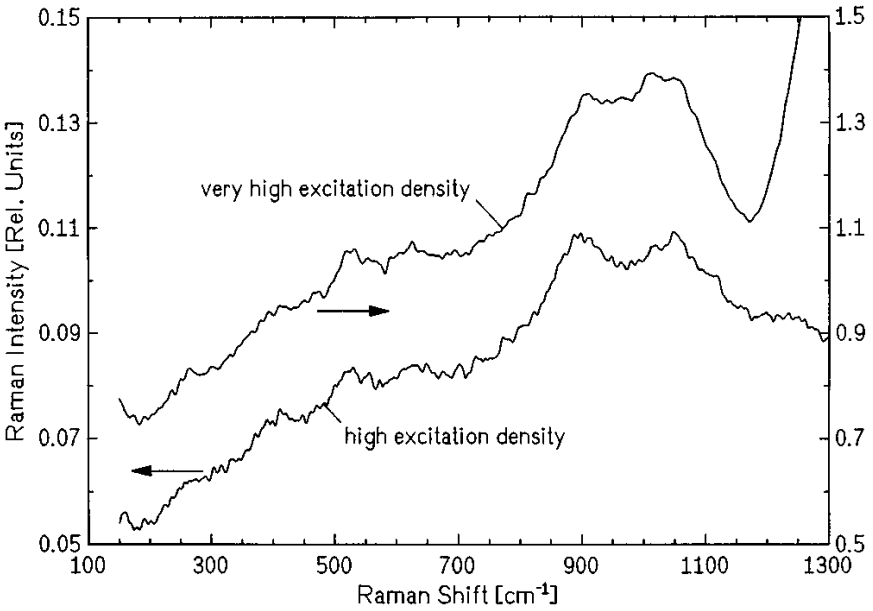

(a) *Werheit and Kuhlmann [28]*

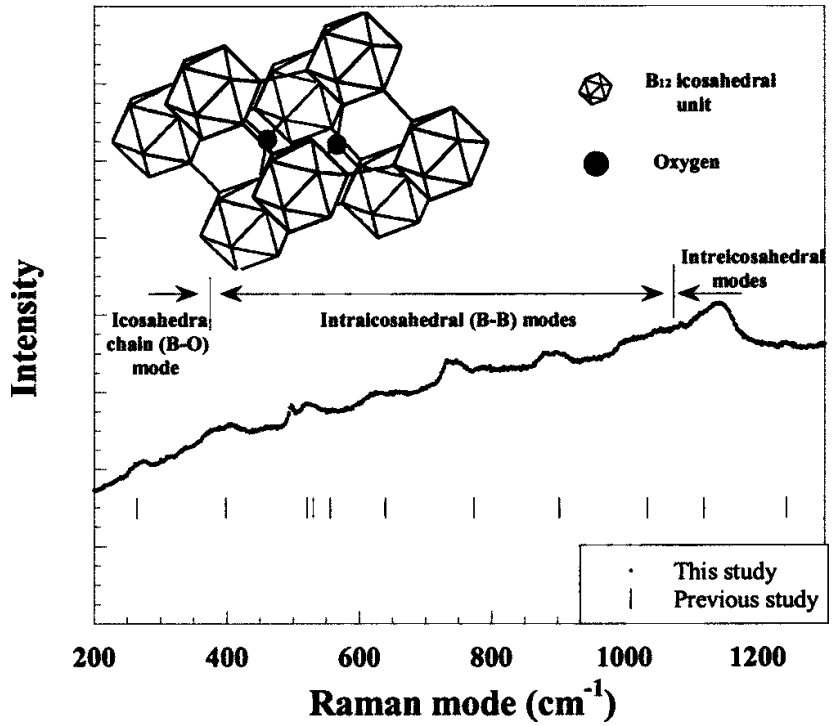

(b) *Wang et al. [26]*

Figure 3.1: *Previously reported Raman spectra of hot-pressed B_6O.*

In this work, we attempt to contribute to the understanding of the Raman scattering response of hot-pressed B_6O measured using a green Ar^+ laser excitation source. We present a systematic solution to this problem by means of deliberately (a.) using low-power excitation beams to minimize the heating and fluorescence effects on the sample surface, (b.) reducing the exposure duration, and (c.) the application of a suitable background

subtraction on the measured Raman spectra. Contrary to prior knowledge, we report on the existence of observable first- and second-order Raman spectra of hot-pressed B_6O measured at ambient conditions using the green Ar^+ ion laser as the source of excitation.

We also extend the comparative study of the first-order Raman spectra of hot-pressed B_6O presented here to the other similar boron-rich based materials (α-rhombohedral boron, B_4C, and $B_{13}N_2$ to previously reported findings on this topic notably by Werheit and Filipov [27] and Solozhenko et al. [16, 24] excluded hot-pressed B_6O in their comparison. The observed B_6O Raman-active modes are also in close agreement with those theoretically calculated for boron-rich icosahedral compounds and strikingly similar to the other icosahedral boron-rich ultra-hard materials [24, 27].

3.2 Experimental details

XRD pattern for phase compositional analysis of the B_6O samples were recorded with a Bruker AXS D8 ADVANCE powder X-ray diffractometer using a Cu K_α (λ = 1.547 Å) monochromatic radiation source. The patterns were collected using the Bragg-Brentano geometry over a $10^\circ - 90^\circ$ 2θ range in steps on 0.02° at a sampling time of approximately 7 s per step. The voltage on the anode of the X-ray tube was 45 kV, and the current was 40 mA. With the aid of the EVA software (Bruker-AXS), crystalline phases were identified by comparison with reference patterns from the JCPDS database. The average crystallite size was calculated by means of the Debye-Scherrer formula. All XRD measurements were carried out under room conditions at CSIR's National Centre for Nano-Structured Materials nanomaterial characterization facility.

The specimen's surface microstructure and composition were characterized by environmental scanning electron microscopy (SEM) and energy-dispersive X-ray spectroscopy (EDX), respectively. A Philips XL30 environmental scanning electron microscope (with an EDX system attachment) operating at 15 keV in backscattered secondary electron geometry was used in thus study. No conducting coating was applied to the samples' surfaces.

The visible micro-Raman spectroscopy measurements were performed in the backscattering configuration at room temperature using a green 514.5 nm Ar^+ ion laser line as the excitation source. The laser power was deliberately kept low to minimize the background fluorescence and temperature variation effects on the sample surface. An 1800 grooves/mm grating in the single spectrograph mode of a Jobin-Yvon T64000 Raman spectrometer was used. The micro-Raman spectroscopy measurements were performed using a $20\times$ Olympus objective (the spot size diameter ~ 1 μm). The Raman measurements were also carried out at CSIR's National Centre for Nano-Structured Materials nanomaterial

characterization facility. Spectrum acquisition and preprocessing were done with LabSpec 3.0 software (Horiba Jobin Yvon). An automated method for fluorescence and background suppression was applied on the Raman scattering measurements using the scheme using a series of linear extrapolations between adjacent minima within the spectrum.

3.3 Theory of Raman spectroscopy

Raman spectroscopy is a non-invasive research method for chemical analysis or solid state physics by inelastic scattering of monochromatic light within the studied sample. It provides access to the lattice dynamics with the information about the chemical composition, orientation, or crystalline quality. This information is generally derived from the Raman peak position, intensity, width, and lineshape.

a detailed description of the Jobin-Yvon T64000 Raman spectrometer used in this study is presented in Appendix A on page 118. The theory of Raman spectroscopy is also presented in Appendix A on page 113. Reports, reviews, and monograms on the theory and applications of Raman spectroscopy are widespread in the literature and for further information the reader is referred elsewhere [6, 19, 29].

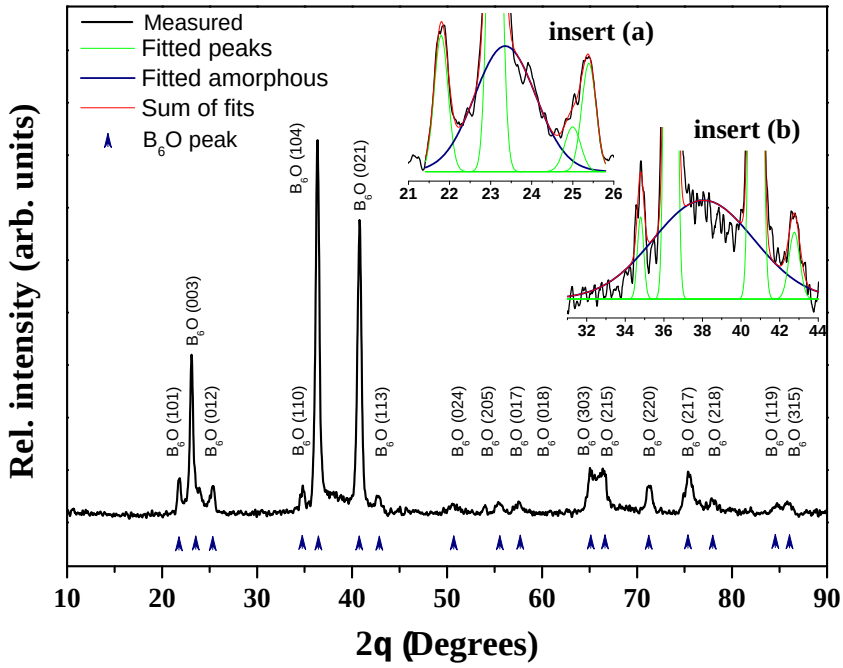

Figure 3.2: *The powder diffraction pattern of a sample of hot-pressed B_6O sample showing the predominance of the B_6O crystalline phase. Inserts (a.) and (b.) illustrate the existence of broad amorphous peak fits.*

3.4 Results and discussion

3.4.1 X-Ray diffraction measurements

Figure 3.2 shows the full profile XRD diffraction pattern measured for the hot-pressed B_6O specimen used in this study.

The diffraction pattern is characteristic of a nominally pure polycrystalline B_6O. All the dominant diffraction peaks can be perfectly indexed to the XRD pattern of the B_6O crystal structure (JCPDS File Card No. 31-210) reported elsewhere [2, 11, 24]. The lattice parameters, a = 5.39 Å and c = 12.34 Å, obtained from XRD analysis are in good agreement with the single crystal data [12]. An average crystallite size of 0.42 μm was determined from the diffraction pattern using the Debye-Scherrer approach.

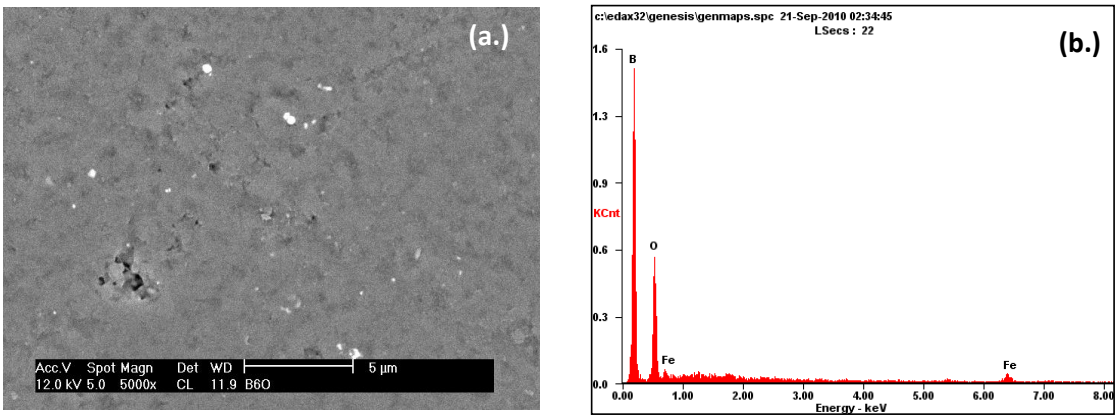

Figure 3.3: *Shows the SEM surface micrograph (a.) and the EDX surface compositional analysis (b.) of the hot pressed B_6O specimen. Iron contamination is responsible for EDX elemental peak observed around 2.25 keV as well as the bright spots on SEM surface micrograph.*

As expected for B_6O material synthesized from amorphous boron, the diffraction pattern contains some broad amorphous peaks centred at the 2θ values ~23.4° (insert (a.)) and ~38° (insert (b.)). The broad amorphous peaks is attributed to very small amounts of either to amorphous boron [3, 13, 22] or amorphous B_6O [22] coexisting with crystalline B_6O.

3.4.2 SEM and EDX measurements

The surface morphology and compositional analysis of hot-pressed B_6O specimen as determined by SEM and EDX are shown in Figures 3.3(a.) and 3.3(b.), respectively. In general, the micrograph shows a homogeneous B_6O phase with visible pores on the surface.

This is a direct result of some considerable practical challenges in the densification of B_6O phases by hot pressing [7, 8, 10].

The analysis of the surface composition by EDX is also indicative of nominally pure B_6O phase. The observed iron contamination (less than 1 wt. percent) is expected and inevitable; it originates from abrasion of the steel ball and the containment cell during powder ball milling [1, 5, 9]. This is consistent with the ICP spectroscopic observations (see Table 2.2) on page 15.

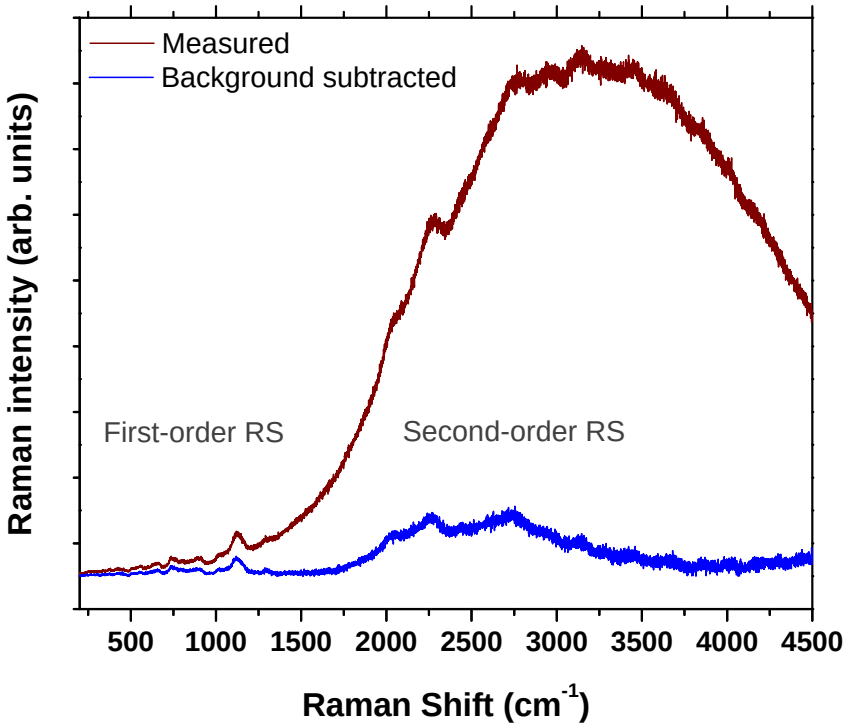

Figure 3.4: *The measured (first-, second-, and higher-order modes) and the fluorescence-background suppressed Raman spectra of hot-pressed B_6O.*

3.4.3 Raman scattering measurements

Applied in this work, Raman spectroscopy is used to investigate the characteristic first- and higher-order spectra measured, the structure and bonding configuration of hot-pressed B_6O. The measured Raman spectra of B_6O is shown in Figure 3.4.

The collected Raman spectra of the hot-pressed B_6O sample is weak and almost masked-out in the presence of the inherent strong fluorescence background, similar observations have been made by Solozhenko et al. [24]. Theoretical calculations predict twelve Raman active phonons modes for B_6O [24, 26], and other boron-rich solids that are based on the β-rhombohedral boron-type crystal structure. However, due to the oxygen deficiency and slight distortions of the B_{12} icosahedra, a direct consequence of the Jahn-Teller effect, in

the hot-pressed B_6O crystal structure [22], Raman modes exceeding twelve were here and previously observed [26, 27].

By means of the application of an efficient fluorescence background suppression scheme using LabSpec 3.0 software (Horiba Jobin Yvon), first-order, second-order, and tentatively the higher-order Raman spectra of B_6O which, till now, were deemed unobservable when using the green 514.5 nm Ar^+ excitation source were recovered. The fluorescence-background corrected Raman spectrum of B_6O is shown on the same axis with the collected Raman spectra in Figure 3.4.

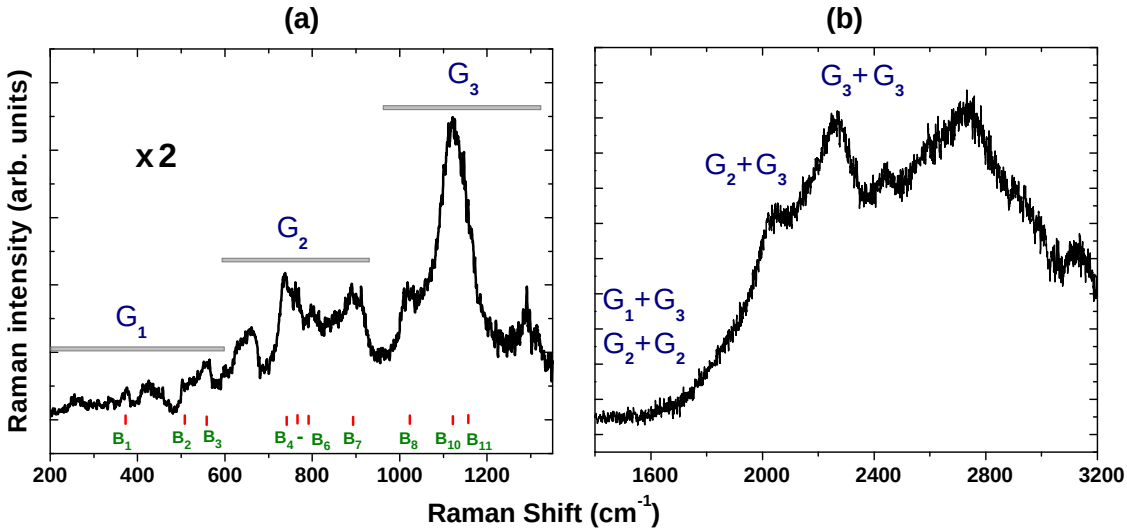

Figure 3.5: *Shows the fluorescence-background corrected first- and second-order Raman spectra of B_6O. The second-order Raman modes are a combination of the first-order Raman active phonons. The peak assignments are summarized in Table 3.1.*

Figures 3.5(a.) and 3.5(b.) shows the fluorescence-background corrected first- and second-order Raman spectra of B_6O, respectively. A summary of the observed Raman peaks and the peak position analysis are given in Table 3.1. We confirm that the peak positions are not affected by the subtraction scheme, but we acknowledge that the width could be slightly influenced [4]. In fact, the peak assignment is in very good agreement with both the previously experimental B_6O Raman data [24, 26, 28] and *ab initio* calculated Raman data [25] published at the same time as the work being reported in Machaka et al. [21], see Table 3.2.

For ease of analysis, the recovered first-order Raman spectra of B_6O has been divided into three spectral band groups – G_1, G_2, and G_3 [26]. The first spectral band G_1, comprising vibrational modes observed below 600 cm^{-1}, the second G_2, of vibrational modes observed between 600 cm^{-1} and 950 cm^{-1}, and the first spectral band G_3, comprising vibrational modes observed between 950 cm^{-1} and 1200 cm^{-1}. The assignment of individual peaks

Table 3.1: *A summary of the measured Raman data and the peak assignments. The peak assignment is in very good agreement with recently published calculated Raman modes in B_6O, Wang et al. [25] as well as data reported in references [24, 28].*

Group	Peak (cm^{-1})		Band	Remarks
First-order Raman modes				
G_1	259.6	b+w		Icosahedral chain (B−O) phonon
	373.4	w	B_1	Vibrational motion of the (O−O) pair
	425.9	b+a		Bending vibration of the B−O−B chain
	500.9	s+w	B_2	Symmetrical stretching of the B−O−B chain
	555.5	m	B_3	Motion of the icosahedral boron atoms about O
	600.6	s+w	τ	
	625.1	b	τ	
G_2	736.9	s+s	B_4	Motion of the boron atoms in the icosahedra
	762.8	s+h	B_5	
	797.4	m	B_6	
	891.9	m	B_7	
G_3	1016.4	m	B_8	The inter-icosahedral boron vibration
	1119.9	s+s	B_{10}	
	1154.8	s	B_{11}	
	1288.2	m	π	
Second-order Raman modes				
G_1+G_3	–		ϕ	G_1−G_3 two-phonon combinations
G_2+G_2	–		ϕ	G_2−G_2 two-phonon combinations
G_2+G_3	2022	s+s	B_7+B_{10}	G_2−G_3 two-phonon combinations
			B_7+B_{11}	
G_3+G_3	2230–2260	s+s	B_{10}+B_{10}	G_3−G_3 two-phonon combinations
			B_{10}+B_{11}	
			B_{11}+B_{11}	
	2430.7	m	B_{12}+B_{12}	
Higher-order Raman modes				
	2723.6	s+b	π	
	2970.8	s	π	
	3134.3	m	π	
	3275.7	m	π	
	3256.4	w	π	

NOTES
ϕ — expected but not observed
π — observed but there is a lack of information
τ — assignment is speculative

The intensity is evaluated qualitatively by the following notations:
s+s, sharp and strong; s+w, sharp but weak; m, medium; w, weak; vw, very weak; b, broad.

follows a similar approach to that used in [24–26], as illustrated in Figure 3.1(b.). The observed Raman bands shown in Figures 3.5(a.) and 3.5(b.) are listed in Table 3.1.

G_1 group of Raman modes

In the same way in which the G_1 group of Raman peaks in B_4C, and in $B_{13}N_2$ can be attributed to the B_{12} icosahedra – C or N chain atom vibrational mode, respectively [23, 27], the G_1 group of peaks can be attributed to vibrational modes involving the oxygen atom in the B−O−B chain or the icosahedra-chain phonon vibrations [23].

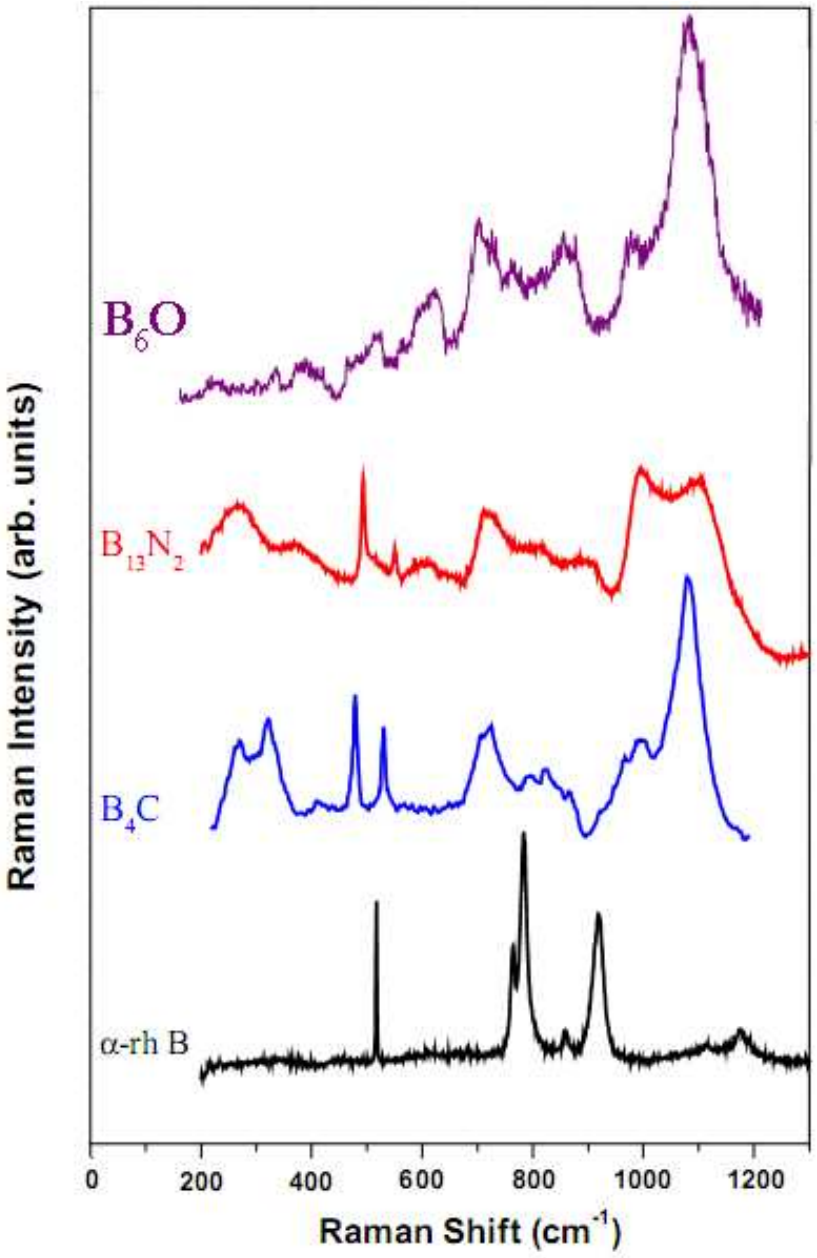

Figure 3.6: *A comparison of the measured Raman spectra of B_6O (in purple), with other boron-rich based materials ($B_{13}N_2$ in red, and B_4C in blue), and α-rhombohedral boron [23]. Note: The B_4C and $B_{13}N_2$ were synthesized under HPHT conditions and all measurements were measured at room temperature.*

When compared to the Raman spectra of α-rhombohedral boron and other α-rhombohedral boron-based superhard materials (HPHT synthesized B_4C, and $B_{13}N_2$, see Figure 3.6 below), the measured spectra shows that the G_1 peaks of the hot-pressed B_6O material are relatively weaker and broader. In particular, the Raman peak observed at 373 cm^{-1}, which is characteristic of the O−O chain vibration, is of very weak intensity and barely visible. The non-stoichiometric composition of the hot-pressed B_6O material have attributed the observations, especially the poor state of the oxygen occupancy of the B−O−B chain linking the icosahedra in hot-pressed B_6O. The overall poor oxygen occupancy of the B−O−B chain linking the B_{12} icosahedra was also predicted theoretically by Lowther [20].

Table 3.2: *Comparison between the frequencies observed in this work and those previously reported.*

This study*	**Wang et al. [25]**†	**Werheit et al. [28]***	**Wang et al. [26]***	**Solozhenko et al. [24]***,‡
259.6		265	260	
373.4	375		380	373 – 374
425.9	416	410	—	—
500.9	—	—	—	495 – 500
—	510	510	520	—
—	532	—	530	—
555.5	555	—	556	543 – 546
600.6	602	595	—	—
625.1	—	—	620	—
736.9	737	733		728 – 734
762.8	782	770	772	780 – 786
797.4	800	—	—	—
—	826	—	—	813 – 825
—	860	850	—	—
891.9	890	885	—	875 – 889
—	900	900	900	—
1016.4	—	—	—	1017
—	1074	1046	1030	—
—	1081	—	—	1087 – 1090
1119.9	1120	1120	1120	1134 – 1139
1154.8	1138	—	—	1154 – 1160
1288.2	—	—	1250	—

NOTES
* – Experimentally determined
† – Theoretically determined
‡ – IR and UV wavelength of the excitation

The relatively sharp feature at 500 cm^{-1} corresponds to the symmetric stretching of the B−O−B triatomic chain, The narrow line just above 500 cm^{-1}, has been been observed before [24], it can be attributed to the motion of the entire B_{12} icosahedron about oxygen atom.

G_2 and G_3 groups of Raman modes

The G_2 group of Raman modes observed between 600 and 1100 cm^{-1} correspond to the intra-icosahedral B−B bonds whilst the G_3 group of Raman modes observed between 950 and 1200 cm^{-1} correspond to the the inter-icosahedral B−B bonds.

We observe that at higher Raman shift frequencies, structural disorder is likely to be responsible for most of the observed broadening [17]. In addition to broadening, both the G_2 and G_3 bands of the Raman peaks appear to be 'riding' on two strong, broad but distinct peaks (800 and 1160 cm^{-1}), respectively, which corresponds to amorphous and β-rhombohedral boron [14, 27] — an observation which is consistent with the XRD pattern observed in Figure 3.2.

Since the B−B distances within B_{12} icosahedra are comparable in β-rhombohedral boron (1.770 Å), $B_{13}N_2$, B_4C (1.751 Å), and B_6O (1.753 Å) [18, 20], we expect their respective G_2 and G_3 bands to be closely related. From Figure 3.6: notably the strong phonon of B_4C at 1430 cm^{-1} due to the stretching mode of the three-atomic chain (5) is missing in the spectrum of B_6O. However, the highest first order mode of 1288 cm^{-1} is observed in the spectrum of B_6O but is not reported in the spectrum of B_4C. The strong phonon of B_6O at 1288 cm^{-1} is therefore attributed to inter-icosahedral phonons like in α-rhombohedral boron [28].

In general, compared with other boron-rich solids based on the α-rhombohedral boron type crystal structure, the Raman effect of first-order in B_6O is overall extraordinarily weak although the B_4C, and $B_{13}N_2$ materials used in the comparison were synthesized under HPHT conditions and the B_6O, which is the subject of this study is a hot-pressed material.

Second- and higher-order groups of Raman modes

Figure 3.5b shows measured Raman bands above 1500 cm^{-1}, the second-order Raman spectra of B_6O. The origins of these bands may be due to the two-phonon combinations of the modes from the G_1, G_2, and G_3 groups of Raman bands [24]. The notable absence of the G_1+G_3 and G_2+G_2 combinations is easy to see given the relatively weaker G_1 phonons observed. It is therefore subsequently tentatively attributed to the non-stoichiometric composition of the hot-pressed B_6O material. In Table 3.1 we summarize all observed second-order Raman modes by considering combination of the first-order Raman active phonons.

If the 1288 cm^{-1} mode is considered as a first-order Raman mode, the medium-sized 2430.7 cm^{-1} peak would easily be considered as second-order [24]. The nature and origins

of the Raman bands above 2500 cm^{-1} is less clear; the number of possible combinations of one-phonon modes remarkably rise in the spectra of third and higher order [24].

3.5 Summary and conclusion

Based on the Raman scattering studies of hot-pressed B_6O measured using the 514.5 nm Ar^+ excitation. We conclude that:

- As previously reported, we have observed a Raman spectra of B_6O characterized by a relatively strong inherent fluorescence background.
- By means of the application of a fluorescence-background suppression scheme, observable first-, second-, and higher- order Raman spectra of B_6O are obtained, which till now had been deemed unobservable when the 514.5 nm excitation line is used.
- Since all the lines below 600 cm^{-1} have been attributed to vibrations with participation of oxygen atoms [15, 24, 26]. The relatively weak G_1 Raman modes of hot-pressed B_6O measured have been tentatively attribute the poor oxygen occupancy in the B−O−B chain linking the icosahedra as theoretically predicted by Lowther [20].
- The peak assignment is in very good agreement with calculated Raman modes in B_6O by published Wang et al. [25] at the same time that this work [21] was also published.
- By comparing our measured results to the Raman spectra of other boron-rich based materials (α-rhombohedral boron, $B_{13}N_2$, and B_4C [23]) measured at ambient conditions using the same excitation source we observe that the Raman modes observed in B_6O are similar in characteristics to those observed for $B_{13}N_2$, and B_4C.
- Second-order Raman spectra are visible and were attributed to two-phonon combinations for first-order Raman modes.

Bibliography

[1] A. Andrews. *Development of boron suboxide composites with improved toughness*. PhD Thesis, School of Chemical and Metallurgical Engineering, University of the Witwatersrand, September 2009.

[2] A. Andrews, M. Herrmann, T.C. Shabalala, and I. Sigalas. Liquid phase assisted hot pressing of boron suboxide-materials. *Journal of the European Ceramic Society*, 28:1613 – 1621, 2008.

[3] E.A. Ekimov, R.A. Sadykov, E.L. Gromnitskaya, M.V. Kondrin, and N.N. Mel'nik. Physical and mechanical properties of dense materials prepared by hot-isostatic pressing of amorphous boron. *Inorganic Materials*, 42:479 – 483, 2006.

[4] R.M. Erasmus, 2009. Personal communication.

[5] C.S. Freemantle. The wear studies of boron suboxide based cutting tool materials in machining applications. MSc Dissertation, School of Chemical and Metallurgical Engineering, University of the Witwatersrand, September 2010.

[6] G. Gouadec and P. Colomban. Raman spectroscopy of nanomaterials: How spectra relate to disorder, particle size and mechanical properties. *Progress in Crystal Growth and Characterization of Materials*, 53:1 – 56, 2007.

[7] M. Herrmann, H.J. Kleebe, J. Raethel, K. Sempf, S. Lauterbach, M.M. Muller, and I. Sigalas. Field-assisted densification of superhard B_6O materials with Y_2O_3/Al_2O_3 addition. *Journal of the American Ceramic Society*, 92:2368 – 2372, 2009.

[8] M. Herrmann, J. Raethel, A. Bales, K. Sempf, I. Sigalas, and M. Hoehn. Liquid phase assisted densification of superhard B_6O materials. *Journal of the European Ceramic Society*, 29:2611 – 2617, 2009.

[9] O.T. Johnson. Improvement on the mechanical properties of boron suboxide (B_6O) based composites using other compounds as second phase. MSc Dissertation, School of Chemical and Metallurgical Engineering, University of the Witwatersrand, July 2009.

[10] O.T. Johnson, I. Sigalas, E.N. Ogunmuyiwa, H.J. Kleebe, M.M. Muller, and M. Herrmann. Boron suboxide materials with Co sintering additives. *Ceramics International*, 36:1767 – 1771, 2010.

[11] A.I. Kharlamov and N.V. Kirillova. Properties of boron suboxide $B_{13}O_2$. *Powder Metallurgy and Metal Ceramics*, 41:97 – 106, January 2002.

[12] H.-J. Kleebe, S. Lauterbach, T.C. Shabalala, M. Herrmann, and I. Sigalas. B_6O: A correlation between mechanical properties and microstructure evolution upon Al_2O_3 addition during hot pressing. *Journal of the American Ceramic Society*, 91:569 – 575, 2008.

[13] M. Kobayashi, I. Higashi, C. Brodhag, and F. Thevenot. Structure of B_6O boron-suboxide by Rietveld refinement. *Journal of Material Science*, 28:2129, 1993.

[14] U. Kuhlmann, H. Werheit, T. Lundström, and W. Robers. Optical properties of amorphous boron. *Journal of Physics and Chemistry of Solids*, 55:579 – 587, July 1994.

[15] O. Kurakevych and V. Solozhenko. Experimental study and critical review of structural, thermodynamic and mechanical properties of superhard refractory boron suboxide B_6O. *Journal of Superhard Materials*, 33:421–428, 2011.

[16] O.O. Kurakevych and V.L. Solozhenko. 300-K equation of state of rhombohedral boron subnitride. *Solid State Communications*, 149:2169 – 2171, December 2009.

[17] R. Lazzari, N. Vast, J.M. Besson, S. Baroni, and A. Dal Corso. Atomic structure and vibrational properties of icosahedral B_4C boron carbide. *Physical Review Letters*, 83:3230 – 3233, October 1999.

[18] T. Letsoalo and J.E. Lowther. Systematic trends in boron icosahedral structured materials. *Physica B: Condensed Matter*, 403(17):2760 – 2767, 2008.

[19] D.A. Long. *Chapter 5: Vibrational Raman Scattering*, pages 85 – 152. John Wiley & Sons, Ltd, 2002.

[20] J.E. Lowther. Possible ultra-hard materials based upon boron icosahedra. *Physica B: Condensed Matter*, 322(1 – 2):173 – 178, 2002.

[21] R. Machaka, B.W. Mwakikunga, E. Manikandan, T.E. Derry, and I. Sigalas. Raman spectrum of hot-pressed boron suboxide. *Advanced Materials Letters*, 2:58 – 64, 2011.

[22] M. Olofsson and T. Lundstrom. Synthesis and structure of non-stoichiometric B_6O. *Journal of Alloys and Compounds*, 257:91 – 95, July 1997.

[23] V.L. Solozhenko and O.O. Kurakevych. New boron subnitride $B_{13}N_2$: HPHT synthesis, structure and equation of state. *Journal of Physics: Conference Series*, 121:062001, 2008.

[24] V.L. Solozhenko, O.O. Kurakevych, and P. Bouvier. First and second-order Raman scattering of B_6O. *Journal of Raman Spectroscopy*, 40:1078 – 1081, August 2009.

[25] Bin Wang, Zhaochuan Fan, Qi Zhou, Xiaoxuan Xu, Min Feng, Xuewei Cao, and Yufang Wang. First principles calculations of the vibrational properties of icosahedral solid boron oxygen $B_{12}O_2$. *Physica B: Condensed Matter*, 406(2):297 – 303, 2011.

[26] Z. Wang, Y. Zhao, P. Lazor, H. Annersten, and S.K. Saxena. In situ pressure Raman spectroscopy and mechanical stability of superhard boron suboxide. *Applied Physics Letters*, 86:041911, January 2005.

[27] H. Werheit and V. Filipov. Raman effect in boron and boron-rich compounds. NATO ARW, Boron-Rich Solids, Orlando, Florida, USA, 2009. Dec. 14 – 18.

[28] H. Werheit and U. Kuhlmann. FTIR and FT-Raman spectra of B_6O. *Journal of Solid State Chemistry*, 133:260 – 263, October 1997.

[29] D. Wolverson. Raman spectroscopy. In C. Lamberti, editor, *Characterization of Semiconductor Heterostructures and Nanostructures*, pages 249 – 288. Elsevier, Amsterdam, 2008.

[30] Shengwen Yu, Yalin Ji, Tianxin Li, Min Han, Guanghou Wang, Xianzhang Yuan, Zhifeng Li, and Pingping Chen. Nanofilms with clusters of boron suboxide and their infrared absorption. *Solid State Communications*, 115:307 – 311, June 2000.

Chapter 4

Microhardness Indentation Size Effect Studies in Hot-Pressed B_6O

In this chapter, the indentation load-size dependence phenomenon in the measured microhardness of hot-pressed B_6O is investigated by means of a comprehensive inter-model comparison of various models proposed in literature. The intrinsic hardness of the material is reported. Furthermore, the nature and the origins of the observed indentation size effect (ISE) are investigated and discussed.

The chapter is based on an article submitted to the *Advances in Materials Science and Engineering* journal under that title '*Indentation size effects studies in microhardness measurements of B_6O*' [11].

4.1 Introduction

With hardness values reported to range between 24 GPa and 45 GPa [8, 9], B_6O is sometimes considered to be the third hardest material after only diamond (~70 to ~100 GPa) and cubic boron nitride (~60 GPa) [9]. To the best of our knowledge, the indentation load-size dependence in the microhardness of hot-pressed B_6O has been observed before, but is being comprehensively examined for the first time in this study. It also appears that the intrinsic hardness of the and the origins of the load-dependence in the measured hardness are not-well studied.

The aim of this investigation is twofold: (1) to report experimental data on the microhardness of hot-pressed B_6O determined by Vickers pyramidal indentation, and (2) to critically examine the ISE phenomenon by means of a comprehensive inter-model comparison of various approaches and models proposed in the literature. The nature and the origins of ISE are investigated and discussed.

4.2 Experimental details

The Vickers microindentation measurements were performed at room temperature using a Future-Tech microhardness tester at different applied test load between 0.1 and 2.0 kgf. At least ten measurements were carefully taken for each load at different locations on the middle of each sample, and the average values were taken as the hardness of the sample at that load. The Vickers indentation impressions were observed using optical microscopy.

4.3 Results and discussion

The surface and compositional characterization of the baseline B_6O specimen investigated by XRD, SEM with EDX, and micro-Raman spectroscopy is reported has been presented in Chapter 3.

4.3.1 Microindentation measurements

To investigate ISE, micro-indentation measurements were conducted at test load between 0.1 and 2.0 kgf using a Vickers diamond indenter. Apparent Vickers microhardness values H_v, were calculated at each load using the conventional approach shown in Equation (4.3.1) below:

$$H_v = \frac{1.8544 \cdot P}{d^2} \tag{4.3.1}$$

where d is the average diagonal length of the Vickers indentation impressions. Figure 4.1 shows the dependence of the measured Vickers microhardness of hot-pressed B_6O on the applied indentation load and the figure insert shows a typical optical micrograph of a Vickers indentation impression. Each of the plotted data point is an average of at least ten measurements at each applied test load.

Evidently, the Vickers hardness is a function of the applied load at low applied indentation test load. The existence of ISE makes it unsatisfactory here to quote a single hardness

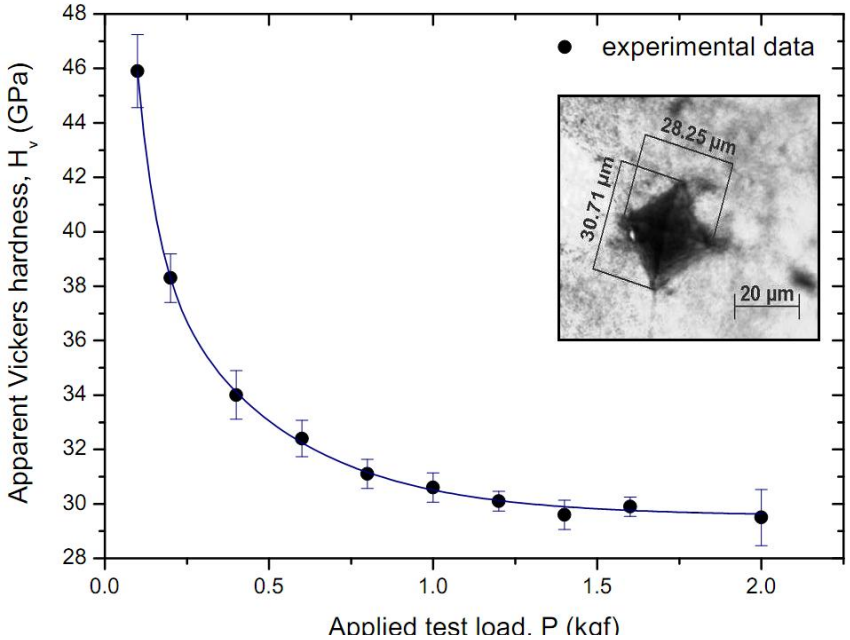

Figure 4.1: *The dependence of apparent Vickers microhardness of hot-pressed B_6O with applied load. The figure insert shows an optical microscope image of a typical indentation impression.*

value when Vickers hardness is used for material characterization. By observation, at applied indentation test loads ~1 kgf, a single load-independent Vickers hardness value of 29.5 GPa seems to exists. The load-independent hardness is also sometimes deemed the intrinsic or 'true' hardness. The observed value is consistent with literature reported values [1, 8, 9].

Meyer's law

The classical power law shown in Equation (4.3.2a), also known as the Meyer's law, is frequently used to indicate the existence of ISE for ceramic and other materials [5]. B is a power-fit constant and the exponent n is the Meyer's index, also known as the size-effect index. The Meyer's index is generally used as a measure of ISE.

$$P = B \cdot d^n \tag{4.3.2a}$$

$$\log P = \log B + n \cdot \log d \tag{4.3.2b}$$

The regression analysis of the experimental data using Equation (4.3.2b) is shown in Figure 4.2. The slope of the linear fit is the Meyer's index, and observed to be $n = 1.75$. Usually when $n = 2$, the microhardness is expected to be independent of the applied load. However,

$n \leq 2$ indicates the existence of an ISE trend; the measured microhardness decreasing with applied load [3, 10].

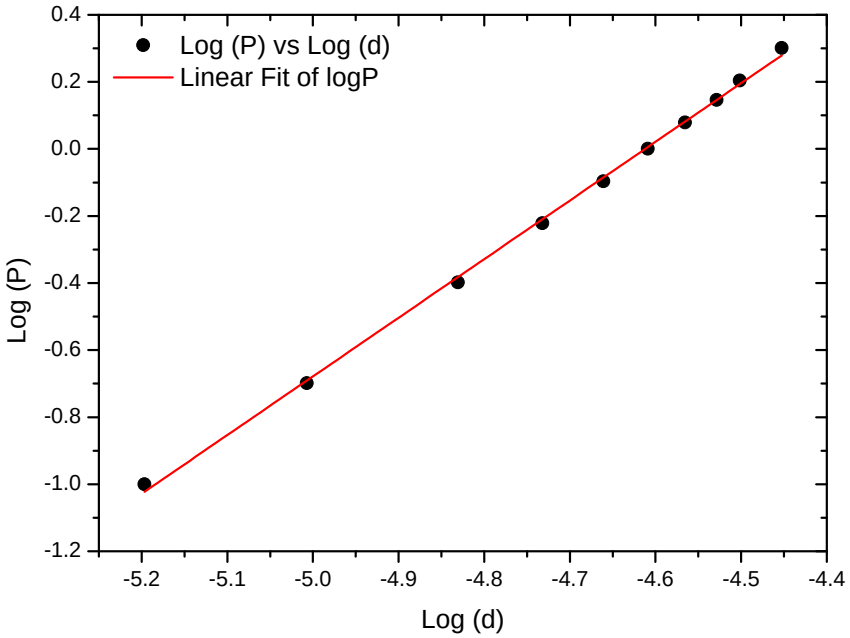

Figure 4.2: *Linear regression analysis of log(P) against log(d) according to the Meyer's law (Equation (4.3.2b)).*

PSR model

Several studies [4, 10] agree that the Meyer law is probably insufficient to describe the origin of the ISE, although it is a good indicator of its existence. According to Li and Bradt [10], the applied indentation load is related to the average indent diagonal length through a polynomial relationship (Equation (4.3.3a)):

$$P = a_1 \cdot d + a_2 \cdot d^2 \tag{4.3.3a}$$

$$= a_1 \cdot d + \frac{H_{psr}}{1.8544} \cdot d^2 \tag{4.3.3b}$$

The parameters a_1 and a_2 are constants for a given material. The parameters are related to the elastic and the plastic deformation properties of the test material, respectively. The parameter a_1 is a measure of the surface effects during microhardness indentation which is directly related to the ISE contribution whilst a_2 is directly related to the load independent microhardness value H_{psr} as demonstrated in Equation (4.3.3b) above.

From Equation (4.3.3a), a plot of P/d against d can be constructed to yield a straight line, where best-fit parameters a_1 and a_2 can easily be obtained by regression analysis. As

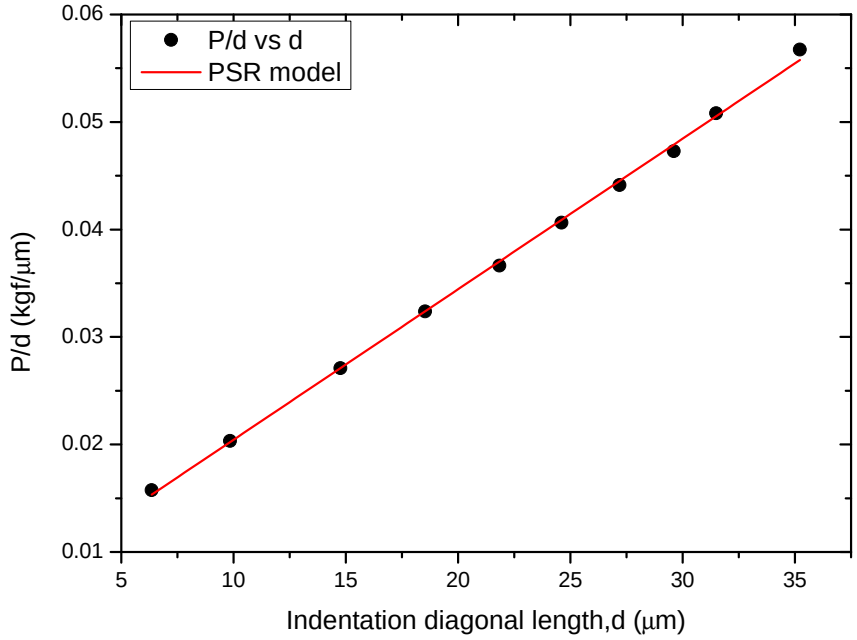

Figure 4.3: *A plot of P/d against d constructed from the experimentally measured data and a best linear fit of the plot.*

shown in Figure 4.3 below, a plot of P/d against d is significantly linear, implying that Equation (4.3.3a) gives an indication of the existence of ISE in hot-pressed B_6O.

As noted previously, the PSR analysis can be extended to determined H_{psr} directly from a_2 using Equation (4.3.3b). In this study H_{psr} was found to be 26.8 ± 0.3 GPa.

Modified PSR model

Gong et al. in reference [7] modified the PSR model to investigate the ISE behaviour in various materials. The resulting MPSR model is defined by Equation (4.3.4a) below:

$$P = a_0 + a_1 \cdot d + a_2 \cdot d^2 \tag{4.3.4a}$$

$$= a_0 + a_1 \cdot d + \frac{H_{psr}}{1.8544} \cdot d^2 \tag{4.3.4b}$$

where a_0 is a constant related to the residual surface stresses associated with the surface grinding and polishing processes during sample preparation. The parameters a_1 and a_2 are constants as defined in the PSR model (refer to Section 4.3.1.2 above). The values of a_0, a_1 and a_2 can be evaluated by plotting the P data against d. The plot of P versus d (and polynomial curve fitting thereof according to the MPSR model) is shown in Figure 4.4 below.

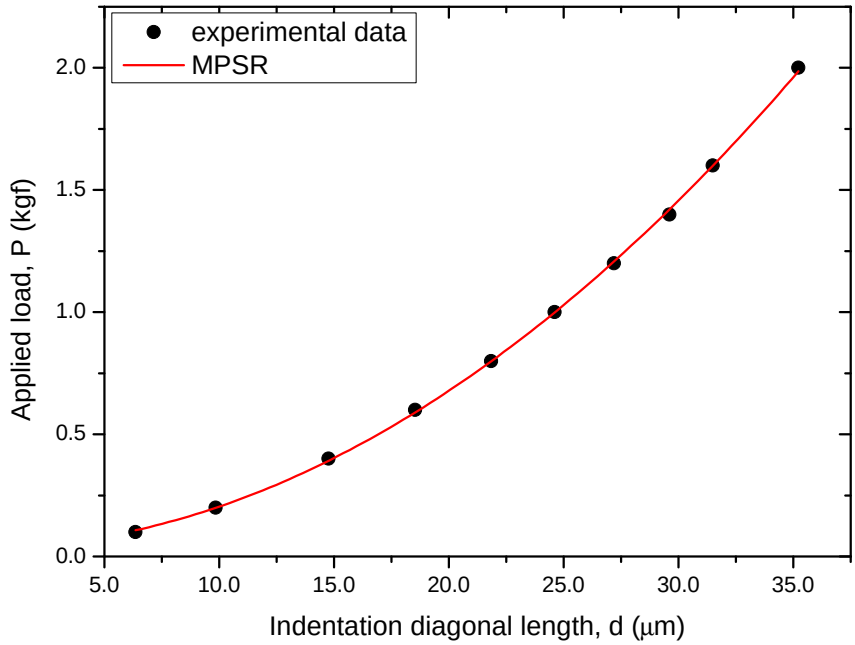

Figure 4.4: *A plot of P versus d, and curve fitting thereof, according to the MPSR model.*

As is the case for the PSR model, a load-independent hardness value, H_{mpsr}, can be determined directly from best-fit value of a_2 from Figure 4.4 using Equation (4.3.4b). In this study, H_{mpsr} was found to be 28.2 ± 0.9 GPa.

The estimated best-fit values of the a_0, a_1, and a_2 parameters corresponding H_{mpsr} values are listed in Table 4.1. The residual surface stresses contribution to the observed ISE is negligible compared to the contribution of bulk material's plastic deformation characteristics.

Model	$\mathbf{a}_0$	$\mathbf{a}_1$	$\mathbf{a}_2$ ($\times 10^{11}$)
PSR	—	19711	6.95
MPSR	0.0026	20591	7.99

Table 4.1: *A summary of the best-fit parameters calculated according to the PSR and MPSR models.*

The PSR and MPRS parameters estimated by regression analysis are summarized in Table 4.1. Based on the values and their physical significance according to in the energy-balance relation [6], we suggest that the residual surface stresses' contribution (a_0) to the observed ISE is negligible compared to the contribution of bulk material's indentation elastic recovery (a_1) and the indenter/specimen interface friction resistance coupled with elastic resistance of the specimen and the mixed elastic/plastic deformation response of material (a_2).

MFSL approach

As illustrated in Figure 4.1, the variation of microhardness with indentation load is a two-parameter problem exhibiting at least two totally different size-dependent regimes: a load-dependent regime and a load-independent regime. The variation of microhardness with indentation load in other words exhibits self-similarity, i.e. by observing the property in different scales a similar, but not exactly the same structure, is obtained – a property of multi-fractals.

According to Carpinteri and Puzzi in [2], ISE in materials follows the multifractal scaling law shown in Equation (4.3.5). However, the indentation size effect property is observed to vanish in the limit of the applied load tending to 'infinity'. From the later, an asymptotic value of hardness which resembles a load-independent or intrinsic value can be determined as illustrated in Figure 4.5. In this study we apply the multifractal scaling law in the analysis of observed indentation size effect in hot-pressed B_6O. Further in-depth discussions on the fractal approach to ISE is refereed to Carpinteri's comprehensive review on the subject [2].

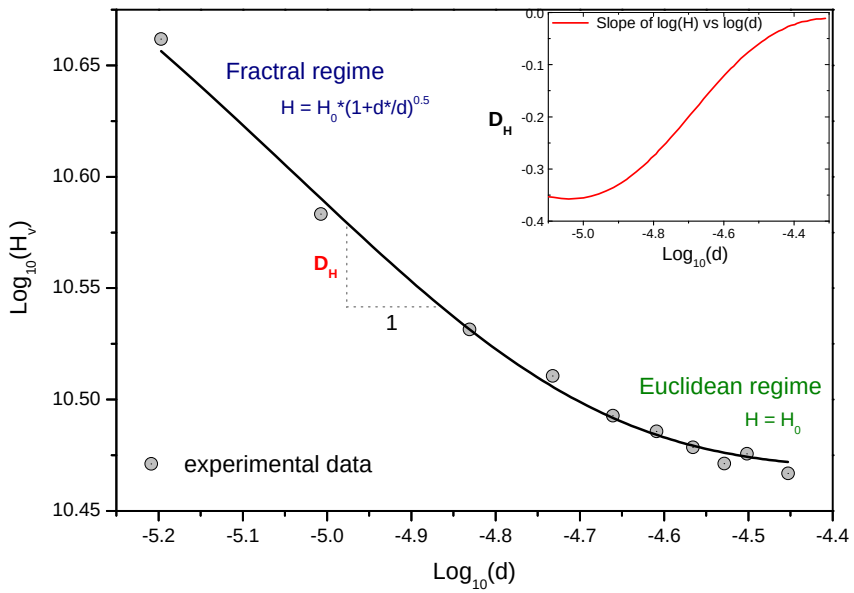

Figure 4.5: *$\log H_v$ plotted as a function of $\log(d)$. The slope of the plot equals D_H, a fractal dimension for hardness with respect to d. In the insert the fractal dimensional increment D_H is plotted as a function of $\log(d)$. Nonlinearity of the scaling fractal dimensional suggests multifractal behaviour.*

On the basis of this approach, the multifractal scaling law (MFSL) for ISE can be written in the following analytical form:

$$H_v = H_{mfsl} \cdot \left(1 + \frac{d^*}{d}\right)^{\frac{1}{2}} \tag{4.3.5}$$

where H_{mfsl} is the intrinsic hardness in the limit of infinite (a huge) applied load and d^* is the critical material characteristic length which individuates the transition between the two regimes, that is, the fractal one and the non-fractal (Euclidean) one.

In order to study the fractal characteristic of the size effect dependence of microhardness depicted in Figure 4.1, a *log-log* plot of the Vickers microhardness and the indentation diagonal length was constructed based on the multifractal scaling law shown in Equation (4.3.5) and presented as Figure 4.5. The result shows that $log(H)$ as a function of the $log(d)$ is approximately linear in two parts of the scale dependence.

In this study both d^* and H_{mfsl} were determined simultaneously by means of non-linear least squares analysis of the experimental data using Mathematica. H_{mfsl} and d^* were determined to be 28.9 GPa and 1.41 μm, respectively. The fractal dimension in the first region can be depicted as the following equation.

The slope of the bi-logarithmic plot shown in Figure 4.5 represents the fractal dimensional increment D_H, which is a measure of the variable influence of ISE on the measured Vickers hardness. The variation of fractal dimension of multifractality D_H with $log(d)$, as determined from $log(H)$ versus $log(d)$, is presented as an insert in Figure 4.5). Two limiting conditions have to be satisfied: $D_H = 0$ for large indents (Euclidean response), and $D_H = 0.5$ for small indents (multifractal behaviour). The last situation corresponds to the highest possible indentation size effect in hardness, which is a theoretical upper bound.

According to the insert in Figure 4.5, D_H tends to zero coincides with the occurrence in a cross-over between fractal and Euclidean behaviour implying the progressive vanishing of fractality in the measured Vickers microhardness with increasing indentation load/size.

4.4 Summary and conclusion

Figure 4.1 shows that the variation of H_v with P indicates that the hot-pressed B_6O ceramic material exhibits a load-size dependency. Based on the observation, a comprehensive study of ISE in microhardness measurements of B_6O was conducted using a number of existing models; i.e. the classical Meyer's law, Li and Bradt's PSR model, Gong's MPSR model

	$H_{psr}(GPa)$	H_{mpsr} (GPa)	H_{mfsl} (GPa)	H_{ave} (GPa)
This study	26.8 ± 0.3	28.2 ± 0.3	28.9 ± 0.1	28.0 ± 0.3

Table 4.2: *A summary of the intrinsic microhardness values calculated according to the PSR model, the MPSR model as well as Carpinteri's MFSL scalling model.*

and Carpinteri's MFSL model. A summary of the hardness values calculated is shown in Table 4.2 below.

The average load-independent hardness of hot-pressed B_6O from this study has been observed to be 28.0 ± 0.3 GPa. The reported hardness values range between 24 GPa and 45 GPa; 45 GPa being the hardness of single crystal B_6O [8, 9].

Based on the analysis of the PSR and MPSR parameters estimated by regression analysis, the origins of ISE in hot-pressed B_6O can be attributed to either the bulk material's indentation elastic recovery, the indenter/specimen friction resistance coupled with elastic resistance of the specimen or/and the mixed elastic/plastic deformation response of material. The residual surface stresses' contribution to the observed ISE is observed to be negligible compared to the aforementioned.

The linear relationship of the double logarithm between measure (microhardness, in this case) and scale (the applied load) shows indentation self-similarity, both in indentation shape and in the results of hardness. We can conclude this to be fractal behaviour. The load dependence of hardness shows dual fractal behaviour given the two different regions of hardness.

We can conclude and suggest that the variation of fractal dimension of multifractality D_H with $log(d)$ is a more resourceful indicator of its existence of ISE that the Meyer's index, for example.

Bibliography

[1] A. Andrews, I. Sigalas, and M. Herrmann. Boron suboxide composite material. WIPO Patent No. 2008132675, 2008.

[2] Alberto Carpinteri and Simone Puzzi. A fractal approach to indentation size effect. *Engineering Fracture Mechanics*, 73:2110 – 2122, 2006.

[3] O. Şahin, O. Uzun, U. Kölemen, and N. Uçar. Mechanical characterization for β-Sn single crystals using nanoindentation tests. *Materials Characterization*, 59:427 – 434, 2008.

[4] O. Şahin, O. Uzun, M. Sopicka-Lizer, H. Gocmez, and U. Kölemen. Dynamic hardness and elastic modulus calculation of porous SiAlON ceramics using depth-sensing indentation technique. *Journal of the European Ceramic Society*, 28:1235 – 1242, 2008.

[5] J. Gong, H. Miao, Z. Peng, and L. Qi. Effect of peak load on the determination of hardness and Young's modulus of hot-pressed Si_3N_4 by nanoindentation. *Materials Science and Engineering: A*, 354:140 – 145, 2003.

[6] J. Gong, J. Wu, and Z. Guan. Analysis of the indentation size effect on the apparent hardness for ceramics. *Materials Letters*, 38:197 – 201, 1999.

[7] J. Gong, J. Wu, and Z. Guan. Examination of the indentation size effect in low-load Vickers hardness testing of ceramics. *Journal of the European Ceramic Society*, 19:2625 – 2631, 1999.

[8] M. Herrmann, J. Raethel, A. Bales, K. Sempf, I. Sigalas, and M. Hoehn. Liquid phase assisted densification of superhard B_6O materials. *Journal of the European Ceramic Society*, 29:2611 – 2617, 2009.

[9] H.-J. Kleebe, S. Lauterbach, T.C. Shabalala, M. Herrmann, and I. Sigalas. B_6O: A correlation between mechanical properties and microstructure evolution upon Al_2O_3 addition during hot pressing. *Journal of the American Ceramic Society*, 91:569 – 575, 2008.

[10] H. Li and R.C. Bradt. The effect of indentation-induced cracking on the apparent microhardness. *Journal of Materials Science*, 31:1065 – 1070, 1996.

[11] R. Machaka, T.E. Derry, I. Sigalas, and M. Herrmann. Analysis of the indentation size effect in the microhardness measurements in B_6O. Article ID 539252, doi:10.1155/2011/539252, March 2011.

Chapter 5

Nanomechanical Properties of Hot-Pressed B_6O

Until now the investigations of the nano-mechanical properties of hot-pressed B_6O by nanoindentation appear to have been neglected in favour of the improvement of densification and fracture toughness of the B_6O-based composites. In the studies presented in this chapter, a combined experimental and finite element method simulation approach for determining mechanical properties of hot-pressed B_6O by nanoindentation is presented. Furthermore, the deformation response of the material under dynamic indentation was also investigated at different stages using a finite element analysis method.

The chapter is based on an article published in *Materials Science and Engineering A* under the title *Nanoindentation hardness of hot-pressed boron suboxide* [24].

5.1 Introduction

Investigations of the nanomechanical properties of hot-pressed B_6O, by nanoindentation for example, appear to have been neglected in favour of the improvement of densification and fracture toughness of the B_6O materials.

For lower applied load indentation tests there is enough experimental evidence to suggests that the measured macro-, micro- and nanohardness values are not single material constants,

but a function of either the applied test load, or the depth of the indentation [3]. The absence of a single value for the hardness is a material property is known as the ISE [11, 12].

The study presented here is aimed at investigating the nano-mechanical properties of bulk hot-pressed B_6O. In particular, (a) the load-displacement indentation response of hot-pressed B_6O is measured and analyzed, (b) the nanoindentation hardness of hot-pressed B_6O is reported, (c) a novel quantitative approach developed in this study for analyzing the loading curve analysis is introduced, (d) the ISE in nanoindentation hardness of hot-pressed B_6O is also analysed and discussed with the aid of an inter-model comparison, and finally, and rather most importantly, (e) using a finite element analysis model, the elastic-plastic deformation behaviour of the material is investigated in response to progressive indentation stress.

5.2 Theory of nanoindentation

Nanoindentation technique has been established as a powerful mean of characterizing the near-surface mechanical properties of materials [6]. This technique relies on high-resolution instruments that simultaneously measure the load P, and indenter displacements h, during the loading and unloading indentation steps. The important parameters obtained from the resultant load-displacement ($P-h$) curve, which are schematically illustrated in Figure 5.1, are the peak load, P_{max}, the maximum penetration depth, h_{max}, final penetration depth, h_f, and the contact stiffness, S. The indentation analysis procedure developed by Oliver and Pharr (O&P) has been widely used for hard materials such as metals and ceramics [6, 30, 31].

The O&P data analysis procedure begins by fitting the unloading curve to the power-law relation given as:

$$P = \alpha \cdot (h - h_f)^m \tag{5.2.1}$$

where m (the displacement exponent in the load-displacement relation for unloading) and α (unloading fitting parameter dependent on the elastic material behaviour) are empirical constants determined using the power fitting of unloading data [9].

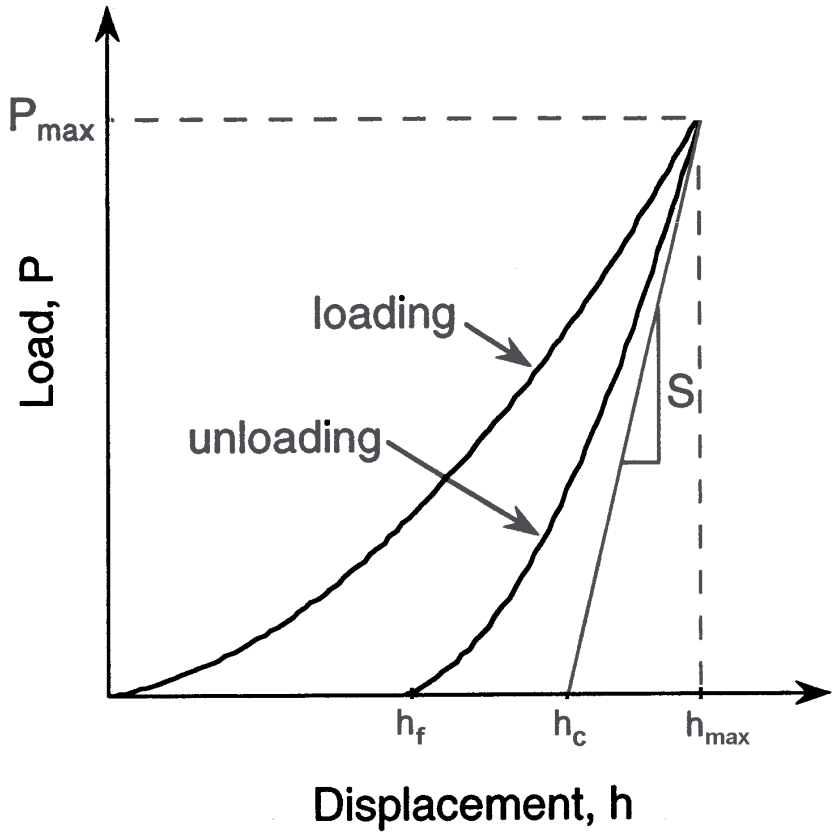

Figure 5.1: *A typical load-displacement curve during a loading-unloading cycle where h_{max} is the maximum indenter displacement at peak indentation load P_{max}, S is the initial unloading slope of the load-displacement curve, and h_c is the contact depth.*

The derivative of P (Equation (5.2.1)) with respect to h yields the contact stiffness S, which is the slope of the unloading $P-h$ curve.

$$\begin{aligned} S &= \left(\frac{dP}{dh}\right)_{unloading} \\ &= m \cdot \alpha \cdot (h - h_f)^{m-1} \end{aligned} \tag{5.2.2}$$

The contact depth of the indent impression h_c can either be derived by extrapolating the initial slope of the unloading $P-h$ curve down to $P = 0$ N or otherwise, determined using an empirical formula as observed by Oliver and Pharr [30, 31] given by:

$$h_c = h_{max} - \epsilon \cdot \frac{P_{max}}{S} \tag{5.2.3}$$

where, in this case for the Berkovich indenter geometry, $\epsilon = 0.75$ [30].

The contact area A_c is the cross sectional area at h_c [8, 10]. Various experimental and numerical studies have established that for the Berkovich indenter geometry, the projected A_c can be approximated by the empirical formula [8, 10]:

$$A_c(h_c) = \Big(24.56 \cdot h_c^2 + C_1 \cdot h_c^{\frac{1}{2}} + C_2 \cdot h_c^{\frac{1}{4}} + C_3 \cdot h_c^{\frac{1}{8}} + \\ ... + C_8 \cdot h_c^{\frac{1}{125}}\Big) \tag{5.2.4}$$

where C_1, C_2, …, C_8 are constants determined by curve-fitting procedures and are all defined based in on the indenter tip radius [9]. However, for the Berkovich indenter geometry, projected area can be reduced to $A_c(h_c) \approx 24.56 \cdot h_c^2$ [6, 8, 15].

When S, and A_c, have been determined,the specimen's elastic modulus (E_s) or simply E can then be evaluated using Equation (5.2.5):

$$\frac{1}{E_r} = \frac{1 - \nu_s^2}{\mathbf{E_s}} + \frac{1 - \nu_i^2}{E_i} \tag{5.2.5}$$

where ν_s and ν_i are respectively the specimen and indenter Poisson ratios, E_i is the indenter elastic modulus [6, 15] and E_r is the reduced elastic modulus given by:

$$E_r = \frac{\sqrt{\pi}}{2\beta} \cdot \frac{S}{\sqrt{A_c}} \tag{5.2.6}$$

where β is a correctional factor introduced by King [17] to address the lack of indenter symmetry; for the Berkovich indenter, $\beta = 1.034$ [15].

The indentation hardness H has been long defined as the test force P divided by the projected area of contact A_c [26].

$$H = \frac{P_{max}}{A_c} \tag{5.2.7}$$

However, it is also generally understood that hardness values derived using Equation (5.2.7) are often depth and load dependent; a single value is often inadequate to implicitly characterize the material property.

In order to extract the true or the intrinsic hardness of the specimen we applied an important material characteristic ratio, P/S^2, first proposed by Josilin and Oliver [16] expressed as:

$$\frac{P}{S^2} = \frac{\pi}{4\beta^2} \cdot \frac{\mathbf{H(E)}}{E_r^2} \tag{5.2.8}$$

P/S^2 is independent of the penetration depth h or A_c [34]. Therefore, if S and E_r have been pre-determined, the intrinsic harness of specimen, $H(E)$ can be evaluated.

In summary, the method outlined here has been applied in this study to extract the material nanomechanical bulk properties (E from Equation (5.2.5) and $H(E)$ from Equation (5.2.8)) from the measured nanoindentation data.

5.3 Experimental details

Nanoindentation measurements (CSM Instruments Nanohardness Tester at NMMU, PE) were performed with a diamond Berkovich indenter with a linear loading/unloading rate of 2000.0 mN/min up to a maximum load of 100 mN the dwelling time of 25 s shown in Figure 5.2. For the evaluation of the $P-h$ curves, the O&P method was used [30], assuming a Poisson's ratio of 0.18 for elastic modulus calculation. For each sample, up to between twelve and twenty-four separate indents were performed at different positions. An averaged loading-unloading cycle curve was used for analysis. However, this excludes anomalous indents on obvious surface pores and artifacts identified by inspecting the optical micrographs of the indented region.

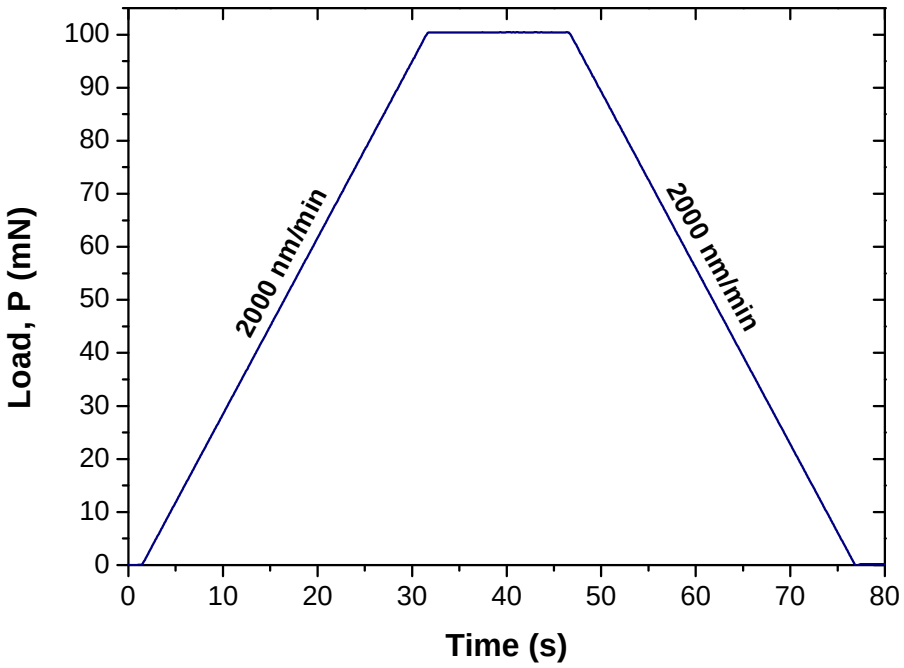

Figure 5.2: *An instrumented indentation load-time profile for all the experiments and all results presented in this article.*

The validity of the analysis techniques are adversely affected by the presence of pile-up, sink-in, and lateral and radial cracks. The topography of surfaces and indent impressions on the B_6O sample was examined for these effects using AFM.

During the holding period (in-between the loading and unloading steps), the indenter displacement was observed to exhibit indentation creep [6] that is, a time-dependent material deformation response during indentation [13]. The nanoindentation creep tests performed in this study were all conducted at room temperature, a constant load of $P_{max} = 100\,mN$, and a single holding times of about 16 s for all specimens. The preliminary results were analyzed using an approach inspired by the one suggested by Goodall and Clyne in reference [13] and are reported here as well.

5.4 Development of the FEM model

In recent years different numerical techniques have been developed to simulate the nanoindentation process in various materials [25]. Finite element modeling (FEM) is one of the most popular techniques [25]. However it is very important to bear in mind that FE simulation can only obtain numerical results and strictly speaking, cannot provide clear parametric relationships to indicate possible physical variables involved and the sensitivity of the final results to those variables. The simulation and analysis of the indentation process is a mathematically complex problem, FEM has been widely adopted by many researchers, see [25] and references therein.

FEM is a numerical analysis technique used by engineers, scientists, and mathematicians to obtain solutions to the differential equations that describe, or approximately describe a wide variety of physical (and non-physical) problems. Physical problems range in diversity from solid, fluid and soil mechanics, to electromagnetism or dynamics.

The indentation process under consideration involves bulk hot-pressed B_6O indented by a rigid Berkovich nanoindenter under the ambient condition. FEM of the nanoindentation process was employed in this study in order to simulate the nanoindentation loading-unloading process of bulk hot-pressed B_6O material, to simulate the development of the very complex elasto-plastic deformation dynamics of bulk hot-pressed B_6O material during indentation, and extract intrinsic material properties ($H(E)$, E) from the examination.

A 3D FE model, as illustrated in Figure 5.3(a), would be ideally desirable. Unfortunately, 3D FE models are generally considered inefficient due to their case-by-case nature and the effort required for creating 3D meshes [2]. Comparison of results using the 2D and 3D models has been observed to show very little difference and thus for most cases the

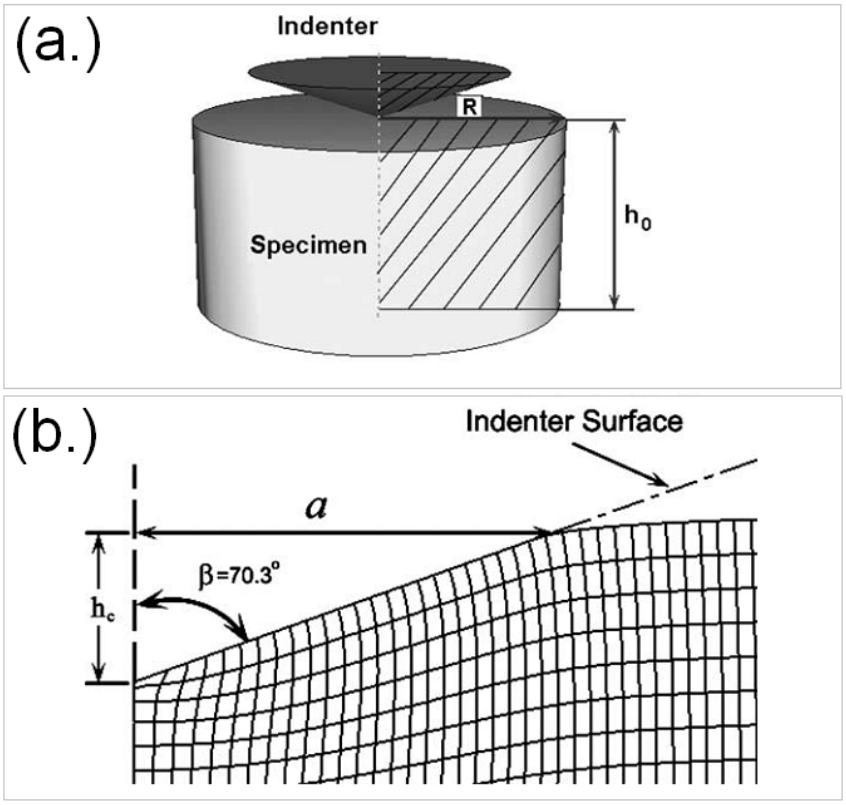

Figure 5.3: *Schematic illustrations of the of finite element 3D nanoindentation model (a.) and the corresponding 2D semi-infinite half space axisymmetric model used in this study.*

2D simulations are all that are required. Besides, using the 2D model minimizes the total computational time [19].

Due to the high level of symmetry of the 3D FE nanoindentation model (Figure 5.3(a)), the cylindrical specimen of arbitrary dimensions and the conical indenter were modeled in order to define a 2D semi-infinite half space axisymmetric model as illustrated in Figure 5.3(b).

The FE meshes used in the indentation analyses are comprised of four-noded isoparametric quadrilateral elements and are gradually refined from the outer boundary of the specimen towards the indented zone. The specimen is modeled with (at least 5000) four-node axisymmetric 'reduced integration' elements (CAX4R[1] element type). In order to improve the accuracy of the results whilst minimizing the computational time, the mesh density refinement was biased toward the centre of the specimen where the largest deformation was expected. Because of high gradients near the indenter tip, the mesh is adequately refined. The typical element size in the refined mesh area is about 0.10 mm. To prevent severe mesh distortion that affects the solution accuracy, the adaptive mesh option is used

[1]Four-node bilinear axisymmetric quadrilateral type elements with reduced integration were used in this model's development to avoid overstiff bending. CAX4R is probably the most popular element-type in FEM.

Ideally, knowledge of the specimen material's elastic–plastic stress-strain behaviour is needed to accurately simulate deformation behaviour. Unfortunately, the brittle nature of B_6O, as well as other ceramics such as B_4C and SiC makes it nearly impossible to obtain the stress-strain data at room temperature by conventional tension or compression testing. This material was assumed to be an isotropic, elastic-plastic material with no dependence on the loading or unloading rates.

Isotropic elastic constants of E = 400 GPa (calculated from the experimental Berkovich indenter using the O&P method) and a Poisson's ratio, ν = 0.18 [22]. In the work reported here the Poisson's ratio of hot-pressed B_4C, whose structure is similar to that of B_6O, was used as an estimate of B_6O's Poisson's ratio. The assumption being that a rough estimation of Poisson's ratio for does not significantly affect the obtained results [32].

A simple conical indenter of 70.3° half-angle has the same projected area-depth function as the standard Berkovich indenter used in the experimental nanoindentation study [19]. Most importantly, conical rigid indenter is modeled to be un-deformable. The indenter was a rigid body with no imperfections and a perfectly sharp tip.

In this study, 2D axisymmetric FE simulations of the conical nanoindentations of hot-pressed B_6O were conducted using a commercially available finite-element package ABAQUS v6.9 EF1 (ABAQUS (Hibbit, Karlson and Sorensen Inc., Providence, RI). State the friction coefficient between material/indenter interactions was taken to be zero – ideal frictionless case.

5.5 Results and discussion

5.5.1 AFM imaging

B_6O is very brittle covalent and therefore are more susceptible to cracking because of the directionality of the atomic bonding. Crack initiation and subsequent crack growth, pile-ups, and sinking-ins can often influence severely the results given by an indentation hardness test and a proper interpretation of indentation parameters becomes difficult [21]. The topography scans of surfaces observed by AFM are shown in Figure 5.4. From the AFM images taken on the indentation impression on the specimen surfaces no pile-ups, sinking-ins or surface cracks were observed.

Using Gwyddion v2.24 for profilometric data analysis [18], the surface roughness of the specimen was determimed from the AFM images. The specimen surface appears to be characterized with an average roughness (R_a) of about 7 nm with a root mean square (rms)

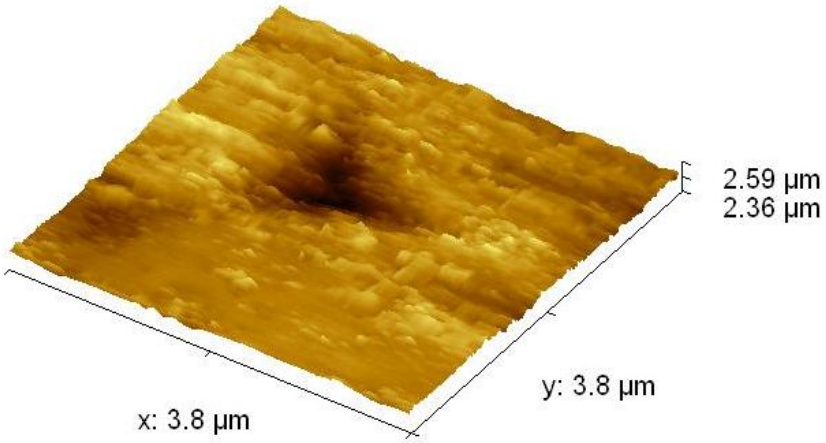

Figure 5.4: *AFM image showing the indentation impression on the specimen surface.*

surface roughness amplitude (R_q) of about 9 nm. Clearly, the surface roughness at the indentation average site is a small fraction of the maximum indentation depth and therefore, do not appear to influence the mechanical properties significantly.

5.5.2 Experimental nanoindentation

Figure 5.5 below depicts the average $P-h$ data for hot-pressed B_6O measured during nanoindentation tests with a Berkovich diamond indenter at room temperature. The curve demonstrates a smooth shape with no pop-in/discontinuity behaviour observed.

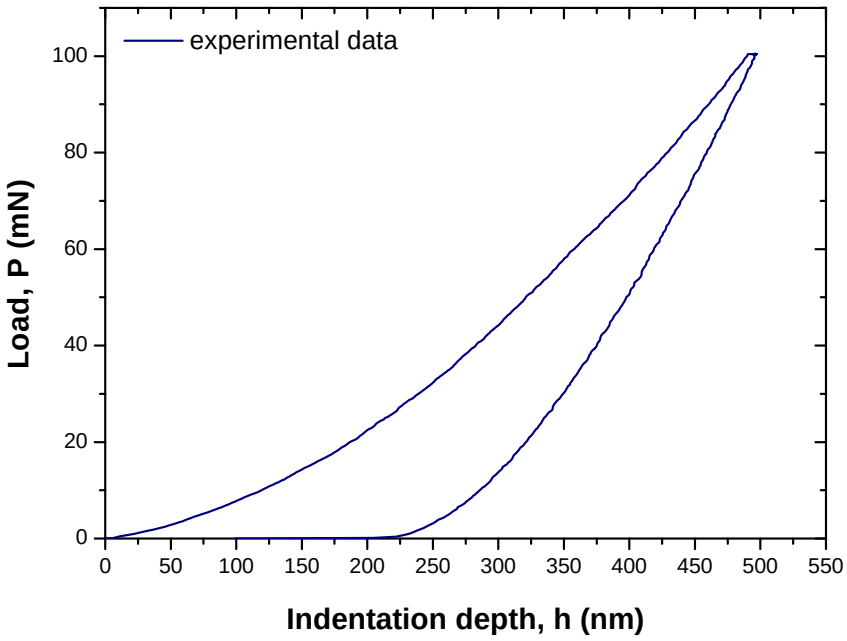

Figure 5.5: *A representative $P-h$ curve measured during the nanoindentation measurements on the uniaxially hot-pressed boron suboxide compact.*

From the $P-h$ unloading curves, the elasticity modulus E and the hardness H_{op} evaluated in accordance with the O&P approach, the intrinsic hardness $H(E)$, and the unloading contact stiffness – S (= $(dP/dh)_{unloding}$) are summarized in Table 5.1 [29–31].

The hardness values of H_{op} and $H(E)$ calculated from the experimentally measured nanoindentation data (Equation (5.2.8)) are consistent with the load-independent Vickers hardness value calculated and reported in Section 4.3.1 on page 37.

	E (GPa)	H_{op} (GPa)	H(E) (GPa)	S (mN/nm)	A(h_c) (10^6 nm^2)	m
this study	363.4	28.4	30.7	0.5667	3.27	1.53
literature cited	230 – 476 [27]	—	—	—	—	—

Table 5.1: *Material properties evaluated using the O&P approach from the data of the $P-h$ curves shown in Figure 5.5.*

Indentation size effect

For ceramic materials, it is now widely accepted that macro-, micro- and nano-hardness measured values are not single material constants, but rather dependent on the applied test load of the indentation. This has been observed for both nanoindentation and microindentation experiments [20].

Numerous investigators have reported studies of ISE using nanoindentation testing for various materials [20]. The typical scheme involves carrying out multicycling nanoindentation tests loading-unloading tests on the same spot and simultaneously measuring the $P-h$ curves under different peak applied load in a defined load range [9, 20, 33]. A closer examination of the reported $P-h$ cycles demonstrates that the individual cycle curves show similar loading and unloading behaviour [33]. Şahin et at. in reference [4] suggests that this indicates similar elastic and plastic deformation mechanism on the load range used.

It is expected that a $P-h$ curve measured at a single peak applied load can adequately define the ISE behaviour of a material since each loading $P-h$ curve is expected to contain a wealth of elastic and plastic deformation characteristics of a material [33], although this approach is not commonly used in the nanoindentation data analysis.

From here onwards, we attempt to make use of the loading segment $P-h$ data recorded during a single nanoindentation measurement to simulate multicycling loading-unloading $P-h$ cycles measured under different peak loads between 0.5 mN and 100 mN. It should be noted that the entire unloading $P-h$ cycle is not easy to simulate using this 'pseudo-multicycling' approach. However, we exploit the notion that the initial unloading slope of

a $P-h$ cycle is a manifestation of the pure elastic recovery of material [9] and therefore seems to be sample invariable.

'Modified' nanoindentation data

By taking the initial unloading slope of a $P-h$ cycle is a manifestation of the pure elastic recovery of material [9], the stiffness of the material, S is assumed here to be material constant determined from the initial slope of the experimentally measured unloading data. By extrapolating the initial unloading slope of the unloading $P-h$ curve (used to calculate S) down to $P=0$ defines a displacement value h_c associated with the peak load, P_{max}. In this approach we use Equation (5.2.3) to calculate $h_c^{(i)}$.

Using a simple code written in MATLAB we have selected and collected ten equally spaced data points, $(P^{(i)}, h^{(i)})$, from the experimentally measured loading $P-h$ data. Given the observation and assumptions alluded to in the previous paragraph, we can speculate that if a sequence of ten loading-unloading nanoindentation cycles were to be carried out at the same position at load in the range $P^{(1)}$ to $P^{(10)}$, then the MATLAB subroutine-collected $(P^{(i)}, h^{(i)})$ could easily be the new set of data defining the maximum load and maximum indentation size defined as $(P_{max}^{(i)}, h_{max}^{(i)})$.

The contact depth, $h_c^{(i)}$, at the maximum load, $P_{max}^{(i)}$, can then be calculated according to Oliver-Pharr's empirical formula:

$$h_c^{(i)} = h_{max}^{(i)} - \epsilon \cdot \frac{P_{max}^{(i)}}{S} \tag{5.5.1}$$

where $\epsilon = 0.75$ is a function of the tip geometry (for the Berkovich indenter) [31].

Using the 'modified' $P-h$ data set, $(P_{max}^{(i)}, h_{max}^{(i)}, h_c^{(i)})$, we attempt to analyze the ISE behaviour in B_6O using various models including the Meyer's law, the PSR and MPSR models, and the multi-fractal scaling approach.

Meyer's law

The classical power law shown in Equation (5.5.2) is also known as the Meyer's equation and is frequently used when describing the ISE for ceramic and other materials [9]. B and n are descriptive parameters that are deduced by power-law curve fitting of experimental $P-h$ curve. B is a power-fit constant and the exponent n is the Meyer's index, also known as the size-effect index.

$$P_{max}^{(i)} = B \cdot \left(h_{max}^{(i)}\right)^n \tag{5.5.2}$$

	B	n	R^2
Values	2.37×10^9	1.64	99.60%

Table 5.2: *Descriptive parameters n and B derived from the Meyer's law fitting of experimental $P-h$ curves as illustrated in Figure 5.6.*

The loading segment of the $P-h$ nanoindentation data and the power-law fitting are all plotted in Figure 5.6 on the same axis. The results summarized in Table 5.2 show the variation of the descriptive parameters n and B derived from the Meyer's law fitting of experimental load-displacement.

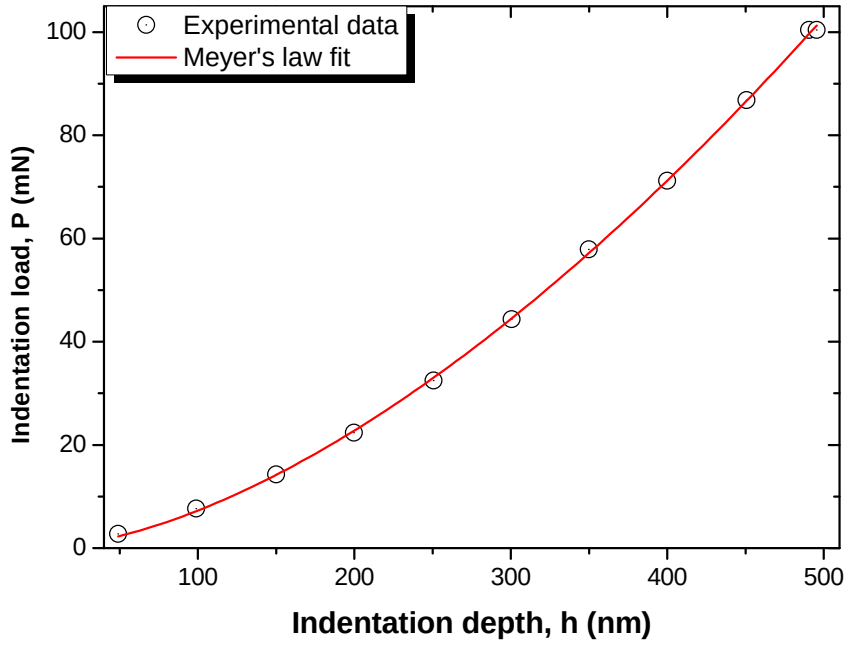

Figure 5.6: *Loading segment classical Meyer's law fitting of $P_{max}^{(i)}$ against $h_c^{(i)}$ curves.*

The value of n determines the trend in the hardness with respect to indentation load. When $n \leq 2$, a material exhibits the normal ISE behaviour and the hardness decreases with load. Conversely, $n \geq 2$ implies a reverse ISE behaviour. While there is no evidence for load size-effects, i.e. the hardness is independent of applied load when $n \approx 2$ [3, 23].

PSR model

However, several studies [4] have reported that the classic Meyer law is probably insufficient to describe and establish the origin of the ISE. Therefore, an alternative method is required to achieve a basic understanding of the ISE of hot-pressed B_6O. According to Li and Bradt's PSR model [4, 23] the applied test load is related to the contact depth as follows:

$$P^{(i)} = a_1 \cdot h_c^{(i)} + a_2 \cdot \left(h_c^{(i)}\right)^2 \tag{5.5.3}$$

The parameters a_1 and a_2 are constants for a given material. The parameters are related to the elastic and the plastic properties of the test material, respectively. The contact depth $h_c^{(i)}$ is calculated from Equation (5.5.1).

From Equation (5.5.3), a plot of $P_{max}^{(i)}/h_c^{(i)}$ against $h_c^{(i)}$ can be constructed to yield a straight line, where best-fit parameters a_1 and a_2 can easily be obtained by regression analysis. As shown in Figure 5.7 below, a plot of $P_{max}^{(i)}/h_c^{(i)}$ against $h_c^{(i)}$ is significantly linear, implying that Equation (5.5.3) does give an indication if the existence of ISE in hot-pressed B_6O.

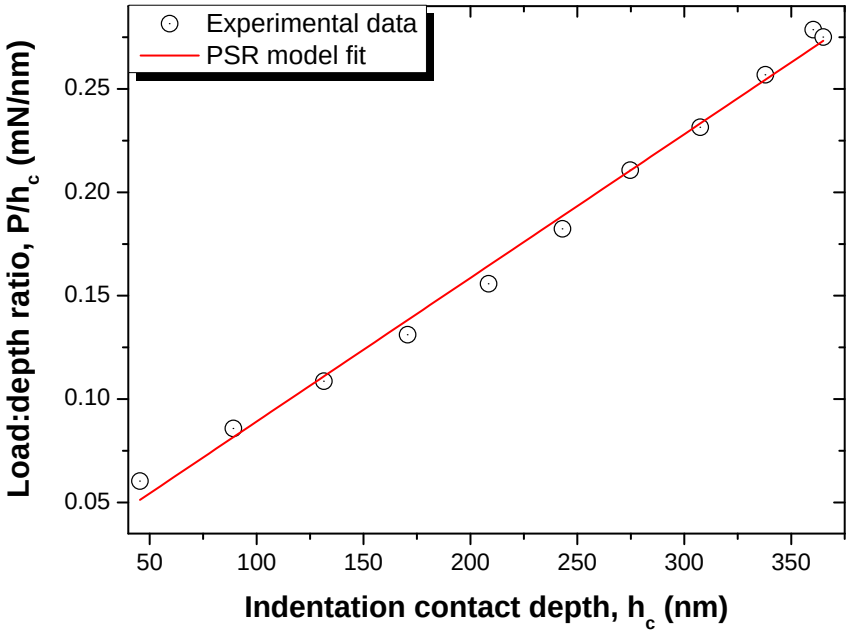

Figure 5.7: *The experimental data in the loading $P-h$ curves shown in Figure 5.6 were re-plotted as $P_{max}^{(i)}/h_c^{(i)}$ against $h_c^{(i)}$ and a best linear fit of the results.*

The PSR analysis can be extended to use the a_2 parameter can be related to the plastic properties of the test material, respectively. Especially, a_2 is suggested to be a measure of the so-called intrinsic hardness, H_{psr}. For the nanoindentation test with a Berkovich diamond indenter, H_{psr} can be determined directly from a_2 using Equation (5.5.4):

$$\begin{aligned} H_{psr} &= \frac{P_{max}^{(i)} - a_1 \cdot h_c^{(i)}}{24.56 \cdot \left(h_c^{(i)}\right)^2} \\ &= \frac{a_2}{24.56} \end{aligned} \tag{5.5.4}$$

Thus, one can conclude that the existing PSR model does provide a satisfactory explanation of the ISE of hot-pressed B_6O.

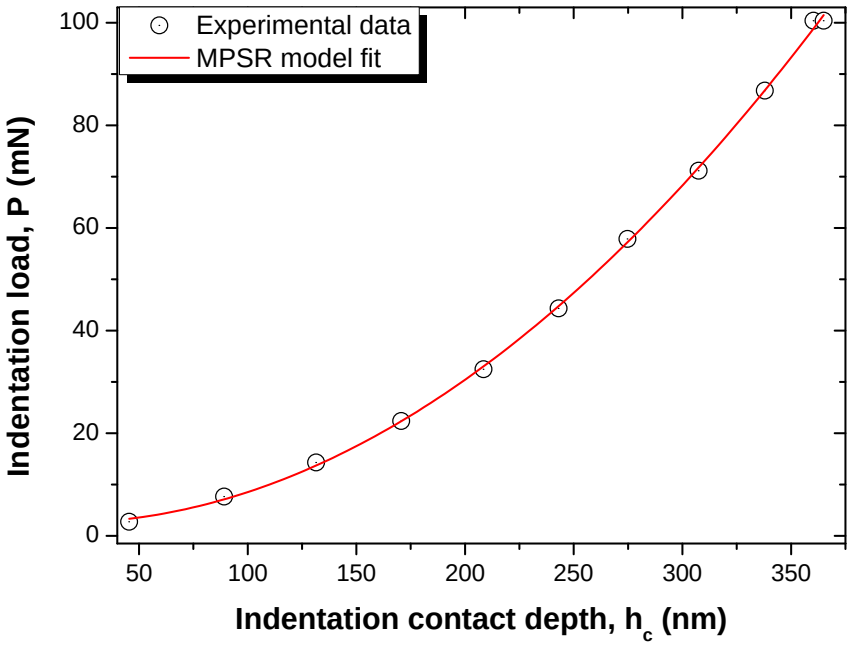

Figure 5.8: *A plot of $P_{max}^{(i)}$ versus $h_c^{(i)}$, and curve fitting thereof, according to the MPSR model.*

Modified PSR model

Gong et al. in reference [12] modified the PSR model to investigate the ISE behaviour in various materials. The resulting MPSR model is defined by Equation (5.5.5) below:

$$P^{(i)} = a_0 + a_1 \cdot h_c + a_2 \cdot \left(h_c^{(i)}\right)^2 \tag{5.5.5}$$

where a_0 is a constant related to the residual surface stresses associated with the surface grinding and polishing processes during sample preparation. The parameters a_1 and a_2 are constants as defined in the PSR model above. The values of a_0, a_1, and a_2 can be evaluated by plotting the $P_{max}^{(i)}$ data against $h_c^{(i)}$. The plot of $P_{max}^{(i)}$ versus $h_c^{(i)}$ (and curve fitting thereof according to the MPSR model) is illustrated in Figure 5.8 below.

As is the case for the PSR model, a hardness value, H_{mpsr} can be determined directly from best-fit value of a_2 from Figure 5.8 as shown in Equation (5.5.6) below:

$$\begin{aligned} H_{mpsr} &= \frac{P_{max}^{(i)} - a_0 - a_1 \cdot h_c^{(i)}}{24.56 \cdot \left(h_c^{(i)}\right)^2} \\ &= \frac{a_2}{24.56} \end{aligned} \tag{5.5.6}$$

Model	a_0	a_1	a_2 ($\times 10^{11}$)	H (GPa)
PSR	–	19711	6.95	28.3±0.3
MPSR	0.0026	20591	7.99	32.5±0.3

Table 5.3: *Best-fit parameters evaluated according to the PSR and MPSR models.*

The estimated best-fit values of the a_0, a_1, and a_2 parameters corresponding H_{mpsr} values are listed in Table 5.3. The residual surface stresses contribution to the observed ISE is negligible compared to the contribution of bulk material's plastic deformation characteristics.

'Pseudo-multicycling' approach

The 'pseudo-multicycling' approach which we attempt to apply to the $P-h$ data collected during a nanoindentation experiment relies on the use of a simple MATLAB subroutine developed to calculate pairs of $h_c^{(i)}$ and $P_{max}^{(i)}$ values as explained in Section 5.5.2.2 above.

The indentation hardness, $H^{(i)}$, of the sample at each peak load, P_{max} can be calculated as:

$$H = \frac{P_{max}}{A_c} \tag{5.5.7}$$

where A_c is the projected area of contact. A_c is normally taken to be a good approximation of the actual contact area at the peak load [9, 31].

$$\begin{aligned} A(h_c^{(i)}) &\approx 24.56 \cdot (h_c^{(i)})^2 \\ &\approx 24.56 \cdot \left(h_{max}^{(i)} - \epsilon \cdot \frac{P_{max}^{(i)}}{S} \right)^2 \end{aligned} \tag{5.5.8}$$

Accordingly, substituting Equation (5.5.8) into Equation (5.5.7) yields the indentation hardness of the sample, $H^{(i)}$.

$$H^{(i)} \approx \frac{P_{max}^{(i)}}{24.56 \cdot \left(h_{max}^{(i)} - \epsilon \cdot \frac{P_{max}^{(i)}}{S} \right)^2} \tag{5.5.9}$$

The hardness values calculated using this approach (Equation (5.5.9)) are plotted against the applied nanoindentation load as shown in Figure 5.9(a) below.

Evidently, as shown thus far in this chapter, the calculated nanoindentation hardness is a function of the indentation load. At low indentation loads there is no constant hardness

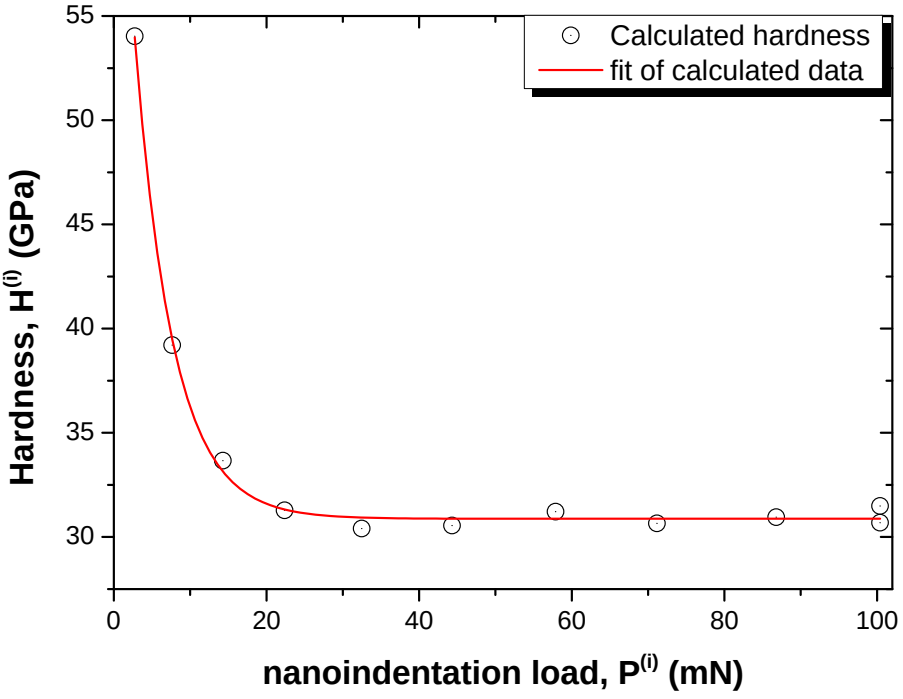

(a) ***Calculated***

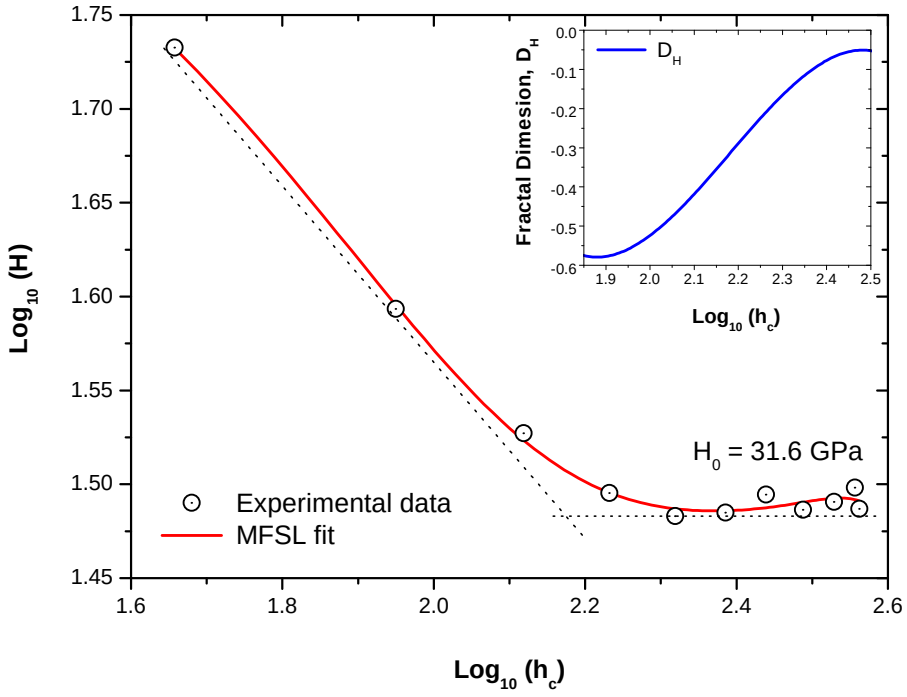

(b) ***MFSL fit***

Figure 5.9: *Hardness calculated according to Equation (5.5.9) plotted against the nanoindentation load, P (a.) and a plot of log(H^i) against log(h_c) according to MFSL, Equation (4.3.5) (b.).*

value whilst at high applied indentation test load, the hardness is load-independent. An average load-independent hardness value close to 31 GPa is observed to a load of less

than 200 mN. Earlier in Chapter 4, the microindentation Vickers hardness was also observed to demonstrate a similar trend for indentation loads of up to 1 kgf. An average load-independent hardness value close to 30 GPa was obtained. These are consistent with literature reported values [1, 5, 14].

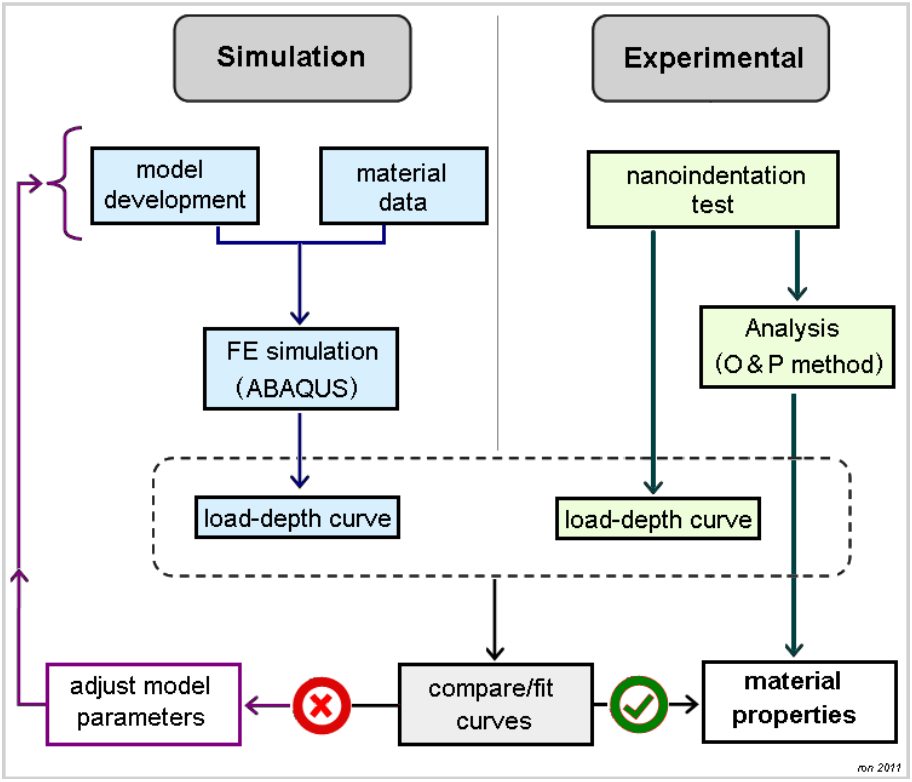

Figure 5.10: *Inverse identification procedure used to fit, analyze and extract material properties from the simulated $P-h$ curves of hot-pressed B_6O.*

5.5.3 Simulated nanoindentation

Simulated load-displacement curves

The identification of intrinsic material properties from simulated $P-h$ curves can be achieved through what is known as inverse analysis. The inverse identification procedure employed in this work is conveniently depicted in the flow diagram given in Figure 5.10. In order to achieve the identification of the material properties, the problem is generally formulated as the minimization, with respect to the unknown material parameters, of a suitable function that quantifies the overall discrepancy between the measured response and the computed response from the FE model. Since we were not privileged enough in this to have the necessary software software at our disposal (e.g. SiDoLo), the optimization was carried our intuitively, and manually.

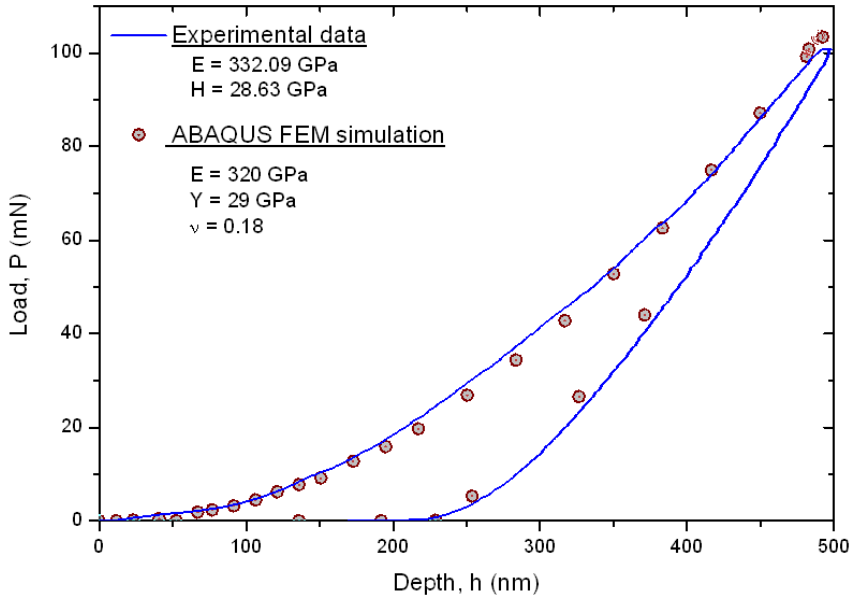

Figure 5.11: *A fit of the FEM simulated and experimentally measured $P-h$ curves.*

Figure 5.11 shows the fit between the experimentally measured and simulated $P-h$ curves of hot-pressed B_6O. The simulated data shows a consistent loading and unloading deformation behaviour with the experimental data, which verifies the feasibility and accuracy of FEM in this case. Once a fit was established, the FE simulated data was analyzed using the O&P method. Now, given the huge number of simulation attempts carried out, Dureza an experimental C^{++} software was used to efficiently analyze the simulated $P-h$ curve data at each trial/iteration in favour of the traditional approach. From the simulated $P-h$ curves, a hardness of 28.6 GPa and an elastic modulus of 320 GPa were calculated.

Experimental, method	Average values (GPa)		
	ν	H(E)	E
FE simulation	0.18	28.6	320.0
nanoindentaion	0.18	30.7	363.4
microindentation	—	28.0	—

Table 5.4: *A comparison of simulated and experimentally evaluated material properties.*

Although FEM is a fascinating tool for simulation of nanoindentation tests, limitations caused by simplification of models can lead to incorrect interpretation of the experimental data. Some limitation in the modeling include: in practice all indenters have a certain degree of roundness at the tip because of machining limitations and blunting during usage. A failure to account correctly for the roundness might The indenter in reality is not rigid but prone to deformation under load. The true stress-strain data is not available. A further limitation concerns the assumed conical geometry for the Berkovich indenter. Interestingly,

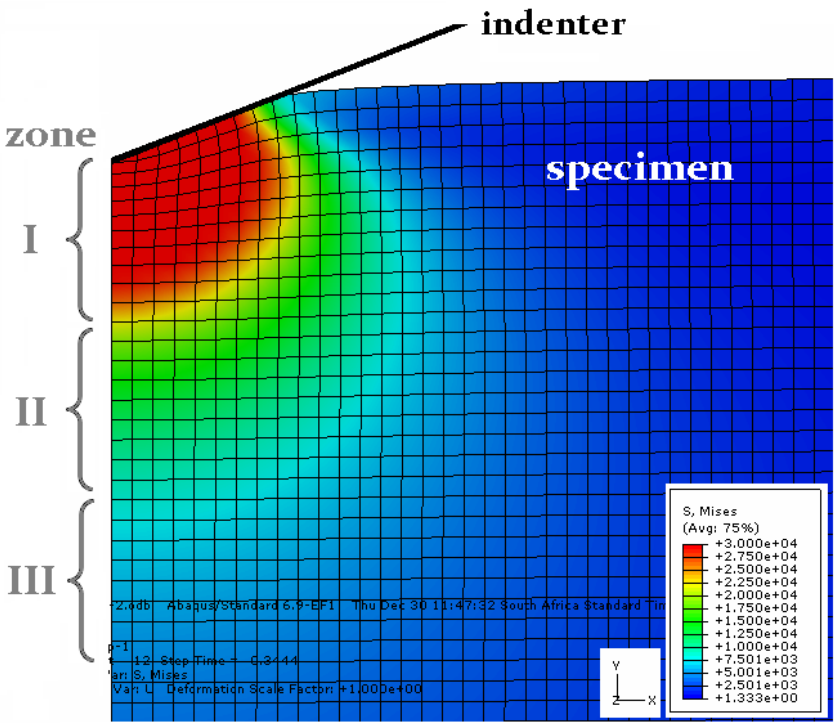

Figure 5.12: *Schematic of the expanding cavity model. The contacting area between the specimen and the indenter is the hydrostatic core (**red**). The core is surrounded by a plastic zone (**green**), which is constrained by the indenter on one side and and a region of elastic deformation (**lighter shades of blue**) on the other.*

this helps to explain the observation that the simulation derived hardness and elastic modulus values are slightly lower than the experimentally determined nanoindentation values although the values are within reasonable agreement.

Nanoindentation-induced deformation mechanisms in hot-pressed B_6O

The simulation of the development of plastic deformation in the hot-pressed B_6O specimen was investigated in order to gain a better understanding of the deformation behaviour in the material as the indentation depth is increased.

Indentation of a surface generates various stresses and strains in different regions around and under the indenter. As soon as the tip penetrates the surface its volume must be accommodated. This normally happens either by plastic flow or brittle failure. The elasto-plastic deformation which occurs in a very small region of the subsurface region during initial loading, can be conceptualized by considering the expanding cavity model [7, 28], as illustrated in Figures 5.12 and 5.13.

Observations of the plastically deformed zone at an arbitrary indentation depth during the test, as illustrated in Figure 5.12, indicates that the shape of the deformed zone under the

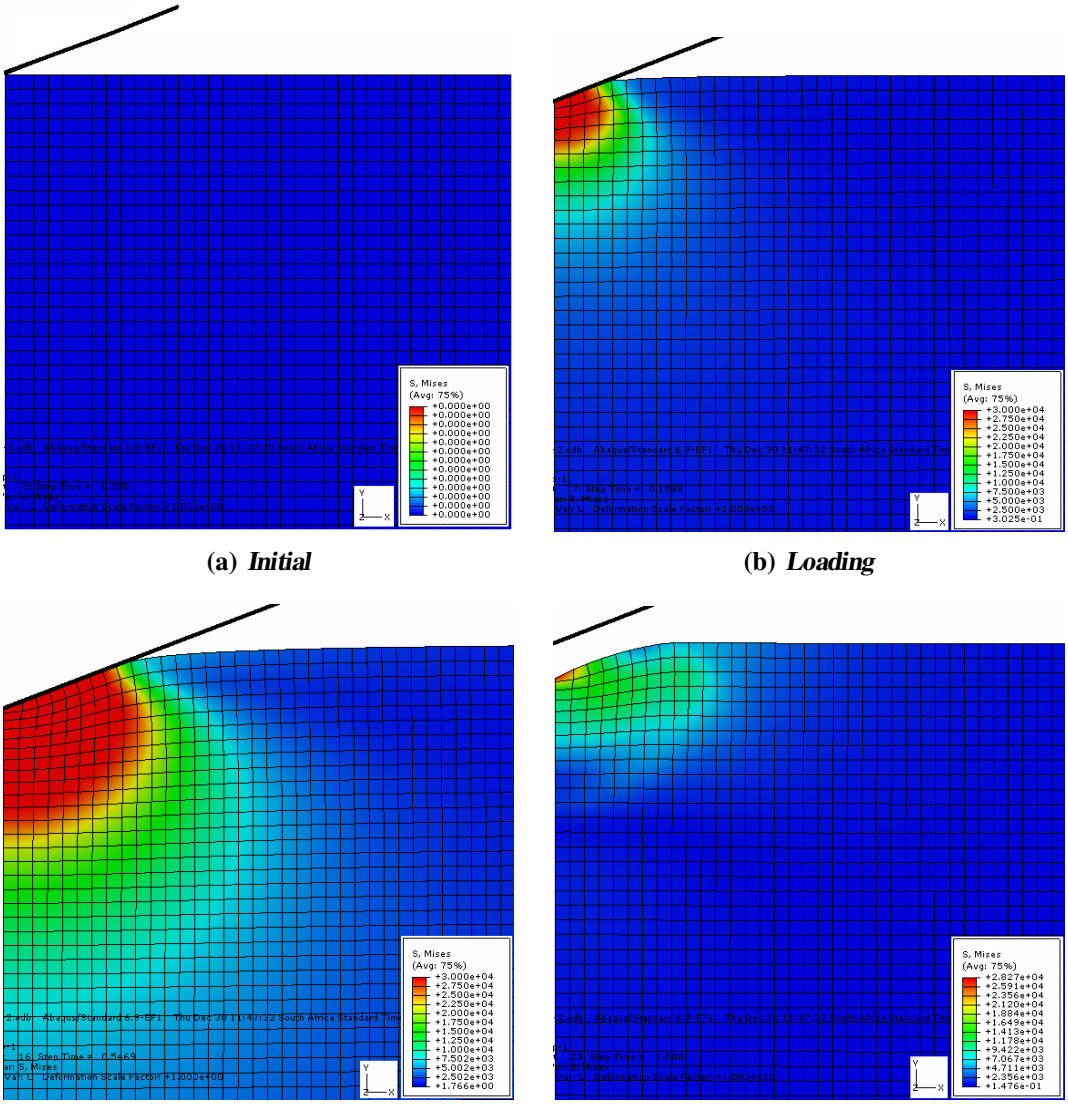

(a) ***Initial*** **(b)** ***Loading***

(c) ***Maximum load*** **(d)** ***Unloading***

Figure 5.13: *The plastic zone development at different stages during the indentation process. As the tip is further indexed into the specimen, the fully plastic core expands in size, by the radial movement of material to accommodate the added indenter volume, also increasing the plastic zone. Upon unloading some plastically deformed volume is retained.*

indenter is approximately hemispherical. The stress under an indent varies from high levels in the vicinity of the indenter tip to vanishingly small values in remote regions (within the specimen B_6O material). According to the expanding cavity model, the influence zone beneath the indenter at a given penetration depth can be divided into three parts: the incompressible hydrostatic fully plastic core (I), a deformable elasto-plastic zone with a strain gradient (II), and an elastic hinterland (III). Therefore, as the indenter is indexed into the surface of the B_6O specimen, the plastic core radius expands, so as the elasto-plastic

and the elastic zones. It is the added volume of the indenter, which is accommodated by the radial expansion of the plastic zone.

However, when the plastic region is no longer elastically constrained under the indenter, and the free surface has a considerable role in the shape of the plastic zone, the volume occupied by the indenter starts to be accommodated in a different way; in other words, the deformed zone under the indenter does no longer resemble a hemispherical geometry, this is best observable in Figure 5.13(c). The material begins to flow plastically with evidence of piling-up around the indenter. At this point the specimen material behaves as a plastic solid, for the elastic deformation is considerably smaller in volume compared to the plastic flow.

Upon complete unloading, a residual indentation impression and the plastically deformed region around it remains. An interesting observation that can be made from these studies is that an increase in the maximum indentation load results in an increase in the volume of the specimen material behaving as a plastic solid and so does the size of the pile-ups. This, probably explains the vigorous indentation cracking observed when large applied loads are used in the Vicker's micro-hardness tests.

5.6 Summary and conclusion

Berkovich nanohardness indentations were conducted and analyzed. The load-dependence of hardness was characterized through the application of Meyer's law, the proportional specimen resistance models, and the 'pseudo-multicycling' approach with good agreement with each other. Based on the studies conducted we conclude that:

For the very first time, the load-displacement indentation response of hot-pressed B_6O samples is measured and analysed comprehensively. The results show that:

- The average intrinsic nanohardness and O&P elastic modulus of hot-pressed B_6O were observed to be 31.6 GPa and 363.4 GPa, respectively.
- An approach was developed to simulate multi-cycling loading load-displacement curves from a single measured load-displacement curve. Based on the results of the proposed approach, the indentation size effect in the nanoindentation hardness of the material is analysed using the classical Meyer's law, the propositional resistance models and the multi-fractal scaling law.

- One of the novel and most bold conclusions drawn from the study is that fractal dimension is a far more resourceful indicator of the extent of indentation size effect than the traditional Meyer's index.

In this study, finite element method simulations of the conical nanoindentations of hot-pressed B_6O were conducted using a commercially available finite-element package ABAQUS v6.9. A 2D axisymmetrical model was specifically developed for this work to simulate the experimental nanoindentation process in hot-pressed B_6O.

The FEM simulation obtained $P-h$ curves show a fairly good agreement with the experimentally determined nanoindentation and microindentation values. An inverse identification procedure used to fit, analyze and extract material properties from the simulated $P-h$ curves of hot-pressed B_6O gives a hardness of 28.6 GPa and an elastic modulus of 320 GPa, values in good agreement with relevant theoretical and experimental results.

Furthermore, the deformation response of the material under dynamic indentation was also investigated at different stages using a finite element analysis method and interpreted using the expanding cavity model.

Bibliography

[1] A. Andrews, I. Sigalas, and M. Herrmann. Boron suboxide composite material. WIPO Patent No. 2008132675, 2008.

[2] Kuo-Shen Chen, Tuo-Cheng Chen, and Kuang-Shun Ou. Development of semi-empirical formulation for extracting materials properties from nanoindentation measurements: Residual stresses, substrate effect, and creep. *Thin Solid Films*, 516:1931 – 1940, 2008.

[3] O. Şahin, O. Uzun, U. Kölemen, and N. Uçar. Mechanical characterization for β-Sn single crystals using nanoindentation tests. *Materials Characterization*, 59:427 – 434, 2008.

[4] O. Şahin, O. Uzun, M. Sopicka-Lizer, H. Gocmez, and U. Kölemen. Dynamic hardness and elastic modulus calculation of porous SiAlON ceramics using depth-sensing indentation technique. *Journal of the European Ceramic Society*, 28:1235 – 1242, 2008.

[5] G.J. Davies, I. Sigalas, M. Herrmann, and T.C. Shabalala. Boron suboxide composite material. US Patent No. 20080317654, December 2007.

[6] A.C. Fischer-Cripps. *Nanoindentation*. Springer, New York, 2nd edition, 2004.

[7] X.L. Gao. An expanding cavity model incorporating strain-hardening and indentation size effects. *International Journal of Solids and Structures*, 43:6615 – 6629, October 2006.

[8] J. Gong, H. Miao, and Z. Peng. Analysis of the nanoindentation data measured with a Berkovich indenter for brittle materials: effect of the residual contact stress. *Acta Materialia*, 52:785 – 793, 2004.

[9] J. Gong, H. Miao, Z. Peng, and L. Qi. Effect of peak load on the determination of hardness and Young's modulus of hot-pressed Si_3N_4 by nanoindentation. *Materials Science and Engineering: A*, 354:140 – 145, 2003.

[10] J. Gong, Z. Peng, and H. Miao. Analysis of the nanoindentation load-displacement curves measured on high-purity fine-grained alumina. *Journal of the European Ceramic Society*, 25:649 – 654, 2005.

[11] J. Gong, J. Wu, and Z. Guan. Analysis of the indentation size effect on the apparent hardness for ceramics. *Materials Letters*, 38:197 – 201, 1999.

[12] J. Gong, J. Wu, and Z. Guan. Examination of the indentation size effect in low-load Vickers hardness testing of ceramics. *Journal of the European Ceramic Society*, 19:2625 – 2631, 1999.

[13] R. Goodall and T.W. Clyne. A critical appraisal of the extraction of creep parameters from nanoindentation data obtained at room temperature. *Acta Materialia*, 54:5489 – 5499, 2006.

[14] M. Herrmann, J. Raethel, A. Bales, K. Sempf, I. Sigalas, and M. Hoehn. Liquid phase assisted densification of superhard B_6O materials. *Journal of the European Ceramic Society*, 29:2611 – 2617, 2009.

[15] N. Janakiraman and F. Aldinger. Indentation analysis of elastic and plastic deformation of precursor-derived Si-C-N ceramics. *Journal of the European Ceramic Society*, 30:775 – 785, 2010.

[16] D.L. Josilin and W.C. Oliver. A new method for analyzing data from continuous depth-sensing microindentation tests. *Journal of Materials Research*, 5:123 – 126, 1990.

[17] R.B. King. Elastic analysis of some punch problems for a layered medium. *International Journal of Solids and Structures*, 23:1657 – 1664, 1987.

[18] P. Klapetek, D. Necas, and C. Anderson. Gwyddion v2.24 (software package). http://gwyddion.net/, 2011.

[19] J.A. Knapp, D.M. Follstaedt, J.C. Barbour, and S.M. Myers. Finite-element modeling of nanoindentation for determining the mechanical properties of implanted layers and thin films. *Nuclear Instruments and Methods in Physics Research B*, 127/128:935 – 939, 1997.

[20] A. Krell and S. Schadlich. Nanoindentation hardness of submicrometer alumina ceramics. *Materials Science and Engineering: A*, 307:172 – 181, 2001.

[21] P.-L. Larsson and A.E. Giannakopoulos. Tensile stresses and their implication to cracking at pyramid indentation of pressure-sensitive hard metals and ceramics. *Materials Science and Engineering: A*, 254:268 – 281, 1998.

[22] T. Letsoalo and J.E. Lowther. Computational investigation of elastic properties of bulk and defective ultrahard B_6O. *Journal of Superhard Materials*, 33(1):19 – 28, 2011.

[23] H. Li and R.C. Bradt. The effect of indentation-induced cracking on the apparent microhardness. *Journal of Materials Science*, 31:1065 – 1070, 1996.

[24] R. Machaka, T.E. Derry, and I. Sigalas. Nanoindentation hardness of hot-pressed boron suboxide ceramics. *Material Science and Engineering: A*, 528:5778 – 5783, July 2011.

[25] Jaroslav Mackerle. Finite element and boundary element simulations of indentation problems: A bibliography (1997 – 2000). *Finite Elements in Analysis and Design*, 37:811 – 819, 2001.

[26] B.W. Mott. *Microindentation Hardness Testing*. Butterworths: London, UK, 1956.

[27] D. Music and J. M Schneider. Elastic properties of amorphous boron suboxide based solids studied using *ab initio* molecular dynamics. *Journal of Physics: Condensed Matter*, 20:195203, 2008.

[28] R. Narasimhan. Analysis of indentation of pressure sensitive plastic solids using the expanding cavity model. *Mechanics of Materials*, 36:633 – 645, 2004.

[29] W.C. Oliver and G.M. Pharr. An improved technique for determining hardness and elastic modulus using load and displacement sensing indentation experiments. *Journal of Materials Research*, 7:1564 – 1583, 1992.

[30] W.C. Oliver and G.M. Pharr. Measurement of hardness and elastic modulus by instrumented indentation: Advances in understanding and refinements to methodology. *Journal of Materials Research*, 19:3 – 20, 2004.

[31] G.M. Pharr and A. Bolshakov. Understanding nanoindentation unloading curves. *Journal of Materials Research*, 17:2660 – 2671, 2002.

[32] G.Z. Voyiadjis, A.H. Almasri, and T. Park. Experimental nanoindentation of BCC metals. *Mechanics Research Communications*, 37:307 – 314, 2010.

[33] B. Wolf and A. Richter. The concept of differential hardness in depth sensing indentation. *New Journal of Physics*, 5:15, 2003.

[34] X.Y. Zhou, Z.D. Jiang, H.R. Wang, and Q. Zhu. A method to extract the intrinsic mechanical properties of soft metallic thin films based on nanoindentation continuous stiffness measurement technique. *Journal of Physics: Conference Series*, 48:1096, 2006.

Part III

Characterization of Ion-Implanted B_6O

Chapter 6

Raman Spectra of Ion Implanted B_6O

First principle *ab initio* density functional calculations of the structural properties of B_6O conducted by Lowther [36] suggest that the strength of the bonding in B_6O and other boron-rich superhard materials such as B_4C and $AlMgB_{14}$ may be enhanced by the presence of a high electronegativity interstitial in the structure. The computational calculations confirm the shortening of covalent bonds which is believed to favour higher elastic constants and hardness values. By introducing energetic fluorine ions into B_6O using ion implantation – a non-equilibrium technique of choice for introducing 'controlled' defects into the near-surface layers. The work undertaken and reported in this chapter seeks to characterize changes in the structural properties of the ion implanted material with respect to the unimplanted specimen. The effects of the F^+-implantation on the near-surface nanomechanical properties are investigated in Chapter 7.

The hot-pressed B_6O specimen were implanted with 150 keV fluorine ions to fluences of up to 5.0×10^{16} ions/cm^2 at room temperature.

The chapter is based on an article, entitled '*Mechanical and surface properties of fluorine-ion-implanted hot-pressed boron suboxide*' published in an *Advances in Materials Science and Engineering* special issue of *Modification, Synthesis, and Analysis of Advanced Materials Using Ion Beam Techniques*.

6.1 Introduction

6.1.1 Ion beam synthesis of nanostructures

Ion implantation is a harsh and non-equilibrium physical technique for the introduction of foreign atomic species into host material surfaces [52, 54]. In principle, the materials engineering technique involves the bombardment of solid target material with high–energy charged particles. As the swift charged particles penetrates and move in the target material, they rapidly loose energy due to stochastic collisions interactions with the host lattice. The interaction between incoming charged particles and target material's lattice can lead to structural changes such as the generation of point defects, the amorphization of crystalline materials, or structural transformations in amorphous atomic networks [48], and accumulation of complex clusters of defects. The ion will eventually come to rest at some depth below the surface in solid solution. Ion irradiation modified surface layers are typically distinct, both physically and chemically, from the underlying bulk surface [48]. Reports detailing the improvements of near-surface hardness, tribological (friction and wear) properties, corrosion and oxidation resistance, optical signal processing in metals, ceramics, polymers, and other materials alike are widespread in literature [5, 8, 9, 20, 27, 29, 44, 51, 58, 59].

The uniqueness of the implantation technology lies in the ability to control of the doping level and spatial location of dopants [53]. The interaction between ion beams and target can lead to the improvement of wear resistance and hardness, the increased average fatigue lifetime, corrosion resistance and high temperature oxidation resistance [9, 41, 44].

It is for this reason that the technique has traditionally been able to drastically modify the near-surface stoichiometry and it's physical and chemical properties in both metals and alloys [33, 50, 59], semiconductors [20, 21, 27, 40, 52, 54], ceramics [8, 9, 41, 44], and polymers and other materials [15, 34, 39] with incredible reproducibility. The technique's primary strength lies in the local control over species and concentration at a well-defined depth. An in-depth discussion on the principles of ion implantation and the ion implanter instrumentation is comprehensively reviewed in Appendix B on page 121, see also references [23, 37, 45, 64, 71].

The potential application of ion implantation as a method of producing the $p-n$ junction by doping semiconductors to replaced chemical (diffusion) doping was first recognized in a patent application filed in 1954 by William Shockley entitled '*Forming Semiconductive Devices by Ionic Bombardment*' [61]. Since then, the most important application of ion implantation has been introduction of dopant species during the fabrication of electronic

devices in the semiconductor electronics field [52, 54, 57]. However, in more recent years there has been substantial efforts in capitalizing on successes of the existing semiconductor processing technologies, ion implantation included. For example, methods such as (a) e-beam lithography and chemical-mechanical polishing have firmly been accepted as next-generation tools for advanced magnetic recording applications. (b) Focussed ion beam processing is now widely used in the semiconductor industry. (c) The use of energetic ions in promoting the nucleation of new and unique non-equilibrium nanostructured phases – also known as ion beam synthesis, is fast becoming a common tool in various research areas and industries, chiefly optoelectronics and fabrication of advanced magnetic nanostructures [5, 12, 27, 29, 35, 70].

Following the commercial applications successes of ion implantation in the semiconductor materials, the ion beam induced formation of nanostructures by swift heavy ions has become a topical research area, see reference [27] for example. Ion beams and cluster ion beams have been used to synthesize stable nanostructures inside materials, deposit nanocrystalline thin films, process surfaces, and create unique structures such as elongated metal nanoclusters inside materials, nanopores extending through thin films,or columnar structures. The created and modified structures have been observed to have interesting electronic, optical, magnetic and mechanical properties. The locally modified chemical behavior of irradiated surfaces may find application for patterned seeding of the growth of deposited materials, modified surface behavior of cell surfaces, or possibly for providing unique catalytic properties.

Among potential applications driving the nanomaterials formed by ion-beam synthesis are all-optical switching that utilizes highly nonlinear optical response of metal nanoclusters embedded into non-conducting matrix [16, 65], optoelectronic devices based on the unique optical response of semiconducting quantum dots [13, 20, 21], nonvolatile memory [7, 22], spintronics [28], and single-electron transistor devices [11, 30]. []

The two fundamental challenges for the nanophased materials are: (1) To achieve perfect control of nanoscale-related properties. (2) On account of their very small dimension, not all conventional techniques are suitable for characterizing nanostructured materials [69]. Fortunately, micro-Raman spectroscopy is particularly well suited to characterize nanostructured materials since it provides non-destructive information about their size, by the adequate modeling of the phonon confinement effect.

Raman spectra of nanostructured materials

The technique provides a nondestructive method to characterize nanostructures. Raman scattering is used for the evaluation of the effects on the crystal structure caused by ion

implantation and for optical characterization of ion implanted samples. The phonon spectra of crystalline solids as well as their modification by changing chemical compositions in the implanted layer can been determined. In addition, the penetration depth of the excitation laser beam is of the order of the depth of penetration of implanted ions [42]. As has been been demonstrated already in Chapter 3, by means of the application of a fluorescence background suppression scheme, observable Raman spectra of hot-pressed B_6O was obtained, which till now had been deemed unobservable when the 514.5 nm Ar^+ laser excitation source is used (refer to reference [38]).

From the shape and the peak position of the first-order Raman scattering bands following properties of nanocrystals can be investigated: the size variation (i.e. estimation of the size of nanocrystals), the phase changes (i.e. observations of crystalline to amorphous transformations), the evolution of the stress on nanocrystals, and the temperature variations on a nanocrystal.

Optical phonon confinement

The conservation of phonon momentum q, during phonon creation or decay upon interaction with the external radiation field (in the present case, first-order Raman scattering) follows the Heisenberg's uncertainty principle [10, 19, 43]:

$$\delta d \cdot \delta q \sim h \tag{6.1.1}$$

According to the principle, in cases of a perfect single crystal of finite size d, that is $\delta d \sim \infty$, then only optical phonons near the centre of the crystal's dispersion curve's Brillouin zone ($\delta q \sim 0$) can interact with visible light in any one phonon process (first order spectrum), – the '$\delta q \sim 0$' selection rule [4, 10, 17]. In such a case, the Raman intensity, $I(\omega)$ is a Lorentzian lineshape centred at ω (the Raman frequency) with a FWHM or linewidth of Γ_o [4, 17, 19, 43].

However, in the case of nanocrystalline materials, as the diameter, $\delta d \to 0$, the bulk phonon wavefunction cannot exist within the small confines of the crystallite. In fact, the phonon wavefunction cannot penetrate significantly beyond the crystallite surface [4, 17, 19, 43].

Due to the uncertainty principle, as $\delta d \to 0$, $\delta q \to \infty$, i.e. the '$\delta q \sim 0$' selection rule is relaxed [4, 17, 43]. Light scattering from a nominally Brillouin zone centre phonon whose wavevector has an 'uncertainty' δq can now be involved in the Raman process [4, 17, 19]. Thus, the phonon's spatial confinement is expected to result in considerable shifting and broadening of the Raman scattering features, reflecting the uncertainty in its energy, as stipulated by Equation (6.1.1).

It has been observed and reported that the phonon confinement effect becomes increasingly dominant when the particle size of the nanoparticle or nanocrystal is $d \leq 20a_o$ [4], where a_o is the lattice constant of the bulk material. Although others, Gouadec and Colomban [17] and Faraci et al. [13] for example, state that the OPC model is valid for average particle sizes of about 100 nm and less.

Assuming a three-dimensional confinement, i.e. spherical nano-crystallites of the mean diameter d, and that the confined phonon which will participate in first-order Raman scattering processes is composed of a sum of bulk-like phonons and the phonon most similar to the bulk Brillouin zone centre phonon possesses a range of wavevectors around the zone centre. Richter et al. [56] have developed a phonon-confinement model to explain the observed Raman spectra in micro-crystalline silicon. The model was later improved by Campbell and Fauchet [10, 13] and is now the accepted tool for Raman lineshape analysis in nanocrystalline materials in general, like silicon [1, 13, 19, 51], germanium [27], and gallium arsenide [4] nanostructures, for example.

The phonon confinement model calculates the shape of the Raman line based on the optical phonon dispersion relations and the average size and shape of the crystallites [1, 4, 5, 10, 13, 17–19]. The intensity of the first-order Raman line $I(\omega)$ can be written as Equation (6.1.2).

$$I(\omega) = A_o \cdot \int_{BZ} \frac{|C(0,q)|^2}{[\omega - \Omega(q)]^2 + \left(\frac{\Gamma_o}{2}\right)^2} \cdot d^3q \tag{6.1.2}$$

A_o is a pre-factor to be determined from a numerical least-squares fit calculation, $|C(0,q)|^2$ is the Fourier coefficient that depend on the size of the particle that scatters the light and the phonon momentum, ω the phonon wave-number, $\Omega(q)$ the phonon dispersion relation for the material in the particle and Γ_o is the FWHM of the phonon peak of the bulk material. According to Faucet and Campbell [14], the square of Fourier coefficient $|C(0,q)|$ can be written as:

$$|C(0,q)|^2 \cdot d^3q = \exp\left(-\frac{q^2d^2}{\alpha}\right) \cdot d^3q \tag{6.1.3}$$

gives the scattering probability of phonons with the different wave vector q. And α is a scaling parameter.

Sample No.	Ion species	Energy (keV)	Fluence (F^+/cm^2)
B1	—	—	—
C1	F^+	150	1.0×10^{14}
B2	F^+	150	5.0×10^{14}
B3	F^+	150	5.0×10^{15}
C2	F^+	150	1.0×10^{16}
C3	F^+	150	3.0×10^{16}
B4	F^+	150	5.0×10^{16}

Table 6.1: *The nomenclature of the unimplanted and implanted samples.*

6.2 Experimental details

A modified Varian-Extrion 200-20A2F type high-current low-energy ion implanter at iThemba LABS (Gauteng), Johannesburg was used for all implants reported here. 150 keV fluorine ions were implanted into hot-pressed B_6O specimen at fluences between 1.0×10^{14} to 5.0×10^{16} ions/cm^2 at room temperature. A comprehensive description of the ion implanter instrument and the ion implantation technique is presented in Appendix B. The nomenclature of the unimplanted and implanted samples is tabulated in Table 6.1.

The depth distribution of the radiation damage and implanted ions profile were estimated using SRIM2010 [72], a suite of Monte Carlo computational codes popular for the simulation of the interactions of energetic ions with the target material.

The specimen's surface microstructure and composition were characterized by SEM and EDX, respectively. Raman measurements performed at ambient conditions using a 514.5 nm Ar^+ ion excitation was used to characterize the ion beam induced structural modifications whilst the mechanical properties of the unimplanted and implanted samples was carried out using nanoindentation. Details of the experimental procedures of the Raman spectroscopy and the nanoindentation measurements are also discussed in Appendix A (on page 119) and Chapter 5.3 (on page 50), respectively.

A modified Richter-Wang-Ley phonon confinement model (Equation (6.1.2)) was fitted to experimental data using a MATHEMATICA code specifically developed during the course of this work to carry out the numerical calculations and least-squares fitting [43, 51]. During a typical numerical calculation for the nanocrystals size, the FWHM, and the phonon dispersion relation(s) are adjusted to produce the best fit to the measured Raman peak using the least squares criterion. By numerical best-fitting Equation (6.1.2), the relevant parameters in this equation were determined.

6.3 Results and discussion

6.3.1 TRIM simulation

We simulate the radiation damage inflicted by the interactions of energetic fluorine ions on hot-pressed B_6O target using SRIM codes. In our simulation. We have used 99999 150 keV fluorine projectiles and defined a stoichiometric B_6O target material with a density of 2.5 g/cm^3.

Figure 6.1 shows SRIM simulation results. Figure 6.1(a) shows the simulated projected ion ranges distribution whilst Figure 6.1(b) shows the plot of damage distribution due to electronic energy dissipation and nuclear (recoil) energy dissipation. A detailed description of the transport and stopping mechanics of projectiles in matter is given in Appendix B on page 129.

From Figure 6.1(a), the standard deviation in range of particles was around 60 nm. Skewness value (-0.73) indicates the most probable depth is greater than that of mean depth 270 nm and Kurtosis value (3.82) signifies the distribution profile of ions having broad tails. In practice, we are aware that the SRIM estimation does not take into account the possible surface sputtering, dynamic annealing and diffusion processes taking place during ion implantation [32, 68].

Figure 6.1(b), the distribution of the deposited energy is split into into the 'ionization' energy dissipation and 'recoil' energy dissipation. The 'ionization' refers to the energy dissipation due to electronic collisions between the projectiles and the target atoms' electrons. The nuclear energy dissipation due to the primary nucleus-nucleus collisions of the incident ions with target atoms, and is refereed to as the energy 'recoils' since it is usually large enough to dislodge the target atoms off their equilibrium lattice sites.

Our simulation for ionization energy loses shows that the dominant ion stopping mechanism of energetic fluorine projectiles in B_6O was observed to be electronic in nature. However, the dominant ion stopping mechanism of energetic fluorine projectiles in B_6O towards the end of the projectile trajectory is observed to be nuclear in nature. The mean depth of electronic energy dissipation is somewhat lower than that of the nuclear counterpart, as electronic stopping decreases more rapidly with decreasing energy.

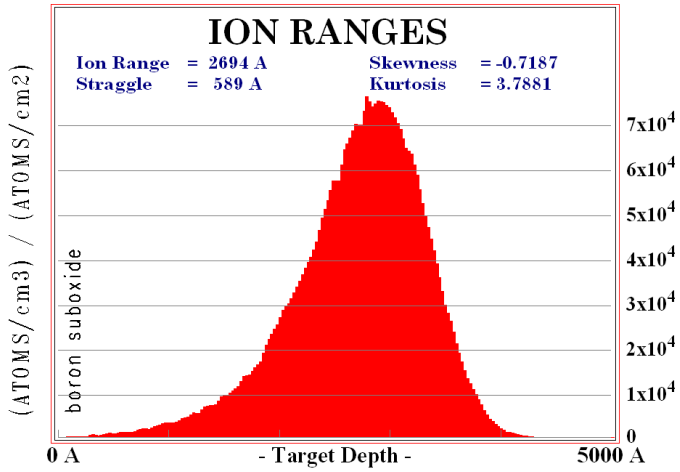

(a) ***Plot of ion ranges distribution***

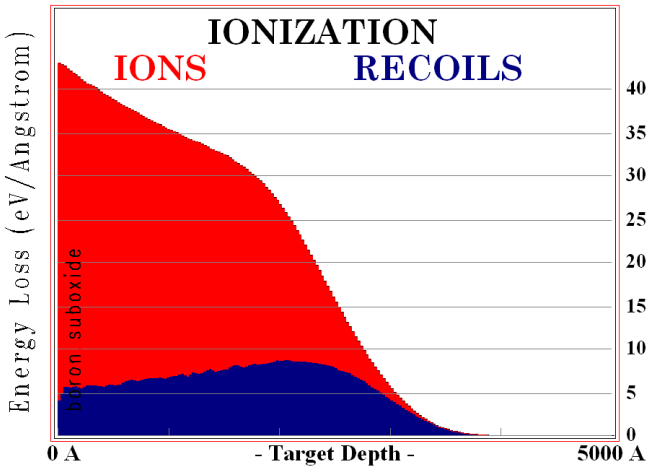

(b) ***Plot of ionization distribution***

Figure 6.1: *SRIM simulated results of the 99999 150 keV F^+ pseudoprojectiles implanted into B_6O. (a) shows a plot of ion ranges distribution whilst (b) shows a plot of electronic (ionisation) and nuclear (recoil) energy dissipation distribution.*

6.3.2 Raman spectroscopy

Raman measurements

Figure 6.2 shows a sequence of Raman scattering spectra for the control B_6O specimen (B1) and B_6O samples implanted with 150 keV fluorine ions at different fluences of up to 5.0×10^{16} ions/cm^2 (C1 – B4). The nomenclature of the samples is tabulated in Table 6.1.

The spectrum of the unimplanted hot-pressed B_6O is dominated by a relatively weak first-order phonon modes towards the lower wavenumbers. This can be attributed to the poor oxygen occupancy in the B−O−B chain linking the icosahedra [38]. Furthermore, it is known that the general broadening of the Raman peaks peaks is consistent with fact

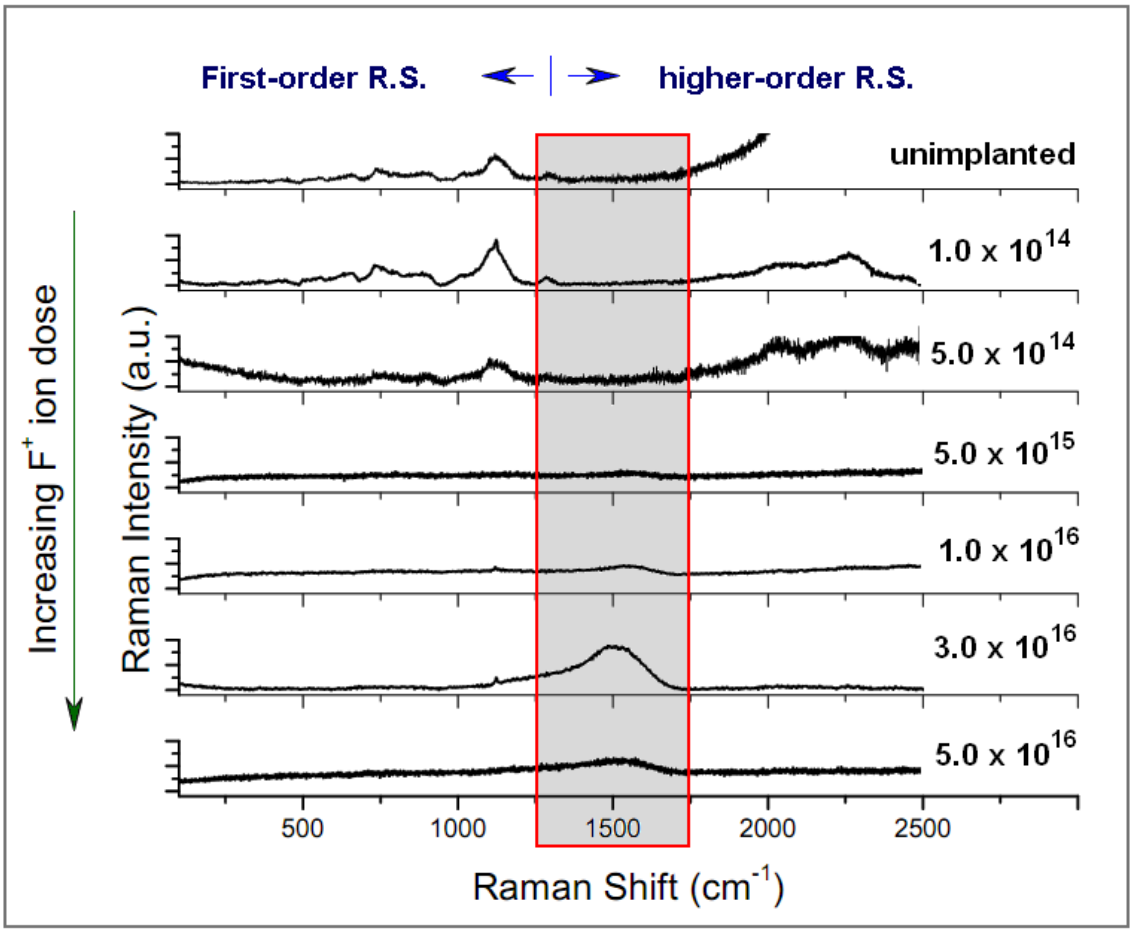

Figure 6.2: *The Raman spectra of unimplanted (B1) and F^+-implanted B_6O specimen. The spectra are normalized and shifted along the* y*-axis for comparison.*

that the B_{12} icosahedra are slightly distorted [47, 66]. Nevertheless, the measured Raman spectrum of the unimplanted specimen B1 is characteristic of nominal composition B_6O (see also Chapter 3).

Although F^+ implantation at fluences below 5.0×10^{15} ions/cm^2 reveals that the material resists amorphization and retains the Raman spectra of B_6O (C1 + B2), implantation at fluences of up to 5.0×10^{15} ions/cm^2 clearly shows that the signature Raman spectrum of B_6O disappears altogether (B3). According to Rama Rao et al. [55, 58], in Raman scattering spectroscopy the main effect in going from the crystalline to amorphous form, for diatomic lattice, is the decrease in intensity of the lattice mode and even the disappearance of these modes at higher ion implantation doses. We therefore attribute the observed disappearance of the signature B_6O Raman spectrum to amorphization as a result of ion induced radiation damage.

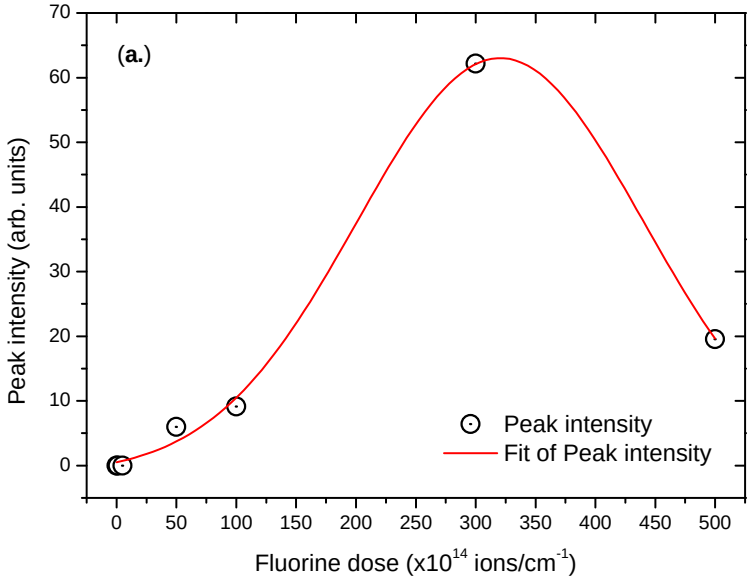

(a) ***I(ω)***

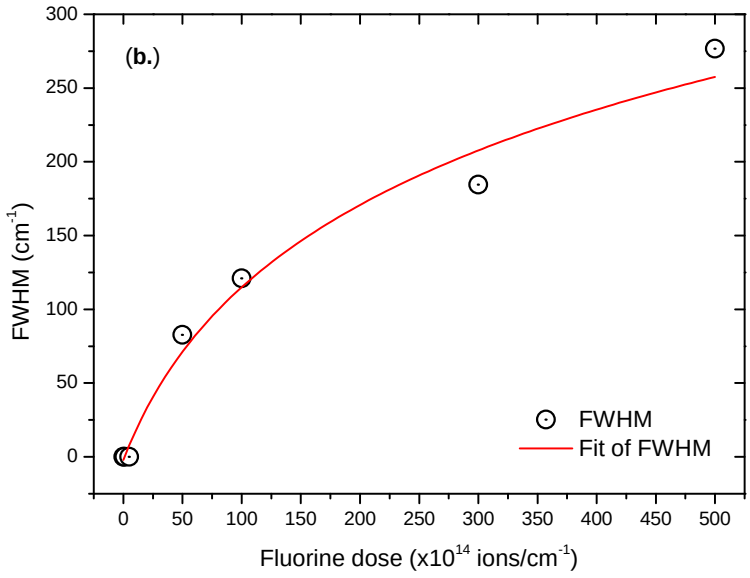

(b) ***FWHM***

Figure 6.3: *The measured (a.) peak intensity and (b.) linewidth (FWHM) of the asymmetrically broadened Raman feature as a function of fluorine fluence.*

At implantation fluences of the order of 5.0×10^{15} ions/cm^2, the measured spectrum reveals an almost unrelated and new asymmetrically broadened feature centred around 1550 cm^{-1} emerging.

Further increase in the implantation fluence beyond 5.0×10^{15} ions/cm^2 towards 3.0×10^{16} ions/cm^2 gives rise to further increase in both width and intensity of the asymmetrically broadened Raman feature as illustrated in Figures 6.3(a) and 6.3(b), respectively. The asymmetrical broadening of Raman modes is a characteristic usually resulting from the

optical phonon confinement. We attribute the observed asymmetrically broadened Raman feature (Figures 6.2 and 6.5) to the phonon confinement effect of optical phonons in ion-beam synthesized nanostructured phase.

The feature's peak intensity can be linked to the volume fraction of the nanostructured phase in the material surface layer. Consequently, a critical fluence[1] of about 3.2×10^{16} ions/cm^2 was observed (Figure 6.3(a)) beyond which the volume fraction of the nanostructured particles evidently reduces with further increases in the ion dose, possibly owing to the existence of surface sputtering and possibly radiation damage [3].

A possible explantation of this Raman scattering characteristic in fluorine ion implanted B_6O could be the nucleation of an ion-beam synthesized nanostructured particles within the implanted region. As illustrated schematically in Figure 6.4, ion implantation creates a non-equilibrium solid state supersaturation of the implanted ions in solutions which could induce the precipitation of ion-beam synthesized nanostructured phase nuclei effectively, due to thermodynamic stabilization. These nuclei grow additionally as a result of the surface deposition of solvated ions [60, 62]. According to Y. Shen et al. [60] and A.L. Stepanov [62], the ion beam synthesis of the nanostructured phase could be conceptualized into several steps: (i.) stopping and accumulation of F implants (and radiation damage/amorphization) in the near-surface area of the host B_6O matrix, (ii.) an excess of neutral F atoms in the matrix, above the solubility limit, supersaturation of the near-surface area, (iii.) formation of nuclei of a $B_xO_yF_z$ phase from the supersaturation and amorphized near-surface area, and (iv.) growth of the nanostructured phase from the nuclei. Recently our group reported on the formation of *c*BN nanocrystals by ion implantation into *h*BN [2, 38]. Several others researchers have also reported on the ion beam synthesis of nanostructured materials [4, 5, 60, 62].

Similar peak shifting, and asymmetrical broadening in the Raman spectra of ion implanted material to those in Figures 6.2 and 6.5 has been reported before by other researchers for nanocrystalline phased of BN [46, 67], silicon [19, 51, 56], and germanium [27], group III-V semiconductor compounds [31, 49], and other materials [1, 4, 6, 63]. To be specific, the existence and variations of the lineshapes of the Raman spectra has been explained as a result of the confinement of optical phonons in the nano-sized crystallites.

[1] An approximation derived by curve fitting using OriginPro 8.0

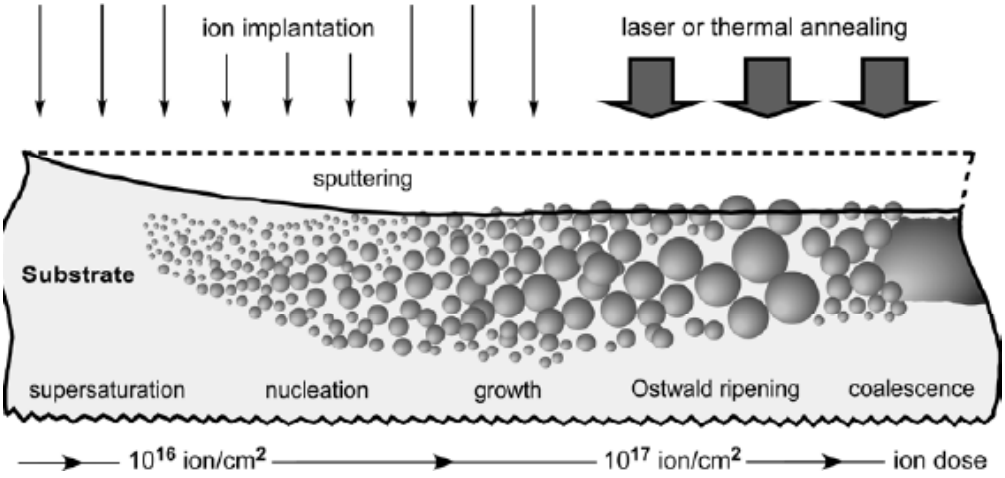

Figure 6.4: *An illustration of the basic physical processes (from left to right) involved in the formation of nanoparticles from an implant with respect to the ion dose. Surface sputtering under irradiation is also considered [45]. (Diagram from reference [62]). Note: All characterization was done on as-implanted specimen, no annealing was done.*

OPCM modeling

In this work we apply a modified Richter-Wang-Ley confinement model [56] of optical phonons in the nanostructured phase to explain the existence and variations of the line-shapes of the Raman spectra of F^+-implanted hot-pressed B_6O. Furthermore, to numerically estimate the mean crystallite sizes of the formed nanostructured phase.

The Richter-Wang-Ley confinement model introduced as Equation (6.1.2) was developed and successfully applied for simple cubic structures of obviously one lattice parameter, a simple and often known phonon dispersion, a simple bulk Raman spectrum, and a single zone centre. The α-rhombohedral B_6O structure has two lattice parameters, prior to this study the phonon dispersion relation was unknown, and the structure has multiple zone centres. In such cases, for n zone centres that display asymmetrical Raman lineshapes, the resultant lineshape should be a summation or convolution of n such lineshapes given as:

$$I(\omega) = \sum_{i=1}^{n} A_{oi} \cdot \int_0^{\infty} \rho(L) dl \cdot \int_0^{\infty} \frac{exp\left(-\frac{q^2 d^2}{\alpha_i}\right)}{\left[\omega - \Omega_i(q,L)\right]^2 + \left(\frac{\Gamma_{oi}}{2}\right)^2} d^3q \tag{6.3.1}$$

$i = 1,2,3,...,n$ are phonon confining zone centres, A_{oi} are the pre-factors, $\rho(L)$ is the crystallite size distribution in the sample, ω is the frequency shift, α_i are the scaling parameters, and Γ_{oi} are the linewidths of the zone centre in the bulk material, for the i^{th}

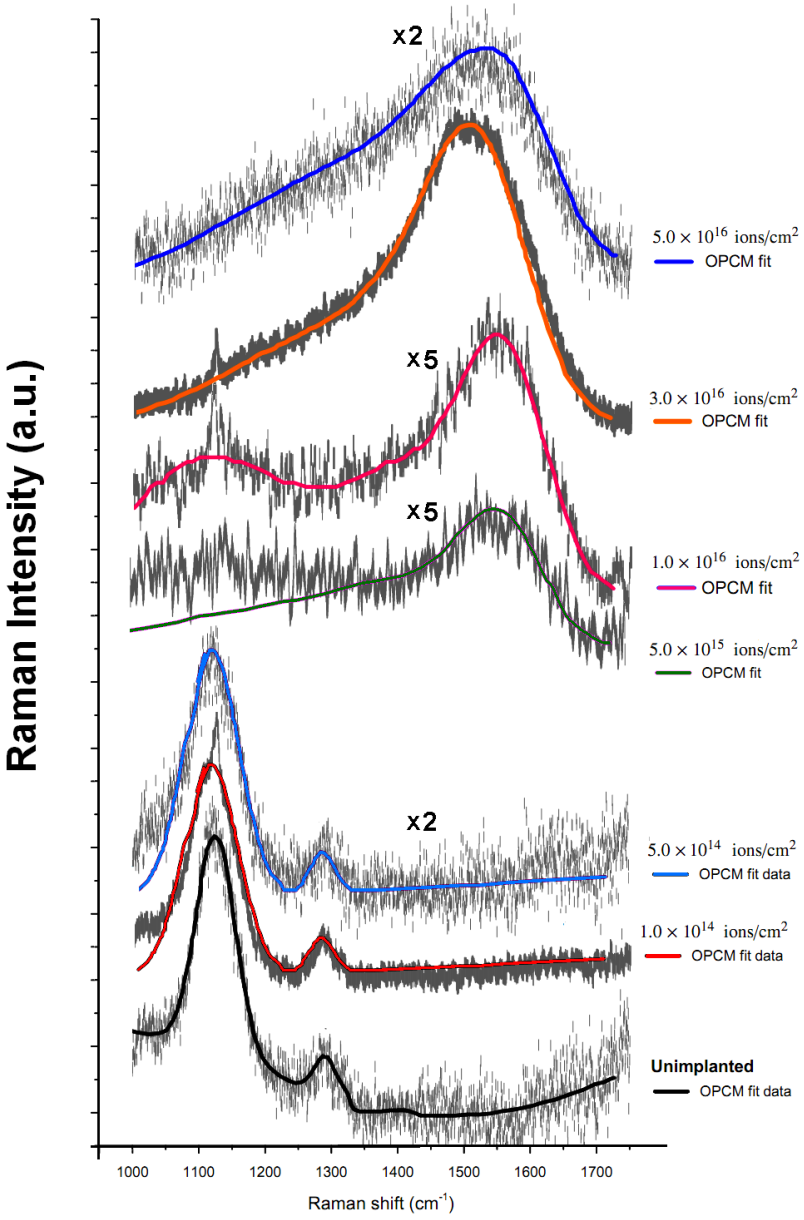

Figure 6.5: *An expanded view of the normalized Raman spectra of the 1550 cm^{-1} mode. A comparison between measured (dotted curve) and calculated first-order Raman lineshapes of ion implanted B_6O. The calculated Raman lineshapes are calculated using a modified Richter-Wang-Ley confinement model. The spectra are shifted along the y-axis for better comparison.*

zone centre $\Omega_i(q, L)$. For most oxides [4], the phonon dispersion relations can be estimated to be:

$$\omega_i(q) \sim \omega_{oi} \pm B_i \sin^2(aq) \tag{6.3.2}$$

where ω_{oi} is the frequency of the i^{th} zone centre and B_i is the dispersion parameter for such an i^{th} zone centre.

By observation (from Figures 6.2 and 6.5), three dominant Raman modes between 1000 to 1700 cm^{-1} frequency range can easily be identified as three zone centres with zone centre frequencies located at $\omega_1 = 1123\ cm^{-1}$, $\omega_2 = 1290\ cm^{-1}$, and $\omega_3 = 1500\ cm^{-1}$. The measured Raman spectra are manifested by differences in the structures responsible for the 'lattice vibration in the NPs' the phonon dispersion relations can be estimated to be:

$$\Omega_1(q, L) \sim 1123 \pm B_1 \cdot \sin^2(aq) \tag{6.3.3a}$$

$$\Omega_2(q, L) \sim 1290 \pm B_2 \cdot \sin^2(aq) \tag{6.3.3b}$$

$$\Omega_3(q, L) \sim 1500 \pm B_3 \cdot \sin^2(aq) \tag{6.3.3c}$$

The dependencies of the average crystallite size of the ion implantation formed nanostructured phase on the fluorine ion fluence was numerically determined by incorporated the phonon dispersion relations (Equation (6.3.3)) into Equation (6.3.1) for the three zone centres. A custom written Mathematica code was used for fitting the expanded Equation (6.3.1) to each Raman spectrum by means of employing the 'NIntegrate' subroutine and performing numerical integration and the 'NonlinearFit' package to perform least squares fit between Equation (6.3.1) and the experimental data.

For the unimplanted sample B1, an average crystallite size of 0.42 μm was determined from the diffraction pattern using the Debye-Scherrer approach. However, since the measured XRD pattern for the implanted samples provides inadequate infomation [2].

Using Equations (6.1.2 – 6.1.3), we can calculate the Raman spectrum and determine the relationship between the peak shift and the peak width. The result is shown as a dashed line in Figure 6.5. It is clear that the phonon confinement model correlates well with the experimental results. Figure 6.5 illustrates the predicted Raman spectra of crystallites as their sizes are reduced. A broadening and low-energy shift are evident as the crystallites become smaller, in agreement with the simple qualitative model of phonon confinement discussed earlier. The dependencies of the average crystallite size of the ion implantation synthesized nanostructured phase on the fluorine ion fluence was numerically determined and is shown in Figure 6.6

The plot of the crystallite size versus implantation dose shown in Figure 6.6 shows a drastic decrease of crystallite size from 60 nm (unimplanted specimen) down to 10 nm (for the

[2]The structural and morphological changes resulting from ion implantation are often below the critical diffractometer detection limit [37]

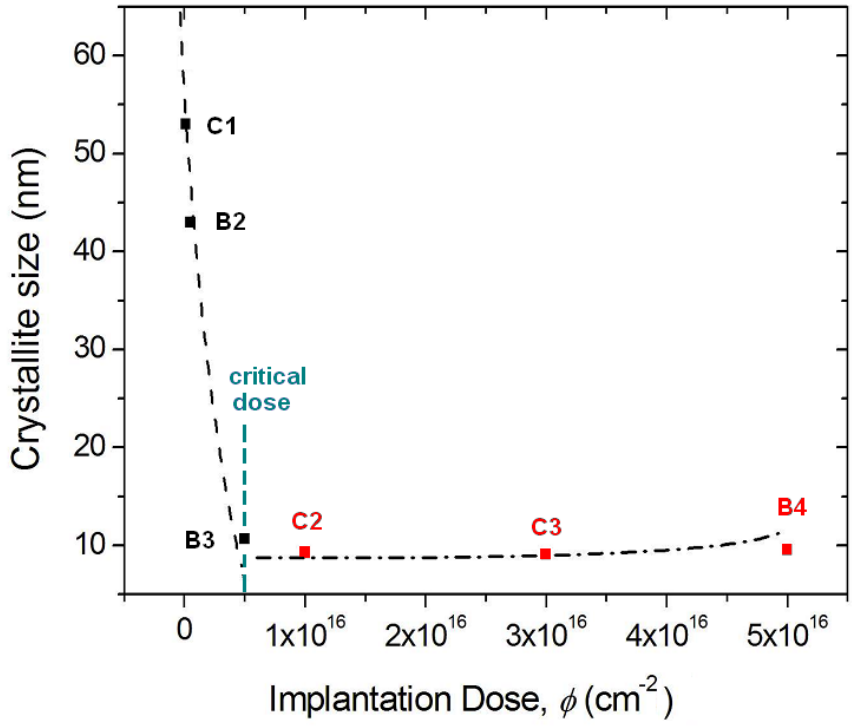

Figure 6.6: *A plot of crystallite sizes versus implantation dose numerically determined from Equation (6.3.1) with the aid of Mathematica code. The asterisk implies that the value was determined from the XRD pattern using the Debye-Scherrer approach.*

specimen implanted with 5×10^{15} F^+ ions/cm^2). However, beyond 5×10^{15} F^+ ions/cm^2, the crystallite size appears to increase at much slower rate. Following the discussion (on the formation of nanostructured phase by ion implantation on page 83) and Figure 6.3(b), the critical dose marks the transition point between the crystalline B_6O and the synthesized-nanostructured phase.

6.3.3 Scanning electron microscopy with EDX

A surface morphology study of the unimplanted and the implanted specimen was carried out by means of SEM with EDX. The SEM and EDX analysis of specimen B1 shown in Figures 6.7(a.) and (b.) shows a homogeneous and nominal B_6O phase characterized with surface pores and isolated iron phases. The iron contamination originates from abrasion of the steel ball and the containment cell during powder ball milling [24–26].

However, SEM and EDX analysis of the heavily implanted specimen (B4 in Figures 6.7(c.) and (d.)) for example, shows there is apparent dissimilarity between the unimplanted and the implanted specimen. In addition to the homogeneity B_6O phase and the iron contamination, SEM shows the existence of additional clusters of nanoparticles. Microstructural

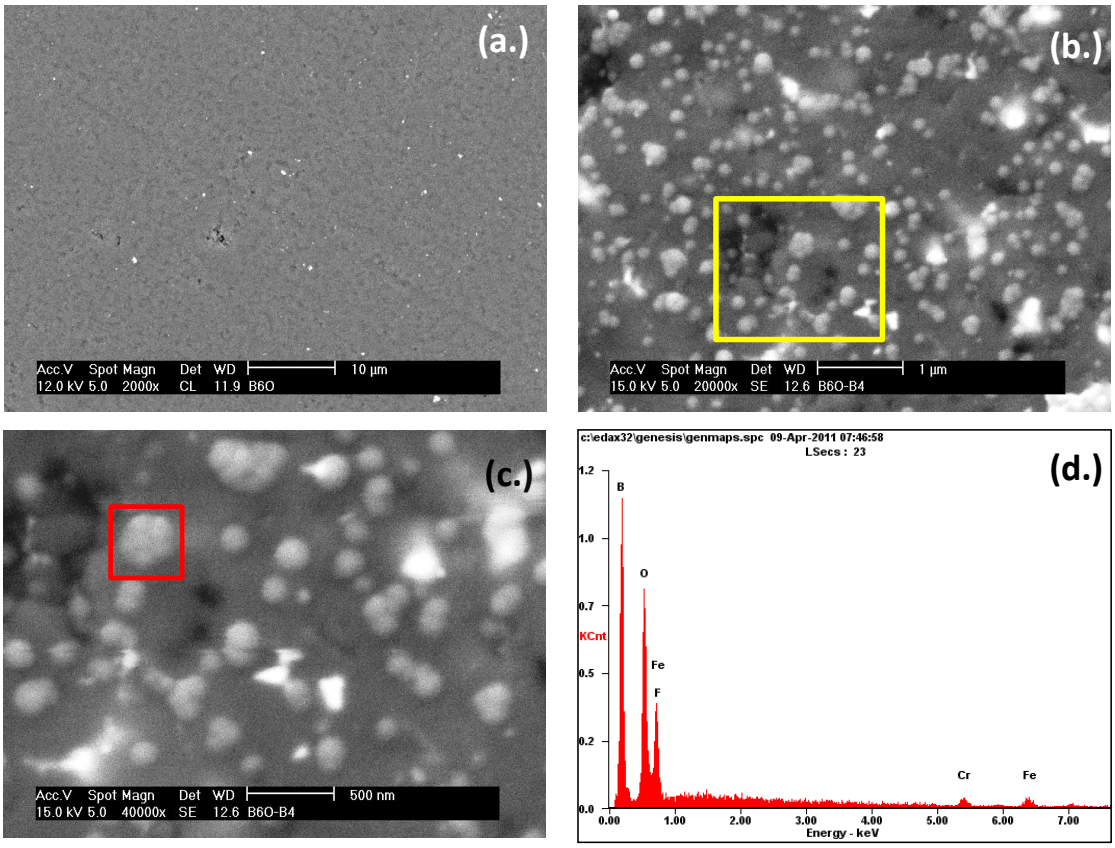

Figure 6.7: *A depiction of SEM images measured on (a.) the surface of an unimplanted B_6O specimen, (b. and c.) a 5.0×10^{15} F^+ ions/cm^2 implanted B_6O specimen showing clusters of particles embedded in the samples synthesized by fluorine ion beam implantation, and an EDX measured pattern on one such ion beam synthesized cluster.*

analysis of Figure 6.7(c) indicates that the average diameter of the formed clusters is 110 nm. Although the position of the iron and fluorine peaks in the measured EDX pattern coincide, there appears to exist just enough evidence to indicate that the clustered particles have a slightly different stoichiometry from the pristine B_6O EDX pattern as shown in Figure 6.7(b.) [24, 25]. The exact stoichiometry and structure of the seemingly ion beam synthesized nanophase are yet to be determined.

Observations of the possible existence ion beam synthesized clusters of nanoparticles SEM agrees with the Raman spectroscopy results on variations of the lineshapes of the Raman spectra has been explained as a result of the confinement of optical phonons in the nano-sized crystallites.

6.4 Summary and conclusion

The following conclusions are obtained from this study:

The radiation damage inflicted by the interactions of energetic fluorine ions on hot-pressed B_6O target has been simulated using SRIM codes. Using 99999 150 keV fluorine projectiles, the mean ion ranges distribution was determined to be 270 nm with a standard deviation in range of particles was around 60 nm. The skewness values obtained indicates the most probable depth is greater than predicted.

The Raman spectra of F^+-implanted B_6O specimen was investigated. Although F^+ implantation at fluences below 5.0×10^{15} ions/cm^2 reveals that the hot-pressed B_6O resists amorphization. The disappearance of the signature B_6O Raman spectrum at 5.0×10^{15} ions/cm^2 is observed. This is a result of ion induced radiation damage of the crystalline B_6O phase.

The Raman spectra of F^+-bombaded B_6O specimen at implantation at fluences beyond 5.0×10^{15} ions/cm^2, appears to reveals the existence of new asymmetrically broadened of Raman modes. This observation seems to be consistent with the phonon confinement of optical phonons. We tentatively attribute this to the precipitation of a new ion-beam synthesized nanostructured phase from the radiation damaged regions.

SEM images taken further compliments the Raman spectroscopy results on the possible existence of a new phase in the implanted region as a result of ion implantation. EDX compositional analysis indicates that the agglomerated nanoparticles have a stoichiometry opposed to the pristine (unimplanted) B_6O signature EDX pattern.

Bibliography

[1] K.W. Adu, H.R. Gutierrez, and P.C. Eklund. Raman-active phonon line profiles in semiconducting nanowires. *Vibrational Spectroscopy*, 42:165 – 175, 2006.

[2] E. Aradi, R.M. Erasmus, and T.E. Derry. Formation of cBN nanoparticles by helium, lithium and boron ion implantation. *Nuclear Instruments and Methods in Physics Research Section B*, 272:57 – 60, 2012.

[3] R. Ares, Y.B. Trudeau, J.L. Brebner, G.E. Kajrys, and M. Jouanne. Determination by Raman scattering of the in depth damage profile in high energy ion implantation. *Nuclear Instruments and Methods in Physics Research Section B*, 90:419 – 423, 1994.

[4] K. Arora, M. Rajalakshmi, T.R. Ravindran, and V. Sivasubramanian. Raman spectroscopy of optical phonon confinement in nanostructured materials. *Journal of Raman Spectroscopy*, 38:604 – 617, 2007.

[5] D.K. Avasthi and J..C Pivin. Ion beam for synthesis and modification of nanostructures. *Current Science*, 98:780 –792, March 2010.

[6] F. Banhart and P.M. Ajayan. Carbon onions as nanoscopic pressure cells for diamond formation. *Nature*, 382:433 – 435, 1996.

[7] C. Bonafos, H. Coffin, S. Schamm, N. Cherkashin, G. Ben Assayag, P. Dimitrakis, P. Normand, M. Carrada, V. Paillard, and A. Claverie. Si nanocrystals by ultra-low-energy ion beam-synthesis for non-volatile memory applications. *Solid-State Electronics*, 49:1734 – 1744, 2005.

[8] S.J. Bull and T.F. Page. High-dose ion implantation of ceramics: benefits and limitations for tribology. *Journal of Materials Science*, 23:4217 – 4230, 1988.

[9] S.J. Bull and T.F. Page. Effects of ion implantation on the hardness and friction behaviour of soda-lime silica glass. *Journal of Materials Science*, 27:3616 – 3616, 1992.

[10] I.H. Campbell and P.M. Fauchet. The effects of microcrystal size and shape on the one phonon Raman spectra of crystalline semiconductors. *Solid State Communications*, 58:739 – 741, 1986.

[11] D.D. Cheam, K. A. Walczak, M. Archaya, C. R. Friedrich, and P. L. Bergstrom. Leakage current in single electron device due to implanted gallium dopants by focus ion beam. *Microelectronic Engineering*, 88(8):1906 – 1909, 2011.

[12] T. Devolder, C. Chappert, Y. Chen, E. Cambril, H. Bernas, J.P. Jamet, and J. Ferre. Sub-50 nm planar magnetic nanostructures fabricated by ion irradiation. *Applied Physics Letters*, 74(22):3383 – 3385, 1999.

[13] G. Faraci, S. Gibilisco, P. Russo, and A.R. Pennisi. Modified Raman confinement model for Si nanocrystals. *Physical Review B*, 73:033307, 2006.

[14] P.M. Faucet and I.H. Campbell. Raman spectroscopy of low-dimensional semiconductors. *Critical Reviews in Solid State and Materials Sciences*, 14:s79 – s101, 1988.

[15] Huiyun Feng, Xuelan Liu, Hang Yuan, Mingguang Kong, Lijun Wu, Yuejing Wu, and Zengliang Yu. Utilizing low-energy ion beams to study living organisms. *Surface and Coatings Technology*, 201:8034 – 8038, 2007.

[16] M. Först, J. Niehusmann, T. Plötzing, J. Bolten, T. Wahlbrink, C. Moormann, and H. Kurz. High-speed all-optical switching in ion-implanted silicon-on-insulator microring resonators. *Optics Letters*, 32:2046 – 2048, 2007.

[17] G. Gouadec and P. Colomban. Raman spectroscopy of nanomaterials: How spectra relate to disorder, particle size and mechanical properties. *Progress in Crystal Growth and Characterization of Materials*, 53:1 – 56, 2007.

[18] G. Gouadec and P. Colomban. Raman spectroscopy of nanostructures and nanosized materials. *Journal of Raman Spectroscopy*, 38:598 – 603, 2007.

[19] S.K. Gupta and P.K. Jha. Modified confinement model for size dependent Raman shift and linewidth of silicon nanocrystals. *Solid State Communications*, 149:1989 – 1992, dec 2009.

[20] Richard F. Haglund. Ion implantation as a tool in the synthesis of practical third-order nonlinear optical materials. *Materials Science and Engineering A*, 253:275 – 283, September 1998.

[21] R.F. Haglund Jr., L. Yang, R.H. Magruder III, C.W. White, R.A. Zuhr, L. Yang, R. Dorsinville, and R.R. Alfano. Nonlinear optical properties of metal-quantum-dot composites synthesized by ion implantation. *Nuclear Inst.and Methods in Physics Research, B*, 91(1 – 4):493 – 504, 1994.

[22] M.Y. Hao, H. Hwang, and J.C. Lee. Silicon-implanted SiO_2 for nonvolatile memory applications. *Solid-State Electronics*, 36:1321 – 1324, 1993.

[23] P.L.F. Hemment, J.E. Mynard, E. Pasztor, C.J. Raymond, and K.G. Stephens. Part 1: A new research implanter at the University of Surrey. In *Ion Implantation: Equipment and Technology*, pages 37 – 44. Springer - Verlag, 1982.

[24] M. Herrmann, H.J. Kleebe, J. Raethel, K. Sempf, S. Lauterbach, M.M. Muller, and I. Sigalas. Field-assisted densification of superhard B_6O materials with Y_2O_3/Al_2O_3 addition. *Journal of the American Ceramic Society*, 92:2368 – 2372, 2009.

[25] O.T. Johnson, I. Sigalas, and M. Herrmann. Microstructure and interfacial reactions between B_6O and (Ni, Co) couples. *Ceramics International*, 36:2401 – 2406, 2010.

[26] O.T. Johnson, I. Sigalas, E.N. Ogunmuyiwa, H.J. Kleebe, M.M. Muller, and M. Herrmann. Boron suboxide materials with Co sintering additives. *Ceramics International*, 36:1767 – 1771, 2010.

[27] K.U. Joshi, A.M. Narsale, D. Kanjilal, T.N. Warang, T.K. Gundurao, and D.C. Kothari. Ion beam synthesis of germanium nanostructures. *Surface and Coatings Technology*, 203:2476 – 2478, June 2009.

[28] R. Kalish. The role of ion-implantation in the realization of spintronic devices in diamond. *Nuclear Instruments and Methods in Physics Research, Section B: Beam Interactions with Materials and Atoms*, 272:42 – 48, 2012.

[29] K.J. Kirkby and R.P. Webb. Ion implanted nanostructures. In H.S. Nalwa, editor, *Encyclopedia of Nanoscience and Nanotechnology*, volume 4, pages 1 – 11. American Scientific Publishers, 2004.

[30] S. Kobayashi, M. Imaeda, and S. Matsumoto. Single electron transistor fabricated with SOI wafer. *Materials Science and Engineering C*, 26(5 – 7):889 – 892, 2006.

[31] F. Komarov, L. Vlasukova, W. Wesch, A. Kamarou, O. Milchanin, S. Grechnyi, A. Mudryi, and A. Ivaniukovich. Formation of InAs nanocrystals in Si by high-fluence ion implantation. *Nuclear Instruments and Methods in Physics Research Section B*, 266:3557 – 3564, August 2008.

[32] S.O. Kucheyev, J.S. Williams, and S.J. Pearton. Ion implantation into GaN. *Materials Science and Engineering: R*, 33:51 – 107, 2001.

[33] V.I. Lavrentiev and A.D. Pogrebnjak. High-dose ion implantation into metals. *Surface and Coatings Technology*, 99:24 – 32, 1998.

[34] E.H. Lee, M.B. Lewis, P.J. Plau, and L.K. Mansur. Improved surface properties of polymer materials by multiple ion beam treatment. *Journal of Materials Research*, 6:610, 1991.

[35] D. Litvinov, J.C. Wolfe, E.B. Svedberg, T. Ambrose, K. Howard, F. Chen, T.E. Schlesinger, and S. Khizroev. Ion implantation of magnetic thin films and nanostructures. *Journal of Magnetism and Magnetic Materials*, 283(1):128 – 132, 2004.

[36] J.E. Lowther. 2009. Personal communication.

[37] R. Machaka. Ion beam modifications of boron nitride by ion implantation. MSc Dissertation, School of Physics, University of the Witwatersrand, 2007.

[38] R. Machaka, B.W. Mwakikunga, E. Manikandan, T.E. Derry, and I. Sigalas. Raman spectrum of hot-pressed boron suboxide. *Advanced Materials Letters*, 2:58 – 64, 2011.

[39] M. Manso, A. Valsesia, M. Lejeune, D. Gilliland, G. Ceccone, and F. Rossi. Tailoring surface properties of biomedical polymers by implantation of ar and he ions. *Acta Biomaterialia*, 1:431 – 440, 2005.

[40] J.W. Mayer, L. Eriksson, and J.A. Davies. *Ion Implantation in Semiconductors*. Academic Press Inc., New York, 1970.

[41] C.J. McHargue. Ion beam modification of ceramics. *Materials Science and Engineering: A*, 253:94 – 105, 1998.

[42] P. Murugan, R. Kesavamoorthy, S. Amirthapandian, R. Saravanan, K. Ramachandran, and N. Krishnamurthy. Raman study on H^+-implantation effects in highly doped n-GaAs. *Physica B: Condensed Matter*, 315:56 – 63, April 2002.

[43] B.W. Mwakikunga. *Nano-size Effects on Opto-Electronic, Structural and Vibrational Properties of Vanadium and Tungsten Oxides Produced by Laser and Ultrasonic Spray Pyrolysis Techniques*. PhD Thesis, School of Physics, University of the Witwatersrand, Johannesburg, 2009.

[44] N. Nakamura, K. Hirao, and Y. Yamauchi. Tribological properties of silicon nitride ceramics modified by ion implantation. *Journal of the European Ceramic Society*, 24:219 – 224, 2004.

[45] M. Nastasi and J.W. Mayer. *Ion Implantation and Synthesis of Materials*. Springer Series in Materials Science. Springer-Verlag Berlin Heidelberg, 2006.

[46] R.J. Nemanich, S.A. Solin, and R.M. Martin. Light scattering in boron nitride microcrystals. *Physical Review B*, 23:6348 – 6356, 1981.

[47] M. Olofsson and T. Lundstrom. Synthesis and structure of non-stoichiometric B_6O. *Journal of Alloys and Compounds*, 257:91 – 95, July 1997.

[48] P.M. Ossi. Radiation-induced phase transitions. In K.E. Sickafus, E.A. Kotomin, and B.P. Uberuaga, editors, *Radiation Effects in Solids*, volume 235 of *NATO Science Series*, pages 259 – 319. Springer Netherlands, 2007.

[49] P. Parayantha and F.H. Polla. Raman scattering in alloy semiconductors: spatial correlation model. *Physical Review Letters*, 52:1822 – 1825, 1984.

[50] S.T. Picraux. Ion implantation in metals. *Annual Review of Materials Science*, 14:335 – 372, 1984.

[51] R. Prabakaran, R. Kesavamoorthy, S. Amirthapandian, and A. Ramanand. Raman scattering and photoluminescence studies on O^+ implanted porous silicon. *Materials Letters*, 58:3745 – 3750, 2004.

[52] J.F. Prins. Ion-implanted structures and doped layers in diamond. *Materials Science Reports*, 7:271 – 364, 1992.

[53] J.F. Prins. *Properties of natural and synthetic diamond*, chapter Chapter 8:Modification, doping and devices in implanted diamond, pages 301 – 341. Academic Press Limited, 1992.

[54] J.F. Prins. Ion implantation of diamond for electronic applications. *Semiconductor Science and Technology*, 18:S27 – S33, 2003.

[55] C.S. Rama Rao, S. Sundaram, R.L. Schmidt, and J. Comas. Study of ion-implantation damage in GaAs:Be and InP:Be using Raman scattering. *Journal of Applied Physics*, 54:1808 – 1815, 1983.

[56] H. Richter, Z.P. Wang, and L. Ley. The one phonon Raman spectrum in microcrystalline silicon. *Solid State Communications*, 39:625 – 629, 1981.

[57] L. Rubin and J. Poate. Ion implantation in silicon technology. *Industrial Physicist*, 9(3):12 – 15, 2003.

[58] S. Saravana Kumar, M. Abdul Khadar, S.K. Dhara, T.R. Ravindran, and K.G.M. Nair. Photoluminescence and Raman studies of ZnS nanoparticles implanted with Cu^+ ions. *Nuclear Instruments and Methods in Physics Research Section B*, 251:435 – 440, 2006.

[59] Y.P. Sharkeev, A.N. Didenko, and E.V. Kozlov. Dislocation structures and strengthening of ion-implanted metals and alloys. *Russian Physics Journal*, 37:478 – 490, 1994.

[60] Y. Shen, X. Li, Z. Wang, D. Zhang, M. Li, B. Yuan, Z. Li, and C. Liu. Fabrication and thermal evolution of nanocrystals in SiO_2 by zn ion implantation. *Journal of Crystal Growth*, 311:4605 – 4609, 2009.

[61] W. Shockley. Forming semiconductor devices by ionic bombardment. US Patent No. 2787564, October 1957.

[62] A.L. Stepanov. Synthesis of silver nanoparticles in dielectric matrix by ion implantation: a review. *Reviews on Advanced Materials Science*, 26:1 – 29, 2010. Advanced Study Center Co. Ltd. (St. Petersburg, Russia).

[63] S. Talapatra, Ju-Yin Cheng, N. Chakrapani, S. Trasobares, A. Cao, R. Vajtai, M.B. Huang, and P.M. Ajayan. Ion irradiation induced structural modifications in diamond nanoparticles. *Nanotechnology*, 17:305 – 309, 2006.

[64] Varian/Extrion. *Production ion implanter model 200-20A2F instruction manual*. Varian Extrion Division, Gloucester UK, 1977.

[65] M. Waldow, T. Plötzing, M. Gottheil, M. Först, J. Bolten, T. Wahlbrink, and H. Kurz. 25 ps all-optical switching in oxygen implanted silicon-on-insulator microring resonator. *Optics Express*, 16(11):7693 – 7702, 2008.

[66] H. Werheit and V. Filipov. Raman effect in boron and boron-rich compounds. NATO ARW, Boron-Rich Solids, Orlando, Florida, USA, 2009. Dec. 14 – 18.

[67] T. Werninghaus, J. Hahn, F. Ritcher, and D.R.T. Zahn. Raman spectroscopy investigation size effects in cubic boron nitride. *Applied Physics Letters*, 70:958 – 960, 1997.

[68] K. Wittmaack. Reliability of a popular simulation code for predicting sputtering yields of solids and ranges of low-energy ions. *Journal of Applied Physics*, 96(5):2632 – 2637, 2004.

[69] D. Wolverson. Raman spectroscopy. In C. Lamberti, editor, *Characterization of Semiconductor Heterostructures and Nanostructures*, pages 249 – 288. Elsevier, Amsterdam, 2008.

[70] S. Zhu, X. Xiang, X.T. Zu, and L.M. Wang. Magnetic nano-particles of Ni in MgO single crystals by ion implantation. *Nuclear Instruments and Methods in Physics Research Section B: Beam Interactions with Materials and Atoms*, 242(1 – 2):114 – 117, 2006.

[71] J.F. Ziegler. *Handbook of ion implantation technology*. North Holland, 1992.

[72] J.F. Ziegler. Srim2010 (software package). http://www.srim.org, 2010.

Chapter 7

Mechanical Properties of F^+-Implanted B_6O

This chapter is a continuation of the work described in Chapter 6 were the evolution of the structural, surface and spectroscopic properties of F^+-implanted B_6O specimen as a function of ion fluence was explored. In the current chapter, the effects of the F^+-implantation on the near-surface nanomechanical properties are investigated. The nanomechanical properties are evaluated by means of the analysis of the characteristic nanoindentation $P-h$ data measured on the F^+-implanted specimen using a Berkovich indenter. The current results are explained in terms of the observations discussed in Chapter 6.

The introduction of highly electronegative oxygen leads to stronger B_{12} intra-cluster bonds in B_6O [18], and improves the overall rigidity of the structure through cross-linking B_{12} icosahedra and filling voids. This explains why B_6O is a superhard material [18, 25].

The chapter is based on a review invited by *Advances in Materials Science and Engineering* for publication in their special issue on the 'Modification, Synthesis, and Analysis of Advanced Materials Using Ion Beam Techniques' [16].

7.1 Introduction

The elasto-plastic and visco-elastic nanomechanical properties of 150 kev F^+-implanted B_6O specimen are evaluated from the measured $P-h$ nanoindentation data using the elastic unloading [3, 20, 22] and room-temperature constant-load time dependent deformation [5, 6] phenomenological models. The former is based on the O&P method and the latter, characterizes the mechanical properties sensitive to creep-related effects – it is a relatively new concept. The influence of ion beams to the observed changes in these nanomechanical properties are interpreted in terms of the evolution of the structural, surface and spectroscopic properties of fluorine ions implanted B_6O specimen as a function of fluorine dose as observed in Chapter 6.

7.2 Experimental details

The experimental methods relevant to the results presented in this chapter have already been discussed in detail herein previous chapters. Details of the F^+-implantation are outlined Section 6.2 whilst details relating to the Raman spectroscopy and nanoindentation measurements are outlined in Sections 3.2 and 6.2, and Section 5.3, respectively.

7.3 Theory

Theories and methods relating to the experimental techniques employed in obtaining the results presented in this chapter have also been previously discussed in Chapter 5 on page 47 and page 50, respectively. The principles of nanoindentation of materials are briefly discussed in Section 5.2 as well as by other researchers [3, 20, 22]. For the more information concerning to the theory, practice, and instrumentation relating to micro-Raman spectroscopy experiments the reader is referred to Appendix A.

7.4 Results and discussion

Changes in the surface microstructure and composition in ion implanted B_6O specimen were characterized by SEM with EDX whilst changes in the specimen surface topography as a result of F^+-implantation into B_6O were characterized by AFM. Changes in the surface vibrational properties in ion implanted B_6O specimen were characterized by

Raman spectroscopy. All these results have been presented already in Chapter 6. In this section changes in the near-surface mechanical properties in ion implanted specimen as a function of ion fluence are discussed.

7.4.1 Nanoindentation analysis

The characteristic nanoindentation $P-h$ curves continuously measured during loading and unloading for four of the specimens under investigation (unimplanted (B1) and fluorine implanted (B2 – B4)) are shown in Figure 7.1. For each of the four specimen under investigation, at least twelve separate indentations were performed at different positions on the sample surface.

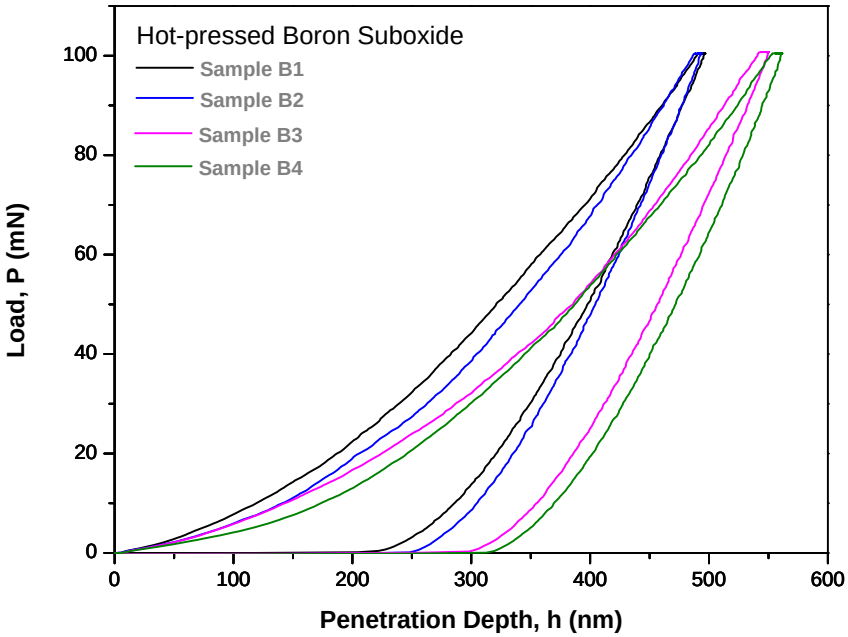

Figure 7.1: *A representative indentation response curves measured during the nanoindentation measurements on the unimplanted (B1), and F^+-implanted (B2–B4) hot-pressed B_6O specimen.*

A mechanism of plastic deformation, namely plastic flow is generally responsible for the changes in hardness during nanoindentation experiments. If the dominant mechanism of deformation during a nanoindentation experiment is phase transformation dislocation discontinuities such as kinks and pop-ins are observed in the $P-h$ curves [10, 23]. The absence of such discontinuities in the measured $P-h$ curves (see Figure 7.1) suggests that the testing performed in this study does not induce significant phase transformation, if there is any. Therefore, the observed deformation during nanoindentation testing in B_6O is most likely accomplished by means of plastic flow. The plastic flow appears to manifest to a greater extent in ion irradiated specimen. This 'softening' of the ion implanted specimen

surface layer can be attributed to the radiation damage as identified by the micro-Raman spectroscopy characterization results further supporting the notion that plastic flow as the deformation mechanism of the ion implanted material.

The elastic modulus (E) and the intrinsic hardness of specimen $H(E)$ values were evaluated from the indentation $P-h$ curves by applying a modified O&P procedure [20–22], see also Chapter 5 on page 56. Table 7.1 shows a summary of the calculated $H(E)$, E values, the ratio H/E and the Meyer's index, n derived from the loading $P-h$ curves.

According to the Archard's equation for abrasive wear [1, 9] hardness is a primary material property in defining the wear resistance of a material. However, there are suggestions that the elastic modulus also has significant influence on wear behaviour [14]. A number of authors have demonstrated the ratio to be a more suitable parameter for predicting wear resistance than is hardness alone [14, 17]. In that case, a high H/E ratio is a reliable indicator of a surface's good wear resistance performance for some materials [13, 14, 17]. In this work, this parameter is used only to quickly predict how ion implantation is likely to modify the wear resistance performance of the material.

Sample	$H(E)$ (GPa)	E (GPa)	H/E	n
B1	30.5± 0.2	328.0 ± 4.1	0.093	1.66
B2	29.3± 0.4	359.0 ± 6.8	0.082	1.92
B3	23.0± 1.2	300.0 ± 3.7	0.076	1.94
B4	21.3± 0.6	291.5 ± 1.5	0.073	1.96

Table 7.1: *A summary of the effect of ion implantation on the intrinsic hardness, $H(E)$, the elastic modulus, E, the ratio H/E, and the Meyer's index, n measured on the unimplanted and implanted specimen.*

In order to exhibit all dependencies (of the mechanical properties on the fluence of implantation) in one figure for ease of comparison, $H(E)$, E, and H/E values are normalized to those measured on the unimplanted specimen, B1 and presented in Figure 7.2.

The measured hardness is evidently influenced by the fluence of implantation. For example, an increase in the ion dose is observed to result in (i) an overall decrease in the hardness and the elastic modulus of the material, (ii) a decrease in the values of the ratio H/E and (iii) a general increase in the Meyer's index values. These trends reflect on the changes in the structure or the material, the mechanism of plastic deformation of the irradiated material and these observations are further discussed below.

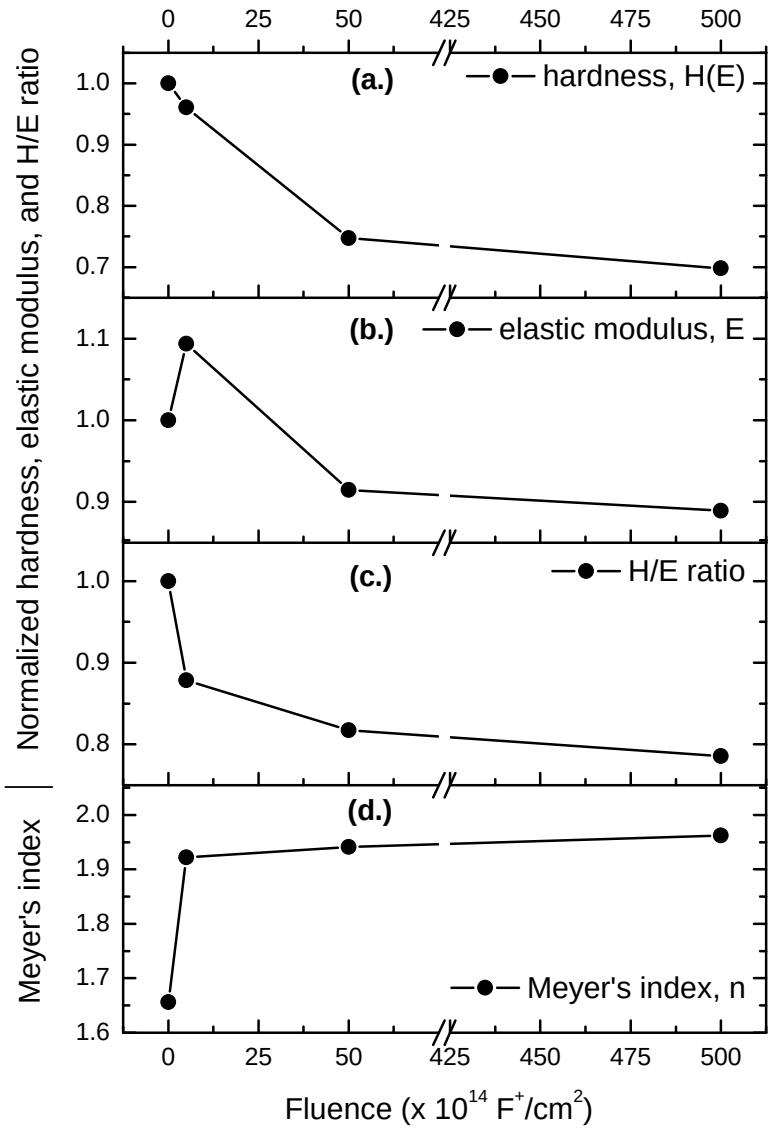

Figure 7.2: *The variations of the intrinsic hardness (a.), the elastic modulus (b.), the H/E ratio (c.), and the Meyer's index (d.) measured for hot-pressed B_6O samples irradiated with various fluences of F^+ ions.*

Intrinsic hardness

From the measured $P-h$ curves, the intrinsic hardness of the pristine B_6O specimen was evaluated to be 31 GPa; a value in close agreement with recently published microhardness [7, 8] and nanohardness [11] values (see also Chapters 4 and 5). The effect of F^+-ion implantation on the surface hardness is summarized in Figure 7.2(a) and Table 7.1. Apparently, ion implantation leads to a progressive decrease in the surface hardness with increasing ion fluence. The change in the hardness value is initially small (about 5%) for

implantation doses of up to 5×10^{14} F^+/cm^2, while considerable decrease (of up to 30%) is observed for implantation doses exceeding 5×10^{15} F^+/cm^2.

The ease of plasticity or deformation in the ion-implanted specimen due to ion-induced amorphization of the crystalline B_6O structure could possibly explain the observed changes in the measured hardness values with increasing ion fluences.

Elastic modulus

From the measured $P-h$ curves, the elastic modulus of the pristine B_6O specimen was evaluated to be 330 GPa; a value also consistent with previously published data [7]. As illustrated in Figure 7.2(b), although for low-irradiation fluences the elastic modulus increases by about 10%, a further increase in the implantation dose rapidly causes a decrease the elastic modulus as amorphization of the crystalline structure supposedly initiates. After which the elastic modulus appears to correlate well with the hardness and H/E ratio. The initial increase might be attributed to the increase of the concentration of the interstitial fluorine atoms in the implanted surface region – these materials are widely thought to be radiation resistant.

Material having crystalline phases has a higher modulus than the materials with amorphous structure [24]. The lower elastic modulus of the implanted hot-pressed B_6O observed in Figure 7.2(b) could be associated with the implantation-induced increase in the degree of amorphization.

H/E ratio

The ratio H/E is a parameter used in explaining the type of behaviour observed in nanoindentation and nano-scratching wear tests [12–14]. The ratio can be regarded as a criteria for evaluating the wear resistance performance of a material. The importance of the simple ration can not be underestimated, as it is to wear resistance performance what elastic strain is to failure. The effect of H/E on wear can be rationalized by assuming that gradual material removal or gradual wear is a consequence of plastic deformation and not by elastic deformation or fracture [17]. A high H/E ratio is often a reliable indicator of good wear resistance in a surface [14, 17, 19].

A comparison of the H/E ratio of hot-pressed B_6O with other super-hard ceramic materials is shown in Table 7.2 below.

Figure 7.2(c) shows that the pristine specimen shows a higher H/E ratio when compared to that of the implanted samples. The intrinsic hardness clearly is correlates well with the H/E ratio; this is no coincidence since hardness (or the plasticity) is known to have the decisive role of the surface layer on friction properties [13, 14]. Therefore it is clear that F

Material	H/E ratio
Diamond	0.09 – 0.1 [12]
Hot-pressed B_6O	**0.093**
B_4C	0.07 – 0.09 [12]
SiC	0.080 [12]
Si_3N_4	0.080 [12]
Silicon	0.062 [13]

Table 7.2: *H/E ratios of B_6O and hard ceramic materials*

ion implantation of the B_6O surface at a larger fluence is expected to cause a considerable increase in the surface amorphization.

Meyer's index

The classic power law relationship between the load, P and indenter displacement, h shown in Equation 7.4.1 is commonly known as Meyer's law [4].

$$P = A \cdot h^n \tag{7.4.1}$$

A is a constant. The Meyer's index n is a also know as the size-effect index, a descriptive parameter that is evaluated by the power-law curve fitting of experimental loading $P - h$ curve [2, 15]. The Meyer index has been experimentally observed to be between 1.5 and 2.0 for ceramics [4]. When $n \leq 2$, a material exhibits the normal ISE behaviour and the hardness decreases with load. Conversely, $n \geq 2$ implies a reverse ISE behaviour. While $n \approx 2$ implies that there is no evidence for load size-effects, i.e. hardness is independent of applied load [2, 15].

Figure 7.2(d) shows the influence of ion implantation dose on the values of n. The figure shows an increase in n with the increasing F^+ dose. At higher implantation doses, where $n \to 2$, a single hardness value for the material exists. There is the diminishing evidence of indentation size effects.

Transient creep properties

Short-term nanoindentation creep of unimplanted and ion implanted B_6O specimen, consisting of transient and steady-state creep stages, have been investigated at room temperature. The goal of this particular study is to determine the effects of ion implantation and the F^+ dose on the measured creep response of the material.

The measured nanoindentation creep curves and the corresponding strain rates of unimplanted and ion implanted B_6O specimens are conveniently shown in Figure 7.3 for better comparison.

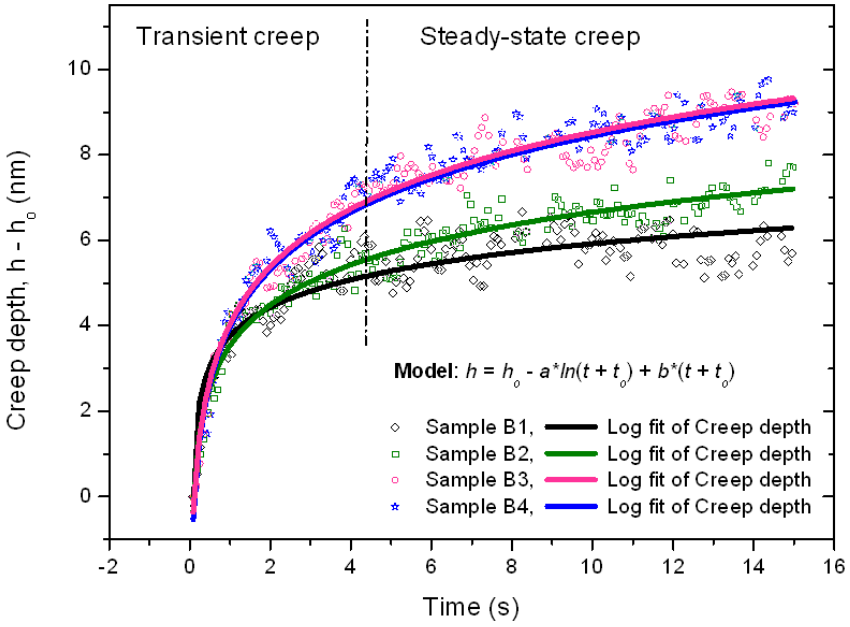

Figure 7.3: *Room temperature transient and steady-state creep behaviour in F^+-implanted B_6O specimen obtained be means of analysing the changes in depth with time at constant load during standard nanoindentation measurements.*

The nanoindentation creep curves of both non-implanted specimen and ion implanted specimens show an expected yet brief transient creep response. The non implanted specimen exhibits nearly no creep when compared to the implanted specimen. This enhanced steady-state creep behaviour in the implanted specimen is, like the changes observed in the hardness and elastic modulus, probably a result of the irradiation-induced plasticity on the specimens' surfaces.

On a structural level, the effects in the changes in the nanomechanical properties appears to be related to the distortion of the individual B_{12} icosahedra and the α-rhombohedral framework, as a result of ion bombardment. The ease of plastic flow or deformation in the ion-implanted specimen explains the changes in the hardness and creep response of the material. The 'softening' of the ion implanted specimen surface layer is due to the radiation damage as observed by the micro-Raman spectroscopy characterization results. This considerably increases the surface plasticity.

7.5 Summary and conclusion

The following conclusions are obtained from this study:

The effects of the fluorine ion implantation on the near-surface nanomechanical properties of hot-pressed B_6O were investigated. The effects in the changes in the nanomechanical properties appears to be related to the radiation damage as a result of ion bombardment. The ease of plastic flow in the ion-implanted specimen due to deformation explains the changes in the hardness and creep response of the material. The 'softening' of the ion implanted specimen surface layer can be attributed to the radiation damage as identified by the micro-Raman spectroscopy characterization results. This considerable increase in the surface plasticity is in line with the diminishing evidence of indentation size effects in hardness in terms of Meyer's index.

Bibliography

[1] J.F. Archard. Contact and rubbing of flat surfaces. *Journal of Applied Physics*, 24:981, 1953.

[2] O. Şahin, O. Uzun, U. Kölemen, and N. Uçar. Mechanical characterization for β-Sn single crystals using nanoindentation tests. *Materials Characterization*, 59:427 – 434, 2008.

[3] A.C. Fischer-Cripps. *Nanoindentation*. Springer, New York, 2nd edition, 2004.

[4] J. Gong, J. Wu, and Z. Guan. Analysis of the indentation size effect on the apparent hardness for ceramics. *Materials Letters*, 38:197 – 201, 1999.

[5] R. Goodall and T.W. Clyne. A critical appraisal of the extraction of creep parameters from nanoindentation data obtained at room temperature. *Acta Materialia*, 54:5489 – 5499, 2006.

[6] R. Goodall, A Kahl, T.W. Clyne, and J.A. Fernie. Investigation of the creep behaviour of a ceramic-based composite, using nanoindention testing of the creeping constituent. *Indentation Techniques in Ceramic Materials Characterization*, 156:73 – 82, 2004.

[7] M. Herrmann, H.J. Kleebe, J. Raethel, K. Sempf, S. Lauterbach, M.M. Muller, and I. Sigalas. Field-assisted densification of superhard B_6O materials with Y_2O_3/Al_2O_3 addition. *Journal of the American Ceramic Society*, 92:2368 – 2372, 2009.

[8] M. Herrmann, J. Raethel, A. Bales, K. Sempf, I. Sigalas, and M. Hoehn. Liquid phase assisted densification of superhard B_6O materials. *Journal of the European Ceramic Society*, 29:2611 – 2617, 2009.

[9] I.M. Hutchings. *Tribology: friction and wear of engineering materials*. CRC Press, October 1992.

[10] Sheng-Rui Jian, Guo-Ju Chen, and Jenh-Yih Juang. Nanoindentation-induced phase transformation in (110) oriented Si single-crystals. *Current Opinions in Solid State Material Science*, 14:69 – 74, 2010.

[11] X. Jiao, H. Jin, F. Liu, Z. Ding, B. Yang, F. Lu, X. Zhao, and X. Liu. Synthesis of boron suboxide (B_6O) with ball milled boron oxide (B_2O_3) under lower pressure and temperature. *Journal of Solid State Chemistry*, 183:1697 – 1703, 2010.

[12] N. Laidani, A. Miotello, and J. Perrike. Chemical, mechanical and electrical properties of CN_x-films produced by reactive sputtering and N^+-implantation in carbon films. *Applied Surface Science*, 99:273 – 284, 1996.

[13] P. Lemoine, J.P. Quinn, P. Maguire, and J.A. McLaughlin. Comparing hardness and wear data for tetrahedral amorphous carbon and hydrogenated amorphous carbon thin films. *Wear*, 257:509 – 522, 2004.

[14] A. Leyland and A. Matthews. On the significance of the H/E ratio in wear control: a nanocomposite coating approach to optimised tribological behaviour. *Wear*, 246:1 – 11, 2000.

[15] H. Li and R.C. Bradt. The effect of indentation-induced cracking on the apparent microhardness. *Journal of Materials Science*, 31:1065 – 1070, 1996.

[16] R. Machaka, T.E. Derry, and I. Sigalas. Mechanical and surface properties of fluorine-ion-implanted hot-pressed boron suboxide. *Advances in Materials Science and Engineering: Special Issue on Modification, Synthesis, and Analysis of Advanced Materials Using Ion Beam Techniques*, Accepted:null, February 2011.

[17] Wangyang Ni, Yang-Tse Cheng, Michael J. Lukitsch, Anita M. Weiner, Lenoid C. Lev, and David S. Grummon. Effects of the ratio of hardness to Young's modulus on the friction and wear behavior of bilayer coatings. *Applied Physics Letters*, 85:4028 – 4030, November 2004.

[18] D. Nieto-Sanz, P. Loubbeyre, W. Crichton, and M. Mezouar. X-ray study of the synthesis of boron oxides at high pressure: phase diagram amd equation of state. *Physical Review B*, 70:214108, 2004.

[19] T.L. Oberle. Properties influencing the wear of metals. *Journal of Metals*, 3:438 – 439, 1951.

[20] W.C. Oliver and G.M. Pharr. An improved technique for determining hardness and elastic modulus using load and displacement sensing indentation experiments. *Journal of Materials Research*, 7:1564 – 1583, 1992.

[21] W.C. Oliver and G.M. Pharr. Measurement of hardness and elastic modulus by instrumented indentation: Advances in understanding and refinements to methodology. *Journal of Materials Research*, 19:3 – 20, 2004.

[22] G.M. Pharr and A. Bolshakov. Understanding nanoindentation unloading curves. *Journal of Materials Research*, 17:2660 – 2671, 2002.

[23] C.A. Schuh. Nanoindentation studies of materials. *Materials Today*, 9:32–40, May 2006.

[24] J.G. Wang, B.W. Choi, T.G. Nieh, and C.T. Liu. Nano-scratch behavior of a Zr-based bulk amorphous alloy. *Journal of Material Research*, 15:798, 2000.

[25] R.F. Zhang, Z.J. Lin, Y.S. Zhao, and S. Veprek. Superhard materials with low elastic moduli: Three-dimensional covalent bonding as the origin of superhardness in B_6O. *Physical Review B*, 83:092101, March 2011.

Part IV

Summary

Chapter 8

Summary

B_6O exhibits a rather unusual and wide range of properties; among these are hardness with low density, mechanical strength, and chemical inertness. However, despite having received intensive research interests, its commercial applications are yet to be realized partly because of (a) it's low fracture toughness, (b) considerable practical challenges in the densification of the material, (c) crystalline and stoichiometric hot-pressed B_6O samples are not easy to synthesize, and (d) a lack of understanding of some of its properties.

The project's aim was to generated practical data for B_6O specimen prepared by uniaxial hot-pressing. In this regard, by means of Raman spectroscopy (Chapter 3), microhardness (Chapter 4)and nanoindentation measurements (Chapter 5). Information concerning the Raman spectra of the material, the material deformation behaviour during indentation as well as the intrinsic hardness of the material has been established. The effects of fluorine ion implantation on the near-surface structural, morphological (Chapter 6) and nanomechanical properties (Chapter 7) have been investigated as well. These results are summarized below.

8.1 Raman spectra of hot-pressed B_6O

Despite uniaxial hot pressing being the most cost effective method for producing poly-crystalline B_6O compacts, the Raman spectrum of hot-pressed B_6O was until now poorly understood. By means of the application of a fluorescence-background suppression scheme, observable first- and higher- order Raman spectra of B_6O, which till now had been deemed unobservable when the 514.5 nm excitation line is used, have been obtained.

By comparing our measured results to the Raman spectra of other superhard boron-rich ceramic materials (α-boron, ceB13N2, and B_4C) measured at ambient conditions using the same excitation source we observe that the Raman modes observed in B_6O are similar in characteristics to those observed for $B_{13}N_2$, and B_4C

Second-order Raman spectra are visible and were attributed to two-phonon combinations for first-order Raman modes.

8.2 Microhardness ISE studies in hot-pressed B_6O

The measured Vickers microhardness was observed to exhibit an indentation load-dependence. Based on the results, a comprehensive model inter-comparison study of indentation size effects is presented and discussed using the classical Meyer's law, the proportional specimen resistance models, and the multifractal scaling law. The average load-independent hardness of hot-pressed B_6O from this study has been observed to be 28.0 ± 0.3 GPa. Furthermore, for the first time, the nature of indentation size effect in hot-pressed B_6O is examined and discussed.

Interpretations based on the results possibly suggests that the origins of the observed indentation size effects can be attributed to either the bulk material's indentation elastic recovery, the indenter/specimen friction resistance coupled with elastic resistance of the specimen or/and the mixed elastic/plastic deformation response of material.

8.3 Mechanical properties of hot-pressed B_6O

Nanoindentation techniques are used characterizing the mechanical properties of hot-pressed B_6O specimen. In the studies presented in this thesis, a combined experimental and FEM simulation approach for determining nanomechanical properties of hot-pressed B_6O by nanoindentation was presented.

8.3.1 Experimental nanoindentation

The $P-h$ indentation response of hot-pressed B_6O samples is measured and analyzed. The results show that:

The average hardness and elastic modulus of hot-pressed B_6O were measured to be 31.6 ± 0.4 GPa and 363.4 ± 4 GPa, respectively.

An approach was developed to analyze the measured nanoindentation $P-h$ curve. Based on the approach, ISE in the nanoindentation hardness of the material was analyzed using the Meyer's law, the propositional resistance models and the multi-fractal scaling law.

One of the conclusions drawn from the study is that fractal dimension is a better indicator of the extent of ISE than the traditional Meyer's index.

8.3.2 Simulated nanoindentation

In this study, FEM simulations of conical nanoindentations into hot-pressed B_6O were performed using the finite-element package ABAQUS v6.9. A 2D axisymmetrical model was specifically developed for this work to simulate the experimental nanoindentation process.

Experimentally determined and simulated nanoindentation $P-h$ curves show a fairly good agreement. An inverse identification procedure used to fit, analyze and extract material properties from the simulated $P-h$ curves of hot-pressed B_6O gives a hardness of 28.6 GPa and an elastic modulus of 320 GPa, values in good agreement with relevant theoretical and experimental results. Furthermore, the deformation response of the material under dynamic indentation was also investigated at different stages using a finite element analysis method and interpreted using the expanding cavity model.

8.4 Ion-beam synthesized nanostructured phase

The evolution of the structural, surface and spectroscopic properties of ion implanted B_6O specimens as a function of fluorine dose were investigated by Raman spectroscopy, SEM with EDX, and AFM imaging.

Raman spectroscopy analysis shows that although F^+ implantation at fluences below 5.0×10^{15} ions/cm^2 reveals that hot-pressed B_6O largely resists radiation damage. However at 5.0×10^{15} ions/cm^2 the Raman spectrum of B_6O disappears, indicating possible ion induced surface amorphization.

Furthermore, Raman spectroscopy analysis also shows that beyond 5.0×10^{15} ions/cm^2, the measured Raman spectra appears to be influenced by the precipitation of a new ion-beam synthesized phase. Both AFM and SEM imaging further compliments this observation. EDX compositional analysis indicates that the agglomerated NPs have a $B_xO_yF_z$ stoichiometry as opposed to the unimplanted B_6O signature EDX pattern.

8.5 Mechanical properties of F^+-implanted B_6O

The effects of the F^+ implantation on the near-surface nanomechanical properties of hot-pressed B_6O were investigated as well.

On a structural level, the effects in the changes in the nanomechanical properties appears to be related to the distortion of the individual B_{12} icosahedra due to ion bombardment. The ease of plastic flow or deformation in the ion-implanted specimen explains the changes in the hardness response of the material. The 'softening' of the ion implanted specimen surface layer can be attributed to the radiation damage as identified by the micro-Raman spectroscopy characterization results. This considerable increase in the plasticity, in line with H/E indicates poor wear resistance performance in fluorine ion implanted materials and diminishing evidence of indentation size effects in hardness in terms of Meyer's index.

8.6 Outlook

The results presented in this thesis, although not exhaustive, indicate a general lack of a comprehensive understanding of various structural and mechanical properties. In as much as the current work makes available new sets of material data; it should forms a basis for further in-depth research into areas such as:

- the computational investigation of nature and origins of the higher-order vibrational modes observed in the Raman spectrum of B_6O,
- the multi-cycling approach proposed in this work might require rigorous testing using different materials to cement its validity,
- although experimental and simulated nanoindentation results are in good agreement the agreement may be enhanced if the material's stress-strain curve is known,
- the investigation of the long-term creep properties of the material and its temperature dependence will contribute further towards the understanding the material's behavior,
- the exact structure of the ion-beam synthesized nanostructured phase and the effects of annealing on the presence, sizes, and it's stability are still yet to be determined,
- the possibilities of engineering the wear properties by means of ion implantation appears an potential option.

In conclusion, although B_6O is touted as a possible candidate to rival polycrystalline cubic boron nitride in abrasive wear resistance applications, a diversified and fresh look at the material's potential is overdue. The material's true potential could lie in MEMS and related miniature systems where it's super-hardness, low density, chemical inertness, oxidation resistance, and superior wear resistance properties act in its advantage.

Part V

Appendices

Appendix A

Raman spectroscopy

Strictly speaking, the theory of Raman scattering is not elementary, since both group theory and perturbation theory in at least second order are required for a proper discussion of the phenomenon. This appendix is devoted to the description of the basic theory of Raman scattering. An overview description of the spectrometer, its attachments and how these instrument can be adapted to achieve the various techniques of Raman microscopy is also included.

The appendix gives the description of the spectrometer, its attachments and how these instrument can be adapted to achieve the various techniques of Raman microscopy.

A.1 Raman Scattering Process

A.1.1 Introduction

When monochromatic light impinges on a sample, some of the incident light is transmitted,some is absorbed and some of it is scattered by the material [3, 5, 8, 9]. Most of the scattered light has the same frequency as the incident light – Rayleigh scattered. However, the frequency of some of the scattered light photons will be different energies from the incident photons. This inelastic scattering of the light is called Raman scattering [3]. The Raman spectrum frequencies of a scattering sample (as illustrated in Figure A.1) are as a result of changes in vibrational, rotational, or electronic energy of that sample due to their inelastic interaction between the incident light and sample matter [10].

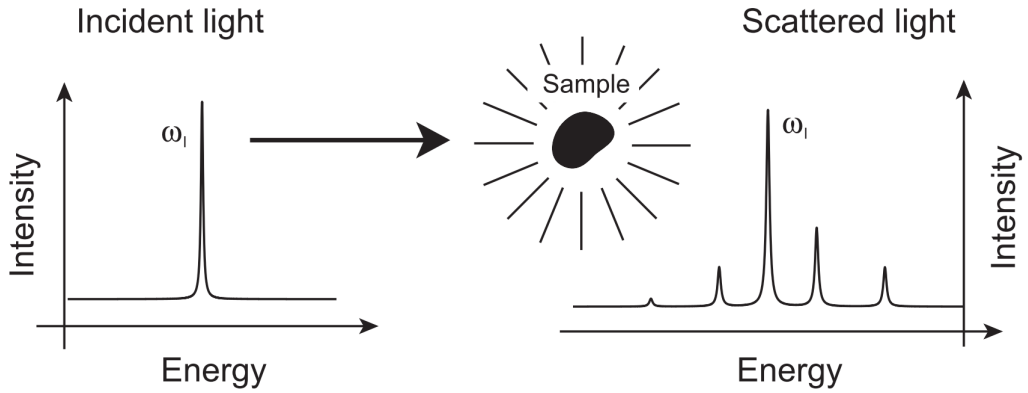

Figure A.1: *Schematic illustration of the Raman experiment. A monochromatic beam of light of frequency ω_i impinge on a sample and the spectrum of the scattered light is recorded.*

The frequency shift of the scattered photons from the incident photons is characteristic of excitations within the sample. This is a property which makes Raman spectroscopy a powerful, non destructive technique for identifying and characterizing materials.

Raman scattering can be interpreted in two ways: using the classical approach or the quantum mechanical approach.

A.1.2 Quantum mechanical Treatment of the Raman Effect

In the quantum mechanical approach, Raman scattering is considered as a two photon process [10]. The process is an example of inelastic photon scattering because of the energy transfer between the photons and the molecules during their interaction. These transitions are depicted graphically in energy level diagram (Jablonkski energy level diagram [4]) of Figure A.2.

According to Figure A.2, when an incident photon of radiation is absorbed by a molecule in a ground state, the system is 'excited' into a virtual state. The lifetime of the virtual state is typically 10^{14} s [7]. After which the molecule will return back to its ground state through the process of de-excitation which gives rise to the scattered photons. (a) If the energy of the scattered and incident photons are the same the mechanism of scattering is known as Rayleigh. (b) If the system was initially in its lowest level (usually the ground state) and the energy of the scattered photon is less than the energy of the incident photon, this corresponds to Stokes Raman scattering. (c) If the system was initially in an excited state, it can make a transition from the virtual state to a lower energy state than the initial one. Its energy will therefore be higher than that of the incident photon, corresponding to anti-Stokes Raman scattering [2, 4].

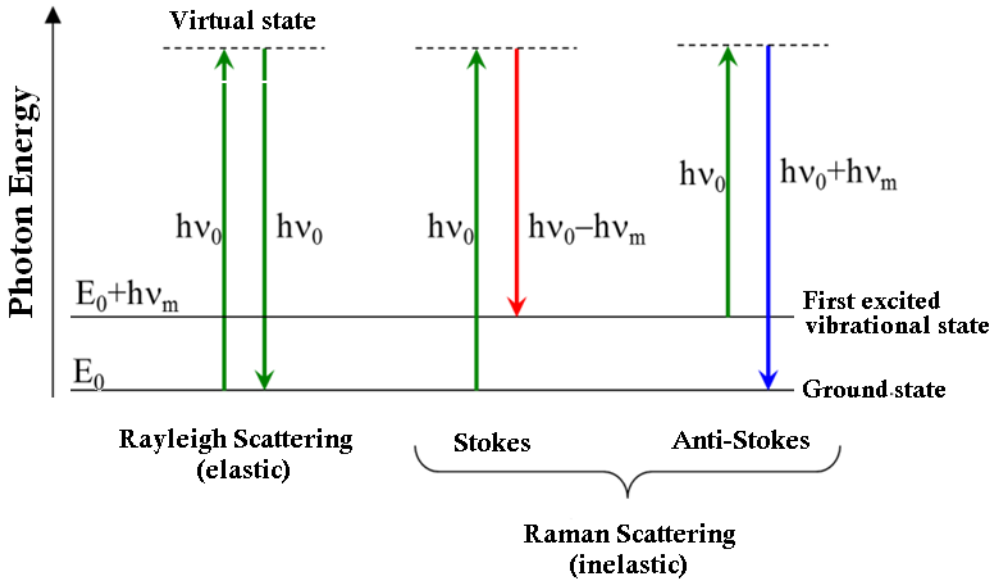

Figure A.2: *Energy level diagrams showing (a) Rayleigh scattering, (b) Stokes Raman scattering, and (c) anti-Stokes Raman scattering in an excited atom resulting in the emission of photons of different energies [7, 10].*

Energy and momentum are conserved in the Raman scattering process. If an incoming photon of frequency ω_i causes a phonon of frequency ω_{ph} to be created or absorbed in scattering a photon of frequency ω_s, then by conservation we have

$$\hbar\omega_i = \hbar\omega_s \pm \hbar\omega_{ph} \tag{A.1.1a}$$

$$q_i = q_s \pm q_{ph} \tag{A.1.1b}$$

where the ± represents a Stokes or anti-Stokes process and q_i, q_s and q_{ph} are the wave vectors of the incident photon, scattered photon and emitted or absorbed phonon, respectively. However, according to Boltzmann statistics, the anti-Stokes Raman scattering effect is less likely at room temperature since the initial excited state has a low occupancy of excited states [4]. Ultimately, in sharp contrast from Equation (A.1.1) Stokes Raman scattering involves the loss of energy from the incident light photons to the molecule is generally observed to give a stronger Raman signal than anti-Stokes scattering.

A.1.3 Classical Treatment of the Raman Effect

Classically, the Raman effect can be viewed as arising from the interaction of the incident electromagnetic radiation photons with the molecule's dipole moment. Both the oscillating electric and magnetic components of the electromagnetic radiation are capable of interacting with the molecule but the magnetic component has a negligible effect on the molecule's dipole moment [6].

The oscillating electric field of the electromagnetic radiation of frequency q_k can give rise and subjects the molecule to an external electric field $\vec{E}_{ext}$. The distortion of the electronic distribution around the molecule leads to an induced dipole moment $\vec{\mu}_{ind}$ around that molecule. This induced dipole moment depends mainly on the polarisability among other characteristics of the molecule.

The components[1] of $\vec{E}_{ext}$ are fixed in space and can be denoted $\vec{E}_j$. Hence the external electric field can be written as:-

$$\vec{E}_j = \vec{E}_j^o \cdot \cos(\vec{k}_{inc} \cdot \vec{r} - 2\pi\nu_{inc}t) \tag{A.1.2}$$

The effect of $\vec{E}_j$ onto the molecule polarisability $\vec{\mu}_{ind}$ (which we now denote $\vec{\mu}_i$) in space is governed by the ease of polarisation of the molecule or the polarisability $\tilde{\alpha}_{ij}(\omega_{inc})$. The polarisability is second rank tensor, the need for introducing a tensor in this case comes from the non−linear cause−effect relationship that is brought about by the anisotropy of the light irradiated molecule/matter. The induced dipole moment can be written as:-

$$\vec{\mu}_i = \alpha_{ij} \cdot \vec{E}_j \tag{A.1.3}$$

If the molecule that has been subjected to an oscillating electromagnetic radiation undergoes a normal vibration under the influence of the external electric field $\vec{E}_j$, the normal vibration will be characterized by the normal coordinate ξ_k and the normal frequency q_k of the normal mode. The normal coordinate can be represented as:-

$$\xi_k = \xi_k^o \cos(\vec{q}_k \cdot \vec{r} - 2\pi\nu_k t) \tag{A.1.4}$$

[1] The subscripts *i,j,k,l,...* run over the three *x, y* and *z* spatial directions.

At some point away from the molecular equilibrium geometry, the instantaneous polarisability is given by:-

$$\alpha_{ij}(\omega_{inc}, q_k) = \alpha^o_{ij}(\omega_{inc}) + \left(\frac{\partial \alpha_{ij}(\omega_{inc}, q_k)}{\partial \xi}\right) \cdot \xi + \text{(higher order terms)} \tag{A.1.5}$$

Substituting equations A.1.5, A.1.4 and A.1.2 into equation A.1.3 gives:-

$$\begin{aligned} \vec{\mu}_i = \Big[\tilde{\alpha}^o_{ij}(\omega_{inc}) + \left(\frac{\partial \tilde{\alpha}_{ij}(\omega_{inc}, q_k)}{\partial \xi}\right) \cdot \xi_k \\ + \text{(higher order terms)}\Big] \cdot \vec{E}^o_j \cos(\vec{k}_{inc} \cdot \vec{r} - 2\pi\nu_{inc} t) \end{aligned} \tag{A.1.6}$$

The second term in A.1.6 can be expanded to:-

$$\begin{aligned} \frac{\partial \tilde{\alpha}_{ij}(\omega_{inc}, q_k)}{\partial \xi} \cdot \frac{\xi^o_k \cdot \vec{E}^o_k}{2} \cdot \Big\{ \cos[(k_{inc} + q_k) \cdot (\vec{r} - \omega_{inc}\, t\,)] \\ + \cos[(k_{inc} - q_k)\vec{r} - (\omega_{inc} - \omega_k)\, t\,] \Big\} \end{aligned} \tag{A.1.7}$$

This term relates to the Raman scattering effect. It shows that the Raman scattering process is a two-photon process, having a net effect on the scattered incident photons by changing their frequencies as $k_{inc} \pm q_k$. This change in the frequency is characteristic of inelastic Stokes and anti-Stokes scattering and provides a basis for Raman spectroscopy, as well as other optical spectroscopies [1].

Of critical importance is the partial differential part of the term; $\frac{\partial \alpha_{ij}(\omega_{inc}, q_k)}{\partial \xi}$ that gives the change in the spatial variation of the polarisability of the light excited molecule. This term is often said to give the classical Raman effect **selection rule** that is if $\frac{\partial \alpha_{ij}(\omega_{inc}, q_k)}{\partial \xi} \neq 0$ then the inelastically scattered Raman modes are observed with intensities proportional to the square of this term in question, else this term is zero, then the molecule can not be polarized and the Raman effect can not be observed, in such a case the material is deemed Raman inactive.

The first term in equation A.1.5, $\alpha^o_{ij}(\omega_{inc})$ is only dependent on ω_{inc}. The term denotes the elastically scattering of the incident radiation. The '*higher order terms*' referred to in equation A.1.6 are as a result of the change in the polarisability arising from the non-linear anharmonic coupled molecular oscillations resulting in combinational frequencies. These manifest themselves on the Raman spectra as low intensity peaks.

A.2 Raman Instrumentation

The Raman scattering measurements done in this work were carried out using a Jobin-Yvon T64000 spectrometer at CSIR's National Centre for Nano-Structured Materials nanomaterial characterization facility. The schematic diagram of the spectrometer is shown in Figure A.3. The motivation being that the resolution of the microscope is of the same order as the implantation-affected surface thickness.

Inelastic scattering is a very weak process and the Raman scattered line is also close to the Rayleigh scattered signal which is several orders of magnitude (typically 10^7) stronger. A careful signal processing is therefore necessary if useful information is to be extracted from the scattered signal components.

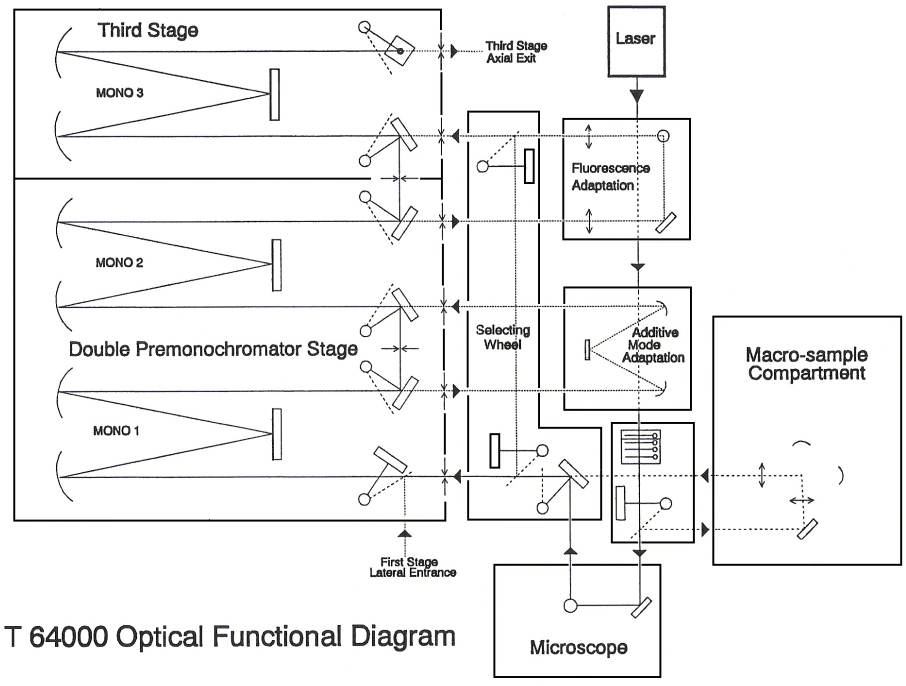

Figure A.3: *The schematic diagram of the Jobin-Yvon T64000 spectrometer used in this work (courtesy of HORIBA Jobin Yvon Ltd (UK)).*

In the Jobin-Yvon T64000 spectrometer used, the Raman excitation is performed with a coherent and intense argon ion (Ar^+) laser beam source. However, lasers are not perfectly monochromatic light sources, as they have a finite linewidth and contain a broadband component of spontaneous light radiation from the lasing material. A custom designed laser transmission filter is inserted into the incident beam path between the source and the sample to further narrow the incident beam linewidth. The filtered beam is focused

down to a small volume (to the order of 1 μm^3) on the sample through the objective of the microscope. The scattered light is collected by the same objective of a microscope. At this stage the Raman signal is swamped by stray light signals (noise), the Rayleigh signal and other fluorescent signals from the scattering material. A *holographic notch filter*, between the sample and the monochromators provide for the necessary rejection of the unwanted light components swamping up the relatively weak Raman signal before they can be detected and measured by the spectrometer. The holographic notch filter is also custom made to operate at 514.5 nm and have a narrow bandpass of down to $\sim$100 cm^{-1}.

The filtered light is directed to the monochromators, the principal components of the spectrometer; an apparatus designed to measure the distribution of a signal in a particular wavelength region. The monochromator separates a broadband signal into single spectral lines according to wavelengths. Monochromators are based on diffraction grating dispersive systems, MONO X in Figure A.3 shows the unit monochromator. However, a single monochromator does not discriminate efficiently to separate the Raman broadband signal. The Jobin-Yvon T64000 spectrometer is a triple monochromator dispersive system as shown in the schematic diagram of the instrument (Figure A.3). In the coupled configuration, a monochromator has the capability for measuring a Raman signal of very low intensity in a broadband vibration/rotation band with high resolution. However, the Jobin-Yvon T64000 spectrometer can be used in single spectrograph mode if the Raman line is not so close ($\sim$1000 cm^{-1}) to the Rayleigh line, without compromising the spectral resolution greatly.

An array of *CCD* detectors are integrated onto the third monochromator exit slit. These optoelectronic devices detect and convert output photons to a digital signal that can be presentation, manipulated and stored on to the interfaced computer.

A.3 Experimental Detail

The Raman experimental spectrometer system interfaced to a PC and thus is software controlled. The spectrometer can be operated either in a macro–Raman mode, where measurements are done in the macro–sample compartment, normally for very large or irregular sample specimen. The spectrometer can also be operated in the micro-Raman mode, where the measurements are done on the microscope stage. The laser light can be focused down to 1 μm on the sample surface and a spectra recorded. The spectrometer can also be operated in the 2-D mapping mode, where the computer controlled measurements are carried out on a motorized X-Y microscope stage. It is also possible to operate the spectrograph in a 3-D scanning mode, also known as Confocal microscopy, with the aid

of a piezo Z- stage scanner. For the experimental work covered in this thesis, the Raman spectrometer was used in the micro-Raman and 2-D mapping measuring operation modes.

All the Raman experiments in this work were carried out under ambient conditions. A 514.5 nm line of Ar^+ ion laser was used as excitation source, at a beam power of 200 mW, using a 20× objective (spot size ~1.5μm), along with a 1800 grooves/mm grating in the spectrometer and a nitrogen cooled CCD detector. In the first set of Raman measurements, virgin and implanted B_6O samples were characterized using micro-Raman operated in single spectrograph mode. The output spectra were measured by a nitrogen cooled CCD detector linked to a computer that displays, analyses and stores the data.

Bibliography

[1] D.W. Ball. Theory of Raman spectroscopy. *Spectroscopy*, 16:32 – 34, 2001.

[2] G. Eckhardt, D.P. Bortfeld, and M. Geller. Stimulated emission of stokes and anti-Stokes Raman lines from diamond, calcite and alpha-sulfur single crystals. *Applied Physics Letters*, 3:137, 1963.

[3] W. Hayes. Scattering of light by solids. *Contemporary Physics*, 16(1):69 – 91, 1975.

[4] A. Jablonski. Efficiency of anti-Stokes fluorescence in dyes. *Nature*, 131:839 – 840, 1933.

[5] D.A. Long. *Chapter 1: Survey of Light-scattering Phenomena*, pages 3 – 18. John Wiley & Sons, Ltd, 2002.

[6] D.A. Long. *Chapter 3: Classical Theory of Rayleigh and Raman Scattering*, pages 31 – 48. John Wiley & Sons, Ltd, 2002.

[7] D.A. Long. *Chapter 4: Quantum Mechanical Theory of Rayleigh and Raman Scattering*, pages 49 – 84. John Wiley & Sons, Ltd, 2002.

[8] D.A. Long. *Chapter 5: Vibrational Raman Scattering*, pages 85 – 152. John Wiley & Sons, Ltd, 2002.

[9] C.V. Raman and K.S. Krishnan. A new type of secondary radiation. *Nature*, 121:501, 1928.

[10] D.F. Walls. Quantum theory of the Raman effect. *Zeitschrift fur Physik A Hadrons and Nuclei*, 237:224 – 233, 1970.

Appendix B

Principles of Ion Implantation

B.1 Introduction

The surface-layers of a solid material play a participatory role in a variety of the material's interactions with its external environment for example in friction, wear, oxidation, fatigue, impact among others, therefore the industrial applications of most materials are largely dependent on their surface characteristics.

Ion implantation is a harsh and non-equilibrium technique of modifying the structural and physical and chemical characteristics of thin films and surface-layer properties of solid-state materials to depths of less than a micrometer. It is achieved by the bombardment of the solid material with high-energy charged particles. Most of the implants will come to rest within the surface-layer of the host material, creating many point defects in the stopping process. It is a direct consequence of the resultant interactions of the created defects that the changes the host material's properties. For example nitrogen ions implantation into a wide range of materials improves their surface hardness and wear resistance, ion beams have been successfully used to synthesize new metastable phases of remarkable properties that are otherwise unattainable by any other technique thermodynamically, dope semiconductor material, thin film synthesis among others.

Ion implantation has been used in a wide variety of fields both as a powerful research tool for investigating solid–state material processes and properties, and as a means of controllably modifying the electrical, physical, chemical, mechanical and optical properties of solid surfaces [21].

B.2 Ion Implanter

B.2.1 Introduction

The method of introducing ions into a solid material requires high voltage equipment that can electrostatically accelerate the ions and direct them onto the target material.

A typical direct beam ion implanter mainly comprises an ion source, a mass analyzing magnet, an acceleration tube, a beam manipulation system, and an end station section which accommodates the target sample. Figure B.1 shows the schematic diagram of such an implanter. All these systems can only operate under high vacuum conditions for the sustainable plasma generation, manipulation and transportation, most importantly beam confinement.

There are two main types of ion implanters; 1. the indirect beam ion implanters used for plasma source ion implantations were the target is placed inside the ion source itself. No ion beam is extracted and none needs to be manipulated or focused. High voltage negative pulses applied to the target attract positive ions in the plasma which naturally strike all parts of the target at normal incidence and 2. the direct beam ion implanters. The work reported herein was carried out on a iThemba LABS (Gauteng) modified 1977 *200−20A2F* model 200 keV Varian/Extrion direct beam ion implanter.

B.2.2 Principle of Operation

The basic function of a direct beam ion implanter is to generate a stream of electrostatically charged particles of a specific atomic weight, accelerate them and direct them to the target sample.

The ion implanter generates a plasma in the ion source. A stream of positively charged ions is then extracted by electrostatic means and subsequently accelerated towards the mass analyzing magnet which steers the ion beam through a 90° bend, 'implanting' opportunistic ions on to the inner wall liners of the magnet and focuses ions of the desired *m/q* ratio through the resolving aperture into the acceleration tube. The acceleration tube further boosts the acceleration of the ion beam to its desired energy. Then the beam passes through an array of electrostatic plates that focus, deflect and scan it, this ion beam manipulation helps maintain the beam focused and maintains a desirable beam radius, further eliminate residual neutral particles, secondary electrons and other opportunistic ions of the same *m/q*

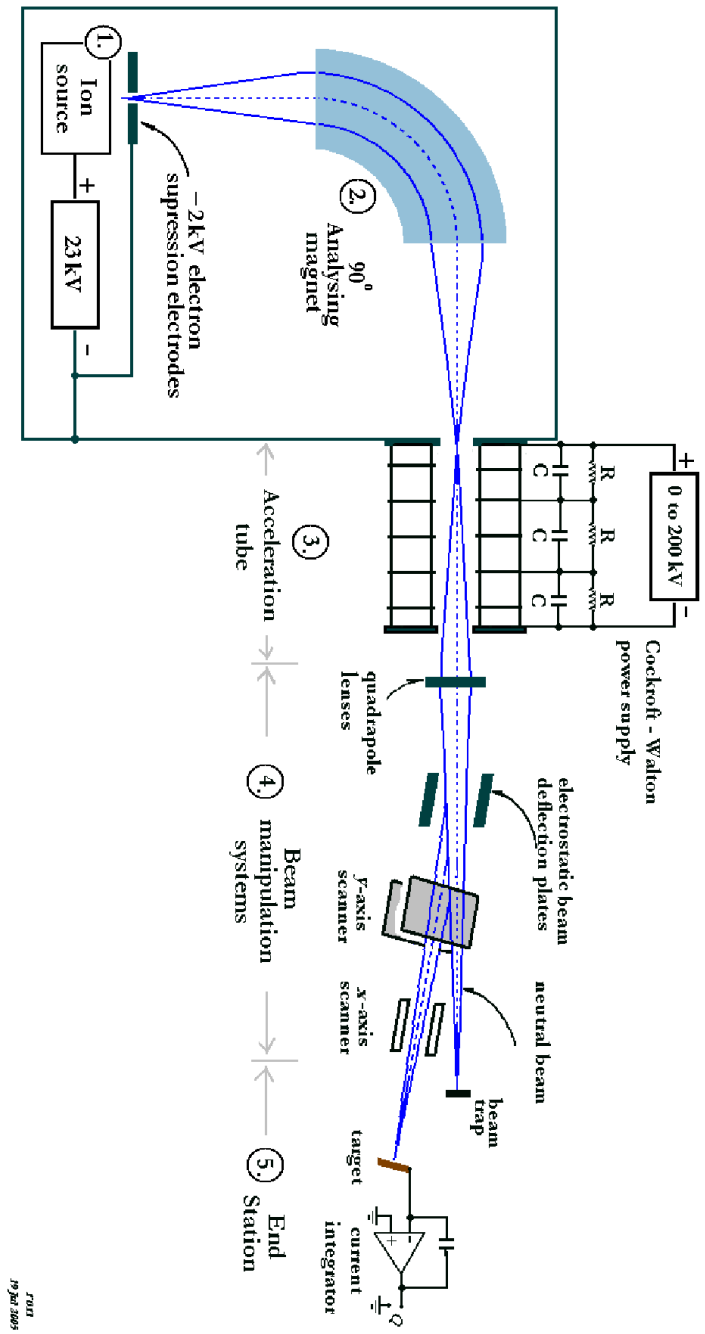

Figure B.1: *A schematic diagram of the ion implanter showing the major components and a sketch of the beam path [16, 20].*

ratio as the desired ion species, ensure uniform sample implantation and most of all direct the ion beam to the target sample in the end station [16].

Ion Source

The *200−20A2F* model ion implanter makes use of a Penning arc discharge ion source type. It comprises seven components namely; the gaseous ion source, vaporiser[1], a gas feed system, extraction electrodes, a cooling system, the vacuum system and a 23 kV driving power supply [20].

This source type makes use of energetic electrons thermionically generated from a heated tungsten filament for bombardment of the low pressure gaseous or vapour charge in the ion source chamber. The electron bombardment ionizes the charge thus creating a plasma in the ion source chamber. An axial magnetic field that is introduced by the walls of the ion source chamber, parallel to the anodic chamber tends to drive the electrons in a continual cyclic motion This circular motion reduces anodic sputtering as well as increases the ionization efficiency.

There is 23 kV voltage bias between the puller electrodes and the ion source chamber, so the ions are extracted with an energy of 23 keV. There also is a – 2 kV voltage bias on the electron suppression electrodes that prevents the primary ionizing electrons from leaving the ion source chamber as well as preventing the secondary electrons and negatively charged ions in the beam line from entering the ion source chamber. Effectively, the ions leaves the ion source with a total energy of 25 keV as the initial acceleration towards the mass analyzing magnet. The ion source is shown in Section 1 of the ion implanter in Figure B.1 [7, 16].

Mass Analyzing Magnet

For ion implantation only the pure ions are desired to implant the target material, these ions have to be separated from the 'impure' ions that are a by-product of ion production and collisions between the accelerated ions from the ion source and the inherent gas particles found in the beam line.

The ionization of the charge in the ion source chamber creates positively charged ions of many different kinds, depending on the complexity of the charge, for example, from BF_3 a common source gas, the mass spectrum of the beam shows that both the F^+ and B^+ ions are generated. Thus ionization can creates many different ion species. The vacuum systems of the ion source and the beam lines are not perfect so there are residual gas particles in the beam lines that have to be filtered out.

The process of separating the desired ions from the ion beam in the beamline is achieved by mass analyzing/selection. A mass analyzing magnet separates different ionic species

[1] for the generation of metal ions

according to their *m/q* ratio, by bending the moving ion beam into a curve and allowing only the desired ions to pass through a narrow resolving aperture.

The *200−20A2F* model ion implanter (and most low energy ion implanters) uses a 90° mass analyzing magnet to do the mass resolution of the stream of ions coming from the ion source and obtain a low impurity ions level in the desired ion beam. The ions of the desired *m/q* ratio of kinetic energy $qV = mv^2/2$ will follow a critical orbit of radius of curvature r and remain in the beamline to the acceleration tube (V is the accelerating potential value set on the implanter control console), the radius of a particular arc trajectory is determined by the strength of field, mass of ion, its speed and charge as shown in Equation (B.2.1), this equation follows from the Lorentz force law which states that the magnetic field B applies a force (Bqv) that must be equal to the centripetal force (mv^2/r) as the ions move in an arc through the magnetic sector. Ions of smaller *m/q* ratios will be steered into smaller orbits and those ions of larger *m/q* ratio will be deflected into larger arc trajectories. These will not pass the resolution aperture to the acceleration tube, instead they are 'implanted' into the liners that form the walls of the analyzer magnet [20], they also may result in the liners getting sputtered and this increasing the density of unwanted ions in the beamline [2].

$$r = \sqrt{\frac{m}{q} \cdot \frac{2V}{B^2}} \tag{B.2.1}$$

For such very low energies, in this case, 25 keV and less, the individual ions in the ion beams tend repel each other and cause the ion beams to diverge, the analyzing magnet in addition to the mass resolution, the analyzing magnet also acts as a confining lens to the desired beam on to the resolution aperture and thus focuses the ion beam on to the acceleration tube. The schematic diagram of an mass analyzing magnet is shown Section 2 of the schematic diagram of an ion implanter in Figure B.1.

Acceleration Tube

After separation, the ion enters the acceleration stage of the ion implanter system with an initial energy of ~25 keV. This stage can accelerates the ion beam to as high ion energies as between 30 keV to 200 keV where it has enough energy to accomplish the implantation effect, that is penetrating beneath the surface layer of the sample material. The acceleration tube can also be used to decelerate the ion beam and achieve as low ion energies in the order of 5 keV [20].

The *200−20A2F* acceleration tube is linear with annular anodes along its axis. Each anode has a negative potential that increases along the direction of propagation of the ion beam. The schematic diagram of an acceleration tube is shown Section 3 of the schematic

diagram of an ion implanter in Figure B.1. The voltages selected (on the ion implanter control console) are a function of the mass of the ion, the charge on the particles as well as the energy we desire to implant the ions with on the surface of the material. Since the positively charged ion is strongly attracted to a negatively charged region, the is drawn faster and faster towards ever higher negative potential terminals along the acceleration tube until it reaches the desired energy.

A high frequency Cockcroft-Walton power supply is used to maintain the high voltage terminal at the accelerating potential. The physical design of the components that make up the acceleration tube so as the high voltage terminal of the *200−20A2F* ion implanter all have rounded terminals and edges to combat the arching effect from the electric field concentration at sharp points [20].

Beam Manipulation Systems

These systems make use of electrostatic and magnetic fields to purify and direct the ion beam on to the desired target as well as ensuring uniform surface implantation of the target sample. This system is illustrated on Section 4 of the schematic diagram of the ion implanter in Figure B.1.

The beam must be kept in a tight focus to be useful. The **beam focusing system** is immediately after the acceleration tube, the focusing is achieved in the *200−20A2F* ion implanter by making use of the electrostatic lenses, by the application of transverse forces to maintain a small beam radius about the main beam axis (other implanters also use magnetic lenses). The ion beam loses its shape as a result of rapid expansions due to its space-charge[2] effect. This is because at low propagation ion energies, the ions are exposed to one another for much longer, resulting in massive mutual repulsions of the individual ions in the beam causing the beam of otherwise desired shape to diverge away from beam main axis. The 'secondary' charged particles created during beam resolution and transportation are also 'swept out' of the beam transport system by the fields with opposite polarities in the quadrupoles. Other positive charges are captured by the negatively biased electrodes, and the negative charges go to the positive electrodes [4].

In as much as the beam focusing system 'sweeps out' the secondary ions of negative polarities and electrons in the beamline the ion implanter has provision for a dedicated system of plates that serve the same purpose – **beam deflection plates**[3]. A plasma is generally created in the beamline when the positively charged beam interacts with residual neutral gas particles, producing ion-electron pairs by way of ionization collisions. The ion

[2] also known as the 'blow-up' effect

[3] the *200−20A2F* ion implanter has this system physically attached and performed by the *x*- beam scan plates

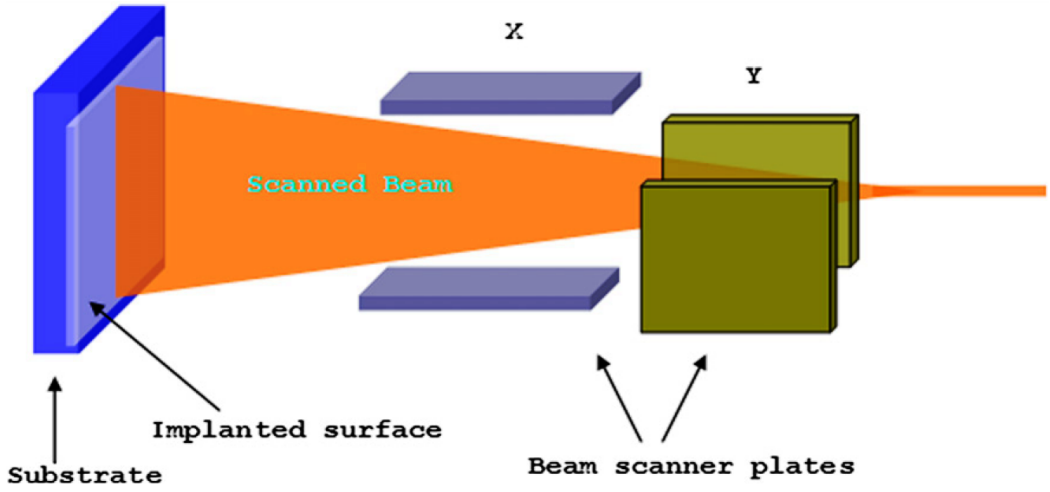

Figure B.2: *A schematic diagram of the ion beam scanner system plates*

beam is partially neutralized, this is termed the neutralization effect. These neutrals as well as other unwanted particles residual in the beam line being accelerated towards the target sample are 'swept out' by way of bending the ion beam with electrostatic plates. These neutral particles cannot be detected by an implanter's dose measurement system, so they must be eliminated to prevent dose errors and implantation of unwanted species. By so doing, the neutrals continue propagating in an undeflected path to the beam trap as shown in Section 4 in Figure B.1. In addition to eliminating unwanted particle species, the beam deflection system also allow for the precise alignment of the ion beam at the target sample surface.

At this stage we have an ion beam of almost the desired ion species only, but the progressive beam manipulation impacts on the shape of the beam. There are two sets of raster **Beam scanning** electrostatic plates which are at controlled x- and y- potentials [6]. As the beam passes between the plates the positive and negative charges are altered to steer the positively charged beam, the steering the beam is in two directions, the $200-20A2F$ ion implanter system, the beam is shaped into a $2-4$cm wide stripe, which is then scanned across the sample, back and forth, much like a can of deodorant spray. The beam has to be raster scanned over the entire sample surface. The ion beam must be uniform upon incidence at the target sample surface to ensure a uniform distribution of the ions over the target. The x- scanner plates in the $200-20A2F$ ion implanter are made in such as way that they also serves as the beam deflection system remotely operated by an electromechanical shutter system on the operator console. The schematic diagram of the beam scanning plates is shown in Figures B.1 and B.2.

End Station

The target is mounted in the target chamber, this is were the ion beam is directed to and where the ion implantation takes place. High dose ion implantations often cause a considerable phonon generation as a result of the nuclear stopping mechanism leading to a considerable temperature rise in the target sample and therefore requires an active cooling mechanisms. The active temperature control system makes use of a heater and liquid nitrogen to maintain the sample at a particular value. The end station also measures the implant dose and minimizes dose errors. To do this it makes use of faraday cups.

If one ion strikes the surfaces of the faraday cup, it ionizes several secondary electrons temporarily from the surface. The temporary emission of the electrons induces current flow from the ground and provides a small current amplification of the signal whenever an ion strikes the cup. A current integrator sums up the total current, from this an implantation dose can be calculated.

The design of the modern faraday cups is that it has four corner cups and the main cup in the centre, all designed an with a -500 V bias electron suppression voltage at the mouth of each. As a result, an electrostatic field is set up in such a way that it prevents slow moving secondary electrons from entering or leaving the faraday cup entrance but they do not inhibit the passage of high energy ion beams. The corner faraday cups measure the current reaching them and the values are compared to ensure uniform dosage in the area of the centre cup, the current signal from the centre cup is integrated over the entire duration of the implantation to get the desired dose.

It is apparent from the description of the operation of the ion implanter that the **vacuum systems** are critical in sustaining plasma in the ion source, the beam transport in the entire beamline as well as dose monitoring.

B.3 The Physics of Ion Implantation

B.3.1 Introduction

The previous section focused on the generation, acceleration, transport and manipulation of ions towards a target material as well as the dose control at the end station terminal. This section focuses on the propagation and subsequent stopping processes of the energetic ions in the target material – ion implantation.

The passage of an energetic ion moving in matter is characterized by an interplay of several scattering processes involving the Coulomb interactions of the projectile ions with the solid target's nuclei and electrons cloud. These interaction mechanisms involve the transfer of momentum or energy, in some cases the transfer of charges between the interacting parties. The predominance and contribution of each of the several interaction processes is reflected by its respective interaction cross-section.

B.3.2 Ion Stopping in Matter

When an ion is implanted into a target material, it rapidly decelerates, transferring its momentum to the target material's atoms and electrons, The ion will eventually come to rest at some depth below the surface [12]. This energy which is lost in a succession of Coulomb interactions between the projectile ion and the material in which it traverses is deposited to the atoms that make up the target material. These energy loss mechanisms have traditionally been separated into two distinct processes based on their characteristics and the energy regimes in which they are predominant; at high propagation velocities the *electronic energy loss mechanism* dominates the ion stopping, its also known as electronic stopping or inelastic energy loss. At low propagation velocities the *nuclear energy mechanisms* dominates, its also known as nuclear stopping or the elastic energy loss mechanism [1, 3, 10–12, 18].

The other processes that are known to take place include the generation of phonons – leading to the local heating of the target material, charge exchange (between the projectile and the target nuclei), the sputtering and degradation of the target surface atoms, nuclear reactions, the emission of high energy radiation (bremsstrahlung and Cherenkov[3] radiation) and the emission of other secondary particles such as Auger electrons [1]. These processes are characterized by very low scattering cross – section as compared to nuclear and electronic interactions and are hence deemed negligible hereinafter.

The nuclear and electronic stopping criteria are normally quantified by their respective 'stopping powers', theoretical quantities given as the energy lost by an ion dE as it traversed a distance dx in matter. The arithmetic sum of the two stopping powers is called the total stopping power, S_t as in Equation (B.3.1) [3, 17]:

$$S_t = -\left[\left(\frac{dE}{dx}\right)_n + \left(\frac{dE}{dx}\right)_e\right] \tag{B.3.1}$$

[3]Is the radiation emitted by a charge moving faster than the local speed of light c/η moving past a target atom in a medium, η is the refractive index of the medium. Sometimes spelt as Cerenkov. This effect reduces to bremsstrahlung if its speed is less than that of the local speed of light

The Equation (B.3.2) shows how the interaction the total interaction cross-section σ_t relates to the total stopping power of the material as well as the number of scattering centres in the target materials, N.

$$\sigma_t = -N\left[\left(\frac{dE}{dx}\right)_n + \left(\frac{dE}{dx}\right)_e\right] \tag{B.3.2}$$

This parameter is relevant only for computational purposes, in practice, the implant final penetration depth as well as the amount of lattice damage created as a result of the ion stopping in matter are of critical importance [3].

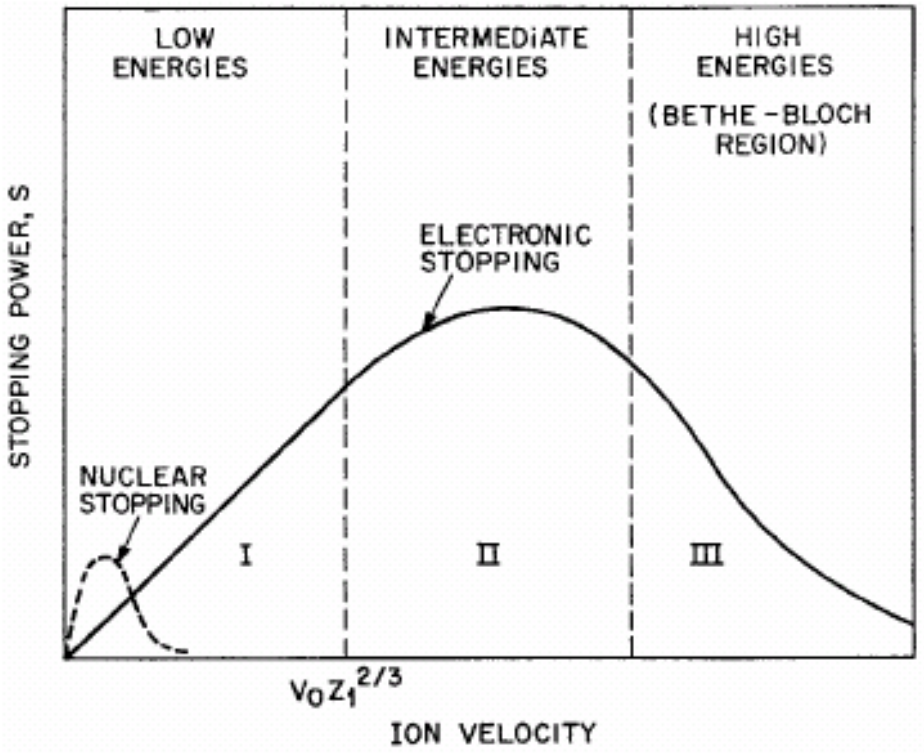

Figure B.3: *Nuclear and electronic components of the ion stopping power as a function of ion velocity.*

Electronic Energy Loss Mechanism

Electronic stopping is normally dominant in the beginning of the incident ion's path in the implanted material, that is when the ion velocity is relatively high [12, 18] as illustrated in Figure B.3.

The electronic stopping arises from the inelastic interaction collision interactions between the projectile ion (and its electrons) and the electrons of the target atoms. These interactions normally result in the excitations and at times ionization of the target atom [10]. The

slowing down can also be attributed to the viscous drag the projectile nucleus experiences when it interacts with the target atoms' cloud of electrons as a result of the electrostatic attractions of charges of opposite polarities [12]. Hence electronic stopping is also known as the inelastic energy loss mechanism.

At such high energies, and also taking into consideration the nature of the interactions, the cross-section of any displacement is low, hence the passage of the ion at such energies is characterized by slight trajectory deflections, behaving like its 'ripping through' the cloud of electrons [19]. Equation (B.3.3) [19] and the Figure B.3 shows the variation and interplay of the electronic and nuclear stopping power with energy and velocity respectively.

$$S_e \propto -E^{0.5} \tag{B.3.3}$$

In as much as the electronic energy stopping increases with projectile velocity, the electronic stopping reaches a maximum at projectile velocities comparable to the Bohr velocities of the valency electrons of the target atoms. At relativistically high projectile velocities, in the Bethe-Bloch formalism, in this region, the electronic stopping decreases as the projectile is stripped of all its valence electrons, becomes smaller and virtually sees neither the target nuclei nor its sea of electrons [3, 10, 21] this is illustrated in the Figure B.3.

Nuclear Energy Loss Mechanism

At the projectile ion's end-of-range, when the ion has slowed down significantly, the electronic stopping process cross-section becomes insignificantly small and the duration at which the projectile nuclei spends in the vicinity of each target nuclei also becomes sizable, as a result, the cross-section of the binary nuclear collisions will become large and will start dominating the ion stopping process [19].

The binary ion-nucleus interaction is basically a simple Coulomb potential interaction between two screened nuclei, that is vigorous and ballistic in nature given the nuclear stopping powers' inverse square dependance in energy [3], as shown in Equation (B.3.4) and Figure B.3.

$$S_n \propto -E^{-2} \tag{B.3.4}$$

These nuclear interactions involve large amounts of energies far much greater than the lattice atom's displacement energy E_d. The lattice atom is therefore dislodged off its lattice site creating a Frenkel pair, if the recoil energy of the newly created recoil/interstitial is larger than E_d, each of the recoils is capable of further dislodging other target atoms from their lattice sites, these secondary knock-on collisions develop into an avalanche of Frenkel pair production known as *collision cascades* [12–14, 18].

Range and Range Distribution of Implants

The ion losses its energy in a series of random discrete collisions and subsequent ion deflection. Hence the energy loss process itself is a stochastic process. It therefore follows that the energy loss per collision, the total path length of penetration and the final density distribution of the implanted ions in matter also have a random variation from ion to ion.

In theory, the final distribution of implants $n(x)$, irrespective of the species are statistically distributed as a function of the depth x, it is defined by statistical parameters and is approximately a Gaussian distribution [3, 11, 21]. The parameters used to define this distribution are the mean projected range R_p, the average deviation from the mean projected range $\triangle R_p$, and the number of ions per unit area ϕ. The implant density as a function of depth is given by Equation (B.3.5) below.

$$n(x) = \frac{\phi}{\triangle R_p \sqrt{2\pi}} \cdot exp - \frac{(x - R_p)^2}{2 \cdot \triangle R_p^2} \tag{B.3.5}$$

The statistical parameters in Equation (B.3.5) are illustrated schematically in Figure B.4.

B.3.3 Radiation Damage

After a series of inelastic electronic collisions and a few elastic knock-on collisions during the high energy regime of the ion trajectory, the projectile's momentum drops drastically. As the ion traverses in this low energy regime the nuclear stopping power which has an inverse square relationship with the ion energy becomes the dominant stopping mechanism as illustrated in Equation (B.3.4) [3, 10].

This is because at low energies the projectile spends too much time in the vicinity of the target nuclei hence the cross-section of ballistic nuclear collisions becomes greater, the disruption of the preexisting lattice atomic arrangement as a result of the ion bombardment is what is known as *radiation damage*.

The projectile ion embarks on vigorous displacement collisions with the target nuclei and if the energy is greater than the displacement energy of that material, E_d (which is the energy required to create a Frenkel pair that has a separation greater than the recombination radius that inhibits spontaneous recombination) then the target atom is dislodged from its lattice position leaving a vacancy site [5, 22]. The recoil atom, in turn if it has recoil energy greater than E_d will further cause the creation of Frenkel pairs. The result is a cascade of displacements in a very short time duration. This is known as a collision cascade and is characterized by a very large number of Frenkel pair defects in a very small volume space

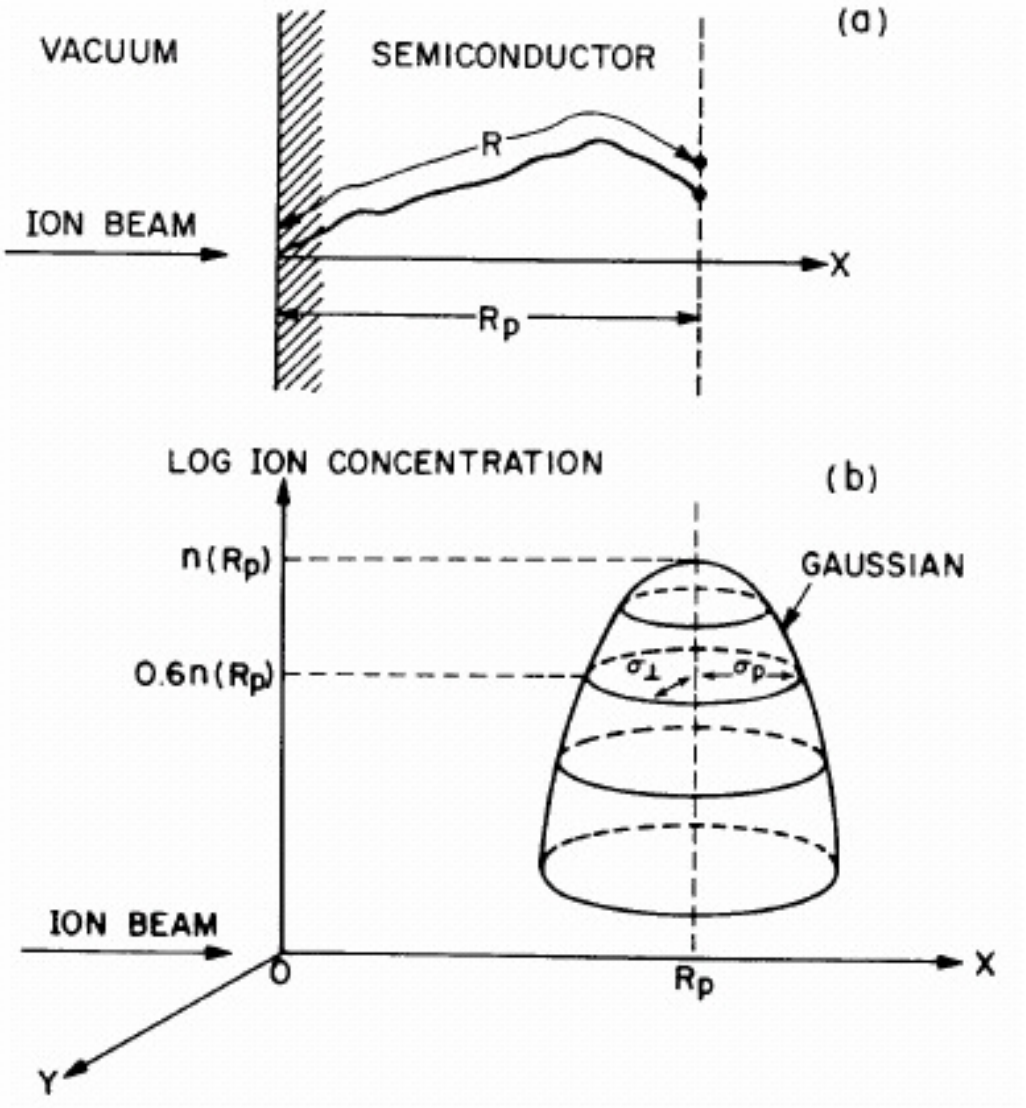

Figure B.4: *The three dimensional distribution (depth and lateral) of the implant concentration with respect to the depth of the implanted material after [11].*

surrounding the ion track, this phenomenon is known as a *displacement spike* [12, 18]. The displacement spike is an amorphous state.

However, if the ion or recoil energy drops below E_d, then the projectile is no longer capable of ejecting the target nuclei from their stable lattice positions, instead , they lose their energy through 'hard' collisions that induce large amplitude vibrations without leaving their lattice sited (which are essentially potential wells). The collision-induced vibration energy is shared by the neighbouring nuclei and appears as a source of heat. This region normally develops into a plasma-like structure, this structure develops rapidly ($\sim 10^{-12}$) s and is known as a *thermal spike*. This is the reason for sample heating during ion

implantation [11]. Thermal spikes occur at the centre of a displacement spikes, this region is also characterized by very high compressive stresses and high thermal energy [5].

Agglomerations of vacancies results in voids these may form when a solid sample is implanted with a gaseous ionic species that do not dissolve in the solid sample or solid samples that dissociates to form gaseous atoms that agglomerate to form gas molecules then subsequently a fine distribution of bubbles in the sample, a good example is the N^+ implantation into GaN whilst agglomerations of interstitials result in dislocation loops [8, 9, 15].

The primary defects of the same sign (that is either interstitials and vacancies) do further interact during and after the ion implantation to form extended defects (disordered regions which extends over a large region of a solid, will occur in the form of dislocation loops, grain boundaries, impurity clusters/agglomerations and crystalline/amorphous inclusions) by either diffusion/migration to other sites or annihilation by recombining with one another at defect recombination sites such as the surface or grain boundaries or other crystallographic extended defects that might act as defect sinks. The defects may also interact by clustering to form extended defects in order to reduce the strain energy as well as the free energy of the system. The interactions are largely governed by the temperatures at which the implantation is done or at which the sample is annealed as well as the respective defect migration energies of the respective defect [1, 9, 18].

Generally at very low temperatures all the primary defects are immobile, at slightly higher temperatures the interstitials become mobile whilst the vacancies remain immobile then at higher temperatures all the primary defects are mobile. The general rule is that the mobility of the interstitials is larger than that of the vacancies. However if the individual primary defects cluster and form secondary defect agglomerations or dislocation loops they become immobile and very stable even at high temperatures. However at very high temperatures the agglomerates dissociates and ‘emits’ the point defects. Annealing makes use of this characteristic of irradiated materials in order to recover from the radiation damage [18].

The overall resultant damage damage is determined by the ion implantation conditions and the properties of the target material as well as the massiveness (with respect to the target nuclei) and swiftness of the projectile ion. [12]

Bibliography

[1] F. Banhart. Irradiation effects in carbon nanostructure. *Reports on Progress in Physics*, 62:1181 – 1221, 1999.

[2] Case Technology Inc. www.casetechnology.com. webpage, November 2010.

[3] M.S. Dresselhaus and R. Kalish. *Ion Implantation in Diamond Graphite and Related Materials*. Springer Series in Material Science 22. Springer - Verlag, 1992.

[4] S.K. Guharay, M. Nishiura, M. Sasao, M. Hamabe, M. Wada, and T. Kuroda. Focusing of He^+ beams using a compact electrostatic quadrapole lens system. *Nuclear Instruments and Methods in Physics Research Section A*, 496:239 – 247, 2003.

[5] J. Gyulai. *Handbook of Ion Implantation*, chapter Chapter 2: Radiation Damage and Annealing in Ion Implantation, pages 69 – 118. North Holland, 1992.

[6] P.L.F. Hemment, J.E. Mynard, E. Pasztor, C.J. Raymond, and K.G. Stephens. Part 1: A new research implanter at the University of Surrey. In *Ion Implantation: Equipment and Technology*, pages 37 – 44. Springer - Verlag, 1982.

[7] J.K. Hirvonen, C.A. Carosella, and G.K. Hubler. Production of high-current metal beams. *Nuclear Instruments and Methods in Physics Research*, 189:103 – 106, 1981.

[8] S.O. Kucheyev. *Ion-Beam Processes in Group III-Nitride*. Phd thesis, Australian National University, Reasearch School of Physical Sciences and Engineering, 2002.

[9] S.O. Kucheyev, J.S. Williams, and S.J. Pearton. Ion implantation into GaN. *Materials Science and Engineering: R*, 33:51 – 107, 2001.

[10] J.W. Mayer, L. Eriksson, and J.A. Davies. *Ion Implantation in Semiconductors*. Academic Press Inc., New York, 1970.

[11] M. Nastasi, J. Mayer, and J.K. Hirvonen. *Ion-Solid Interactions: Fundamentals and Applications*. Cambridge University Press, 1996.

[12] J.F. Prins. Ion-implanted structures and doped layers in diamond. *Materials Science Reports*, 7:271 – 364, 1992.

[13] J.F. Prins. *Properties of natural and synthetic diamond*, chapter Chapter 8:Modification, doping and devices in implanted diamond, pages 301 – 341. Academic Press Limited, 1992.

[14] J.F. Prins. Ion implantation of diamond for electronic applications. *Semiconductor Science and Technology*, 18:S27 – S33, 2003.

[15] C. Ronning, E.P. Carlson, and R.F. Davis. II into GaN. *Physics Reports*, 351:349, 2001.

[16] P.H. Rose. A history of commercial implantation. *Nuclear Instruments and Methods in Physics Research Section B*, 6:1 – 8, 1985.

[17] P. Sigmund. Stopping powers in perspective. *Nuclear Instruments and Methods in Physics Research Section B*, 135:1 – 15, 1998.

[18] R.A. Spits. Dynamical behaviour of implanted ions in diamond. MSc Dissertation, University of the Witwatersrand, Physics Department, 1990.

[19] P.D. Townsend, J.C. Kelly, and N.E.W. Hartley. *Ion Implantation Sputtering and their Applications*. Academic Press Inc., 1976.

[20] Varian/Extrion. *Production ion implanter model 200-20A2F instruction manual*. Varian Extrion Division, Gloucester UK, 1977.

[21] J.S. Williams. Materials modification with ion beams. *Reports on Progress in Physics*, 9:491 – 587, 1986.

[22] J.F. Ziegler. *Handbook of Ion Implantation*, chapter Chapter 1: Ion Implantation Physics, pages 1 – 68. North Holland, 1992.

Appendix C

Published Articles

Research Article Adv. Mat. Lett. 2011, **2**(1), 58-64 ADVANCED MATERIALS Letters

www.vbripress.com, www.amlett.com, DOI: 10.5185/amlett.2010.9167 Published online by the VBRI press in 2011

Raman spectra of hot-pressed boron suboxide

Ronald Machaka[1,2]*, Bonex W. Mwakikunga[3,4], Elayaperumal Manikandan[5], Trevor E. Derry[1,6], Iakovos Sigalas[1,2]

[1]*DST/NRF Centre of Excellence in Strong Materials, University of the Witwatersrand, Private Bag 3, Wits, Johannesburg 2050, South Africa*

[2]*School of Chemical and Metallurgical Engineering, University of the Witwatersrand, Private Bag 3, Wits, Johannesburg 2050, South Africa*

[3]*CSIR National Laser Centre, P.O. Box 395, Pretoria 0001, South Africa*

[4]*Department of Physics and Biochemical Sciences University of Malawi, The Polytechnic Private Bag 303, Chichiri, Blantyre 0003 Malawi*

[5]*CSIR National Centre for Nano-Structured Materials, P.O. Box 395, Pretoria 0001, South Africa*

[6]*School of Physics, University of the Witwatersrand, Private Bag 3, Wits, Johannesburg 2050, South Africa*

*Corresponding author. Tel: (+27) 11-717-7534; Fax: (+27) 11-717-6879; E-mail: ronald.machaka@wits.ac.za

Received: 24 Sept 2010, Revised: 8 Nov 2010 and Accepted: 15 Nov 2010

ABSTRACT

Despite hot pressing being the most popular method of consolidating B_6O powder, the Raman spectrum of polycrystalline hot-pressed B_6O was until now poorly understood. Yet, recent reports have contributed to the understanding of only high-pressure and high-temperature sintered B_6O. Using an automated method for subtraction of the fluorescence background from Raman measurements, the first- and second-order Raman spectra of B_6O and their dependence on the wavelength of the excitation line from a green Argon ion (Ar^+) laser are reported. Our results confirm the existence of observable highly resolved first- and second-order Raman modes measured at ambient conditions using a green Ar^+ ion laser as the source of excitation. We also extend our study to present a comparative analysis of our recovered first-order Raman spectra and previously reported first-order Raman spectra other α-rhombohedral boron type based ultra-hard boron-rich ceramic materials. The results show an overall good agreement.

Keywords: Hot-pressed boron suboxide; B_6O; Raman spectroscopy; fluorescence background subtraction.

Ronald Machaka is a Ph.D candidate at the University of the Witwatersrand, in the School of Chemical and Metallurgical Engineering. Ronald obtained his M.Sc. by Research in Material Science Physics with merit from the University of the Witwatersrand. Ronald also holds a B.Sc. (Hons) in Applied Physics from the National University of Science and Technology, Zimbabwe. Ronald is affiliated to the DST/NRF Centre of Excellence in Strong Materials, Powder Metallurgy Association (SA), and the South African Institute of Physics. Current interests include boron-rich superhard ceramic composites, ion beam modifications, finite element modelling, Ni-base superalloys, and foot-bridges.

Bonex Wakufwa Mwakikunga is a Senior Lecturer in the Department of Physics and Biochemical Sciences at the Polytechnic of the University of Malawi. He obtained his PhD from the University of the Witwatersrand in 2009. He has taught and done research in environmental radioactivity and solid state physics. His interests in materials science led him to win many scholarships and awards, including the Joint Japan/World Bank Graduate Scholarship Programme, enabling him to conduct research both at the University of the Witwatersrand and the Council for Scientific and Industrial Research (CSIR). At the CSIR he has worked in the National Centre for Nano-Structured Materials (NCNSM) and the National Laser Centre (NLC) where he is currently carrying out research on smart materials.

E. Manikandan is working as Senior Research Scientist at National Centre for Nano Structured Materials (NCNSM), Council for Scientific & Industrial Research (CSIR), Pretoria, SA. He is actively involved with the synthesis, characterization and functionalization of advanced industrials materials (AIM) for a variety of applications. He has keen interest on in-situ/online measurements (such as GIXRD, Raman Spectroscopy, FIB-Electron Microscopy) during (i) ion implantation, (ii) PLD growth of nanoparticles SW/MW-CNTs, oxide semiconductor multi-layer, metal/Si and metal/metal systems. Moreover, He has recently established

LIPS/LIBS technique (laser induced plasma/breakdown spectroscopy) for laser synthesis of single-wall CNTs and their growth mechanism.

akovos Sigalas is currently Element Six Professor of Ceramic Science at the University of the Witwatersrand. He is also Focus Area Coordinator (Ceramics Focus Area) in the DST/NRF Centre of Excellence in Strong Materials. He holds a PhD in experimental solid-state physics from the University of Manchester, U.K, a Diploma in Advanced Studies in Science also from the University of Manchester, U.K. and a BSc Physics (Honours) from Athens University, Greece. Prior to joining the University of the Witwatersrand, Prof Sigalas worked as lecturer at various Greek Universities (1975-1980), at CSIR, RSA (1980) and then at Element Six Pty Ltd as research manager (1991). He has 54 publications in international refereed journals, 25 patents, over 60 technical reports, and contributed to two books. His research interests include hard ceramic materials, suitable for cutting tool and wear part applications, nanostructured ceramics, and ceramics reinforced titanium metal.

Introduction

Boron has the second most complicated structural chemistry among all elements at ambient conditions after carbon. This is evident from the extremely large number of simple and complex compounds and structures that it can form and their wealth of interesting physical and chemical properties [**1**]. Among other fascinating compounds it can form is boron suboxide – B_6O, a boron-rich super-hard ceramic material characterised by an α-rhombohedral boron type structure (space group $R\bar{3}m$) [**1–5**] which is similar to those of boron carbide – B_4C [**6, 7**], aluminium magnesium boride – $AlMgB_{14}$ [**8**], and the newly synthesized boron subnitride – $B_{13}N_2$ [**9, 10**].

With hardness values reported between 24 GPa and 45 GPa [**7, 11, 12**], B_6O is sometimes considered to be the third hardest material only after diamond (~ 100 GPa) and cubic boron nitride (~ 60 GPa) [**4, 13, 14**]. In addition to the super-high hardness and low density, the ceramic material exhibits a rather unusual and wide range of superior properties that includes high mechanical strength, high chemical inertness, thermal stability, a high melting point, and good wear resistance [**4, 15**]. Furthermore, B_6O can be synthesized without the need for high pressures [**4; 16**] (hot-pressing is also an example, see [**4, 14, 17**]) unlike diamond or cubic boron nitride [**15, 18**]. This significantly augments to the commercial attractiveness of B_6O-based composites as potentially attractive candidates for high-wear applications where both abrasive resistance and thermal stability are required [**15, 18, 19**].

Raman spectroscopy is a valuable non-destructive technique universally used to characterize materials. A Raman spectrum often serves as a material fingerprint, with each peak in the spectrum corresponding to a unique vibrational mode of the lattice. In most typical laboratories, the green Argon ion (Ar^+) laser beam is the commonly used Raman excitation sources 514.5 nm.

Recently, Solozhenko *et al.* [**20**] reported that the first- and second-order Raman spectra of HPHT B_6O powders become observable when UV or IR wavelengths excitation beams are used. However, uniaxial hot pressing is the most cost-effective method of consolidating ceramic powders to full density ceramic compacts with controlled microstructures in a typical laboratory [**18, 19**]. A literature survey of the Raman response of polycrystalline hot-pressed B_6O shows very little has previously been reported on the characterization to understand the Raman spectrum of hot-pressed B_6O [**21**]; partly because B_6O is characterized by a relatively weak Raman signal and a strong inherent fluorescence background. In fact, some of the previously reported spectra are far from observable [**20**]. As a result, an understanding of the Raman spectra of uniaxially hot-pressed B_6O is a limited if not poor, especially when a green Ar^+ laser excitation source is used.

In this work, we attempt to investigate the local vibrational modes of hot-pressed B_6O using Raman spectroscopy using a green Ar^+ laser excitation source. We present a systematic investigation of this problem by means of deliberately (a.) using low-power excitation beams to minimize the heating and fluorescence effects on the sample surface, (b.) reducing the exposure duration, and (c.) the application of a suitable background subtraction on the measured Raman spectra. We report on the existence of observable first- and second-order Raman spectra of hot-pressed B_6O measured at ambient conditions using the green Ar^+ ion laser as the source of excitation.

We also extend the comparative study of the first-order Raman spectra of hot-pressed B_6O presented here to the other similar boron-rich based materials (α-rhombohedral boron, B_4C, and $B_{13}N_2$ to previously reported findings on this topic notably by Werheit and Filipov [**22**]) and Solozhenko *et al.* [**9; 10**] who all excluded hot-pressed B_6O in their comparison. The observed B_6O Raman-active modes are in close agreement with those theoretically calculated for boron-rich icosahedral compounds and strikingly similar to the other icosahedral boron-rich ultra-hard materials [**10**].

Experimental

Materials and Methods

Pure B_6O powder was prepared using a method described by Andrews *et al.* [**11, 14**] and Shabalala *et al.* [**19**]. The powders were uniaxially hot-pressed in hBN pots in argon gas environment at a temperature of 1800°C and a pressure of 50 MPa for 20 minutes. Hot-pressed samples were approximately 20 mm in diameter and 2 mm in thickness. The hot-pressed samples were sectioned to desired dimensions, mounted on Bakelite medium and then metallographically prepared to a 0.05 µm OPS finish for characterization by means of a unique combination of grinding and polishing.

The polished B_6O samples were analysed for phase composition using X-ray diffraction, with λ = 1.547 Å Cu K_α radiation. The powder diffraction patterns were collected using the Bragg-Brentano geometry over a 10° – 90° 2θ range in steps on 0.02° at a sampling time of

approximately 7 s per step and analysed. The voltage on the anode of the X-ray tube was 45 kV, and the current was 40 mA. The specimen's surface microstructure and composition were characterized by scanning electron microscopy (SEM) and energy-dispersive X-ray spectroscopy (EDX), respectively. A Philips XL30 environmental scanning electron microscope operating at 25 keV in backscattered secondary electron geometry was employed.

The micro-Raman spectroscopy measurements were performed in the back-scattering configuration at room temperature using a green 514.5 nm Ar^+ ion laser as the excitation source. An 1800 grooves/mm grating in the single spectrograph mode of a Jobin-Yvon T64000 Raman spectrometer was used. The measurements were performed using a 20 × Olympus objective and a ~ 1µm spot size diameter. The spectrum acquisition and pre-processing was done using the Horiba Jobin-Yvon LabSpec® 3.0 software package. An appropriate automated fluorescence suppression and background subtraction method was applied on the Raman scattering measurements. The scheme uses a series of linear extrapolations between adjacent minima within the spectrum. The laser power was deliberately kept low during all measurements to minimize the background fluorescence and possible temperature variation effects on the sample surface.

Results and discussion

Surface and compositional analysis

The surface morphology and compositional analysis of hot-pressed B_6O specimen as determined by SEM and EDX are shown in **Fig. 1**(**a**) and (**b**), respectively.

In general, the micrograph shows a homogeneous B_6O microstructure with visible pores on the specimen surface as a direct result of some considerable practical challenges in the densification of B_6O by hot pressing [**7, 17, 23**]. The analysis of the surface composition by EDX is also indicative of nominally pure B_6O phase. The observed iron contamination (< 1 wt. %) is expected and inevitable; it originates from abrasion of the steel ball and the containment cell during powder ball milling.

X-ray diffraction measurements

Fig. 2 shows the full profile X-ray powder diffraction pattern measured on the hot-pressed B_6O samples. As expected for B_6O material synthesized from amorphous boron, the pattern contains some broad amorphous peaks centred at the 2θ values 23.4° and 38° illustrated in **Fig. 2** inserts **(a)** and **(b)**, respectively [**24**]. The broad amorphous peaks can be attributed to either to small amounts of starting amorphous boron or amorphous B_6O co-existing with crystalline B_6O [**19, 24**].

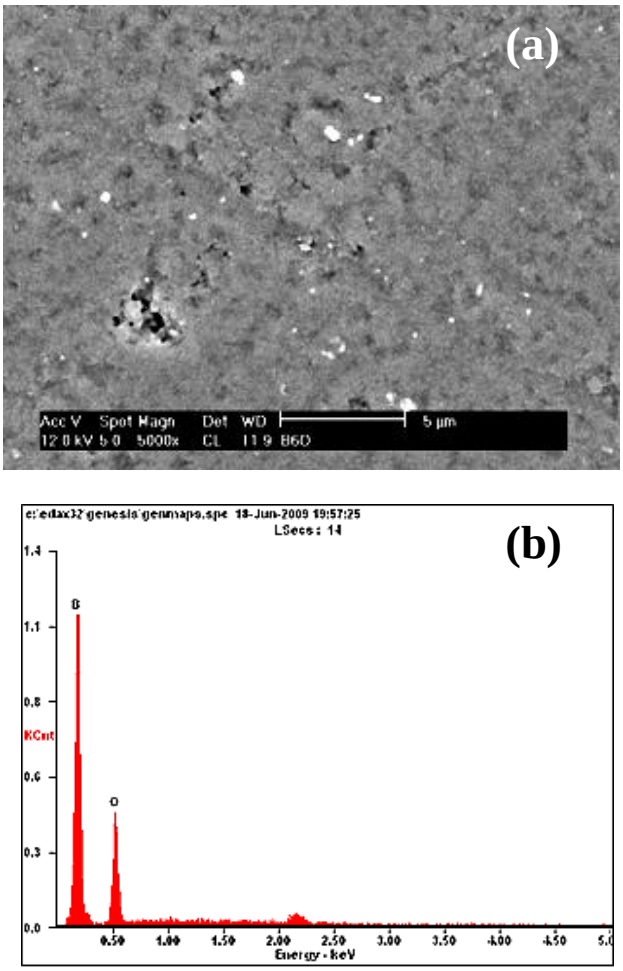

Fig. 1. Shows the SEM surface micrograph (a) and the EDX surface compositional analysis (b) of a hot pressed B_6O specimen. Iron contamination is responsible for EDX elemental peak observed around 2.25 keV.

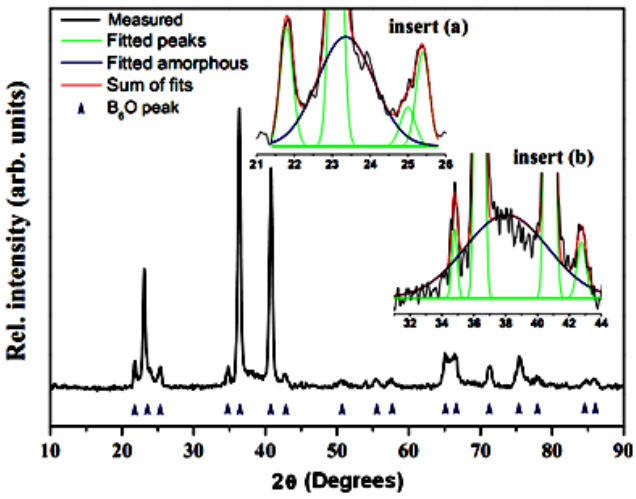

Fig. 2. The powder diffraction pattern of a sample of hot-pressed B_6O sample showing the predominance of the B_6O crystalline phase. Inserts (a) and (b) illustrate the broad amorphous peak fits.

The marked peaks in **Fig. 2** have been assigned to the α-rhombohedral boron structure (space group $R\bar{3}m$, JCPDS card number 31-210) consistent with the presence of a nominally pure polycrystalline B_6O phase [**19, 20, 25**]. An average crystallite size of 60 nm was determined using the conventional Scherrer method from the measured XRD pattern.

Raman scattering measurements

Boron has the second most complicated structural chemistry among all elements at ambient conditions after carbon. This is evident from the extremely large number of simple and complex phases and structures that it can form [**2, 26**]. In this work, Raman spectroscopy is a powerful analytical tool used here to investigate the local vibrational modes of the B_6O structure.

The experimentally measured and the fluorescence-background corrected Raman spectra of the uniaxially hot-pressed B_6O are shown on the same axis in **Fig. 3**. As expected [**20**], the experimentally measured Raman spectrum is weak and almost obscured in the presence of the inherent strong fluorescence background. The fluorescence-background corrected spectrum was obtained by means of the application of a fluorescence background suppression scheme, using the Horiba Jobin-Yvon LabSpec® 3.0 software.

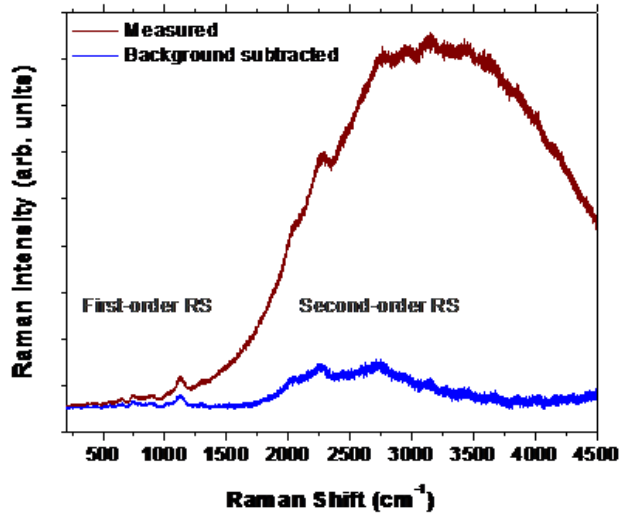

Fig. 3. The measured first- and second-order Raman spectra of B_6O and the fluorescence-background suppressed Raman spectra of B_6O.

The recovered the first-order, and second-order and tentatively the higher-order Raman spectra of B_6O are shown in **Fig. 4 (a)** and **(b)**, respectively. This demonstrates that even when the green 514.5 nm Ar^+ ion excitation laser is used, observable first- and second-order Raman spectra of B_6O can be observed. Simple precautions have to be taken, including: (a) deliberately using low-power excitation beams to minimize the heating and fluorescence effects on the sample surface, (b) reducing the exposure duration, and (c) the application of a suitable background subtraction scheme on the measured Raman spectra. **Table 1** below gives a summary of the observed Raman peaks and the tentative peak position analysis.

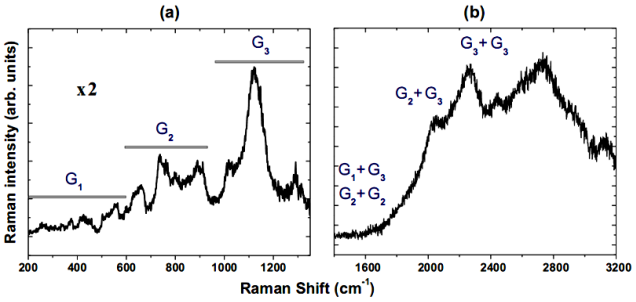

Fig. 4. Shows the fluorescence-background corrected first- and second-order Raman spectra of B_6O, respectively. The second-order Raman modes are a combination of the first-order Raman active phonons.

We confirm that the peak positions are not affected by the subtraction scheme, but we acknowledge that the width could be slightly influenced.

For B_6O [**20, 27**], and other boron-rich solids that are based on the β-rhombohedral boron type crystal structure [**26, 22**], theoretical calculations predict twelve Raman active phonons modes, for an ideal $R\bar{3}m$ α-rhombohedral structure. However, for a real hot-pressed polycrystalline B_6O structure characterized with oxygen deficiency, intrinsic defects, and a slightly distorted β-rhombohedral boron type crystal structure Raman modes exceeding twelve are expected [**22, 27**].

For analysis, the first-order Raman spectra of B_6O has been sub-divided into three spectral band groups of the observed modes based on their positions (G_1, G_2, and G_3) as illustrated in **Fig. 4 (a)**. The G_1 band comprises vibrational modes observed below 600 cm^{-1}, G_2, modes between 600 cm^{-1} and 950 cm^{-1}, while G_3, comprises modes between 950 cm^{-1} and 1200 cm^{-1}. The assignment of individual peaks follows a similar approach to that reported by Solozhenko *et al.* [**20**]. **Table 1** summarises the observed Raman bands shown in **Fig.** 4 (a) and **(b)**.

First-order groups of Raman modes

G_1 group of Raman modes: We have attributed the G_1 group of Raman peaks to vibrational modes involving the oxygen atom.

(a) When compared to the Raman spectra of HPHT synthesized B_4C, and $B_{13}N_2$ (illustrated in **Fig. 5** below), the G_1 Raman modes of the uniaxially hot-pressed B_6O material measured in this work are relatively weaker and broader.

(b) In particular, the Raman peak observed at 373 cm^{-1}, which is characteristic of the O–O chain vibration, is of very weak intensity and barely visible.

(c) The vibration at 425 cm^{-1} is attributed to the bending mode of the three-atomic chain.

(d) The relatively sharp feature at 500 cm^{-1} corresponds to the symmetric stretching of the B–O–B triatomic chain,

(e) The narrow line just above 500 cm^{-1}, has been attributed to the motion of the entire B_{12} icosahedron about oxygen atom [**20**].

Table 1. Shows a summary of the measured Raman data and the peak assignments. The following notations evaluate the intensity qualitatively: s+s, sharp and strong; s+b, sharp but broad; s+w, sharp but weak; m, medium; w, weak; vw, very weak; b, broad.

Group	Peak Position (cm^{-1})		Band	Remarks
FIRST ORDER RAMAN MODES				
	259.6	b+w	π	Icosahedral chain (B-O) phonon
	373.4	w	B_1	Vibrational motion of the (O-O) pair
	425.9	b+a	π	Bending vibration of the B-O-B chain
G_1	500.9	s+w	B_2	Symmetrical stretching of the B-O-B chain
	555.5	m	B_3	
	600.6	s+w	τ	Motion of the icosahedral boron atoms about O
	625.1	b	τ	
	736.9	s+s	B_4	
G_2	762.8	sh	B_5	Motion of the boron atoms in the icosahedra
	797.4	m	B_6	
	891.9	m	B_7	
	1016.4	m	B8	
G_3	1119.9	s+s	B_{10}	The inter-icosahedral boron vibration
	1154.8	sh	B_{11}	
	1288.2	m	B_{12}	
SECOND-ORDER RAMAN MODES				
G_1+G_3	—	—	ψ	G_1 + G_3 two-phonon combinations
G_2+G_2	—	—	ψ	G_2 + G_2 two-phonon combinations
G_2+G_3	2022	s+s	B_7+B_{10} B_7+B_{11}	
G_3+G_3	2230—2260	s+s	$B_{10}+B_{10}$ $B_{10}+B_{11}$ $B_{11}+B_{11}$	G_2 + G_3 two-phonon combinations
	2430.7	m	$B_{12}+B_{12}$	
HIGHER-ORDER RAMAN MODES				
	2723.6	s+b	π	
	2970.8	sh	π	
	3134.3	m	π	Observed but there is a lack of information
	3275.7	m	π	
	3256.4	w	π	

NOTES
π — observed but there is a lack of information
τ — assignment is speculative
ψ — expected but not observed

We have attributed the observations items (a) and (b) to the non-stoichiometric composition of the hot-pressed B_6O material. Following the conclusions of Olofsson and Lundstrom in ref. [**24**], oxygen atoms are situated at interstitial holes between icosahedra at non-bonding distances from each other. We also speculate here that the weak modes referred to in items (c– e) are relatively weak, this is indicative to the poor state of occupancy of the B–O–B chain linking the icosahedra.

Fig. 5 extends the comparison of the Raman spectra of boron-rich solids that are based on the α-rhombohedral boron type crystal structure made in reference [**10**], and references therein. Note that the B_4C, and $B_{13}N_2$ therein were synthesized under HPHT conditions and the B_6O, which is the subject of this study is a hot-pressed material. Compared with other icosahedral boron-rich solids, the Raman scattering of hot-pressed polycrystalline B_6O is extraordinarily weak.

G_2 and G_3 groups of Raman modes: It is generally accepted that all the lines observed between 600 and 1200 cm^{-1} are usually attributed to vibrations of the atoms of boron-rich B_{12} icosahedra. The G_2 group of Raman modes observed between 600 and 1100 cm^{-1} correspond to the intra-icosahedral B–B bonds.

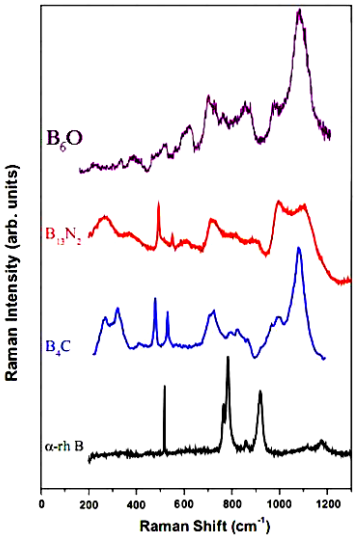

Fig. 5. A comparison of the Raman spectra of B_6O (our measurements, in purple) and other boron-rich based materials, $B_{13}N_2$, and B_4C. Note: The B_4C and $B_{13}N_2$ materials were synthesized under HPHT conditions. Diagram adapted from ref. [**10**] and all the measurements were measured at room temperature.

The G_3 group of Raman modes were observed between 950 and 1200 $cm^{-1}$and these correspond to the inter-icosahedral modes.

(i) We observe that at higher Raman shift frequencies, structural disorder is likely to be responsible for most of the observed broadening [**28**].

(ii) In addition to broadening, both the G_2 and G_3 bands of the Raman peaks appear to be riding on two strong, broad but distinct peaks (800 and 1160 cm^{-1}), respectively, which corresponds to amorphous and β-rhombohedral boron [**22**] – observation is consistent with the XRD pattern observed in **Fig. 2**.

(iii) Since the distances of B_{12} icosahedral boron atoms are nearly the same in B_6O, B_4C and $B_{13}N_2$, we expect their respective G_2 and G_3 bands to be closely related. From **Fig. 5**: notably the strong phonon of B_4C at 1430 cm^{-1} due to the stretching mode of the three-atomic chain [**10**] is missing in the spectrum of B_6O.

(iv) However, the highest first order mode of 1288 cm^{-1} is observed in the spectrum of B_6O but is not reported in the spectrum of B_4C.

(v) The strong phonon of B_6O at 1288 cm^{-1} is attributed to intericosahedral phonons like in α-rhombohedral boron [**20**].

Second- and higher-order groups of Raman modes

Fig. 4(b) shows measured Raman bands above 1500 cm^{-1}, the second-order Raman spectra of B_6O. The origins of these bands may be due to the two-phonon combinations of the modes from the G_1, G_2 and G_3 groups of Raman bands [**20**]. The notable absence of the G_1 + G_3 and G_2 + G_2 combinations is easy to see given the relatively weaker G_1 phonon modes observed. Subsequently, it is therefore tentatively attributed to the non-stoichiometric composition

of the hot-pressed B_6O material. In **Table 1**, we satisfactorily summarize all observed second-order Raman modes by considering combination of the first-order Raman active phonons with good agreement. If the 1288 cm^{-1} mode is considered as a first-order Raman mode, we can speculate that the medium-sized 2430 cm^{-1} peak would also be easily considered as second-order as well [**20**].

The weak Raman features observed beyond 2430 cm^{-1} clearly do not appear to follow the same phonon-phonon linear combination rule as the second-order Raman modes. However, although these higher-order Raman bands have well-defined frequencies and widths their nature and origins is less clear to us at present. Probably because they are inherently weak and the number of possible phonon-phonon mode combinations remarkably rises [**10**], simultaneously.

Conclusion

Based on the Raman scattering studies of hot-pressed B_6O we conducted using the 514.5 nm Ar^+ excitation, we conclude that as previously reported in [**20, 21**], we observed that the Raman spectrum of hot-pressed B_6O is characterized by a relatively weak Raman signal and a strong inherent fluorescence background. However, contrary to some reports that the Raman spectrum of hot-pressed B_6O is unobservable when the 514.5 nm Ar^+ excitation source is used for the Raman scattering studies, our results confirm the existence of observable highly resolved first-, second- and higher-order Raman spectra. The measured Raman spectrum of hot-pressed B_6O is comparable to the Raman spectra of HPHT synthesized $B_{13}N_2$ and B_4C materials measured at ambient conditions using the same excitation source. For analysis, the first-order Raman spectrum of B_6O has been conventionally divided into three spectral band groups of the observed vibrational modes. The G_1 band comprises vibrational modes observed below 600 cm^{-1}, G_2, modes between 600 cm^{-1} and 950 cm^{-1}, while G_3, comprises modes between 950 cm^{-1} and 1200 cm^{-1}. The G_1 Raman modes of hot-pressed B_6O measured are relatively weak and sometimes barely visible; we have tentatively attributed the poor oxygen occupancy in the B–O–B chain linking the icosahedra. When compared to the Raman spectra of $B_{13}N_2$ and B_4C measured at ambient conditions using the same excitation source, the G_2 and G_3 Raman modes of hot-pressed B_6O are generally similar in characteristics. The general broadening of the G_2 and G_3 modes is consistent with fact that the B_{12} icosahedra are slightly distorted. The second- and higher-order Raman spectra are also observable; the origin of the second-order Raman modes has been attributed to the two-phonon combinations of the first-order vibrations (as illustrated in **Table 1** above). However, the nature and the origins of the higher-order Raman spectrum is less clear at present and required further investigations.

Acknowledgements
The useful contributions of R. Erasmus, and H. Werheit and the financial support from the DST/NRF Centre of Excellence in Strong Materials are gratefully acknowledged.

References

1. Albert, B.; Hillebrecht, H. *Angew. Chem. Int. Edit.* **2009**, *48*, 1521. **DOI:** 10.1002/anie.200903246
2. Lowther, J.E. *Physica B* **2002**, *322*, 173. **DOI:** 10.1016/S0921-4526(02)01180-8
3. Shirai, K. *J. Superhard Mater.* **2010**, *32*, 205. **DOI:** 10.3103/S1063457610030068
4. McMillan, P.F.; Hubert, H.; Chizmeshya, A.; Petuskey, W.T.; Garvie, L.A.J.; Devouard, B. *J. Solid State Chem.* **1999**, *147*, 281. **DOI:** 10.1006/jssc.1999.8272
5. Hubert, H.; Devouard, B.; Garvie, L.A.J.; O'Keeffe, M.; Buseck, P.R.; Petuskey, W. T.; McMillan, P.F. *Nature* **1998**, *391*, 376. **DOI:** 10.1038/34885
6. Suri, A.K.; Subramanian, C.; Sonber, J.K.; Murphy, T.S.R.Ch. *Int. Mater. Rev.* **2010**, *55*, 4. **DOI:** 10.1179/095066009X12506721665211
7. Herrmann, M.; Raethel, J.; Bales, A.; Sempf, K.; Sigalas, I.; Hoehn, M. *J. Euro. Ceram. Soc.* **2009**, *29*, 2611. **DOI:** 10.1016/j.jeurceramsoc.2009.03.002
8. Roberts, D.J.; Zhao, J.; Munir, Z.A. *Int. J. Refract. Met. H.* **2009**, *27*, 556. **DOI:** 10.1016/j.ijrmhm.2008.07.009
9. Kurakevych, O.O.; Solozhenko, V.L. *Solid State Commun.* **2009**, *149*, 2169. **DOI:** 10.1016/j.ssc.2009.09.019
10. Solozhenko, V.L.; Kurakevych, O.O. *JPCS* **2008**, *121*, 62001. **DOI:** 10.1088/1742-6596/121/6/062001
11. Andrews, A.; Sigalas, I.; Herrmann, M. WIPO Patent No. WO/2008/132675 **2008**.
12. Davies, G.J.; Sigalas, I.; Herrmann, M.; Shabalala, T.C. WIPO Patent No. WO/2007/029102 **2007**.
13. Chen, C.; He, D.; Kou, Z.; Peng, F.; Yao, L.; Yu, R.; Bi, Y. *Adv. Mater.* **2007**, *19*, 4288. **DOI:** 10.1002/adma.200700836
14. Andrews, A.; Herrmann, M.; Shabalala, T.C.; Sigalas, I. *J. Euro. Ceram. Soc.* **2008**, *28*, 1613. **DOI:** 10.1016/j.jeurceramsoc.2007.10.011
15. Itoh, H. *J. Ceram. Soc. Jpn.* **2004**, *112*, 121. **DOI:** 10.2109/jcersj.112.121
16. Jiao, X.; Jin, H.; Liu, F.; Ding, Z.; Yang, B.; Lu, F.; Zhao, X.; Liu, X. *J. Solid State Chem.*, **2010**, 183,1697 **DOI:** 10.1016/j.jssc.2010.05.031
17. Johnson, O.T.; Sigalas, I.; Ogunmuyiwa, E.N.; Kleebe, H.J.; Muller, M.M.; Herrmann, M. *Ceram. Int.* **2010**, *36*, 1767. **DOI:** 10.1016/j.ceramint.2010.02.035
18. Johnson, O.T.; Sigalas, I.; Herrmann, M. *Ceram. Int.* **2010**, *36*, 2401. **DOI:** 10.1016/j.ceramint.2010.07.018
19. Shabalala, T.C.; McLachlan, D.S.; Sigalas, I.; Herrmann, M. *Ceram. Int.*, **2008**, *34*, 1713 **DOI:** 10.1016/j.ceramint.2007.05.010
20. Solozhenko, V.L.; Kurakevych, O.O.; Bouvier, P. *J. Raman Spectrosc.* **2009**, *40*, 1078. **DOI:** 10.1002/jrs.2243
21. Werheit, H.; Kuhlmann, U. *J. Solid State Chem.* **1997**, *133*, 260. **DOI:** 10.1006/jssc.1997.7452

22. Werheit, H.; Filipov, V. *In Raman Effect in Boron Rich Solids*, Orlovskaya, N.; Lugovy, M. (Eds.), Springer Netherlands, **2011**, pp. 29-43.

DOI: 10.1007/978-90-481-9818-4_3

23. Herrmann, M.; Kleebe, H.J.; Raethel, J.; Sempf, K.; Lauterbach, S.; Muller, M.M.; Sigalas, I. *J. Am. Ceram. Soc.* **2009**, *92*, 2368.

DOI: 10.1111/j.1551-2916.2009.03197.x

24. Olofsson, M.; Lundstrom, T. *J. Alloy Comp.* **1997**, *257*, 91.

DOI: 10.1016/s0925-8388(97)00008-x

25. Itoh, H.; Yamamoto, R.; Iwahara, H. *J. Am. Ceram. Soc.* **2000**, *83*, 501.
DOI: 10.1111/j.1151-2916.2000.tb01224.x

26. Werheit, H. *In Electric Refractory Materials;* Kumashiro, Y., Ed.; Marcel Dekker Inc., **2000**, pp. 589-654.

DOI: 10.1201/9780203908181

27. Wang, Z.; Zhao, Y.; Lazor, P.; Annersten, H.; Saxena, S. K. *Appl. Phys. Lett.* **2005**, *86*, 041911.
DOI: 10.1063/1.1857091

28. Lazzari, R.; Vast, N.; Besson, J. M.; Baroni, S.; dal Corso, A. *Phys. Rev. Lett.*,**1999**, *83*, 3230.
DOI: 10.1103/PhysRevLett.83.3230

Hindawi Publishing Corporation
Advances in Materials Science and Engineering
Volume 2011, Article ID 539252, 6 pages
doi:10.1155/2011/539252

Research Article

Analysis of the Indentation Size Effect in the Microhardness Measurements in B_6O

Ronald Machaka,[1] Trevor E. Derry,[2] Iakovos Sigalas,[1] and Mathias Herrmann[3]

[1] *DST/NRF Centre of Excellence in Strong Materials, School of Chemical and Metallurgical Engineering, University of the Witwatersrand, Johannesburg, Private Bag 3, Johannesburg 2050, South Africa*
[2] *DST/NRF Centre of Excellence in Strong Materials and School of Physics, University of the Witwatersrand, Johannesburg, Private Bag 3, Johannesburg 2050, South Africa*
[3] *Fraunhofer Institute for Ceramic Technologies and Systems, Winterbergstra_e 28, 01277 Dresden, Germany*

Correspondence should be addressed to Ronald Machaka, ronald.machaka@wits.ac.za

Received 9 February 2011; Accepted 13 April 2011

Academic Editor: Paul Munroe

The Vickers microhardness measurements of boron suboxide (B_6O) ceramics prepared by uniaxial hot-pressing was investigated at indentation test loads in the range from 0.10 to 2.0 kgf. Results from the investigation indicate that the measured microhardness exhibits an indentation load dependence. Based on the results, we present a comprehensive model intercomparison study of indentation size effects (ISEs) in the microhardness measurements of hot-pressed B_6O discussed using existing models, that is, the classical Meyer's law, Li and Bradt's proportional specimen resistance model (PSR), the modified proportional specimen resistance model (MPSR), and Carpinteri's multifractal scaling law (MFSL). The best correlation between literature-cited load-independent Vickers microhardness values, the measured values, and applied models was achieved in the case of the MPSR and the MFSL models.

1. Introduction

With hardness values reported to range between 24 GPa and 45 GPa [1, 2], boron suboxide (B_6O) is sometimes considered to be the third hardest material after only diamond (from ~70 to ~100 GPa) and cubic boron nitride (~60 GPa) [2]. The boron-rich icosahedral ultrahard material belongs to the α-rhombohedral boron type structure ($R\bar{3}m$) [2] which is similar to those of other ultrahard boron-rich materials namely boron carbide B_4C [3], aluminium magnesium boride $AlMgB_{14}$ [4], and the newly synthesized boron subnitride $B_{13}N_2$ [5].

B_6O exhibits a rather unusual and wide range of superior properties; among these are high hardness with low density, high mechanical strength, and high chemical inertness [2, 6]. Along with the other boron-rich ultrahard materials, the potential applications of B_6O have been an object of intense interest in recent years [2]. However, despite the intensive research efforts, the commercial applications are yet to be realized partly because of (a) the low fracture toughness of polycrystalline B_6O [7] and considerable practical challenges in the densification of that material [2, 6, 7] by hot-pressing, (b) stoichiometric B_6O samples that are not easy to synthesize [1, 2], (c) poor crystallinity [1, 7], and hence (d) numerous mechanical properties of the material that are still poorly understood [8]—indentation size effect (ISE) in microhardness measurements is one such property.

Until now, the investigation of the mechanical properties of B_6O by indentation has been neglected in favour of the improvement of densification and fracture toughness of the composites [2, 6, 7]. The hardness reported for the material by different workers often remains a topic of debate, with literature-cited values varying from 24 GPa to 45 GPa. To the best of our knowledge, the indentation load-size dependence in the microhardness of hot-pressed B_6O is being comprehensively examined for the first time in this paper. The aim of this paper is twofold: (1) to report experimental data on the microhardness of hot-pressed B_6O determined by Vickers pyramidal indentation and (2) to critically examine the ISE phenomenon by means of a comprehensive intermodel

comparison of various approaches and models proposed in the literature. The nature and the origins of ISE are investigated and discussed.

2. Materials and Experimental Method

B_6O powder was prepared by the reaction of B and B_2O_3 as detailed by Andrews et al. in [9] that were uniaxially hot-pressed in *h*BN pots under argon environment at 1800°C and 50 MPa for 20 minutes. The hot-pressed compacts were then metallographically prepared using a method prescribed by Machaka et al. in [10]. The density of the hot-pressed compacts measured 2.44 g/cm^3. The polished samples were analyzed for phase composition using X-ray diffraction, with Cu K_α radiation. The powder diffraction patterns were collected using the Bragg-Brentano backscattering geometry over a 10°–90° 2θ range, with a 0.02° step size.

The measurements were performed at room temperature by a Future-Tech microhardness tester at different applied test load between 0.1 and 2.0 kgf. At least ten hardness measurements were carefully taken for each load at different locations on the middle of each sample, and the average values were taken as the hardness of the sample at that load. The Vickers indentation impressions were observed using optical microscopy.

3. Results

3.1. XRD Measurements. Figure 1 shows the full profile X-ray powder diffraction pattern measured on the starting hot-pressed B_6O samples. The diffraction pattern is characteristic of a nominally pure polycrystalline B_6O. All the dominant diffraction peaks can be perfectly indexed to the XRD pattern of B_6O (JCPDS File Card no. 31-210) reported elsewhere [9]. The lattice parameters, $a = 5.39$ Å and $c = 12.34$ Å, obtained from XRD analysis are in good agreement with the single crystal data [2].

3.2. Microindentation Measurements. To investigate ISE, microindentation measurements were conducted at test load between 0.1 and 2.0 kgf using a Vickers diamond indenter. Apparent Vickers microhardness values H_v were calculated at each load using the conventional approach shown in:

$$H_v = \frac{1.8544 \cdot P}{d^2}, \tag{1}$$

where d is the average diagonal length of the Vickers indentation impressions and P is the indentation test load in kgf. Figure 2 shows the dependence of the measured Vickers microhardness of hot-pressed B_6O on the applied indentation load. Each of the plotted data point is an average of at least ten measurements at each applied test load. The insert in Figure 2 depicts an optical micrograph of a typical Vickers indentation impression.

Evidently, the Vickers hardness is a function of the applied load at low applied indentation test load. The existence of ISE makes it unsatisfactory here to quote a single hardness value when Vickers hardness is used for material

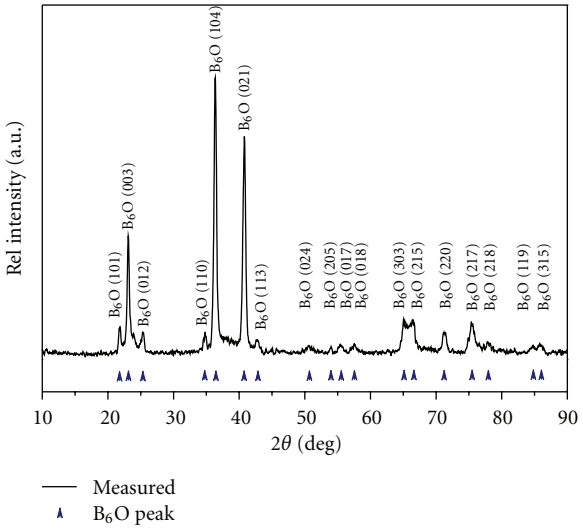

Figure 1: The powder diffraction pattern of a sample of hot-pressed B_6O showing the predominance of the B_6O crystalline phase.

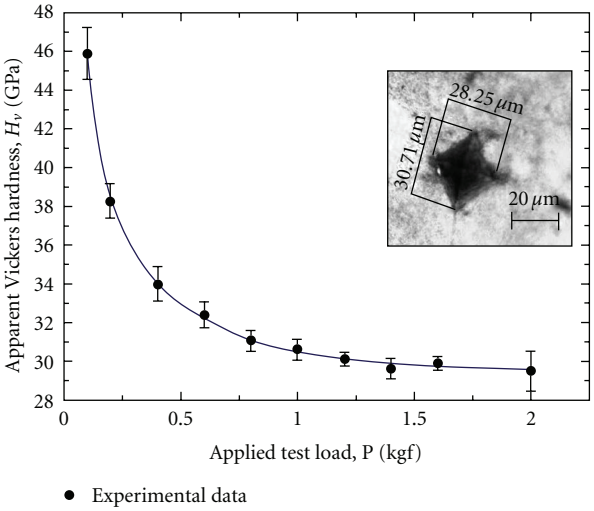

Figure 2: The dependence of apparent Vickers microhardness of hot-pressed B_6O with applied load. The figure insert shows the optical micrograph of a typical Vickers indentation impression.

characterization. By observation, at applied indentation test loads $\gtrsim$1 kgf, a single load-independent Vickers hardness value of 30.0 GPa seems to exists. The load-independent hardness is also sometimes deemed the intrinsic or "true" hardness. The observed value is consistent with literature reported values [1, 2, 11].

3.2.1. Meyer's Law. The classical power law shown in (2a), also known as the Meyer's law, is frequently used to indicate the existence of ISE for ceramic and other materials [12]. B is a power-fit constant, and the exponent n is the Meyer's

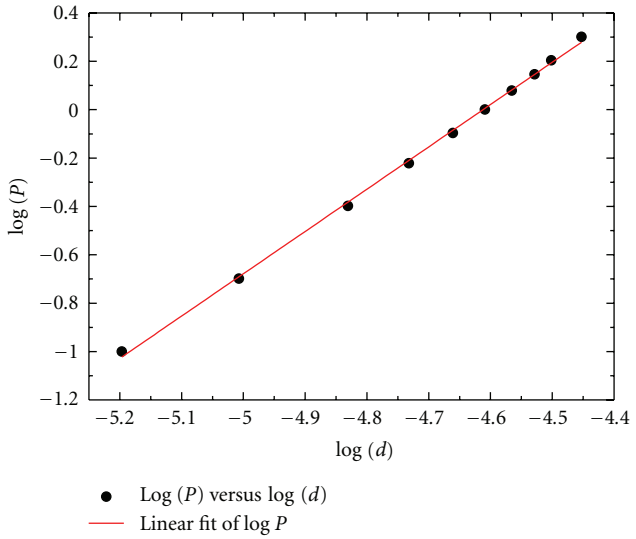

FIGURE 3: Linear regression analysis of $\log P$ against log of the indentation diagonal length, d according to the Meyer's law (2b).

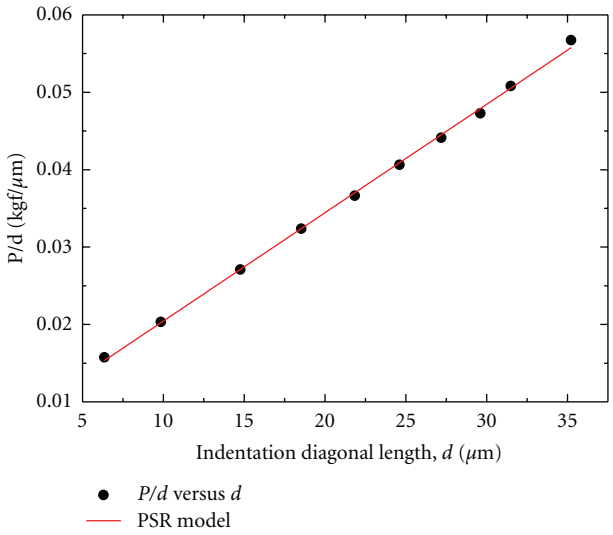

FIGURE 4: A plot of P/d against d constructed from the experimentally measured data and a best linear fit of the plot.

index, also known as the size-effect index. The Meyer's index is generally used as a measure of ISE:

$$P = B \cdot d^n, \tag{2a}$$

$$\log P = \log B + n \cdot \log d. \tag{2b}$$

The regression analysis of the experimental data using (2b) is shown in Figure 3. The slope of the linear fit is the Meyer's index, and observed to be $n = 1.75$. When $n = 2$, the microhardness is expected to be independent of the applied load. However, $n \leq 2$ indicates the existence of an ISE trend, the measured microhardness decreasing with applied load [13, 14].

3.2.2. PSR Model. Several studies [14, 15] agree that the Meyer law is probably insufficient to describe the origin of the ISE, although it is a good indicator of its existence. According to Li and Bradt [14], the applied indentation load is related to the average indent diagonal length through a polynomial relationship (3a):

$$P = a_1 \cdot d + a_2 \cdot d^2 \tag{3a}$$

$$= a_1 \cdot d + \frac{H_{\text{psr}}}{1.8544} \cdot d^2. \tag{3b}$$

The parameters a_1 and a_2 are constants for a given material. The parameters are related to the elastic and the plastic deformation properties of the test material, respectively. The parameter a_1 is a measure of the surface effects during microhardness indentation which is directly related to the ISE contribution, whilst a_2 is directly related to the load-independent microhardness value H_{psr} as demonstrated in (3b).

From (3a), a plot of P/d against d can be constructed to yield a straight line, where best-fit parameters a_1 and a_2 can easily be obtained by regression analysis. As shown in Figure 4, a plot of P/d against d is significantly linear, implying that (3a) gives an indication of the existence of ISE in hot-pressed B_6O.

As noted previously, the PSR analysis can be extended to determine H_{psr} directly from a_2 using (3b). In this study H_{psr} was found to be 26.8 ± 0.3 GPa.

3.2.3. Modified PSR Model. Gong et al. in [16] modified the PSR model to investigate the ISE behaviour in various materials. The resulting MPSR model is defined by (4a):

$$P = a_0 + a_1 \cdot d + a_2 \cdot d^2 \tag{4a}$$

$$= a_0 + a_1 \cdot d + \frac{H_{\text{psr}}}{1.8544} \cdot d^2, \tag{4b}$$

where a_0 is a constant related to the residual surface stresses associated with the surface grinding and polishing processes during sample preparation. The parameters a_1 and a_2 are constants as defined in the PSR model (refer to Section 3.2.2). The values of a_0, a_1, and a_2 can be evaluated by plotting the P data against d. The plot of P versus d (and polynomial curve fitting thereof according to the MPSR model) is shown in Figure 5.

As is the case for the PSR model, a load-independent hardness value, H_{mpsr}, can be determined directly from best-fit value of a_2 from Figure 5 using (4b). In this study, H_{mpsr} was found to be 28.2 ± 0.9 GPa.

The estimated best-fit values of the a_0, a_1, and a_2 parameters corresponding H_{mpsr} values are listed in Table 1. The residual surface stresses contribution to the observed ISE is negligible compared to the contribution of bulk material's plastic deformation characteristics.

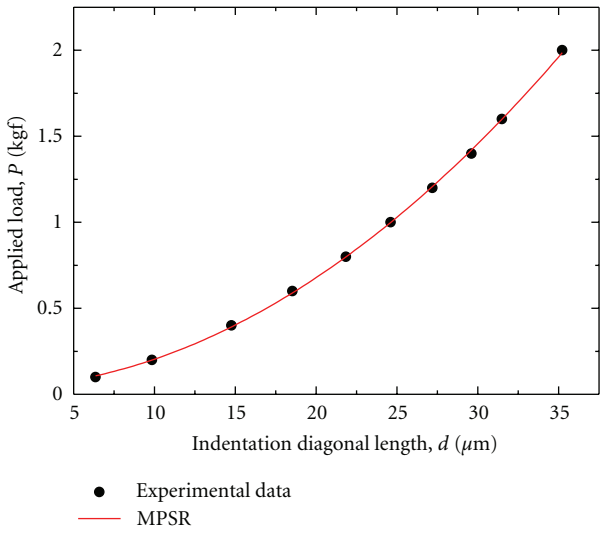

FIGURE 5: A plot of P versus d, and curve fitting thereof, according to the MPSR model.

TABLE 1: A summary of the best-fit parameters calculated according to the PSR and MPSR models.

Model	a_0	a_1	$a_2 \times 10^{11}$	H (GPa)
PSR	—	19711	6.95	26.8 ± 0.3
MPSR	0.0026	20591	7.99	28.2 ± 0.9

The PSR and MPRS parameters estimated by regression analysis are summarized in Table 1. Based on the values and their physical significance according to the energy-balance relation [17], we suggest that the residual surface stresses' contribution (a_0) to the observed ISE is negligible compared to the contribution of bulk material's indentation elastic recovery (a_1) and the indenter/specimen interface friction resistance coupled with elastic resistance of the specimen and the mixed elastic/plastic deformation response of material (a_2).

3.2.4. MFSL Approach. As illustrated in Figure 2, the variation of microhardness with indentation load is a two-parameter problem exhibiting at least two totally different size-dependent regimes: a load-dependent regime and a load-independent regime. The variation of microhardness with indentation load in other words exhibits self-similarity; that is, by observing the property in different scales, a similar, but not exactly the same structure, is obtained—a property of multifractals.

According to Carpinteri and Puzzi in [18], ISE in materials follows the multifractal scaling law shown in (5). However, the indentation size effect property is observed to vanish in the limit of the applied load tending to infinity. From the later, an asymptotic value of hardness which resembles a load-independent or intrinsic value can be determined as illustrated in Figure 6. In this study, we apply the multifractal scaling law in the analysis of observed

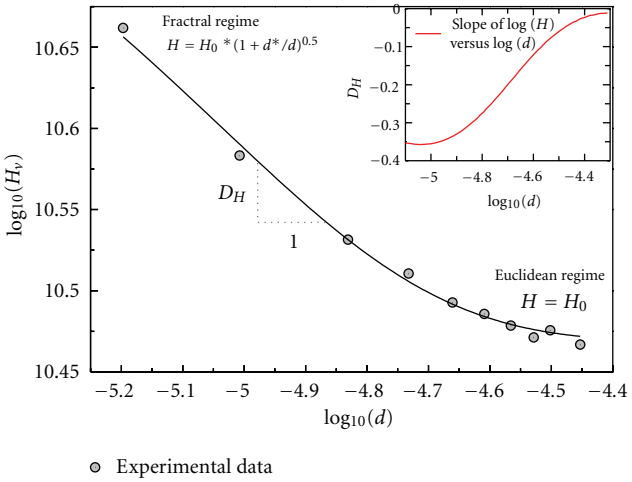

FIGURE 6: A bilogarithmic plot of the hardness calculated according to (5) plotted against the measured indentation diagonal length. The slope of the plot equals D_H, a fractal dimension for hardness with respect to d. In the insert, the fractal dimensional increment D_H is plotted as a function of $\log d$. Nonlinearity of the scaling fractal dimensional suggests multifractal behaviour.

indentation size effect in hot-pressed B_6O. Further in-depth discussions on the fractal approach to indentation size effect are refereed to Carpinteri's comprehensive review on the subject [18].

On the basis of this approach, the multifractal scaling law (MFSL) for ISE can be written in the following analytical form:

$$H_v = H_{\text{mfsl}} \cdot \left(1 + \frac{d^*}{d}\right)^{0.5}, \tag{5}$$

where H_{mfsl} is the intrinsic hardness in the limit of infinite (a huge) applied load and d^* is the critical material characteristic length which individuates the transition between the two regimes, that is, the fractal one and the nonfractal (Euclidean) one.

In order to study the fractal characteristic of the size effect dependence of microhardness depicted in Figure 2, a log-log plot of the Vickers microhardness and the indentation diagonal length was constructed based on the multifractal scaling law shown in (5) (and presented as Figure 6). The result shows that $\log H$ as a function of the $\log d$ is approximately linear in two parts of the scale dependence.

In this study, both d^* and H_{mfsl} were determined simultaneously by means of nonlinear least squares analysis of the experimental data using Mathematica. H_{mfsl} and d^* were determined to be 28.9 GPa and 1.41 μm, respectively. The fractal dimension in the first region can be depicted as the following equation.

The slope of the bilogarithmic plot shown in Figure 6 represents the fractal dimensional increment D_H, which is a measure of the variable influence of ISE on the measured Vickers hardness. The variation of fractal dimension of multifractality D_H with $\log d$, as determined from $\log H$ versus $\log d$, is presented as an insert in Figure 6. Two limiting

Table 2: A summary of the intrinsic microhardness values calculated according to Li and Bradt's PSR model, the Gong's MPSR model, and Carpinteri's MFSL model.

	H_{psr} (GPa)	H_{mpsr} (GPa)	H_{mfsl} (GPa)	H_{ave} (GPa)
Microhardness	26.8 ± 0.3	28.2 ± 0.3	28.9 ± 0.1	28.0 ± 0.3

conditions have to be satisfied: $D_H = 0$ for large indents (Euclidean response) and $D_H = -0.5$ for small indents (multifractal behaviour). The last situation corresponds to the highest possible indentation size effect in hardness, which is a theoretical upper bound.

According to the insert in Figure 6, D_H tends to zero and coincides with the occurrence in a crossover between fractal and Euclidean behaviour implying the progressive vanishing of fractality in the measured Vickers microhardness with increasing indentation load/size.

4. Summary and Conclusions

Figure 2 shows that the variation of H_v with P indicates that the hot-pressed B_6O ceramic material exhibits ISE. Based on the observation, a comprehensive study of ISE in microhardness measurements of B_6O was conducted using a number of existing models, that is, the classical Meyer's law, Li and Bradt's proportional specimen resistance model (PSR), the modified proportional specimen resistance model (MPSR), and Carpinteri's multifractal scaling law (MFSL). A summary of the hardness values calculated is shown in Table 2.

The average load-independent hardness of hot-pressed B_6O from this study has been observed to be 28.0 ± 0.3 GPa.

Based on the values of the PSR and MPSR parameters estimated by regression analysis, the origins of ISE in hot-pressed B_6O can be attributed to either the bulk material's indentation elastic recovery, the indenter/specimen friction resistance coupled with elastic resistance of the specimen, or/and the mixed elastic/plastic deformation response of material. The residual surface stresses' contribution to the observed ISE is observed to be negligible compared to the aforementioned.

The linear relationship of the double logarithm between measure (the microhardness) and scale (the applied load) shows indentation self-similarity, both in indentation shape and in the results of hardness. We can conclude this to be fractal behaviour. The load dependence of hardness shows dual fractal behaviour given the two different regions of hardness.

We can conclude and suggest that the variation of fractal dimension of multifractality D_H with $\log d$ is a more resourceful indicator of the existence of ISE than the Meyer's index, for example.

Acknowledgments

The authors gratefully acknowledge the useful contributions of O. T. Johnson and the financial support from the DST/NRF Centre of Excellence in Strong Materials and the University of the Witwatersrand Mellon Award.

References

[1] M. Herrmann, J. Raethel, A. Bales, K. Sempf, I. Sigalas, and M. Hoehn, "Liquid phase assisted densification of superhard B_6O materials," *Journal of the European Ceramic Society*, vol. 29, no. 12, pp. 2611–2617, 2009.

[2] H. J. Kleebe, S. Lauterbach, T. C. Shabalala, M. Herrmann, and I. Sigalas, "B_6O: A correlation between mechanical properties and microstructure evolution upon Al_2O_3 addition during hot pressing," *Journal of the American Ceramic Society*, vol. 91, no. 2, pp. 569–575, 2008.

[3] A. K. Suri, C. Subramanian, J. K. Sonber, and T. S. R. C. Murthy, "Synthesis and consolidation of boron carbide: a review," *International Materials Reviews*, vol. 55, no. 1, pp. 4–38, 2010.

[4] D. J. Roberts, J. Zhao, and Z. A. Munir, "Mechanism of reactive sintering of $MgAlB_{14}$ by pulse electric current," *International Journal of Refractory Metals and Hard Materials*, vol. 27, no. 3, pp. 556–563, 2009.

[5] O. O. Kurakevych and V. L. Solozhenko, "300 K equation of state of rhombohedral boron subnitride," *Solid State Communications*, vol. 149, no. 47-48, pp. 2169–2171, 2009.

[6] O. T. Johnson, I. Sigalas, E. N. Ogunmuyiwa, H. J. Kleebe, M. M. Müller, and M. Herrmann, "Boron suboxide materials with Co sintering additives," *Ceramics International*, vol. 36, no. 6, pp. 1767–1771, 2010.

[7] M. Herrmann, H. J. Kleebe, J. Raethel et al., "Field-assisted densification of superhard B_6O materials with Y_2O_3/Al_2O_3 addition," *Journal of the American Ceramic Society*, vol. 92, no. 10, pp. 2368–2372, 2009.

[8] Z. Wang, Y. Zhao, P. Lazor, H. Annersten, and S. K. Saxena, "In situ pressure Raman spectroscopy and mechanical stability of superhard boron suboxide," *Applied Physics Letters*, vol. 86, no. 4, Article ID 041911, 2005.

[9] A. Andrews, M. Herrmann, T. C. Shabalala, and I. Sigalas, "Liquid phase assisted hot pressing of boron suboxide-materials," *Journal of the European Ceramic Society*, vol. 28, no. 8, pp. 1613–1621, 2008.

[10] R. Machaka, B. W. Mwakikunga, E. Manikandan, T. E. Derry, and I. Sigalas, "Raman spectrum of hot-pressed boron suboxide," *Advance Matterial Letters*, vol. 2, no. 1, pp. 58–64, 2011.

[11] A. Andrews, I. Sigalas, and M. Herrmann, "Boron suboxide composite material," WIPO Patent 2008132675, 2008.

[12] J. Gong, H. Miao, Z. Peng, and L. Qi, "Effect of peak load on the determination of hardness and Young's modulus of hot-pressed Si_3N_4 by nanoindentation," *Materials Science and Engineering A*, vol. 354, no. 1-2, pp. 140–145, 2003.

[13] O. Şahin, O. Uzun, U. Kölemen, and N. Uçar, "Mechanical characterization for β-Sn single crystals using nanoindentation tests," *Materials Characterization*, vol. 59, no. 4, pp. 427–434, 2008.

[14] H. Li and R. C. Bradt, "The effect of indentation-induced cracking on the apparent microhardness," *Journal of Materials Science*, vol. 31, no. 4, pp. 1065–1070, 1996.

[15] O. Şahin, O. Uzun, M. Sopicka-Lizer, H. Gocmez, and U. Kölemen, "Dynamic hardness and elastic modulus calculation of porous SiAlON ceramics using depth-sensing indentation technique," *Journal of the European Ceramic Society*, vol. 28, no. 6, pp. 1235–1242, 2008.

[16] J. Gong, J. Wu, and Z. Guan, "Examination of the indentation size effect in low-load vickers hardness testing of ceramics," *Journal of the European Ceramic Society*, vol. 19, no. 15, pp. 2625–2631, 1999.

[17] J. Gong, J. Wu, and Z. Guan, "Analysis of the indentation size effect on the apparent hardness for ceramics," *Materials Letters*, vol. 38, no. 3, pp. 197–201, 1999.

[18] A. Carpinteri and S. Puzzi, "A fractal approach to indentation size effect," *Engineering Fracture Mechanics*, vol. 73, no. 15, pp. 2110–2122, 2006.

Materials Science and Engineering A 528 (2011) 5778–5783

Contents lists available at ScienceDirect

Materials Science and Engineering A

journal homepage: www.elsevier.com/locate/msea

Nanoindentation hardness of hot-pressed boron suboxide

Ronald Machaka[a,b,*], Trevor E. Derry[a,c], Iakovos Sigalas[a,b]

[a] DST/NRF Centre of Excellence in Strong Materials, University of the Witwatersrand, P. Bag 3, Wits, Johannesburg, South Africa
[b] School of Chemical and Metallurgical Engineering, University of the Witwatersrand, P.O. Bag 3, Wits, Johannesburg 2050, South Africa
[c] School of Physics, University of the Witwatersrand, P.O. Bag 3, Wits, Johannesburg 2050, South Africa

ARTICLE INFO

Article history:
Received 22 February 2011
Received in revised form 16 March 2011
Accepted 25 March 2011
Available online 6 April 2011

Keywords:
Hardness measurement
Nanoindentation
Boron suboxide
Indentation size effect

ABSTRACT

The existence of the indentation size effect implies the absence of a single hardness value for the material under investigation especially at low applied loads. In this paper we present an investigation of the indentation size dependence behaviour of nanoindentation hardness in boron suboxide ceramic compacts prepared by uniaxial hot-pressing. Berkovich nanohardness indentations were conducted and analyzed accordingly. In addition to the ordinary Oliver and Pharr method of nanoindentation data analysis, a quantitative approach for the loading curve analysis is proposed. Using the proposed approach, the description and characterization of the observed indentation size effect through the application of the Meyer's law, and the classical and the modified proportional specimen resistance models as well as the multi-fractal scaling law was conducted and is reported. The load-independent hardness values deduced from our quantitative approach are comparable to the results calculated with conventional methods, especially with the multi-fractal scaling law.

1. Introduction

Hot-pressed boron suboxide (B_6O) is a boron-rich icosahedral super-hard ceramic material with hardness values reported 24 GPa and 45 GPa [1–3]. The material belongs to the α-rhombohedral boron type structure ($R\bar{3}m$) [4,5] which is similar to those of other ultra-hard boron-rich materials namely boron carbide (B_4C) [6] aluminium magnesium boride ($AlMgB_{14}$) [7], and the newly synthesized boron subnitride ($B_{13}N_2$) [8,9].

Although the hot-pressed B_6O materials exhibit a rather unusual and wide range of superior properties such as high hardness with low density, high mechanical strength, and high chemical inertness [1,3,10], the commercial applications are yet to be realized. Reasons for this include the low fracture toughness of hot-pressed B_6O materials [11], considerable practical challenges in the densification of the material [1,3,10,11], stoichiometric B_6O samples are not easy to synthesize [1,3,10], and the poor crystallinity [1,11]. As a result, numerous mechanical properties of the material are still poorly understood [12]. In fact, data concerning the investigation of the nanomechanical properties of hot-pressed B_6O by nanoindentation do not exist in literature in spite of the fact that the analysis of nanomechanical properties is fast becoming an increasingly useful tool in a large variety of scientific and engineering fields.

For lower applied load indentation tests there is enough experimental evidence to suggests that the measured macro-, micro- and nano-hardness values are not single material constants, but a function of either the applied test load, or the depth of the indentation [13]. This absence of a single value for the hardness is a material property known as the indentation size effect (ISE) [13–15]. Numerous investigators have reported studies of ISE using nanoindentation testing for various materials, Gong et al. [16] is a good example. The typical scheme involves carrying out multicycling nanoindentation tests loading–unloading tests on the same spot and simultaneously measuring the $P-h$ curves under different peak applied load in a defined load range [16–19].

Nevertheless, a closer examination of the reported load-displacement ($P-h$) cycles demonstrates that the individual $P-h$ cycle curves show similar loading and unloading behaviour [18]. Şahin et al. [20] suggests that this indicates similar elastic and plastic deformation mechanism on the load range used. It is therefore expected that a $P-h$ curve measured at a single peak applied load can adequately define the ISE behaviour of a material since each loading $P-h$ curve is expected to contain a wealth of elastic and plastic deformation characteristics of a material [18], although this approach is not commonly used in the nanoindentation data analysis.

The objectives of the study presented here is two-fold. First, it seeks to report on the nanomechanical properties of hot-pressed B_6O determined directly from the analysis of the $P-h$ response curves measured during nanoindentation testing. Secondly, a quantitative analysis approach for studying a single loading curve to

* Corresponding author at: University of the Witwatersrand, P.O. Box 283, Wits, Johannesburg 2050, South Africa. Tel.: +27 11 717 7534; fax.: +27 11 717 6879.
E-mail address: Ronald.Machaka@wits.ac.za (R. Machaka).

0921-5093/$ – see front matter © 2011 Elsevier B.V. All rights reserved.
doi:10.1016/j.msea.2011.03.104

simulate multicycling indentation loading data is proposed in this paper. The method is similar in concept to that used by Carneiro et al. [21] to calculate instantaneous hardness values. Using the simulated data, we present an investigation of the the apparent indentation size dependent behaviour of nanohardness as observed upon the analysis of the nanoindentation data using Li and Bradt's proportional specimen resistance model (PSR) [22], Gong's modified PSR model (MPSR) [15], and Carpinteri and Puzzi's fractal interpretation of ISE by means of the multifractal scaling law (MFSL) [23]. In each case, a measure of the load-independent nanohardness value is obtained.

2. Materials and experimental method

2.1. Specimen preparation

Pure B_6O powder was prepared at the University of the Witwatersrand using a method described by Andrews et al. [2,24]. The powders were uniaxially hot-pressed (Thermal Technologies HP20 uniaxial hot press) in hBN pots in an argon gas environment at a temperature of 1900° C and a pressure of 50 MPa for 20 min. Hot-pressed compacts were approximately 20 mm in diameter and 2 mm in thickness. The compacts were sectioned to desired dimensions, mounted on bakelite medium and then metallographically polished with successive grades of diamond papers by means of a unique combination of grinding and polishing in order to reduce the contribution of the surface roughness on the nanoindentation measurement.

2.2. Surface characterization

The polished B_6O samples were analyzed for crystal structure and phase composition using X-ray diffraction, with Cu Kα radiation. The powder diffraction patterns were collected using the Bragg–Brentano backscattering geometry over a 10–90° 2θ range, with a 0.02° step size.

All the microstructural observations were done using scanning electron microscopy (SEM) with energy-dispersive X-ray spectroscopy analysis (EDX). whilst the specimen surface roughness and topography were characterized using atomic force microscopy (AFM). Gwyddion v2.22, a modular multiplatform software for profilometric data analysis was used to analyze both SEM and AFM images.

2.3. Nanoindentation measurements

Nanoindentation measurements were performed with using a CSM Instruments NHTX Nano-hardness Tester at Nelson Mandela Metropolitan University, Port Elizabeth. The characteristic nanoindentation $P-h$ curve of B_6O was measured under a 100 mN peak load using a Berkovich diamond indenter. The indentation load-time profile shown in Fig. 1 is characterized with loading/unloading rate of 2000 nm/min and a holding time of 25 s. The indentations were carried out under room environment.

For the evaluation of the measured $P-h$ curves, the O& P method was used [25–27], assuming a Poisson's ratio of 0.16 for elastic modulus calculation. In the work reported here the Poisson's ratio of hot-pressed B_4C, whose structure is similar to that of B_6O, was used as an estimate of B_6O's Poisson's ratio. The assumption being that a rough estimation of Poisson's ratio for does not significantly affect the obtained results [28]. At least twelve separate indents were performed at different positions on the sample surface.

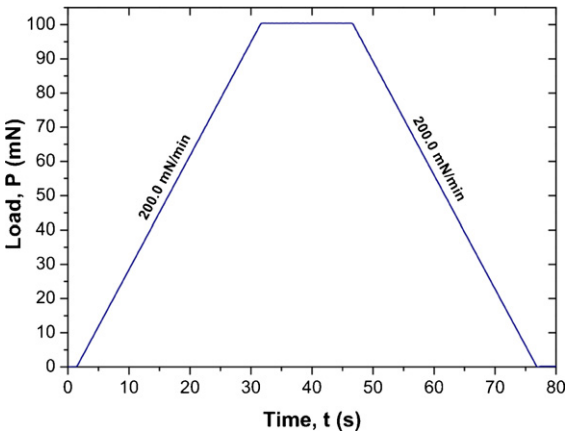

Fig. 1. An instrumented indentation load-time profile for all the experiments and all results presented in this article.

3. Results and discussions

3.1. Surface characterization

The full profile X-ray powder diffraction pattern shown in Fig. 2 is characteristic of a nominally pure polycrystalline B_6O. The dominant diffraction peaks can be perfectly indexed to the XRD pattern of B_6O reported elsewhere [24,29].

The surface morphology and compositional analysis of hot-pressed B_6O specimen as determined by SEM and EDX are shown in Fig. 3(a) and (b), respectively.

In general, the micrograph shows a homogeneous B_6O microstructure with visible pores on the specimen surface as a direct result of some considerable practical challenges in the densification of B_6O by hot pressing [1,10,11]. The analysis of the surface composition by EDX is also indicative of nominally pure B_6O phase. The observed iron contamination (a few wt.%) is negligible, however, inevitable and expected, since it originates from abrasion of the steel ball and the containment cell during powder ball milling.

A typical AFM image of the specimen is shown in Fig. 4. Apparently, the image shows a fairly uniform surface topography with no evidence of visible elastic deformation artifacts (such as pile-ups or sink-ins) around the indentation residual impression over a scan size of 3.8 μm×3.8 μm.

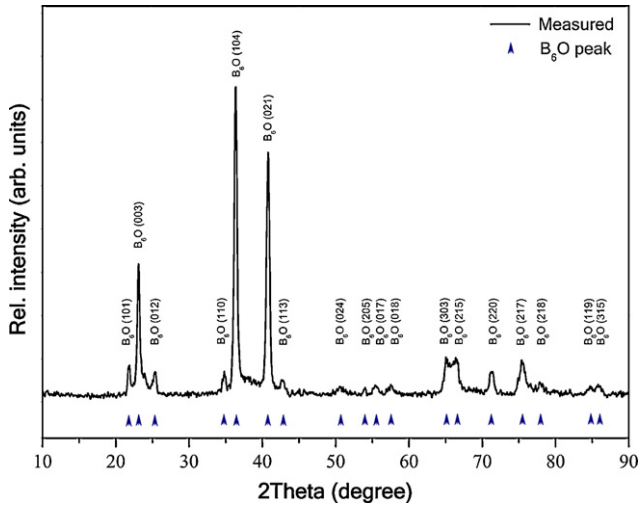

Fig. 2. The powder diffraction pattern of a sample of hot-pressed B_6O sample showing the predominance of the B_6O crystalline phase.

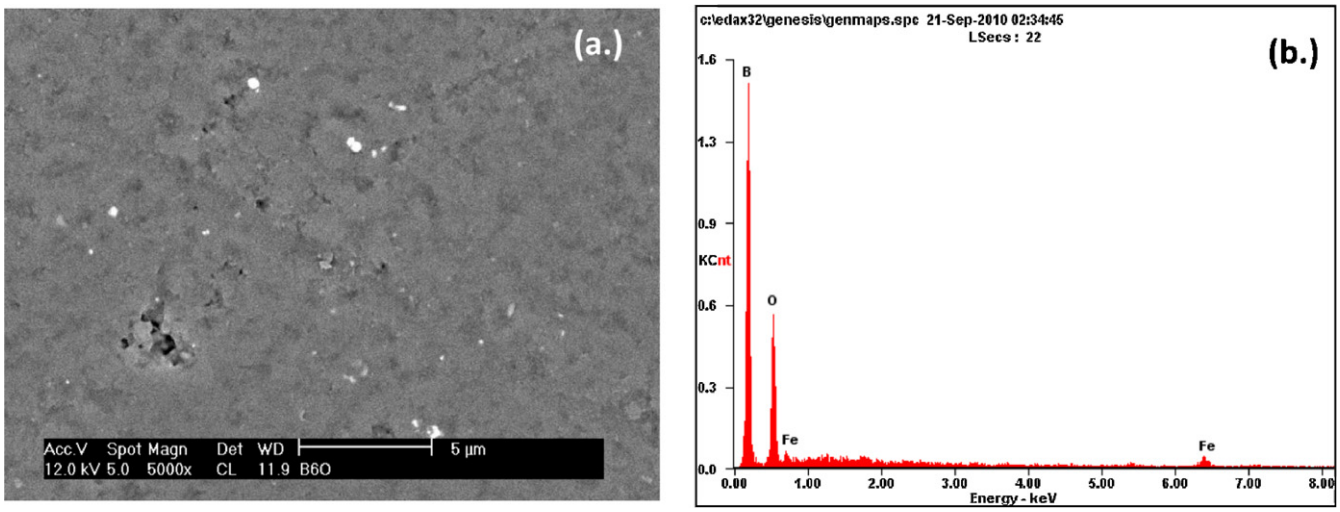

Fig. 3. Shows the SEM surface micrograph (a) and the EDX surface compositional analysis (b) of a hot pressed B_6 O specimen. Iron contamination is responsible for EDX elemental peak observed around 2.25 keV.

Using Gwyddion v2.22 for profilometric data analysis, the surface roughness of the specimen was determimed from the AFM images. The specimen surface appears to be characterized with an average roughness (R_a) of about 7 nm with a root mean square surface roughness amplitude (R_q) of 9 nm. Clearly, the surface roughness at the indentation an average site is a very small fraction of the maximum indentation depth and therefore, it does not appear to influence the mechanical properties significantly.

3.2. Nanoindentation measurements

3.2.1. Measured nanoindentation data

Fig. 5 below depicts the representative $P-h$ data for hot-pressed B_6O measured during nanoindentation tests with a Berkovich diamond indenter at room temperature. The curve demonstrates a smooth shape with no pop-in behaviour observed.

From the measured $P-h$ unloading curves, the nanohardness – H_{op}, the intrinsic hardness – $H(E)$, the elasticity modulus – E, and the unloading contact stiffness – S (=$(dP/dh)_{unloding}$) are evaluated in accordance with the O& P approach [25–27]. The results are summarized in Table 1.

The hardness values of H_{op} and $H(E)$ calculated from the experimentally measured nanoindentation data are consistent with literature reported values [1–3].

Since a close examination of the reported $P-h$ cycles demonstrates that the individual cycle curves show similar loading and unloading behaviour [18], see also Gong et al. [16]. Şahin et al. [20] suggest that this indicates similar elastic and plastic deformation mechanism on the load range used. We therefore expect that a load-displacement ($P-h$) curve measured at a single peak applied load can adequately define the ISE behaviour of a material since each loading $P-h$ curve is expected to contain a wealth of elastic and plastic deformation characteristics of a material [18], although this approach is not commonly used in the nanoindentation data analysis.

From here onwards, we attempt to make use of the loading $P-h$ data segment recorded during a single nanoindentation measurement to simulate multicycling loading–unloading $P-h$ cycles measured under different peak loads between 0.5 mN and 100 mN. It should be noted that the entire unloading $P-h$ cycle is not easy to simulate using this 'pseudo-multicycling' approach. However, we exploit the notion that the initial unloading slope of a $P-h$ cycle is a manifestation of the pure elastic recovery of material [19] and therefore seems to be sample invariable.

3.2.2. 'Modified' nanoindentation data

The stiffness of the material, S is assumed here to be material constant determined from the initial slope of the experimentally measured unloading data. By extrapolating the initial unloading slope of the unloading $P-h$ curve (used to calculate S) down to $P=0$ defines a displacement value h_c associated with the peak load,

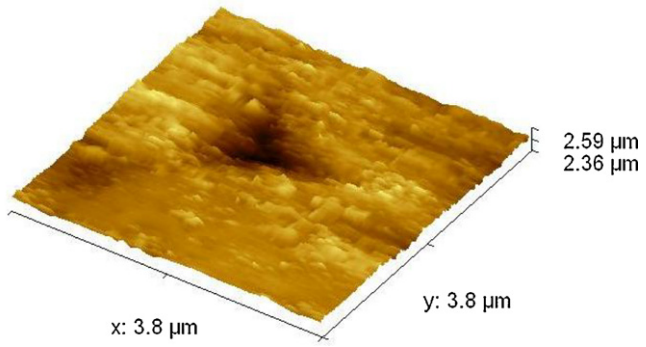

Fig. 4. AFM image showing the indentation impression on the specimen surface.

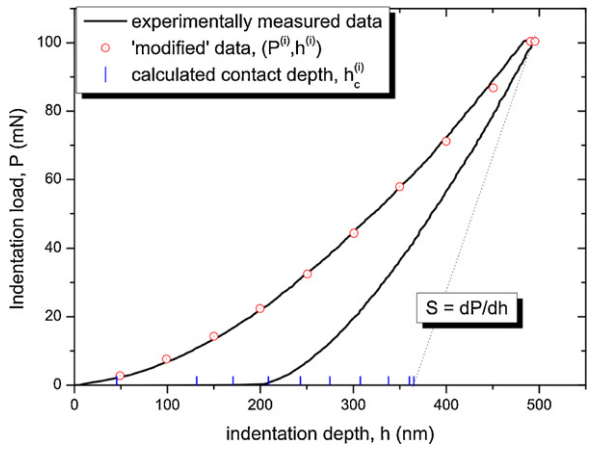

Fig. 5. A representative load-displacement curve measured during the nanoindentation measurements on the uniaxially hot-pressed boron suboxide compact also showing the modified data.

Table 1
Nanomechanical material properties evaluated using the O& P approach from the data of the $P-h$ curves shown in Fig. 5.

	E (GPa)	H_{op} (GPa)	H(E) (GPa)	S (mN/nm)	A(h_c) (10^6 nm^2)	m
This study	363.4	28.4	30.7	0.5667	3.27	1.53
Literature cited	230 – 476 [30]	–	–	–	–	–

P_{max}. However, if prior knowledge of the variation of the stiffness with indenter displacement is available, it can be used instead of S.

Using a simple code written in MATLAB we have selected and collected ten equally spaced data points, $(P^{(i)}, h^{(i)})$, from the experimentally measured loading $P-h$ data. Given the observation and assumptions alluded to in the previous paragraph, we can speculate that if a sequence of ten loading–unloading nanoindentation cycles were to be carried out at the same position at load in the range $P^{(1)}$ to $P^{(10)}$, then the MATLAB subroutine-collected $(P^{(i)}, h^{(i)})$ could easily be the new set of data defining the maximum load and maximum indentation size defined as $(P^{(i)}_{max}, h^{(i)}_{max})$.

The contact depth, $h_c^{(i)}$, at the maximum load, $P^{(i)}_{max}$, can then be calculated according to Oliver–Pharr's empirical formula:

$$h_c^{(i)} = h^{(i)}_{max} - \epsilon\frac{P^{(i)}_{max}}{S} \tag{1}$$

where $\epsilon = 0.75$ is a function of the particular tip geometry (for the Berkovich indenter) [27].

By definition, the indentation hardness, H, of the sample at each peak load, P_{max} can be calculated as:

$$H = \frac{P_{max}}{A_c} \tag{2}$$

where A_c is the projected area of contact [19,27]. In general, A_c is known to be a function of contact depth of the indent impression and is normally taken to be a good approximation of the actual contact area at the peak load [19,27] given as:

$$\begin{aligned} A(h_c^{(i)}) &\approx 24.56(h_c^{(i)})^2 \\ &\approx 24.56\left(h^{(i)}_{max} - \epsilon\frac{P^{(i)}_{max}}{S}\right)^2 \end{aligned} \tag{3}$$

Accordingly, substituting Eq. (3) into Eq. (2) yields the indentation hardness of the sample, $H^{(i)}$.

$$H^{(i)} \approx \frac{P^{(i)}_{max}}{24.56\left(h^{(i)}_{max} - \epsilon\frac{P^{(i)}_{max}}{S}\right)^2} \tag{4}$$

which is similar to the one proposed by Carneiro et al. [21]. The hardness values calculated using the current approach (Eq. (4))) are plotted against the applied nanoindentation load as shown in Fig. 6 below.

Evidently, the calculated hardness is a function of the indentation load. At low indentation load there is no constant hardness value. At high applied indentation test load, the hardness is load-independent. The observed load-independent hardness value close to 31 GPa is consistent with the load-independent Vickers hardness value of 30 GPa derived earlier on in this paper as well the literature reported values [1–3].

Using the 'modified' nanoindentation data set, $(P^{(i)}_{max}, h_c^{(i)}, H^{(i)})$, we attempt to analyze the ISE behaviour in B_6O using various models including: the Meyer's law, PSR and MPSR models, and the MFSL model.

3.2.3. Meyer's law

The classical power law shown in Eq. (5) is also known as the Meyer's equation and is frequently used when describing the ISE

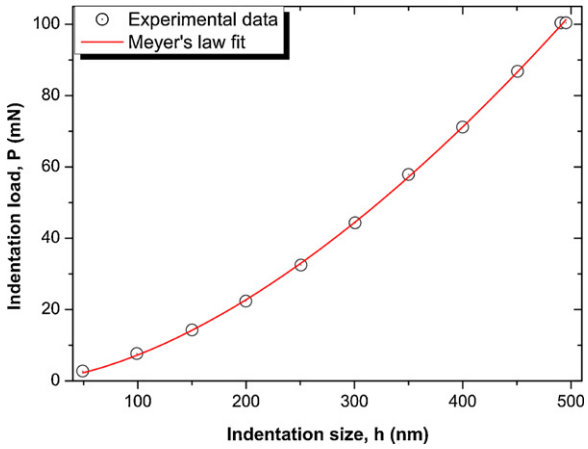

Fig. 6. Hardness calculated according to Eq. (4) plotted against the nanoindentation load, P.

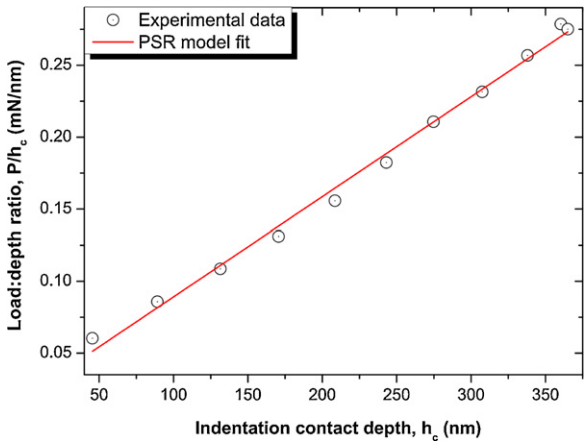

Fig. 7. Loading segment classical Meyer's law fitting of $P^{(i)}_{max}$ against $h_c^{(i)}$ curves.

for ceramic and other materials [19]. B and n are descriptive parameters that are deduced by power-law curve fitting of experimental $P-h$ curve. B is a power-fit constant and the exponent n is the Meyer's index, also known as the size-effect index.

$$P^{(i)}_{max} = B(h^{(i)}_{max})^n \tag{5}$$

The loading segment of the $P-h$ nanoindentation data and the power-law fitting are all plotted in Fig. 7 on the same axis. The results summarized in Table 2 show the variation of the descriptive parameters n and B derived from the Meyer's law fitting of experimental $P-h$ data.

The size-effect index indicates the decrease in the measured hardness with the increasing applied indentation test load or, as in this case, the indentation size. It has been reported that when a

Table 2
Descriptive parameters n and B derived from the Meyer's law fitting of experimental load-displacement as illustrated in Fig. 7.

	B	n	R^2
Values	2.37×10^9	1.64	99.60%

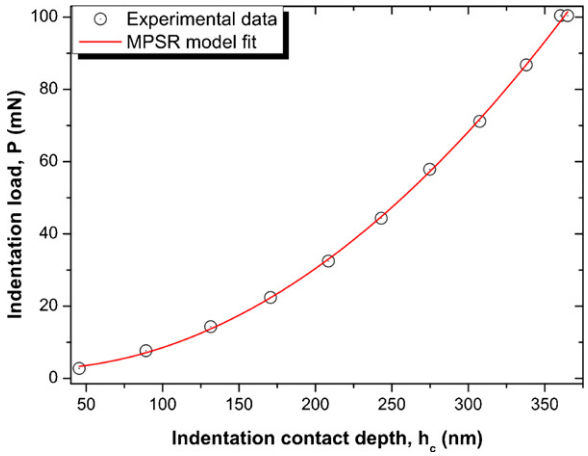

Fig. 8. The experimental data in the loading segments of the load-displacement curves shown in Fig. 2 were re-plotted as $P^{(i)}_{max}/h^{(i)}_c$ against $h^{(i)}_c$ and a best linear fit of the results.

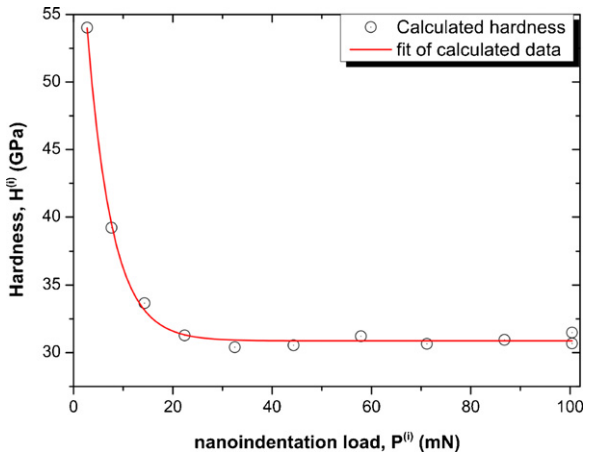

Fig. 9. A plot of $P^{(i)}_{max}$ versus $h^{(i)}_c$, and curve fitting thereof, according to the MPSR model.

material exhibits the normal ISE behaviour, then $n \leq 2$, when $n \geq 2$, there is reverse ISE behaviour and when $n = 2$, the hardness is independent of applied load. In other words when n bears the value of $n \approx 2$ there is no evidence for indentation size effects [13,22].

3.2.4. PSR model

However, several studies [20] have reported that the classic Meyer law is probably insufficient to describe the origin of the ISE. Therefore, an alternative method is required to achieve a basic understanding of the ISE of hot-pressed B_6O. According to Li and Bradt's PSR model [20,22] the applied test load, $P^{(i)}$ is related to the contact depth h_c as follows:

$$P^{(i)} = a_1 h^{(i)}_c + a_2 (h^{(i)}_c)^2 \tag{6}$$

The parameters a_1 and a_2 are constants for a given material. The parameters are related to the elastic and the plastic properties of the test material, respectively. The contact depth $h^{(i)}_c$ is calculated from Eq. (1).

From Eq. (6), a plot of $P^{(i)}_{max}/h^{(i)}_c$ against $h^{(i)}_c$ can be constructed to yield a straight line, where best-fit parameters a_1 and a_2 can easily be obtained by regression analysis. As shown in Fig. 8 below, a plot of $P^{(i)}_{max}/h^{(i)}_c$ against $h^{(i)}_c$ is significantly linear, implying that Eq. (6) does give an indication if the existence of ISE in hot-pressed B_6O.

The PSR analysis can be extended to use the a_2 parameter can be related to the plastic properties of the test material, respectively. Especially, a_2 is suggested to be a measure of the so-called intrinsic hardness, H_{PSR}. For the nanoindentation test with a Berkovich diamond indenter, H_{PSR} can be determined directly from a_2 using Eq. (7):

$$H_{PSR} = \frac{P^{(i)}_{max} - a_1 h^{(i)}_c}{24.56 (h^{(i)}_c)^2} = \frac{a_2}{24.56} \tag{7}$$

Thus, one can conclude that the existing PSR model does provide a satisfactory explanation of the ISE of hot-pressed B_6O.

3.2.5. Modified PSR model

Gong et al. [15] modified the PSR model to investigate the ISE behaviour in various materials. The resulting MPSR model is defined by Eq. (8) below:

$$P^{(i)} = a_0 + a_1 h_c + a_2 (h^{(i)}_c)^2 \tag{8}$$

where a_0 is a constant related to the residual surface stresses associated with the surface grinding and polishing processes during sample preparation. The parameters a_1 and a_2 are constants as defined in the PSR model above. The values of a_0, a_1 and a_2 can be evaluated by plotting the $P^{(i)}_{max}$ data against $h^{(i)}_c$. The plot of $P^{(i)}_{max}$ versus $h^{(i)}_c$ (and curve fitting thereof according to the MPSR model) is illustrated in Fig. 9 below.

As is the case for the PSR model, a hardness value, H_{MPSR} can be determined directly from best-fit value of a_2 from Fig. 9 as shown in Eq. (9) below:

$$H_{MPSR} = \frac{P^{(i)}_{max} - a_0 - a_1 h^{(i)}_c}{24.56 (h^{(i)}_c)^2} = \frac{a_2}{24.56} \tag{9}$$

The estimated best-fit values of the a_0, a_1, and a_2 parameters corresponding H_{MPSR} values are listed in Table 3. The residual surface stresses contribution to the observed ISE is negligible compared to the contribution of bulk material's plastic deformation characteristics.

3.2.6. MFSL model

According to Carpinteri and Puzzi [23], like other material properties such as surface roughness, tensile strength, and fracture data analysis, ISE in nanohardness can be described by the multifractal analysis following Eq. (10):

$$H^{(i)} = H_{MFSL} \sqrt{\left(1 + \frac{h^*}{h^{(i)}_c}\right)} \tag{10}$$

where H_{MFSL} is the intrinsic hardness in the limit of infinite (a huge) applied load and h^* is the critical material characteristic length which individuates the transition between the two regimes; a Euclidean one ($h \to \infty$) and a fractal one ($h \to 0$). ISE is observed to vanish in the limit of the applied load.

In the Euclidean regime, In this study H_{MFSL}, an asymptotic value of hardness which resembles a load-independent or intrinsic value and h^* were determined simultaneously by means of non-linear

Table 3
A summary of the best-fit parameters calculated according to the PSR and MPSR models.

Model	a_0	a_1	a_2 ($\times 10^{11}$)	H (GPa)
PSR	–	19711	6.95	28.3±0.3
MPSR	0.0026	20591	7.99	32.5±0.3

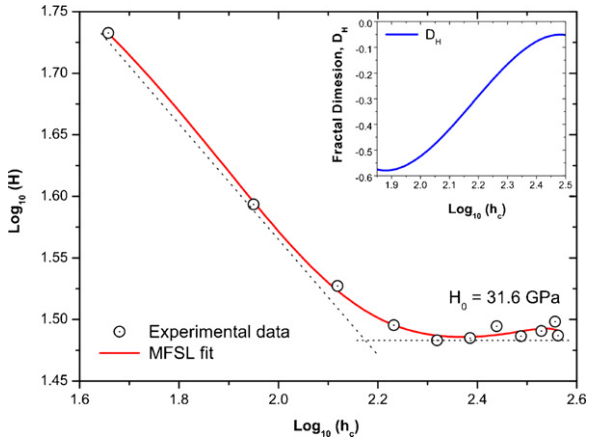

Fig. 10. Hardness calculated according to Eq. (10) plotted against the Vickers microindentation load, P. The slope of the plot equals D_H, a fractal dimension for hardness with respect to log (h_c). In the insert the fractal dimensional increment D_H is plotted as a function of log (h_c). Nonlinearity of the scaling fractal dimensional suggests multifractal behaviour.

Table 4
Summary of hardness values evaluated in this study. The average intrinsic nanohardness of hot-pressed B_6O was observed to be 31.6 ± 0.4 GPa.

	Hardness values (GPa)			
	$H(E)$	H_{PSR}	H_{MPSR}	H_{MFSL}
This study	30.7 ± 0.1	28.3 ± 0.3	32.5 ± 0.3	31.6 ± 0.4

least squares analysis of the experimental data using Mathematica. H_{MFSL} was determined to be 31.6 GPa.

In the ISE regime, in order to study the fractal characteristic depicted in Fig. 10, a bi-logarithmic plot of the nanohardness and the indentation contacts displacement was constructed based on Eq. (10). The slope of the log–log plot shown as an insert in Fig. 10 represents the fractal dimensional increment D_H. The result shows that log H as a function of the log h_c is approximately linear in two limiting conditions of the scale dependence: $D_H \approx -0.6$ for small indents (fractal response), whilst $D_H \approx 0$ for large indents (Euclidean response). The fractal response corresponds to the highest possible ISE behaviour in hardness and as mentioned earlier, whilst the Euclidean response corresponds to the scale invariant or true hardness, H_{MFSL}. Accordingly, the cross-over between the extremes implying a progressive vanishing of fractality in the measured hardness with increasing indentation size.

It is in our view that, although the Meyers index (Eq. (5)) is commonly considered a measure of ISE [20], the multi-fractal analysis presented here shows that the fractal dimensional D_H, can be interpreted as a measure of the variable influence of ISE on the measured nanoindentation hardness with obvious advantages.

4. Summary and conclusions

Vickers microhardness and Berkovich nanohardness indentations were conducted and analyzed. The load-dependence of hardness was characterized through the application of Meyer's law, the proportional specimen resistance models, and the 'pseudo-multicycling' approach with good agreement with each other.

From these results, it can be concluded that the surface residual stresses' contribution to the observed ISE is negligible compared to the contribution of bulk specimen's plastic deformation characteristics. Although there is not enough evidence from this study, the friction between the indenter and the test specimen may as well contribute to the origins of the ISE.

A summary of the hardness values calculated is shown in Table 4 below. The average intrinsic nanohardness of hot-pressed B_6O was observed to be 31.6 ± 0.4 GPa. The hardness of HPHT B_6O has been reported elsewhere to be 45 GPa [1].

Even though the presented 'pseudo-multicycling' analysis is in good agreement with other seasoned models, it should be noted that this analysis still requires further experimental work to verify its validity. That work is in progress.

Acknowledgements

The authors gratefully acknowledge the useful contributions of S. Shrivastava, W. Goosen, O.T. Johnson, M. Herrmann, and J. Neethling and the generous financial support from the DST/NRF Centre of Excellence in Strong Materials and the University of the Witwatersrand Mellon Postgraduate Award.

References

[1] M. Herrmann, J. Raethel, A. Bales, K. Sempf, I. Sigalas, M. Hoehn, J. Eur. Ceram. Soc. 29 (12) (2009) 2611–2617.
[2] A. Andrews, I. Sigalas, M. Herrmann, Boron suboxide composite material, WIPO Patent no. 2008132675, 2008.
[3] G.J. Davies, I. Sigalas, M. Herrmann, T. Shabalala, Boron suboxide composite material, US Patent no. 20080317654, 2008.
[4] J.E. Lowther, Physica B 322 (1–2) (2002) 173–178.
[5] H. Werheit, Chapter 23: Boron and Boron-Rich Compounds in Electric Refractory Materials, Tech. Rep., 2000.
[6] A.K. Suri, C. Subramanian, J.K. Sonber, T.S.R.C. Murthy, Int. Mater. Rev. 55 (1) (2010) 4–40.
[7] D.J. Roberts, J. Zhao, Z.A. Munir, Int. J. Refract.Met. H. Met. Hard Mater. 27 (2009) 556–563.
[8] V.L. Solozhenko, O.O. Kurakevych, JPCS 121 (2008) 62001.
[9] O.O. Kurakevych, V.L. Solozhenko, Solid State Commun. 149 (47–48) (2009) 2169–2171.
[10] O.T. Johnson, I. Sigalas, E.N. Ogunmuyiwa, H.J. Kleebe, M.M. Muller, M. Herrmann, Ceram. Int. 36 (6) (2010) 1767–1771.
[11] M. Herrmann, H.J. Kleebe, J. Raethel, K. Sempf, S. Lauterbach, M.M. Muller, I. Sigalas, J. Am. Ceram. Soc. 92 (10) (2009) 2368–2372.
[12] Z. Wang, Y. Zhao, P. Lazor, H. Annersten, S.K. Saxena, Appl. Phys. Lett. 86 (4) (2005) 041911.
[13] O. Şahin, O. Uzun, U. Kölemen, N. Uçar, Mater. Charact. 59 (4) (2008) 427–434.
[14] J. Gong, J. Wu, Z. Guan, Mater. Lett. 38 (3) (1999) 197–201.
[15] J. Gong, J. Wu, Z. Guan, J. Eur. Ceram. Soc. 19 (15) (1999) 2625–2631.
[16] J. Gong, H. Miao, Z. Peng, Acta Mater. 52 (2004) 785–793.
[17] A. Krell, S. Schädlich, Mater. Sci. Eng. A 307 (1–2) (2001) 172–181.
[18] B. Wolf, A. Richter, New J. Phys. 5 (1) (2003) 15.
[19] J. Gong, H. Miao, Z. Peng, L. Qi, Mater. Sci. Eng. A 354 (1) (2003) 140–145.
[20] O. Şahin, O. Uzun, M. Sopicka-Lizer, H. Gocmez, U. Kölemen, J. Eur. Ceram. Soc. 28 (6) (2008) 1235–1242.
[21] J.O. Carneiro, V. Teixeira, A. Portinha, S.N. Dub, R. Shmegera, Rev. Adv. Mater. Sci. 7 (2004) 83–90.
[22] H. Li, R.C. Bradt, J. Mater. Sci. 31 (1996) 1065–1070.
[23] A. Carpinteri, S. Puzzi, Eng. Fract. Mech. 73 (2006) 2110–2122.
[24] A. Andrews, M. Herrmann, T.C. Shabalala, I. Sigalas, J. Eur. Ceram. Soc. 28 (8) (2008) 1613–1621.
[25] W.C. Oliver, G.M. Pharr, J. Mater. Res. 7 (6) (1992) 1564–1583.
[26] W.C. Oliver, G.M. Pharr, J. Mater. Res. 19 (1) (2004) 3–20.
[27] G.M. Pharr, A. Bolshakov, J. Mater. Res. 17 (10) (2002) 2660–2671.
[28] G.Z. Voyiadjis, A.H. Almasri, T. Park, Mech. Res. Commun. 37 (3) (2010) 307–314.
[29] V.L. Solozhenko, O.O. Kurakevych, P. Bouvier, J. Raman Spectrosc. 40 (8) (2009) 1078–1081.
[30] D. Music, J.M. Schneider, J. Phys.: Condens. Matter 20 (19) (2008) 195203.

Hindawi Publishing Corporation
Advances in Materials Science and Engineering
Volume 2012, Article ID 792973, 11 pages
doi:10.1155/2012/792973

Research Article

Mechanical and Structural Properties of Fluorine-Ion-Implanted Boron Suboxide

Ronald Machaka,[1,2] Bonex W. Mwakikunga,[3,4] Elayaperumal Manikandan,[3,5] Trevor E. Derry,[1,6] Iakovos Sigalas,[1,2] and Mathias Herrmann[7]

[1] *DST/NRF Centre of Excellence in Strong Materials, University of the Witwatersrand, Private Bag 3, Wits, Johannesburg 2050, South Africa*
[2] *School of Chemical and Metallurgical Engineering, University of the Witwatersrand, Private Bag 3, Wits, Johannesburg 2050, South Africa*
[3] *National Centre for Nano-Structured Materials, CSIR, P.O. Box 395, Pretoria 0001, South Africa*
[4] *Department of Physics and Biochemical Sciences, University of Malawi, The Polytechnic, Private Bag 303, Chichiri, Blantyre 0003, Malawi*
[5] *Nano Centre, Polymer Nanotechnology Center & Department of Physics, B. S. Abdur Rahman University, Vandalur, Chennai-600048, India*
[6] *School of Physics, University of the Witwatersrand, Private Bag 3, Wits, Johannesburg 2050, South Africa*
[7] *Fraunhofer Institute for Ceramic Technologies and Systems, Winterbergstraße 28, 01277 Dresden, Germany*

Correspondence should be addressed to Ronald Machaka, ronald.machaka@wits.ac.za

Received 30 April 2011; Revised 18 September 2011; Accepted 19 September 2011

Academic Editor: W. Ensinger

Results on a systematic study on the effects of ion implantation on the near-surface mechanical and structural properties of boron suboxide (B_6O) prepared by uniaxial hot pressing are reviewed. 150 keV fluorine ions at fluences of up to 5.0×10^{16} ions/cm^2 were implanted into the ultrahard ceramic material at room temperature and characterized using Raman spectroscopy, atomic force microscopy, and scanning electron microscopy with energy-dispersive X-ray spectroscopy. Evidence of ion-beam-assisted nucleation of novel clustered $B_xO_yF_z$ particles by ion implantation is revealed. In addition, obtained results also reveal that fluorine implantation into the B_6O specimen leads to an overall degradation of near-surface mechanical properties with increasing fluorine fluence. Implications of these observations in the creation of amorphous near-surface layers by high-dose ion implantation are discussed in this paper.

1. Introduction

Energetic ions have been of interest to researchers for their capability of (i) characterization of materials, (ii) modification of materials, and more recently (iii) synthesis of new materials. Of particular interest is the possibility of ion beams to circumvent thermodynamic limits related to conventional methods such as diffusion, solubility, deposition, and alloy formation by providing high kinetic energy through ion impact and utilizing ballistic effects during ion-solid interaction [1–4]. Moreover, ion implantation allows the precise control of the ion energy, ion fluence, dopant distribution as well as a choice of the ion species. As a result the surface modification conditions can also be influenced with a great deal of reproducibility and control for specific needs, that is, either synthesis, modification, or characterization of materials.

The increasing fascination with low-dimensional material structures is mainly motivated by the search for new materials with tunable novel properties of evident technological relevance. It is therefore not surprising that nanostructured materials are gaining growing importance due to their unique properties that are intermediate between those corresponding to the bulk solids and molecules. In recent years many groups have reported on the ion-beam-assisted

synthesis of novel nanostructured materials by ion implantation [3, 5–7]. In addition, unique and sometimes superior mechanical [1, 8], structural [2, 9–11], optoelectronic [7, 12], corrosion, and tribomechanical surface properties [2, 13] of the ion-implanted materials have also been reported.

Boron suboxide, B_6O, is an superhard boron-rich ceramic material. It exhibits a rather unusual and wide range of superior properties; among these are high hardness with low density, high mechanical strength, oxidation resistance up to high temperatures as well as its chemical inertness [14–18]. The potential applications of B_6O as ideal wear-reduction coatings for high-speed cutting tools, abrasives, or other high-wear applications, for example, have been an object of intense interest in recent years [19, 20]. However, despite the intensive research efforts, the commercial applications are yet to be realized. This is partly because of the low fracture toughness of hot-pressed materials [17, 18] and the considerable practical challenges associated with the densifying stoichiometric B_6O material with good crystallinity [17, 18]. Furthermore, numerous mechanical properties of the material were until recently rather poorly understood [14, 21].

Preliminary first-principle ab initio density functional calculations of the structural properties of boron suboxide (nominally B_6O) by Lowther suggest that the strength of the bonding in B_6O (and other boron-rich superhard materials such as B_4C and $AlMgB_{14}$) may be enhanced by the presence of a high electronegativity interstitial in the structure [22]. The computational calculations confirm the shortening of covalent bonds which is believed to favour higher elastic constants and hardness values. By introducing energetic fluorine ions into B_6O using ion implantation—a nonequilibrium technique of choice for introducing "controlled" defects into the near-surface layers [4, 23]. To the best of our knowledge, no work has been reported on effect of ion implantation on the near-surface mechanical and structural properties of B_6O.

In our work, the radiation effects of the ceramic material under heavy ion irradiation have been studied to develop an understanding of the radiation resistance evolution with respect to the material properties. We apply nanoindentation, Raman spectroscopy, atomic force microscopy (AFM), and scanning electron microscopy (SEM) with energy-dispersive X-ray spectroscopy (EDX) to demonstrate the synthesis of $B_xO_yF_z$ clustered particles using 150 keV fluorine ion implantation into B_6O. This paper reviews results obtained in the study.

2. Experimental Methods

B_6O powder synthesized at the Fraunhofer Institute for Ceramic Technologies and Systems, Dresden, Germany, by reacting B and B_2O_3 as detailed by Andrews et al. in [18] was prepared and uniaxially hot-pressed in *h*BN pots under argon environment at 1800°C and 50 MPa for 20 min at the School of Chemical and Metallurgical Engineering, University of the Witwatersrand, Johannesburg, South Africa. The hot-pressed compacts were then prepared using a method prescribed by Machaka et al. in [21]. The density of the hot-pressed compacts measured 2.44 g/cm^3.

Table 1: The nomenclature of the unimplanted and implanted samples.

Sample no.	Ion species	Energy keV	Fluence F^+/cm^2
A	—	—	—
B	F^+	150	1.0×10^{14}
C	F^+	150	5.0×10^{14}
D	F^+	150	5.0×10^{15}
E	F^+	150	1.0×10^{16}
F	F^+	150	3.0×10^{16}
G	F^+	150	5.0×10^{16}

150 keV fluorine ions were implanted into hot-pressed B_6O specimen at fluences between 1.0×10^{14} to 5.0×10^{16} ions/cm^2 at room temperature. A modified Varian-Extrion 200-20A2F model ion implanter at iThemba LABS (Gauteng), Johannesburg was used. The nomenclature of the unimplanted and implanted samples is tabulated in Table 1. The depth distribution of the radiation damage and implanted ion profile were estimated using SRIM2010 [24], a suite of Monte Carlo computational codes popular for the simulation of the interactions of energetic ions with the target material.

The specimen's surface microstructure and composition were characterized by SEM and EDX, respectively. The specimen surface topography was characterized using AFM. Gwyddion v2.24 [25], a modular multiplatform software for profilometric data analysis, was used to analyze AFM images. The powder diffraction patterns were collected using a Cu K_α source in the Bragg-Brentano backscattering geometry over a 10°–90° 2θ range, with a 0.02° step size. Raman measurements performed at the CSIR's National Centre for nanostructured materials nanomaterial characterization facility under ambient conditions using a 514.5 nm Ar^+ ion excitation were used to characterize the ion beam induced structural modifications whilst the mechanical properties of the unimplanted and implanted samples were determined using nanoindentation at Nelson Mandela Metropolitan University, Port Elizabeth. Details of the experimental procedures of the Raman spectroscopy and the nanoindentation measurements are also reported elsewhere [14, 26].

3. Results and Discussions

3.1. Structural Characterization

3.1.1. Implant Depth Profile. The distribution of the implanted fluorine ions estimated using SRIM2010 can be described as a near-Gaussian shape function characterized with a projected range of about 450 nm and an estimated range straggling of about 60 nm. However, in practice we are aware that the SRIM estimation does not take into account the possible surface sputtering, dynamic annealing, and diffusion processes taking place during ion implantation.

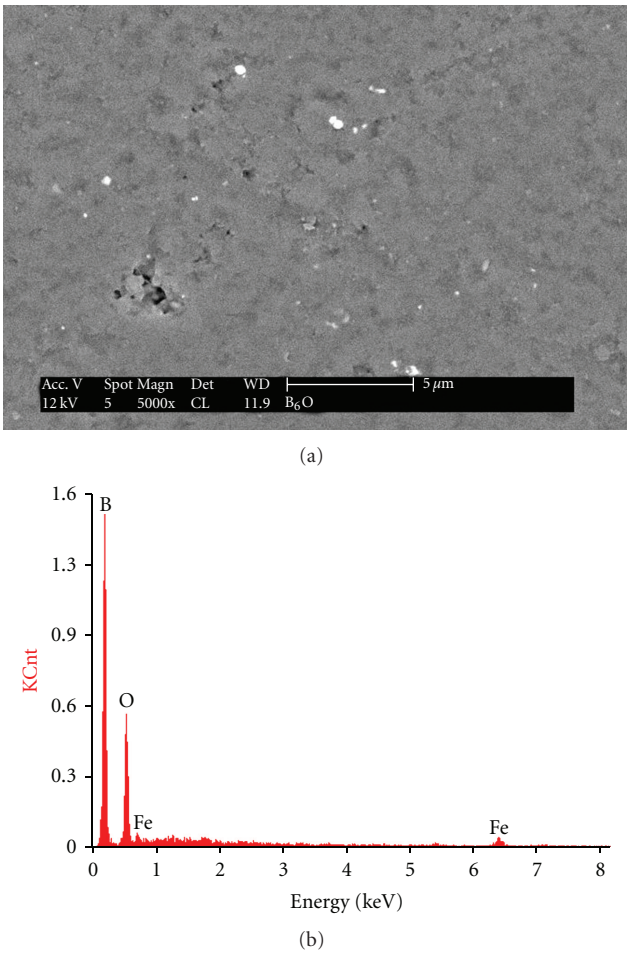

FIGURE 1: It shows the SEM surface micrograph (a) and the EDX surface compositional analysis (b) of the hot-pressed B_6O specimen. Iron contamination (bright spots on SEM micrograph) is responsible for EDX elemental peaks observed.

3.1.2. SEM and EDX Analysis. The surface morphology and compositional analysis of unimplanted B_6O specimen as determined by SEM and EDX are shown in Figures 1(a) and 1(b), respectively. By and large, the SEM micrograph shows a homogeneous B_6O microstructure with visible pores on the specimen surface as a direct result of some considerable practical challenges in the densification of B_6O by hot pressing [15–17].

The analysis of the surface composition by EDX is also indicative of nominally pure B_6O phase. The observed iron contamination (typically a few wt.%) is expected and unavoidable possibly as a direct consequence of the abrasion of the steel ball and the containment cell during powder ball milling [19, 20, 27].

The SEM and EDX analysis of the heavily implanted specimen (B4 in Figures 2(b)–2(d)), for example, shows obvious dissimilarities between the unimplanted and the implanted specimen. Firstly, in addition to the homogeneous B_6O phase the surface pores and the iron and chromium contamination, SEM micrographs show evidence of the existence of additional clusters of ion-beam-synthesized particles. Secondly, image analysis of the microstructure (Figures 2(b) and 2(c)) indicates that the average particle sizes of the formed clusters is 110 nm. Thirdly, the measured EDX pattern shows two weak iron peaks at 0.75 ev and 6.4 eV. Although the positions of the 0.75 eV iron peak and the fluorine peak coincide, there appears to exist enough evidence observed to indicate a $B_xO_yF_z$ stoichiometry for the ion-beam-synthesized clustered particles. We have also observed that the compositional change becomes more significant with increasing fluorine implantation dose. The B_6O signature EDX pattern unimplanted specimen is depicted in Figure 1(b) [15, 28].

3.1.3. Raman Spectroscopy Analysis. Raman scattering spectroscopy is very sensitive to the nature of crystalline structure, disorder, and amorphization and is often employed to characterize ion-implantation-induced defects and any irregularity in the crystalline symmetry. The rather popular technique offers a rapid, nondestructive, and simple diagnostic probe for the evaluation of the structural modifications imposed by ion implantation and for optical characterization of ion-implanted specimens since the penetration depth of the laser beam is often of the order of the depth of penetration of implanted ions.

Figures 3 and 4 show the Raman spectra of pristine (specimen A) and F^+-implanted hot-pressed B_6O (specimens B to G). The Raman spectrum of the pristine specimen is characteristic of nominal composition B_6O [21, 29–32].

The measured Raman spectra are evidently characterized by a relatively low Raman signal to noise ratio. Nevertheless, it is not difficult to see that F^+ implantation at fluences up to 5.0×10^{15} ions/cm^2 reveals that the material resists amorphization and retains the crystal structure of B_6O. At the same time, implantation at fluences above 5.0×10^{15} ions/cm^2 clearly shows that the signature Raman spectrum of B_6O predominately disappears (specimen D).

Rao et al. [33, 34], in Raman scattering spectroscopy, the main effect in going from the crystalline to amorphous form is the introduction of characteristic features in the frequencies and line shapes of the Raman modes. However, for a diatomic lattice, the effect of amorphization should be a decrease in intensity of the lattice modes and even the disappearance of these modes at higher ion implantation doses. Accordingly, we tentatively attribute the disappearance of the signature B_6O Raman spectrum at implantation fluences exceeding 5.0×10^{15} ions/cm^2 to amorphization as a result of ion-induced radiation damage.

Measured spectra on samples implanted at fluences beyond 5.0×10^{15} ions/cm^2 reveal an almost unrelated and new asymmetrically broadened Raman feature centred around 1550 cm^{-1}. In general, it is widely accepted in the field that the observed line shape asymmetry is consistent with the size-dependent effects in measured Raman modes—optical phonon confinement [35]. The existence of ion-beam-synthesized aggregates made up of micro- and/or nanosized particles is known to exhibit this phenomenon. For example, we recently reported on the Raman spectra of *c*BN nanocrystals formed by He^+ ion implantation into

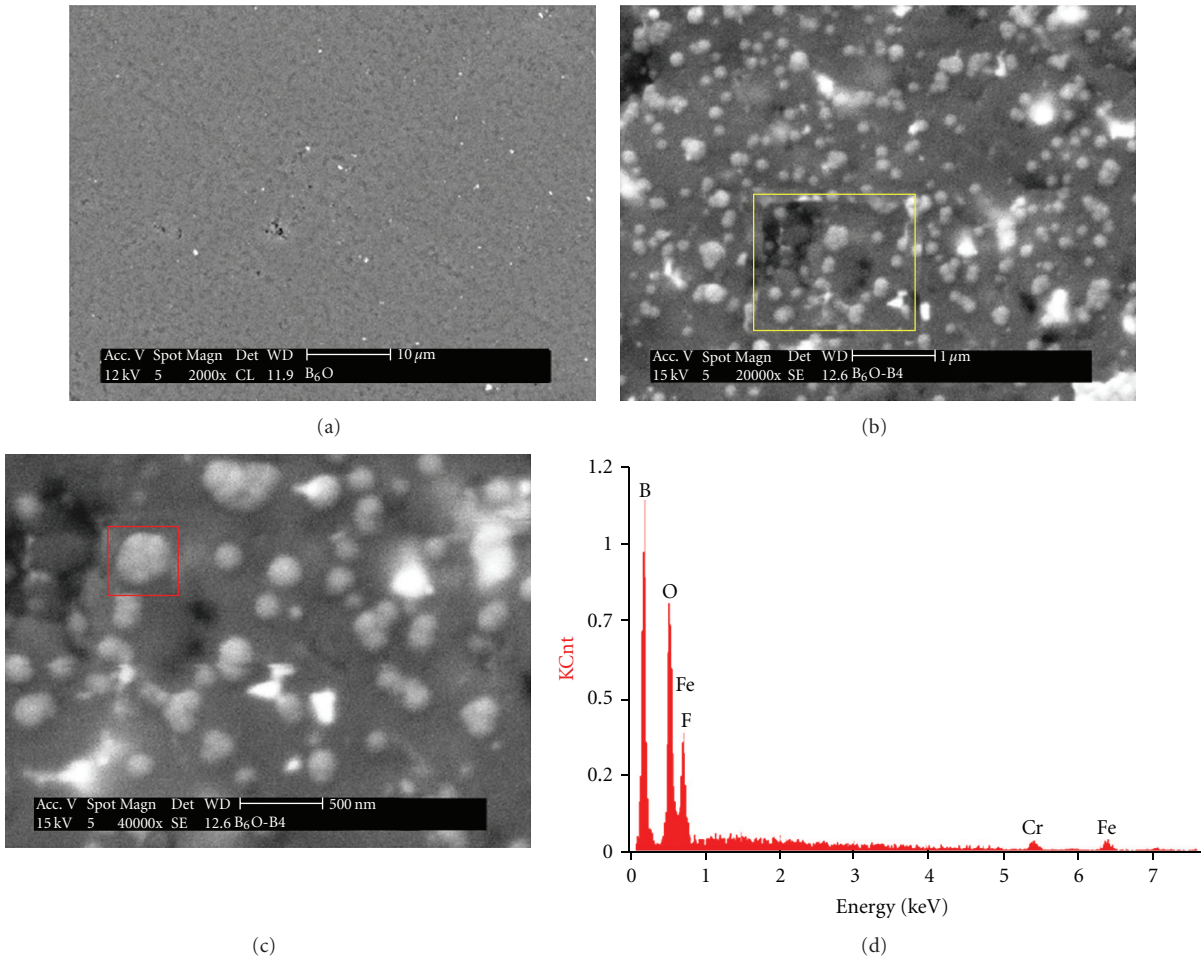

FIGURE 2: A depiction of SEM images measured on the surface of (a) an unimplanted B_6O specimen, ((b) and (c)) a 5.0×10^{15} F^+ ions/cm^2 implanted B_6O specimen showing clusters of particles embedded in the samples synthesized by fluorine-ion-beam implantation, and (d) an EDX measured pattern on one such ion-beam-synthesized cluster which is highlighted in micrograph (c).

*h*BN [9]. Several other researchers have also reported on the ion-beam synthesis of other nanostructures phased by ion bombardment [3, 5, 6]. In fact, ion implantation is a method of choice for synthesizing nc-Si in optoelectronics [7].

A further increase in the implantation fluence beyond 5.0×10^{15} ions/cm^2 gives rise to further increase in both width and intensity of the asymmetrically broadened Raman feature. Furthermore, increases in the feature's peak intensity with increasing ion dose may be a result of the increase in volume fraction of the clustered particles in the material surface layer. A critical fluence of about 3.0×10^{16} ions/cm^2 was observed beyond which the volume fraction of the clustered particles will reduce owing to the existence of surface sputtering and possibly radiation damage.

In summary, a possible explanation of this Raman scattering characteristic in ion-implanted B_6O could be the nucleation of a new micro- or nanocrystalline phase in the B_6O matrix. At higher doses, ion implantation creates a nonequilibrium solid-state supersaturation of the implanted ions in solutions which could induce the precipitation of ion-beam-synthesized nanostructured particle nuclei effectively, due to thermodynamic stabilization. These nuclei grow additionally as a result of the surface deposition of solvated ions. According to Shen et al. [8], the ion beam synthesis of the nanostructured particles could be conceptualized into several steps: (i) stopping and accumulation of F implants in the near-surface area of the host B_6O matrix, (ii) supersaturation of this area by F implants, (iii) formation of nuclei of a $B_xO_yF_z$ phase, and (iv) growth of the nanoparticles from the nuclei. Stepanov in reference [3] best illustrates the basic physical processes involved in the formation of nanoparticles from an implant with respect to the ion dose in Figure 5 shown below.

3.2. Mechanical Characterization. The representative indentation load-displacement (P-h) curves continuously measured during loading and unloading for the four specimens under investigation (unimplanted (specimen A) and fluorine implanted (specimens C, D, and G)) are shown in Figure 6. The intrinsic hardness $H(E)$ and the elastic modulus E of specimen were evaluated from the nanoindentation response curves by applying a modified O&P procedure as outlined in

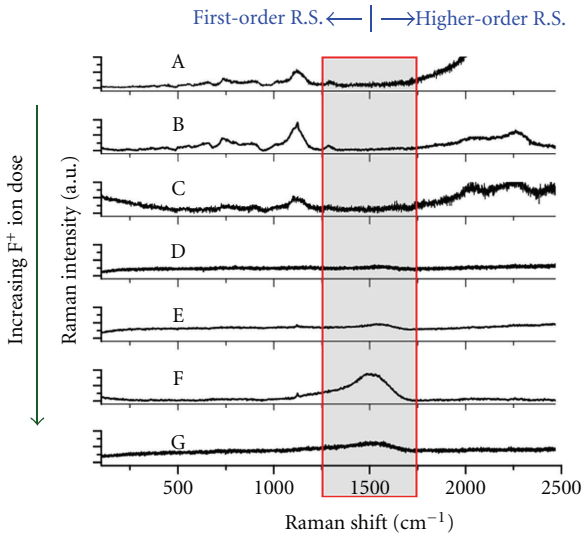

Figure 3: The Raman spectra of unimplanted (specimen A) and fluorine-ion-implanted (specimens B to G) B_6O specimen. The spectra are shifted along the y-axis for better comparison. The y-axis is normalized.

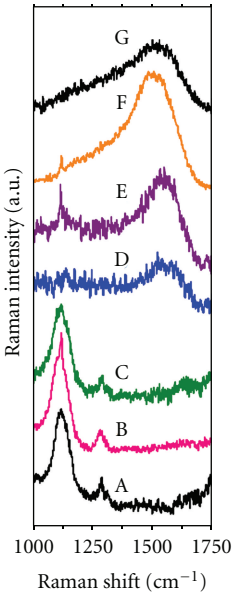

Figure 4: An expanded view of the normalized Raman spectra of the 1550 cm^{-1} mode. A comparison between measured (dotted curve) and calculated first-order Raman line shapes of ion-implanted B_6O. Again, the y-axis is normalized, and the spectra are shifted along the y-axis for better comparison.

Appendix A [37–39]. The AFM imaging of the indentation impressions and analysis has been relegated to Appendix B. An average surface roughness (determined from the AFM images, see Figure 9) of about 7 nm R_a measured on the surface appears to be a very small fraction of the maximum indentation depth and does not appear to influence the mechanical properties significantly. Table 2 shows a summary of the calculated values of $H(E)$ and E, as well as the ratio H/E and the Meyer's index, n (see (1) below), also calculated from the experimentally measured loading P-h curves.

In order to exhibit all dependences (of the mechanical properties on the fluence of implantation) in one figure for

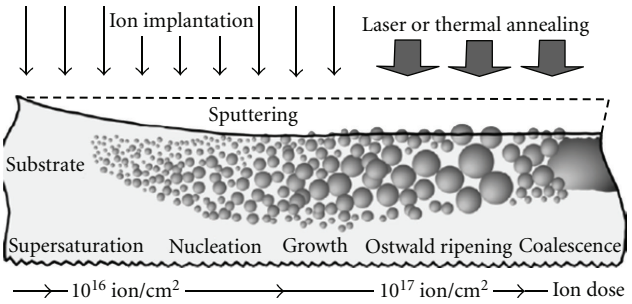

Figure 5: An illustration of the basic physical processes (from left to right) involved in the formation of clustered particles from an implant with respect to the ion dose. Surface sputtering under irradiation is also considered [36]. Diagram courtesy of Stepanov [3]. *Note*. In this study, all characterization was done on as-implanted specimen; no annealing was done.

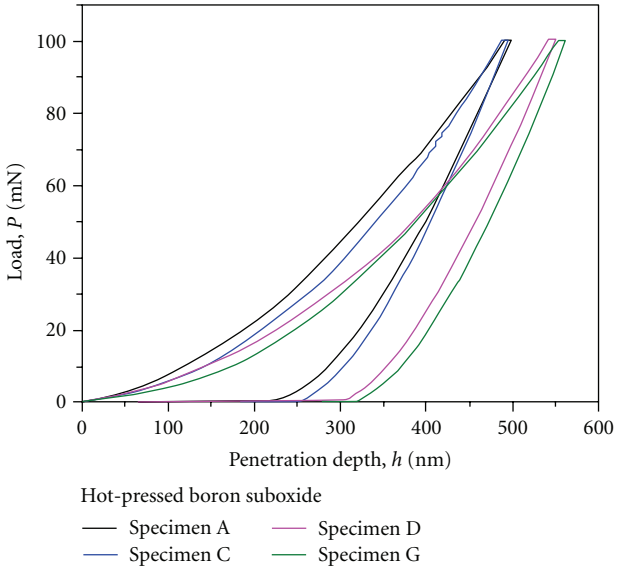

Figure 6: Representative indentation response curves measured during the nanoindentation measurements on the unimplanted (specimen A), and fluorine-implanted (specimen C, D, and G) hot-pressed boron suboxide specimen.

Table 2: A summary of the effect of ion implantation on $H(E)$, E, the ratio H/E, and the Meyer's index n.

Specimen	$H(E)$ GPa	E GPa	H/E	n
A	31.0	328.0	0.093	1.66
C	29.0	359.0	0.082	1.92
D	23.0	300.0	0.076	1.94
G	21.0	292.0	0.073	1.96

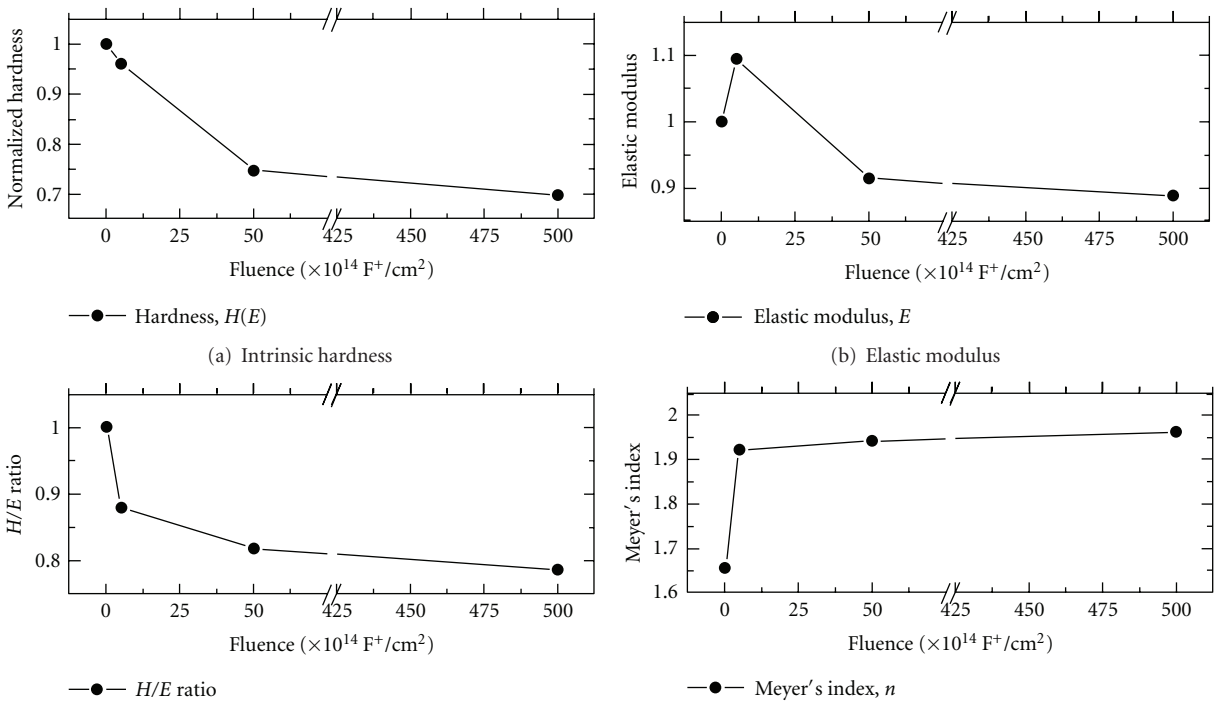

(a) Intrinsic hardness

(b) Elastic modulus

(c) H/E ratio

(d) The Meyer's index measured for hot-pressed B_6O samples irradiated with various fluences of F ions

Figure 7

ease of analysis and comparison, the calculated values were normalized to those measured for the control specimen A and presented in Figure 7.

The characterized mechanical properties are evidently influenced by the fluence of implantation. For example, an increase in the fluorine ion dose is observed to result in an overall decrease in the intrinsic hardness and the elastic modulus of the material, a decrease in the values of the ratio H/E, and a general increase in the Meyer's index values. These trends reflect the changes in the structure or the material, the mechanism of plastic deformation of the irradiated material, and most probably, after ion-implantation-induced amorphization of the pristine structure, as further discussed below.

3.2.1. Intrinsic Hardness. From the measured *P-h* curves, the intrinsic hardness of the control pristine B_6O specimen was evaluated to be 31 ± 0.2 GPa, a value in close agreement with recently published microhardness [15, 16] and nanohardness [40] values. The effect of F-ion implantation on the hardness value $H(E)$ is summarized in Figure 7(a). The change in the hardness value is quite small for implantation doses of up to 5×10^{14} F$^+$/cm^2, while a severe decrease of about 30% is observed for a dose of 5×10^{16} F$^+$/cm^2.

Two mechanisms of plastic deformation, namely, phase transformation and plastic flow, can be responsible for a change in hardness *during* a nanomechanical testing experiment. The main indicator for the operation of phase transformation during the nanoindentation experiment is the appearance of dislocation discontinuities (kinks or pop-ins) in the *P-h* curves [41, 42]. Their absence in the *P-h* curves of hot-pressed B_6O presented here (see Figure 6) suggests that the testing performed in the present study does not induce significant phase transformation; we suspect that the plastic deformation of hot-pressed B_6O is accomplished by plastic flow. We consider the plastic flow to be associated with structural changes caused by radiation damage and the subsequent fluorine irradiation-induced amorphization. This relation supports the suggestion of plastic flow as the deformation mechanism of the ion-implanted hot-pressed ceramic B_6O material. The softening of the ion-implanted specimen can be attributed to the amorphization of the surface layer, as identified by the micro-Raman spectroscopy characterization results.

3.2.2. Elastic Modulus. From the measured *P-h* curves, the elastic modulus of the pristine B_6O specimen was evaluated to be 330 ± 4 GPa, a value also consistent with previously published data [15].

The Young's modulus is clearly correlated with the amorphization of the crystalline structure, although for low-irradiation fluences the values increase by about 10% before rapidly decreasing as amorphization of the crystalline structure supposedly takes place. We propose that the effect of ion implantation on the elastic modulus is related to the induced decrease in the short-range order (distortion) of the B_{12} icosahedral network. The initial increase might be attributed to the increase of the concentration of the interstitial nitrogen ions in the implanted surface region. A lower elastic modulus of the implanted hot-pressed B_6O

Table 3: *H/E* ratios of B_6O and hard ceramic materials.

Material	*H/E* ratio
Diamond	0.09–0.1 [44]
Hot-pressed B_6O	**0.093**
B_4C	0.07–0.09 [44]
SiC	0.080 [44]
Si_3N_4	0.080 [44]
Silicon	0.062 [46]

could be associated with the implantation-induced increase in the B–B bond angle deviations or simply the collective distortion of the individual B_{12} icosahedra or/and the α-rhombohedral framework, as a result of ion bombardment (see Figure 7(b)); it is well accepted that material having crystalline phases has a higher modulus than the materials with amorphous structure [43]. This is an observation which correlates well with the measured Raman results discussed in this paper (Figure 3).

3.2.3. H/E Ratio. The ratio of $H(E)$ to E, (H/E) is known as the rigidity index, a key parameter in determining the type of behaviour observed in nanoindentation and nanoscratching wear [44–46]. The ratio H/E can be regarded as a tool to describe, rank, or calculate values for performance criteria which are important in defining the wear resistance of a material, such as the elastic strain to failure, the critical yield pressure for plastic deformation, and the fracture toughness. A high H/E ratio is often a reliable indicator of good wear resistance in a coating or layers [45, 47].

The pristine specimen shows a higher H/E ratio when compared to that of the implanted samples (refer to Figure 7(c)). This implies that F ion implantation of the B_6O surface at a larger fluence is expected to cause a considerable increase in the surface plasticity. The experimental sliding wear test data is not available at present. However, using this rigidity index approximation, we suspect that the wear resistance from the ion-irradiated surfaces is expected to degrade at a larger fluences of implantation.

The intrinsic hardness clearly correlates very well with the H/E ratio; this is no coincidence since hardness (or the plasticity) is known to have the decisive role of the surface layer on friction properties [45, 46].

A comparison of the H/E ratio of hot-pressed B_6O with other ultrahard ceramic materials is shown in Table 3.

3.2.4. Meyer's Index. To date, there exists immense experimental and theoretical evidence suggesting that, for some ceramic materials, the evaluated hardness value is not a material constant but rather a function of either the applied test load or the depth of the indentation—the indentation size effect (ISE) [48–52]. Several studies have reported that Meyer's law is sufficient to indicate the existence of ISE, although considered inadequate when describing the origins of ISE [48, 50]. The classic power law relationship shown in (1) is commonly known as Meyer's law:

$$P = A \cdot h^n. \tag{1}$$

Both A and n are constants for a particular sample. The descriptive parameters are usually deduced by a suitable regression analysis of the experimental load-displacement relations for the loading segment.

The parameter n is also known as the size-effect index. It is usually considered as a measure of ISE [50, 52]. The Meyer index has been experimentally observed to be between 1.5 and 2.0 for ceramics [48]. For the normal ISE behaviour, the exponent $n < 2$—the measured hardness apparently decreases with increasing applied test load. When $n > 2$, there is the reverse ISE behaviour. When $n = 2$, the hardness is independent of the applied test load.

In this study ISE curves were modelled on the basis of the Meyer's model [50, 53]. Figure 7(d) shows an increase in n with the increasing ion dose of fluorine ions. In other words, there is a point to make at higher doses where $n \to 2$; it appears there is the diminishing evidence of indentation size effects in hardness with increasing fluorine ion doses, and a single hardness value for the material exists.

4. Conclusions

The following conclusions are obtained from this study.

(i) For F^+ implantation at fluences below 5.0×10^{15} ions/cm^2 the hot-pressed B_6O samples resist amorphization and retain the B_6O crystal structure. However, for fluences above 5.0×10^{15} ions/cm^2, the signature Raman spectrum of B_6O disappears. Furthermore, beyond 5.0×10^{15} ions/cm^2, the Raman spectra appear to reveal that the fluorine implants in B_6O matrix could influence the precipitation of ion-beam-synthesized clusters of a $B_xO_yF_z$ phase.

(ii) AFM and SEM images complement the Raman spectroscopy results on the existence of agglomerated ion-beam-synthesized clustered particles on the ion-implanted specimen surface. Although not conclusive, the EDX compositional analysis hints that the clustered particles have a $B_xO_yF_z$ stoichiometry. The exact structure and stoichiometry of the new phase are yet to be determined.

(iii) In general, fluorine implantation of the specimen leads to an overall decrease in the intrinsic hardness and the elastic modulus of the material. These trends reflect on the changes in the structure or the material, the mechanism of plastic deformation of the irradiated material, and most probably, ion-implantation-induced amorphization of the pristine structure.

  (a) This relation tentatively supports the suggestion that plastic flow is the main deformation mechanism in ion-implanted hot-pressed ceramic B_6O material. The softening of the ion-implanted specimen can be attributed to the amorphization of the surface layer, as identified by the micro-Raman spectroscopy characterization results.

(iv) The decrease in both the H/E ratio and the Meyer's index with ion dose might imply that F ion implantation of the B_6O surface at a larger fluence is expected to cause a considerable increase in the surface plasticity.

Appendices

A. Oliver and Pharr Analysis Approach

The nanoindentation technique has been established as a powerful means of characterizing the near-surface mechanical properties of materials [54]. This technique relies on high-resolution instruments that simultaneously measure the load P and indenter displacements h, during the loading and unloading indentation steps. The important parameters obtained from the resultant P-h curve, which are schematically illustrated in Figure 8, are the peak load $P_{\max}$, the maximum penetration depth $h_{\max}$, final penetration depth h_f, and the contact stiffness S. The indentation analysis procedure developed by Oliver and Pharr (O&P) has been widely used for hard materials such as metals and ceramics [38, 39, 54].

The O&P method makes use of the data taken from the upper portion of the unloading curve fitted with the power-law relation given as

$$P = \alpha \cdot \left(h - h_f\right)^m, \tag{A1}$$

where m, the displacement exponent in the load-displacement relation and a, an unloading fitting parameter dependent on the elastic response of the material, are empirical constants to be determined using the power fitting of unloading data [49].

The derivative of P (A1) with respect to h yields the contact stiffness S, which is the initial unloading slope of the P-h curve:

$$\begin{aligned} S &= \left(\frac{dP}{dh}\right)_{\text{unloading}} \\ &= m \cdot \alpha \cdot \left(h - h_f\right)^{m-1}. \end{aligned} \tag{A2}$$

The contact depth of the indent impression h_c can either be derived by extrapolating the initial slope of the unloading P-h curve down to $P = 0$ or otherwise determined using an empirical formula as observed by Oliver and Pharr [38, 39] given by

$$h_c = h_{\max} - \epsilon \cdot \frac{P_{\max}}{S}, \tag{A3}$$

where, in this case for the Berkovich indenter geometry, $\epsilon = 0.75$ [38].

The contact area A_c is the cross-sectional area at h_c [55, 56]. Various experimental [56] and numerical [57] studies have established that, for the Berkovich indenter geometry,

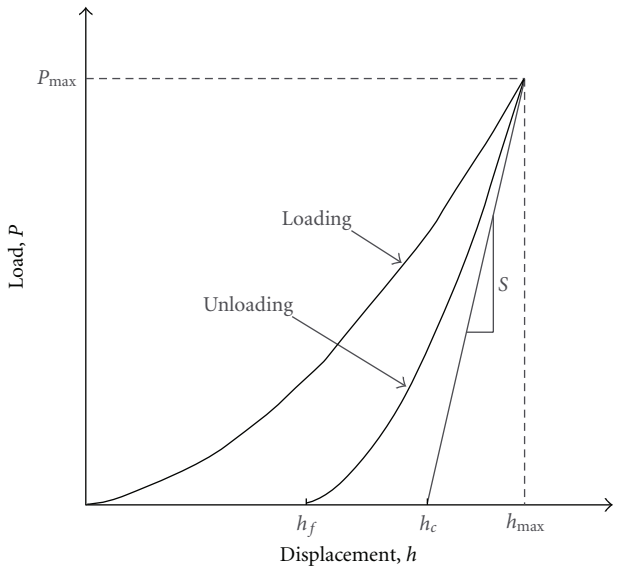

Figure 8: A typical load-displacement curve during a loading-unloading cycle where $h_{\max}$ is the maximum indenter displacement at peak indentation load $P_{\max}$, S is the initial unloading slope of the load-displacement curve, and h_c is the contact depth.

the projected A_c can be approximated by the empirical formula:

$$\begin{aligned} A_c(h_c) = \Big(&24.56 \cdot h_c^2 + C_1 \cdot h_c^{1/2} + C_2 \cdot h_c^{1/4} \\ &+ C_3 \cdot h_c^{1/8} + \cdots + C_8 \cdot h_c^{1/125}\Big), \end{aligned} \tag{A4}$$

where $C_1, C_2, \ldots, C_8$ are constants determined by curve-fitting procedures [55, 56] and are all defined based on the indenter tip radius [49]. However, for the Berkovich indenter geometry, projected area can be reduced to $A_c(h_c) \approx 24.56 \cdot h_c^2$ without compromising the accuracy of the results [54, 55, 58].

When S and A_c have been determined, the specimen's elastic modulus E_s or simply E can then be evaluated using

$$\frac{1}{E_r} = \frac{1 - \nu_s^2}{\mathbf{E_s}} + \frac{1 - \nu_i^2}{E_i}, \tag{A5}$$

where ν_s and ν_i are, respectively, the specimen and indenter Poisson ratios, E_i is the indenter elastic modulus [54, 58], and E_r is the reduced elastic modulus given by

$$E_r = \frac{\sqrt{\pi}}{2\beta} \cdot \frac{S}{\sqrt{A_c}}, \tag{A6}$$

where β is a correctional factor introduced by King [59] to address the lack of indenter symmetry; for the Berkovich indenter $\beta = 1.034$ [58].

The indentation hardness H has long been defined as the test force P divided by the projected area of contact A_c [60]:

$$H = \frac{P_{\max}}{A_c}. \tag{A7}$$

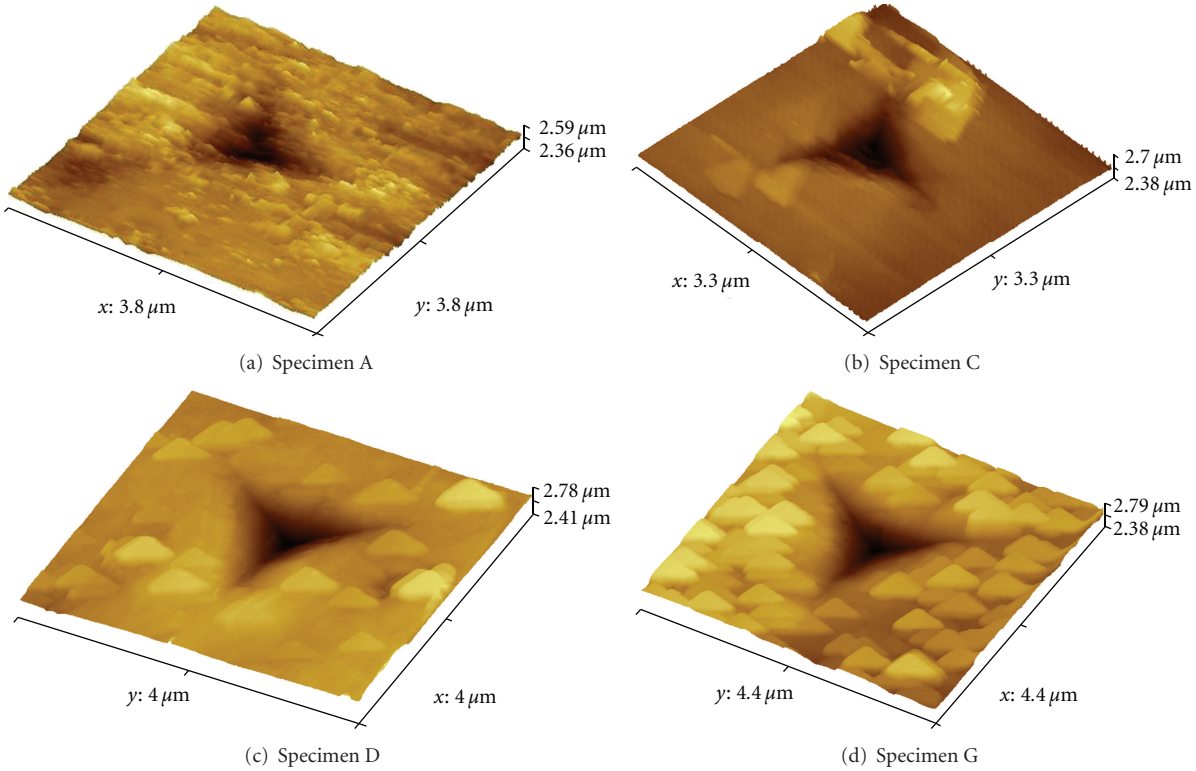

FIGURE 9: AFM images showing what could possibly be clusters of nanoparticles embedded in the samples synthesized by fluorine-ion-beam implantation, (a) unimplanted specimen A, and ((b)–(d)) fluorine-implanted specimens C, D, and G.

However, it is also generally understood that hardness values derived using (A7) are often depth and load dependent; a single value is often inadequate to implicitly characterize the material property.

In order to extract the true or the intrinsic hardness of the specimen we applied an important material characteristic ratio, P/S^2, first proposed by Joslin and Oliver [61, 62], expressed as

$$\frac{P}{S^2} = \frac{\pi}{4\beta^2} \cdot \frac{\mathbf{H}(\mathbf{E})}{E_r^2}. \tag{A8}$$

Evidently, P/S^2 is independent of h and A_c [62]. Therefore, if P is known and S and E_r have been predetermined, the intrinsic harness of specimen, $H(E)$, can be evaluated using (A8).

In summary, the method outlined here has been applied in this study to extract the material nanomechanical properties (E from (A5) and $H(E)$ from (A8) [62]) from the measured nanoindentation data.

B. Supplementary Results: AFM Analysis

The AFM image of the pristine B_6O specimen surface is shown in Figure 9(a). Using Gwyddion v2.24 for profilometric data analysis, the surface roughness of the specimen was determined from the AFM images. The specimen surface appears to be characterized with an average roughness (R_a) of about 7 nm with a root mean square surface roughness amplitude (R_q) of 9 nm.

The AFM images all bear Berkovich indenter impressions from hardness testing because the imaging was originally intended to give an intuitive understanding of the state of the specimen surfaces after nanoindentation. However, as shown in Figures 9(b)–9(d), striking morphological and structural transformations of the pristine material under ion irradiation have been observed.

The AFM images taken on the implanted samples depict an entirely different surface character from the pristine. Firstly, the images show compelling visual evidence of ion-beam-synthesized nanocrystalline structures decorating the specimen surfaces. Similar AFM structures have been also observed in metal ion-implanted oxide insulators by several authors and are usually attributed to the formation of the nanoparticles. Secondly, detailed image analysis measurements have demonstrated that the height of the particles is in the order of a few nanometres, with the average horizontal size of about 60 nm. However, it should be pointed out (at this stage) that, by using AFM observations, lateral dimensions of nanoclusters are usually enlarged due to the tip-object convolution effect and only height measurements can provide the real size of the main-size objects. Thirdly, we have also attributed the ion-beam-synthesized nanocrystalline structures observed in Figures 9(b)–9(d) to explain the variations of the line shapes of the Raman spectra of F ion-implanted hot-pressed B_6O as

shown in Figure 3 and reference [14]. Fourthly and lastly, the surfaces of the implanted samples appear to be much smoother in appearance than those of the pristine sample [63], tentatively suggestive that possible sputtering and other dynamic processes could have influenced the surface morphology of the specimen during implantation.

Acknowledgments

The authors are appreciative for the valuable contributions of O. T. Johnson, M. Herrmann, W. Goosen, J. Neethling, the Nelson Mandela Metropolitan University, and the Centre for Scientific and Industrial Research's National Centre for Nanostructured Materials. The financial support from the DST/NRF Centre of Excellence in Strong Materials and University of the Witwatersrand Mellon Postgraduate Award is also gratefully acknowledged.

References

[1] K. J. Kirkby and R. P. Webb, "Ion Implanted Nanostructures," in *Encyclopedia of Nanoscience and Nanotechnology*, H. S. Nalwa, Ed., vol. 4, pp. 1–11, American Scientific Publishers, 2004.

[2] I. Jain and G. Agarwal, "Ion beam induced surface and interface engineering," *Surface Science Reports*, vol. 66, no. 3-4, pp. 77–172, 2011.

[3] A. L. Stepanov, "Synthesis of silver nanoparticles in dielectric matrix by ion implantation: a review," *Reviews on Advanced Materials Science*, vol. 26, no. 1-2, pp. 1–29, 2010.

[4] J. F. Prins, "Modification, doping and devices in implanted diamond," in *Properties of Natuaral and Synthetic Diamong*, chapter 8, pp. 301–341, Academic Press Limited, 1992.

[5] J. Ghatak, B. Satpati, M. Umananda et al., "Characterization of ion beam induced nanostructures," *Nuclear Instruments and Methods in Physics Research B*, vol. 244, no. 1, pp. 45–51, 2006.

[6] D. K. Avasthi and J. C. Pivin, "Ion beam for synthesis and modification of nanostructures," *Current Science*, vol. 98, no. 6, pp. 780–792, 2010.

[7] H. Hosono and H. Kawazoe, "Approach to novel crystalline and amorphous oxide materials for optoelectronics by ion implantation," *Materials Science and Engineering B*, vol. 41, no. 1, pp. 39–45, 1996.

[8] Y. Shen, X. Li, Z. Wang et al., "Fabrication and thermal evolution of nanoparticles in SiO_2 by Zn ion implantation," *Journal of Crystal Growth*, vol. 311, no. 21, pp. 4605–4609, 2009.

[9] R. MacHaka, R. M. Erasmus, and T. E. Derry, "Formation of cBN nanocrystals by He^+ implantation into hBN," *Diamond and Related Materials*, vol. 19, no. 10, pp. 1131–1134, 2010.

[10] I. D. Desnica-Frankovi, K. Furi, U. V. Desnica, M. C. Ridgway, and C. J. Glover, "Structural modifications in amorphous Ge produced by ion implantation," *Nuclear Instruments and Methods in Physics Research B*, vol. 178, no. 1–4, pp. 192–195, 2001.

[11] T. W. H. Oates, L. Ryves, F. A. Burgmann et al., "Ion implantation induced phase transformation in carbon and boron nitride thin films," *Diamond and Related Materials*, vol. 14, no. 8, pp. 1395–1401, 2005.

[12] F. Komarov, L. Vlasukova, W. Wesch et al., "Formation of InAs nanocrystals in Si by high-fluence ion implantation," *Nuclear Instruments and Methods in Physics Research B*, vol. 266, no. 16, pp. 3557–3564, 2008.

[13] J. I. Oñate, F. Alonso, and A. García, "Improvement of tribological properties by ion implantation," *Thin Solid Films*, vol. 317, no. 1-2, pp. 471–476, 1998.

[14] R. Machaka, T. E. Derry, and I. Sigalas, "Nanoindentation hardness of hot-pressed boron suboxide," *Materials Science and Engineering A*, vol. 528, no. 18, pp. 5778–5783, 2011.

[15] M. Herrmann, H. J. Kleebe, J. Raethel et al., "Field-assisted densification of superhard B_6O materials with Y_2O_3/Al_2O_3 addition," *Journal of the American Ceramic Society*, vol. 92, no. 10, pp. 2368–2372, 2009.

[16] M. Herrmann, J. Raethel, A. Bales, K. Sempf, I. Sigalas, and M. Hoehn, "Liquid phase assisted densification of superhard B_6O materials," *Journal of the European Ceramic Society*, vol. 29, no. 12, pp. 2611–2617, 2009.

[17] O. T. Johnson, I. Sigalas, E. N. Ogunmuyiwa, H. J. Kleebe, M. M. Müller, and M. Herrmann, "Boron suboxide materials with Co sintering additives," *Ceramics International*, vol. 36, no. 6, pp. 1767–1771, 2010.

[18] A. Andrews, M. Herrmann, T. C. Shabalala, and I. Sigalas, "Liquid phase assisted hot pressing of boron suboxide-materials," *Journal of the European Ceramic Society*, vol. 28, no. 8, pp. 1613–1621, 2008.

[19] A. Andrews, *Development of boron suboxide composites with improved toughness*, Ph.D. thesis, School of Chemical and Metallurgical Engineering, University of the Witwatersrand0, 2009.

[20] C. S. Freemantle, *The wear studies of boron suboxide based cutting tool materials in machining applications*, M.S. thesis, School of Chemical and Metallurgical Engineering, University of the Witwatersrand, 2010.

[21] R. Machaka, B. W. Mwakikunga, E. Manikandan, T. E. Derry, and I. Sigalas, "Raman spectrum of hot-pressed boron suboxide," *Advanced Materials Letters*, vol. 2, p. 68, 2011.

[22] J. Lowther, Personal Communication, 2009.

[23] J. F. Prins, "Ion-implanted structures and doped layers in diamond," *Materials Science Reports*, vol. 7, no. 7-8, pp. 271–364, 1992.

[24] J. Ziegler, SRIM2010 (Software package), 2010, http://www.srim.org/.

[25] P. Klapetek, D. Necas, and C. Anderson, Gwyddion v2.24 (Software package), 2010, http://gwyddion.net/.

[26] R. Machaka, B. W. Mwakikunga, E. Manikandan, T. E. Derry, and I. Sigalas, "Structural transformation in ultrahard B_6O induced by F-ion implantation studied by micro-Raman spectroscopy," Unpublished.

[27] O. T. Johnson, *Improvement on the mechanical properties of boron suboxide (B_60) based composites using other compounds as second phase*, M.S. thesis, School of Chemical and Metallurgical Engineering, University of the Witwatersrand, 2009.

[28] O. T. Johnson, I. Sigalas, and M. Herrmann, "Microstructure and interfacial reactions between B_6O and (Ni, Co) couples," *Ceramics International*, vol. 36, no. 8, pp. 2401–2406, 2010.

[29] Z. Wang, Y. Zhao, P. Lazor, H. Annersten, and S. K. Saxena, "In situ pressure Raman spectroscopy and mechanical stability of superhard boron suboxide," *Applied Physics Letters*, vol. 86, no. 4, Article ID 041911, pp. 1–41911, 2005.

[30] H. Werheit and U. Kuhlmann, "FTIR and FT Raman spectra of B_6O," *Journal of Solid State Chemistry*, vol. 133, no. 1, pp. 260–263, 1997.

[31] S. Yu, Y. Ji, T. Li et al., "Nanofilms with clusters of boron suboxide and their infrared absorption," *Solid State Communications*, vol. 115, no. 6, pp. 307–311, 2000.

[32] V. L. Solozhenko, O. O. Kurakevych, and P. Bouvier, "First and second-order Raman scattering of B_6O," *Journal of Raman Spectroscopy*, vol. 40, no. 8, pp. 1078–1081, 2009.

[33] C. S. R. Rao, S. Sundaram, R. L. Schmidt, and J. Comas, "Study of ion-implantation damage in GaAs:Be and InP:Be using Raman scattering," *Journal of Applied Physics*, vol. 54, no. 4, pp. 1808–1815, 1983.

[34] S. S. Kumar, M. A. Khadar, S. K. Dhara, T. R. Ravindran, and K. G. M. Nair, "Photoluminescence and Raman studies of ZnS nanoparticles implanted with Cu^+ ions," *Nuclear Instruments and Methods in Physics Research B*, vol. 251, no. 2, pp. 435–440, 2006.

[35] A. K. Arora, M. Rajalakshmi, T. R. Ravindran, and V. Sivasubramanian, "Raman spectroscopy of optical phonon confinement in nanostructured materials," *Journal of Raman Spectroscopy*, vol. 38, no. 6, pp. 604–617, 2007.

[36] M. Nastasi and J. W. Mayer, *Ion Implantation and Synthesis of Materials*, Springer, Berlin, Germany, 2006.

[37] W. C. Oliver and G. M. Pharr, "Improved technique for determining hardness and elastic modulus using load and displacement sensing indentation experiments," *Journal of Materials Research*, vol. 7, no. 6, pp. 1564–1580, 1992.

[38] W. C. Oliver and G. M. Pharr, "Measurement of hardness and elastic modulus by instrumented indentation: advances in understanding and refinements to methodology," *Journal of Materials Research*, vol. 19, no. 1, pp. 3–20, 2004.

[39] G. M. Pharr and A. Bolshakov, "Understanding nanoindentation unloading curves," *Journal of Materials Research*, vol. 17, no. 10, pp. 2660–2671, 2002.

[40] X. Jiao, H. Jin, F. Liu et al., "Synthesis of boron suboxide (B_6O) with ball milled boron oxide (B_2O_3) under lower pressure and temperature," *Journal of Solid State Chemistry*, vol. 183, no. 7, pp. 1697–1703, 2010.

[41] S. R. Jian, G. J. Chen, and J. Y. Juang, "Nanoindentation-induced phase transformation in (1 1 0)-oriented Si single-crystals," *Current Opinion in Solid State and Materials Science*, vol. 14, no. 3-4, pp. 69–74, 2010.

[42] C. A. Schuh, "Nanoindentation studies of materials," *Materials Today*, vol. 9, no. 5, pp. 32–40, 2006.

[43] J. G. Wang, B. W. Choi, T. G. Nieh, and C. T. Liu, "Crystallization and nanoindentation behavior of a bulk Zr-Al-Ti-Cu-Ni amorphous alloy," *Journal of Materials Research*, vol. 15, no. 3, pp. 798–807, 2000.

[44] N. Laidania, A. Miotello, and J. Perrière, "Chemical, mechanical and electrical properties of CN_x-films produced by reactive sputtering and N^+-implantation in carbon films," *Applied Surface Science*, vol. 99, no. 4, pp. 273–284, 1996.

[45] A. Leyland and A. Matthews, "On the significance of the H/E ratio in wear control: a nanocomposite coating approach to optimised tribological behaviour," *Wear*, vol. 246, no. 1-2, pp. 1–11, 2000.

[46] P. Lemoine, J. P. Quinn, P. Maguire, and J. A. McLaughlin, "Comparing hardness and wear data for tetrahedral amorphous carbon and hydrogenated amorphous carbon thin films," *Wear*, vol. 257, no. 5-6, pp. 509–522, 2004.

[47] T. Oberle, "Properties influencing the wear of metals," *Journal of Metrologia*, vol. 3, p. 438, 1951.

[48] J. Gong, J. Wu, and Z. Guan, "Analysis of the indentation size effect on the apparent hardness for ceramics," *Materials Letters*, vol. 38, no. 3, pp. 197–201, 1999.

[49] J. Gong, H. Miao, and Z. Peng, "A new function for the description of the nanoindentation unloading data," *Scripta Materialia*, vol. 49, no. 1, pp. 93–97, 2003.

[50] O. Şahin, O. Uzun, U. Kölemen, and N. Uçar, "Mechanical characterization for β-Sn single crystals using nanoindentation tests," *Materials Characterization*, vol. 59, no. 4, pp. 427–434, 2008.

[51] O. Sahin, O. Uzun, M. Sopicka-Lizer, H. Gocmez, and U. Kölemen, "Dynamic hardness and elastic modulus calculation of porous SiAlON ceramics using depth-sensing indentation technique," *Journal of the European Ceramic Society*, vol. 28, no. 6, pp. 1235–1242, 2008.

[52] K. Sangwal, "On the reverse indentation size effect and microhardness measurement of solids," *Materials Chemistry and Physics*, vol. 63, no. 2, pp. 145–152, 2000.

[53] H. Li and R. C. Bradt, "The indentation load/size effect and the measurement of the hardness of vitreous silica," *Journal of Non-Crystalline Solids*, vol. 146, pp. 197–212, 1992.

[54] A. Fischer-Cripps, *Nanoindentation*, Springer, New York, NY, USA, 2nd edition, 2004.

[55] J. Gong, H. Miao, and Z. Peng, "Analysis of the nanoindentation data measured with a Berkovich indenter for brittle materials: effect of the residual contact stress," *Acta Materialia*, vol. 52, no. 3, pp. 785–793, 2004.

[56] J. Gong, H. Miao, and Z. Peng, "On the contact area for nanoindentation tests with Berkovich indenter: case study on soda-lime glass," *Materials Letters*, vol. 58, no. 7-8, pp. 1349–1353, 2004.

[57] K. D. Bouzakis and N. Michailidis, "Indenter surface area and hardness determination by means of a FEM-supported simulation of nanoindentation," *Thin Solid Films*, vol. 494, no. 1-2, pp. 155–160, 2006.

[58] N. Janakiraman and F. Aldinger, "Indentation analysis of elastic and plastic deformation of precursor-derived Si-C-N ceramics," *Journal of the European Ceramic Society*, vol. 30, no. 3, pp. 775–785, 2010.

[59] R. B. King, "Elastic analysis of some punch problems for a layered medium," *International Journal of Solids and Structures*, vol. 23, no. 12, pp. 1657–1664, 1987.

[60] B. Mott, *Microindentation Hardness Testing*, Butterworths, London, UK, 1956.

[61] D. L. Joslin and W. C. Oliver, "New method for analyzing data from continuos depth-sensing microindentation tests," *Journal of Materials Research*, vol. 5, no. 1, pp. 123–126, 1990.

[62] X. Y. Zhou, Z. D. Jiang, H. R. Wang, and Q. Zhu, "A method to extract the intrinsic mechanical properties of soft metallic thin films based on nanoindentation continuous stiffness measurement technique," *Journal of Physics*, vol. 48, no. 1, article 204, pp. 1096–1101, 2006.

[63] E. H. Lee, M. B. Lewis, P. J. Blau, and L. K. Mansur, "Improved surface properties of polymer materials by multiple ion beam treatment," *Journal of Materials Research*, vol. 6, no. 3, pp. 610–628, 1991.